Università degli Studi di Palermo

Denominazione Dottorato – Energia e Tecnologia dell'Informazione.

Denominazione del Dipartimento di riferimento – Dipartimento di Ingegneria.

Settore Scientifico Disciplinare – ING-INF/07

Study, project and implementation of new metrics for distributed measurement system in medium voltage smart grid

IL DOTTORE

Giuseppe Caravello

IL COORDINATORE

Prof. Maurizio Cellura

IL TUTOR

Prof. Antonio Cataliotti

CO TUTOR

Ing. Francesco Sergi

CICLO XXXIV° - Energia e Tecnologia dell'Informazione.

ANNO CONSEGUIMENTO TITOLO 2022.

Sommary

Abstract, Context and Motivations

In recent years there has been a fast evolution of the electricity grids, such as the high penetration into the grid by non-programmable renewable sources and the liberalization of the electricity market. These changes have led to the evolution of the network concept itself, no longer seen as a passive network, with few centralized generation systems and unidirectional power flows (bulk model), Figure 1, but as an active intelligent network, a smart grid, characterized by the presence of distributed energy resources DER also in distribution MV/LV grid (distributed model), Figure 2. To be more precise, the high voltage HV grid has been designed as active network with different distributed generators and for that reason this concept is not new for HV networks however the MV/LV network was thought as unidirectional power flow network in a "fit and forget" point of view. The shifting from bulk model to distributed model in a MV distribution network, more in detail, caused:

1. Bidirectional power flows or reverse power flows in MV distribution network

2. Unpredictability of renewable energy sources

3. Power quality degradation

4. Problem with protection automation

5. Increasing of short circuit current

6. Islanding

7. Stability issues

8. Increasing the complexity of diagnostic of new DC system

More in detail, the variability and unpredictability of distributed energy production, due to the aleatory nature of the renewable energy sources, in fact, can cause the inversion of the energy flow both in LV branches than in secondary and primary substation of MV grid. This inversion of the power flow produces power quality degradation due to overvoltage of the line. A further problem in passing the operation of the distribution network from passive to active is the power quality degradation due to the great number of power electronics-based systems (such as inverter and rectifier) which cause the injection of high order harmonics to the grid, the problems of the harmonic injection will be discussed next in detail. In addition, this reverse power flow causes some incompatibility with the automation of the network because, for example, the overvoltage can cause collision with transformers tap charger

or the reverse power flow can cause failure in the short circuit coordination because DER in health branches inject current into broken line and this current can be seen as a fault by the protection of the health line. This injected current produces also the fifth problem, specifically, the increasing of short circuit current. The islanding, sixth problem, is directly linked to the previous, specifically, when the entire network or a portion of its goes down, all of the generators must be disconnected from the grid, however, in the case of DER, this is made by local measurements but in such cases the algorithms fail to recognise the blackout. This allow to unsafe operation in particular for the operators. The seventh point, stability issues, is particularly critical for isolated grid. The unpredictable variability of solar and wind source can cause frequency variation when there is a temporarily inequality between produced power and absorbed power. Frequency variation is a power quality issue which can cause the activation of some protection system specially from the generation side. Finally, the last point, refers in the increasing percentage in the grid of DC systems. This shifting from AC to DC both to high power than to low voltage system like home user grid allows to have several diagnostic issues, because DC system cannot be monitored with the devices and protections of AC system.
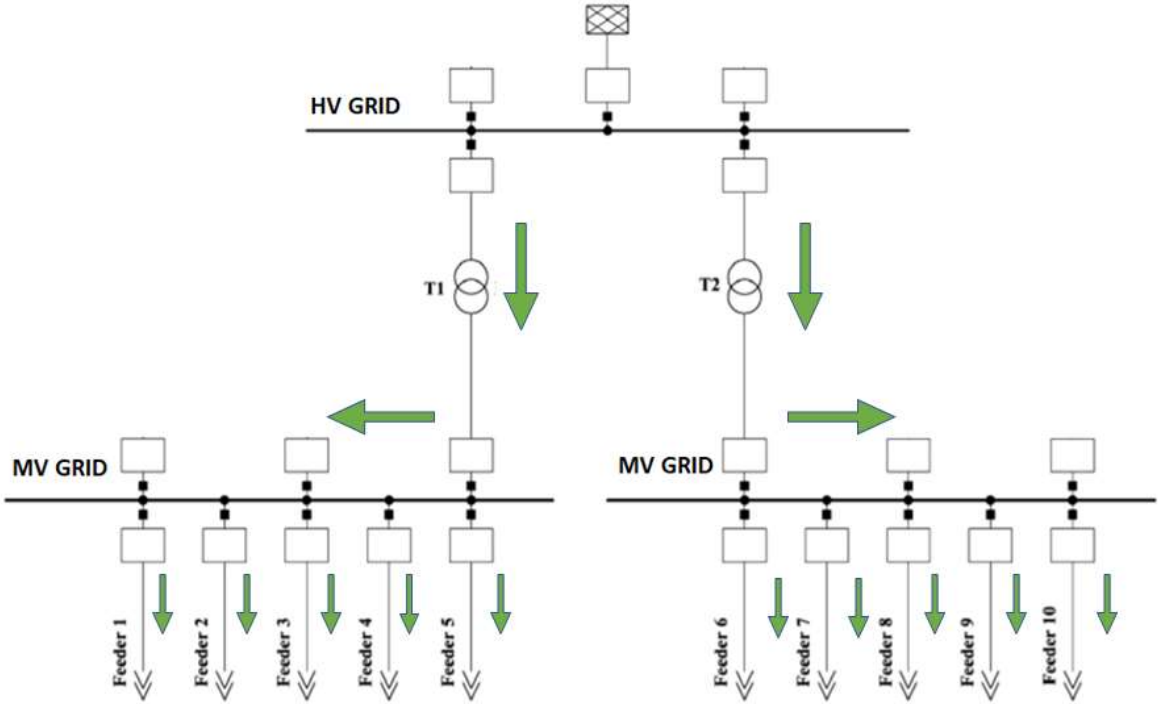
Figure 1 Bulk model, traditional grid
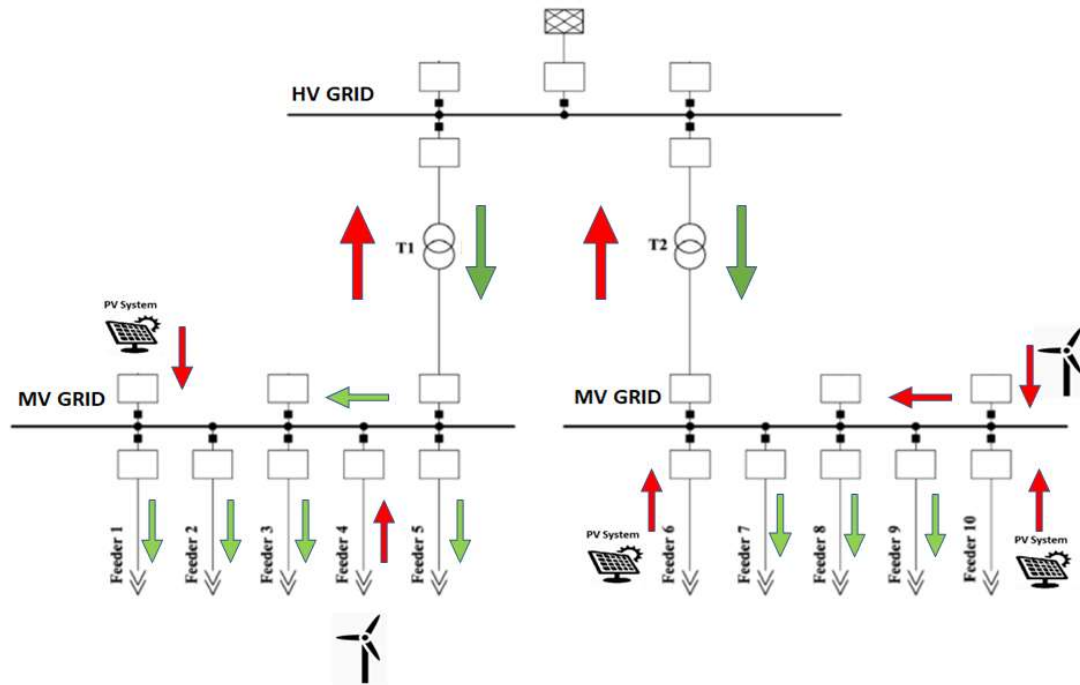
Figure 2 Actual grid with renewable sources and reverse power flows

In order to mitigate the power fluctuation of distributed generation, storage systems can be installed at different side of the grid able of injecting or absorbing energy when is needed (Figure 3). However, due to increase of the complexity of the system some new tools can be developed for the management and observability of the system. These issues can be managed only introducing a real time cooperation of distributed generators and energy storage systems in voltage and frequency regulation. Thus, traditional MV/LV electrical networks should evolve into smart grids with the introduction of a real-time monitoring system or a dedicate Supervisory Control And Data Acquisition (SCADA), which can take decisions and send commands to distributed generators, energy storage systems and energy users. SCADA provides real-time system information to the modelling and analysis tools. Hence the data integrity and expandability of the SCADA database are critical. Data integrity should be independent of any applications and new functions should be able to be integrated easily with the SCADA system without affecting existing applications. The first step to implement a SCADA is the diffusion of an accurate and cheap as possible communication infrastructure in the distribution network (Figure 4).

Some of the problems, in fact, could be avoided by resorting to direct communication between the distributor and the interface device of the DER and the storage systems. The communication vector would make it possible to implement new control and protection logics that would allow the possibility

of suddenly disconnecting the DERs in the case of possible failure events. However, the metrics and the protocols to react to a contingency on the grid are still an open problem to be solved.
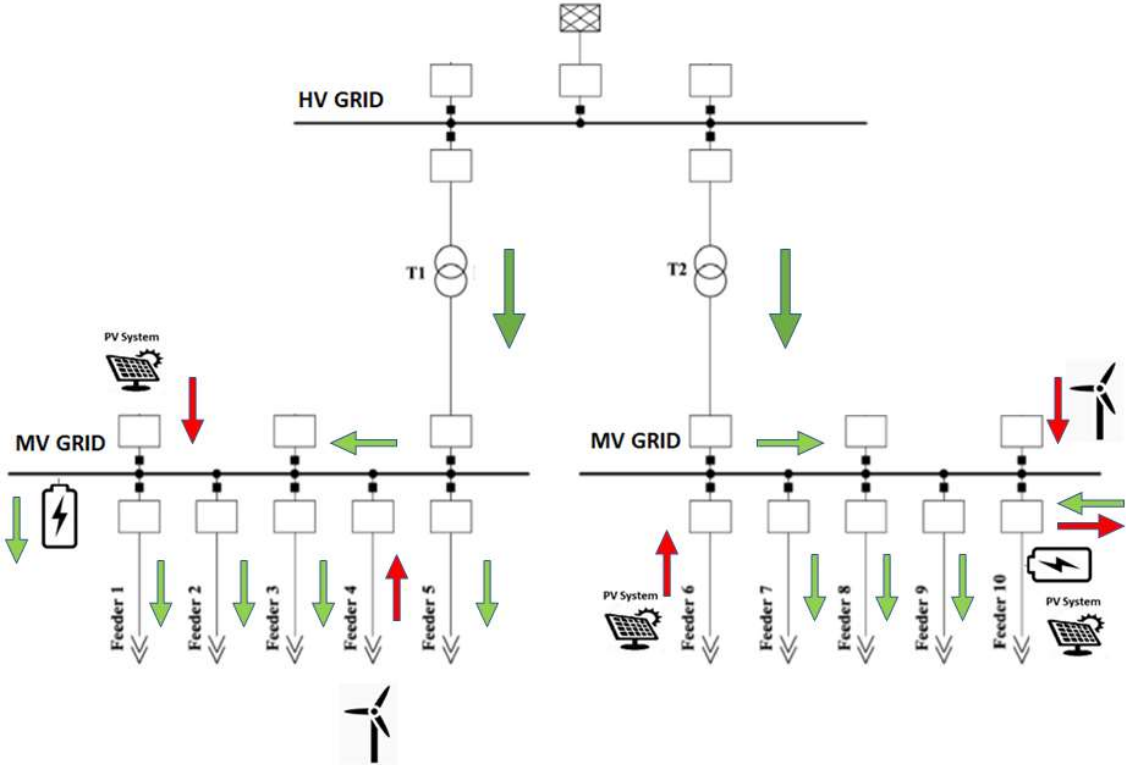
Figure 3 Integration of energy storage in power system
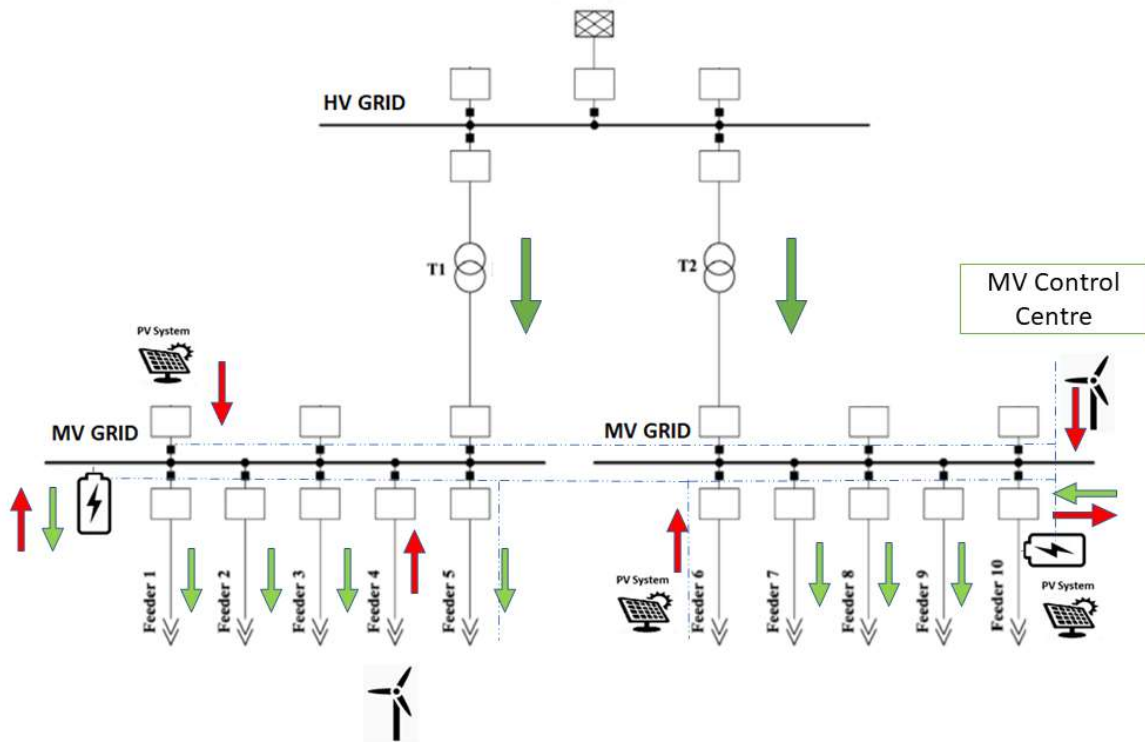
Figure 4 Schematic of communication infrastructure

In the MV grid is already existing a communication infrastructure but the main purposes are the protection control like circuit breaker and switches and the energy metering from LV users. However, the infrastructure is not thought to directly communicate with DER or storage energy system and mostly with a distributed metering infrastructure. In addition, almost all of the previous problem are new for the MV distribution grids and few are totally new for the entire grid. These problems need not only a distributed metering infrastructure but also new algorithms able to solve them, because, as said before, it is not possible to make the same assumption and hypothesis of HV grids. Nevertheless, there are a lot of drawbacks for using the high voltage technology also to medium and low voltage systems, first of all, the cost. The high voltage network are the arteries of the system and for this reason they are thought with no limitations of the budget. This approach cannot be applied to MV/LV grid because they are the capillary of the system.

In summary, the main issues to apply these technologies in the case of MV distribution grids are:

- The cost of the measurement infrastructure;

- The availability and the cost of communication systems from public or private providers or eventually the installation cost of a dedicated infrastructure;

- New types of load and generators connected to the grid;

- Market liberalization.

From the previous issue is clear that the distributed measurement infrastructure must be first of all easily installed and cheapest as possible, secure against cyber attack and accurate enough to observe the required metrics, Figure 5. As regard this last feature, it must be clear that metrics depends by purpose of the SCADA so in this sense algorithm and hardware have to walk together.

-
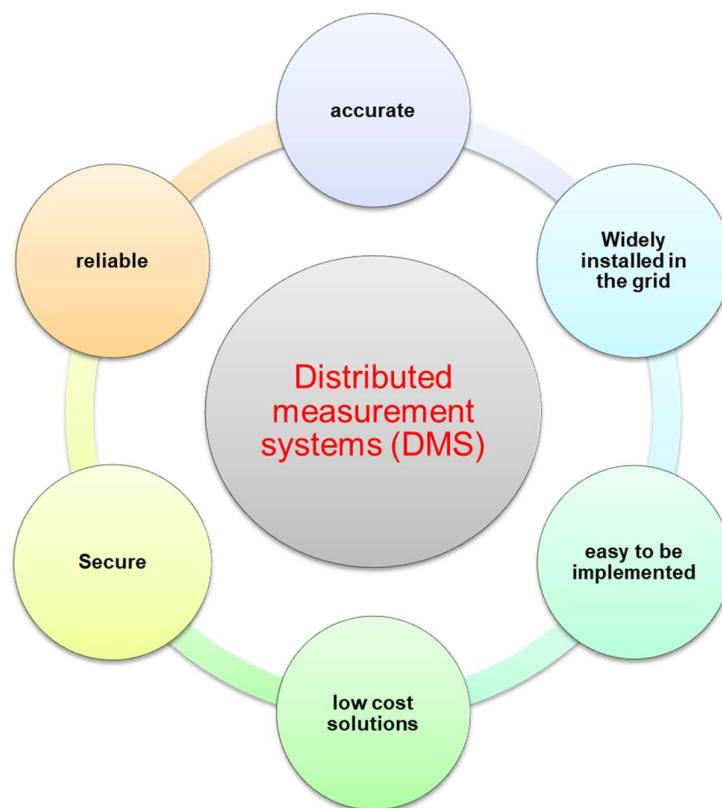
Figure 5 Main features of a distributed measurement system

The challenges shown in Figure 5 depend not only by the physical infrastructure but also by the software implemented. As regard the infrastructure, in the following, a possible low-cost architecture will be presented able to solve the previous discussed limitations however the main purpose of this thesis is the discussion of new algorithms for MV SCADA. These tools have been thought to support the management of the network and their implementability must be compared with the limits and peculiarity on the MV/LV SCADA infrastructure. It is, in fact, unreal thinking to apply the technology actually used in the high

voltage power system HVAC also to MV and LV grid because the cost and the expertise necessary in HVAC are to high and unjustified for microgrid use.

With regard to the algorithm and tools for MV SCADA, the minimal requirements can be summarized as follow:

- Power flow monitoring and control;

- Power quality monitoring;

- Diagnostic of DC system (photovoltaic and ESS battery);

- Load and DG forecasting;

Power flow monitoring and control is the first brick, in fact, specific algorithm must be developed in order to avoid inversion of power flow, islanding and stability issues. In some cases, the appropriate power flow monitoring algorithm combined with power quality measurement can solve also problems related to protection and automation. Dedicated algorithm for the diagnostic of the new component must be developed safety and operational problem. Finally, forecasting tools, actually, are the only instrument to overcame the problem of impredictability of load and DG [1].

In this thesis the first three arguments are under consideration because they are considered to be fundamentals for the smart grid development. This thesis wants to demonstrate how the previous challenges can be overcome with new algorithms for the distribution measurement system. In fact, power flow monitoring and control, power quality assessment and DC diagnostic are the essential requirement for the safe operation of the network. In the following, the state of the art and the reasons of why these tools are so important is shown for each argument.

Power flow monitoring and control

The management of modern smart grids must support the implementation of innovative logic of interaction between users, while responding to the need to increase the energy efficiency of users and guarantee grid stability and adequate levels of power quality. The goal, therefore, must be to obtain an electricity network that is able to distribute energy based on the availability, costs and needs of end consumers, no longer seen as an unpredictable source of consumption but as active participants in the

management of energy flows which, due to the increase in energy costs, encourages small residential customers and commercial buildings to increase efficiency by reducing energy consumption and pushing the market to an increasingly development of so-called intelligent buildings and microgrid. The transition from passive electricity grids to active electricity grids capable of optimizing energy flows in order to allow the integration of smart buildings and microgrids will be possible thanks to the evolution of smart metering technologies and, more generally, of distributed measurement systems and ICT (Information & Communications Technology), which will have the task of conveying an increasingly capillary flow of information and of using this information for the implementation of adequate monitoring metrics and network control logics. Currently, for example, there is no possibility for the operator to control the distributed generation (GD) both due to the shortcomings of the current interface systems of the GDs, and due to the lack of appropriate information exchange systems between the GD and the Distributor (DSO) itself. In this sense, to ensure stability and maintain adequate levels of power quality, a crucial role will be played by energy storage systems, ESS, capable of both providing services aimed at a better use of energy by prosumers than from the system operator side. Aimed at increasing the stability and safe operation of the network power services. In fact, if on the one hand consumers, or rather, active users, are interested in maximizing the gains coming from this type of investment, mainly by implementing the right energy distribution strategy (peak shaving, self-consumption, optimal scheduling...), the system operators are more interested in having a safe operation of the network.

The basis for smart grid management is the state observability, i.e., the real-time knowledge of all the network quantities (branch currents, node voltages, and power flows). This is usually obtained by means of proper load flow (LF) algorithms [2], [3], whose implementation requires an accurate model of the network and a continuous update of the input load data. Toward this end, power quality analysers (PQAs) or phasor measurement units are usually adopted for the case of distribution networks [4]–[5]. However, such equipment is not widely used in medium-voltage (MV) distribution networks, and their installation entails high costs for the instruments, the related MV current and voltage transducers [6] in the secondary substation (SS), and the energy interruption for installation. Thus, in the literature, state estimation algorithms have been proposed to achieve the network observability with a reduced number of MV measurement points. These algorithms are based on the use of few measurements at the MV level, which are integrated with pseudo-measurements, i.e., estimations of the missing data. Different state estimation approaches are proposed, which basically differ on the choice of the state variables estimators (usually based on node voltage, branch current, or branch powers) and in the way they include heterogeneous measurements and pseudo-measurements [7], [8]. Many studies also focus

on the choice of the instrument types and their placement in the network to obtain the desired accuracy performances[9], [10]. On the contrary, state estimation (SE) algorithms require an accurate model of the network and some historical information on the powers drawn by the loads (pseudo-measurements) [8], [10]. These approaches also have better performance with meshed grid because, in these grids is simplest to achieve the observability of the grid but for the case of radial grids the optimization algorithm can fail the running. Network observability could be obtained also with well-known load flow algorithms as suggested in [11] that is based on the use of load power measurements at low-voltage (LV) level.

Starting from the network observability the next step is the possibility to manage the grid after a contingency. Actually, the great percentage of automation is composed by protection manoeuvres, however, in order to avoid, for example, islanding or reverse power flow phenomenon it is necessary from the DSO to acts also with the distributed generators in general.

In the first chapter of this thesis the study and implementation of a possible monitoring architecture is presented. While in the second chapter the architecture is extended for the integration of a new generation of prosumer. The prosumer is intended as a low voltage user with a distributed generator and a storage energy system.

Power quality monitoring and harmonic source assessment

The integration of renewable energy generators and the use of non-linear loads in the modern smart grid may cause power quality disturbances. Various types of disturbances can occur, and among them one of the most important is harmonic distortion; voltage and current waveforms are distorted and consist of different harmonic orders. It must be clear that each renewable generator has a power electronic interface which cause voltage distortion in the grid but, in addition, also non-linear load like rectifiers and electronic equipment in general can cause voltage distortion as summarized in Figure 6.
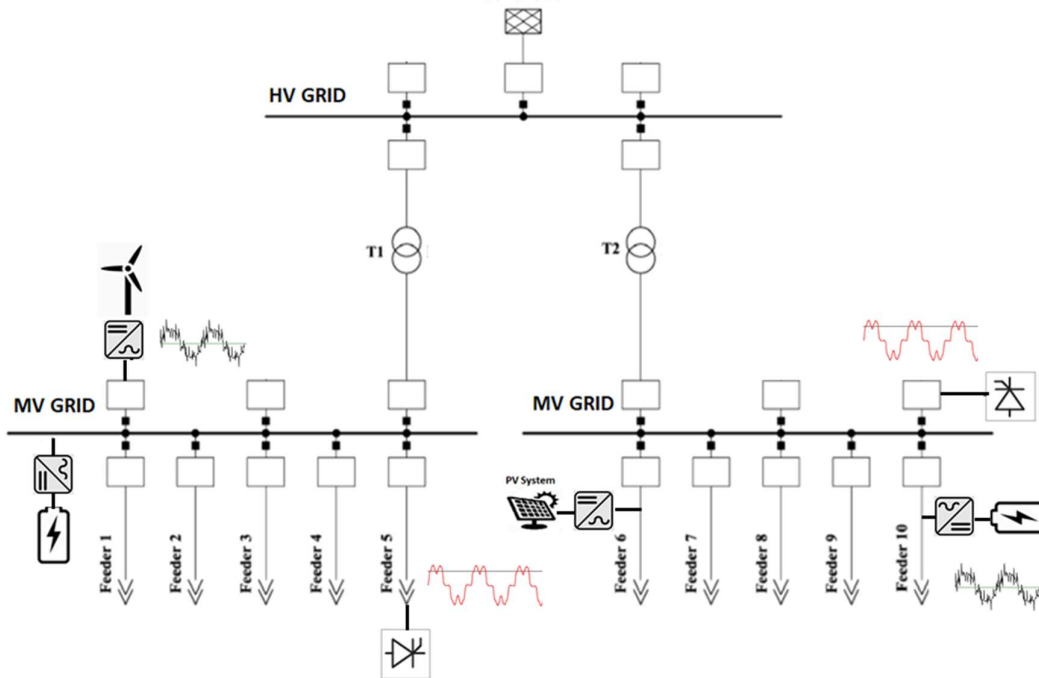
Figure 6 Voltage harmonic propagation due to power electronic interface

The degradation of the power quality may cause several problem like: equipment failures resulting from overheating, shorten life expectancy of transformers due to the deterioration of insulation levels, and increases in equipment power losses [12]. Disturbances can be caused by any customer connected within the grid and can influence the customers situated at the remote branches of the power grid. According to the working principle, the harmonic sources in regional power grid are divided into the following types:

(1) Ferromagnetic saturation [13], which mainly refers to power equipment with an iron core, such as transformers and reactors; these harmonic sources can produce low levels of harmonic currents under non-saturated and stable operation.

(2) Electronic switch [13], which includes various alternating current (AC) and direct current (DC) converter equipment, such as rectifiers, inverters, and thyristor switches. This type of equipment is widely applied in metallurgy, chemistry, and electrified locomotives, typically including electric locomotives, frequency converters, medium frequency furnaces, DC transmission, and household appliances, and is the most extensively distributed in current regional power grids with the largest number.

(3) Arc type[14], which mainly includes steelmaking furnaces, metal melting equipment, and welding machine groups. Notably, the arc furnace is an asymmetrical, time-varying, and nonlinear load with

impact. It is not only another major source of harmonics in the system but also a factor that causes three phase imbalance, voltage fluctuation, and flickering.

This is the reason why the international standard IEC 61000 has increased the verification range of power quality analysis until fiftieth harmonic. There are standards [15], [16] with the set of limits is used to monitor the individual and total harmonic distortion (THD) levels of current and voltage at the PCC. Reference [17] gave the measurement of electric power quantities definitions under sinusoidal, non-sinusoidal, balanced or unbalanced conditions. However, only the harmonic analysis of voltage and current is insufficient anymore and the investigation of harmonic propagation needs new industrial tools. As consequence, it is important to define not only methods for quantifying harmonic distortion levels, but also methods that provide information about the location of disturbance sources. This assumes considerable importance not only for the aspects related to power quality, but also for the possible attribution of billing responsibilities for the presence of disturbances between the energy producer and the final customer [18], [19]. In literature, there are different methods for the harmonic sources detection based on the measurement or the estimation of different parameters. Studies are conducted with the theoretical idea in mind that the harmonic distortion at the PCC is solely caused by a customer load, which is not true on a real-life situation. The amount of harmonic distortion present at the PCC is subjected to the installation of a customer and the background harmonic as part of the utility side [20].

There are several review papers based on harmonic source detection in general, although, as far as the authors know, there is no review paper focusing on the practical method and easy to use in the industry [21]. From the perspective of the large-scale application of such methodologies, a very important aspect is related to the ease of implementation on smart meters (SMs) platforms, as well as on other typical measurement instruments, such as power quality analysers (PQAs) and other intelligent electronic devices (IEDs). In fact, these instruments are widespread used in distribution grids both at the substation level and the customer side for energy billing and grid monitoring [14], [22]. Thus, they could also integrate simple metrics for harmonic emission assessment, without the need of installing new metering equipment in the power grid. Voltage and current total harmonic distortion factors (THDV and THDI, respectively) are the most known indicators for the assessment of harmonic distortion. They are able to quantify the total amount of distortion; however, they cannot give information about the source of pollution. For this last purpose, several approaches have been studied for assessing harmonic emission levels and locating harmonic sources; such methods have been based on both distributed measurements and single-point measurement at PCC [6], [20], [23]. From the customer viewpoint, single-point measurements are more suitable since they can allow users to easily

obtain information about the harmonic emission level and to be aware of the impact of harmonics at the delivery point. On the other hand, distributed measurements' strategies are more suitable for the distribution system operator (DSO) who can collect measurements coming for different points of the network. This can allow DSO to achieve more complete information about the harmonic state of the power grid and to separate customers' contributions to harmonic pollution in each PCC from distortion coming from the grid.

In the third chapter of this thesis the author tries to show a practical method, particularly suitable for industry application, based on some indicators coming from IEEE 1459 standard and some new indicators proposed by the author for the localization of harmonic sources in a power system.

Diagnostic of DC system

All the distributed generator based on renewable energy system have a DC state. This causes the spread different system with different layout and voltage levels this can cause that a solution simple to apply for a case is not possible to be applied for another. This diversification became tricky especially in the case of diagnostic after a fault. We can consider a fault as a not normal working condition which can became dangerous for both the devices but, in some case, also for people. Obviously, it is necessary to recognise the fault before it became a damage however more diversified are the system and more difficult can be to find the right identification metrics. General speaking, the main failure in DC power system can be summarized as follow.

- Failure at device level;

- Pole to pole PP or pole to ground PG fault;

- Interruption of the pole or ground.

Failure at device level can born for example in a PV panel or in a battery cell. However, they, generally don't cause a danger for the human but can lead to unregular working of the power plant in addition they are technology specific and for that reason it is difficult to resume the common failure modes. Focus the attention on the network of the DC grid the main fault conditions are two: short circuits and interruption. Short circuit is the most common breakdown condition. It occurs when two conductors at different potential are directly shorted, for example, when the aging of insulation in cable cause the conductor getting in contact with the ground. This lead that the dc voltage across the fault point

decrease near to zero while the current magnitude rises high and fast. For this reason, also for DC system, short circuit identification is general simple to diagnostic. On the opposite site there are the interruptions. The interruption is the break of galvanic continuity in a conductor. It is less frequent of short circuit because it is due only to mechanical source. The fast interruption of the conductor allows the rapid increase of the voltage magnitude due to magnetic energy stored on the devices. This overvoltage can evolve in two manners:

a) Overvoltage breaks the insulation and cause a short circuit in a different part of the plant

b) Overvoltage creates an arcing condition at the point of fault

In the case of first option the fault condition will be solved by the short circuit protection. The second option, on the contrary, is more severity because the arc leads to have current and voltage near to rate values and for this reason, difficult to identify. If the fault condition is not identified in time the arc can cause the deflagration of fire due to heat generated.

In order to protect homes against ac arc faults, arc fault circuit interrupters (AFCIs) have been introduced in U.S., and since 2011, the National Electrical Code (NEC) has required their installation in all living areas. Furthermore, NEC 2011 has introduced AFCI protection also for photovoltaic (PV) systems; in fact, arc faults can also occur in dc electric circuits, with the same dangerous consequences for dwelling units or commercial buildings. The AFCI requirements for home protection are covered by the UL standard UL 1699 [24], [25], while UL 1699B covers dc AFCIs for PV applications [26]. The detection of an arc fault is not a simple task [27]–[29]. For ac systems, main problems arise because in some cases appliances currents can be very similar to arcing currents, even when arcs are not occurring; in other cases, arc fault characteristics are masked or attenuated by appliances' current absorptions; furthermore, arcs are generally nonstationary and sporadic, and thus segments of arcing current can coexist with segments of normal (nonarcing) current. The issue is particularly complicated in the case of series arcs, while the loads influence is minimal in the case of parallel (or line-to-neutral) arc occurrence [30].

In the chapter four, the author presents an experimental study focused on the characterization of series arc faults in direct current (DC) photovoltaic (PV) systems. The aim of the study is to identify some relevant characteristics of arcing current, which can be obtained by means of low frequency spectral analysis of current signal.

1. Architecture Of Distributed Measurement System For Power Flow Monitoring

State of the art on distribution monitoring and control infrastructure

Apart from actual energy policies and regulatory frameworks, or technical capabilities enabled by advanced modelling and analysis tools, an important issue for effectively increasing the distributed generation and storage systems presence in distribution networks is the possibility for DSOs to achieve new simple and versatile tools for power system monitoring and management purposes. These tools have to be based on proper communication and measurement infrastructures, which should be feasible for DSOs themselves, in terms of low cost, flexibility and expandability features, in order to allow their development starting from the existing instrumentation and equipment typically employed in such networks. Several papers can be found in the literature concerning the measurement and communication technologies in distribution systems. For example, in [31]–[35], a wide overview is given of measurement technologies and architectures for the smart distribution grids, including metering and communication infrastructures. For distribution networks, especially those of isolated islands, supervisory control and data acquisition (SCADA) systems are typically employed for monitoring, protection and control purposes. As regards measurement instrumentation, several kinds of equipment are considered, such as smart meters and sensors, power quality analysers, phasor measurement units (PMUs) and micro-PMUs (PMUs), and so on, which can be more or less suitable, depending on the considered distribution system management applications and the particular characteristics of the considered network. In particular, many recent researches have been focused on PMUs and PMUs for distribution network monitoring, control and diagnostic applications [36]–[42]. However, such solutions can be unsuitable for small island micro-grids, because power lines are short and/or the intrinsic costs of such instrumentation are high. To reduce the installation costs, some authors propose to use a few measurement points and to integrate them with load estimations [43]–[46]; however, when dealing with load estimations (or pseudo-measurements), higher uncertainty levels are generally expected and more sophisticated algorithms can be needed for the distribution system state's estimation, which also may entail higher computational costs. The integration of differently distributed measurement solutions have also been investigated, for example, considering the possibility of smart meter and power quality meter exploitation or SCADA and PMU-enhanced integration, for a number of applications (load forecasting, optimization, demand side management, fault detection and so on) [43], [47]–[52]. If the application of such solutions is envisaged for distribution networks, such as those addressed in this paper, the main problems are related to the processing of algorithms' accuracy and complexity, considering the reasonable computational

capabilities of the DSOs control centres. Another fundamental element to enable network observability is the communication between these measurement devices and the control room of the micro-grid. Different solutions can be used for this purpose: optic fiber, power line communications, GSM, wireless and so on. The different communication solutions must be compared in terms of cost, reliability, security, environmental impact and power quality effects [53]–[55], considering also their availability and suitability in islanded micro-grids.

There are different possible architectures proposed in literature able to cover and solve the previous requirements. The core of a distributed measurement architecture is the communication system. It is the link between the meters and the control room. It must have different feature in order to be suitable for smart grid. In this revolution the distributed measurement system have to be accurate, reliable, secure, low cost, and simple as summarized in Figure 5

The main communication protocol emerging in the smart grid layout can be divided by wireless and wired system as summarized in the following:

    Wireless

- IEEE 802.11n

- Global System for Mobile GSM

- LTE

- 3G/4G/5G

- ZiGBee

    Wired

- Optic fiber

- Ethernet

- Serial

- Power Line Communication PLC

There are also several standards that have been proposed for the communication infrastructure like IEC 61850 and IEEE P1901. Many of them came from the industry and each of them have advantages and drawbacks and, actually, not anyone emerged as the best. For example, internet-based protocol like ethernet or optic fiber have the top performance in terms of data rate and security, however they

have a high installation cost. Wireless systems, on the contrary, like GSM have low installation cost but they must be maintained with a periodical payment to telecommunication provider. Other technology like ZiGBee and IEEE 802.11 were imported from industry but have a coverage area of hundreds of meters. The compromise in the next future seems to be 5G based protocol but actually it was not implemented by the industry by smart meter applications. Finally, PLC is regularly used in LV networks and there are several papers the demonstrated their applicability also in MV grids [11]. The technology seems to be particularly suitable for islanded or rural networks.

In [56] a solution based on the use of low-cost equipment to monitor the network and control distributed generator and energy storage systems is shown. In detail, the active and reactive power drained in each secondary substation are measured at LV side of MV/LV power transformers, thus reducing the installation costs related to MV switchboard and transducers [57]. The proposed architecture is shown in Figure 7. Starting from these LV load power measurements and an additional voltage measurement at the beginning of each feeder, a load flow algorithm was developed and implemented in the SCADA control center to calculate power flows all over the MV network. Based on the load flow analysis, the SCADA system can detect dangerous conditions for network stability and take proper actions to maintain its correct operation. To do this, a new feature to be implemented into smart grid infrastructures is the possibility to interact with distributed generators and energy storage systems [58] of the prosumer. The authors propose a solution based on two new devices: an interface protection system (IPS) and a concentrator [59]. The first one implements both an anti-islanding protection algorithm and the communication capabilities to interact on one side with distributed generators and storage system inverters and on the other side with DSOs. The second device, named concentrator, has to be installed in the secondary substation and it allows delivering DSO messages to the IPS of the addressed distributed generator or storage system. As regards the communication system, a wireless network is proposed to connect secondary substations to the SCADA control center, while the power line communication over the LV network is proposed to connect IPS to the concentrator. This solution is suggested as it is already widely implemented with success for automatic meter reading (AMR) purposes[60]. Furthermore, the proposed solution contemplates the presence of a MV coupler in each substation, in order to keep a double redundant communication system [61]. When a substation is not reachable via wireless network, data can be delivered by a nearby substation that receives them via MV network, which represents an always-on secure communication channel. Such a system can be also extended to be used not only in a disaster recovery situation, but as a parallel communication channel in order to double check the measures at

the end point. Such a system can be also extended to be used not only in a disaster recovery situation, but as a parallel communication channel in order to double check the measures at the end point.
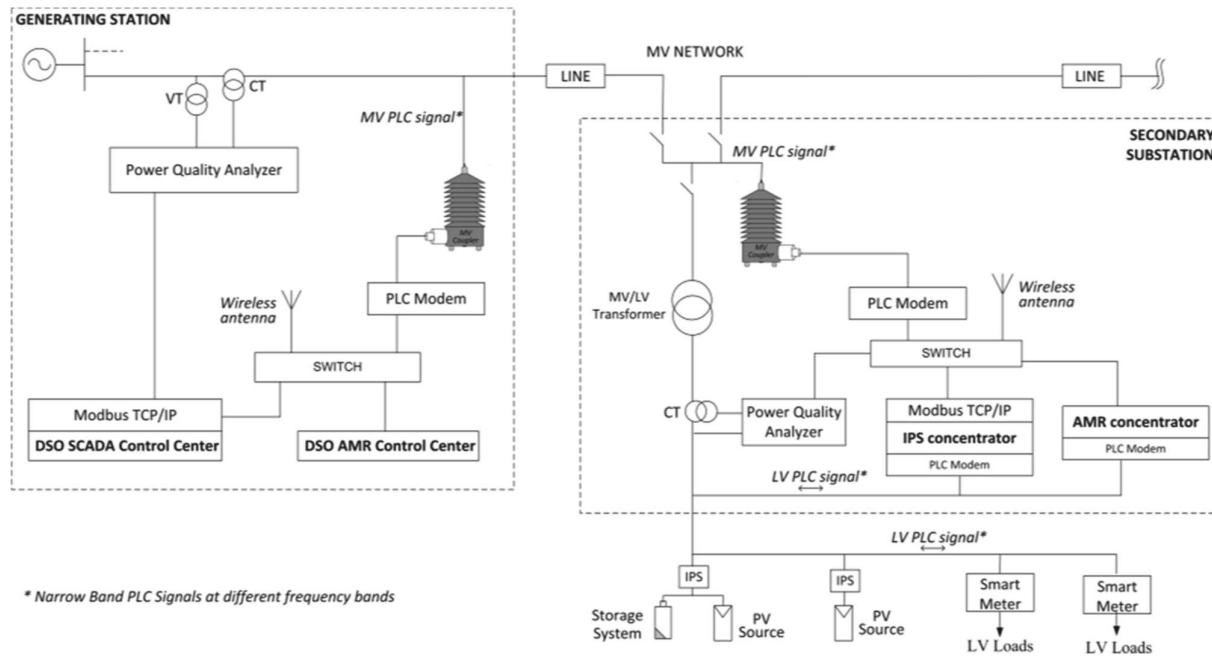

Figure 7 System architecture for power flow monitoring and distributed generator and storage systems remote control with two communication channels: wireless and PLC on medium voltage network.

More in detail regards storage energy systems, according to CEI 0-21 [62], *the network services that (currently) must be provided must be the following.*

- *-Active power adjustment (par. 8.5.3)*
- *Limitation of active power for voltage values close to 110% of Un (par.8.5.3.1)*
- *Operating conditions in over-frequency (par. 8.5.3.4 and 8.5.3.4.1) the generator must be able to interrupt any discharge cycle in progress and implement, compatibly with the state of charge of the system, an absorption of active power. This function must be excludable.*
- *Underfrequency operating conditions (par.8.5.3.4 and 8.5.3.4.1) the generator must be able to interrupt any charge cycle in progress and implement, compatibly with the state of charge of the system, a supply of active power. This function must be excludable.*
- *Participation in voltage control (par. 8.5.2)*
- *Voltage support during short circuit (ONLY CEI 0-16) (currently under study)*

In addition to the disconnection functions performed by the SPI, the GD units for mains voltage values close to 110% of Un must contribute to the limitation of the voltage measured at the output terminals by absorbing reactive power (inductive behavior), according to the control logics. contained in Annex E. The Distributor or the User has the right to activate the local voltage control logic, which must be reported in the Operation Regulations. If the request is from the User, the Distributor must justify any refusal.

In the presence of an <u>appropriate communication system</u>, the GD units used in systems with a total size greater than 11.08 kW, can be enslaved to centralized regulation. They must operate according to the logic specified in Annex E and the external regulation and remote control signals that will be supplied by the Distributor as established in Annex D. In these cases the GD units must be able to absorb reactive power (inductive behavior) close to 110% of Un and deliver reactive power (capacitive behavior) close to 90% of Un.

Even if there are no anomalies in the effective voltage value, the absorption and delivery of the reactive power is aimed at limiting the overvoltages / undervoltages caused by the generator itself following the injection of active power according to a characteristic curve of type cos = f (P).

For systems with power greater than 11.08 kW it is possible for the distributor to request a different operation from the previous one, according to a Q = f (V) type curve. this type of request, by the DSO, represents in all respects a network service and is therefore subject to the regulatory terms and remuneration mechanisms (which will be) established by ARERA.

In the presence of a centralized logic, the standard specifies: *"In the presence of centralized regulation, an appropriate active power level signal will be sent to be limited by the GD unit. This mode must be activated only in systems with a total power greater than 11.08 kW. The possible values of the set-points sent by the grid operator will be expressed as a percentage of the nominal power of the inverters, in steps with a maximum amplitude equal to 10% Pn. There will therefore be 10 possibilities of reduction with respect to the nominal power. If the inverter is already at a lower power level than required, it will not have to further reduce the power itself. The power level required by the set-point must be reached within 1 min of receiving the signal, and with a tolerance of ± 2.5% Pn. In the case of a set point equal to 10% Pn, the tolerance will be between 12.5% Pn and 0% Pn, and the inverter will then have the right to disconnect".*

The previous operating procedures, reported in extended form in CEI 0-21, illustrate the current status of the limits, obligations and terms relating to the network services offered by the storage systems for the Italian standard however the gist of it is valid also for the international community. At present, the

services that are already included in the market are related to secondary regulation (Italy) and power sharing (Germany). In Europe, in particular, the topic seems to became more important with the publication of energy community EU Directive 2018/2001.

The current trends relating to demand response are summarized in the review article [63], which highlights the differences between the possible DR services offered by the different generators, including storage systems. The different services are also distinguished, divided by:

- Incentive based
- Price based
- Mixed based

The substantial differences between a price-based bargaining mechanism rather than an incentive-based bargaining mechanism are evident. While the former are easy to quantify and adapt perfectly to the mechanisms relating to the secondary regulation of active power, the latter are indispensable in order to use the various network services such as voltage regulation or primary regulation, which is why they are typically used in mixed form.

In the following, is assumed a communication infrastructure with the limitations and constraints of the architecture proposed in Figure 7. In this infrastructure, a power flow implementation is first tested. The power flow algorithm is then enslaved to an innovative demande response solution with a price base infrastructure.

Load flow based monitoring algorithm

An ad hoc monitoring system was implemented in LabView, the algorithm was tested in the previous architecture implemented in Favignana island grid. However, it can be simply transpose to generic radial distribution network. The solution is based on the use of power quality analyzers (PQAs) in distribution network substations, which are less expensive than PMUs. Moreover, they are installed at the low-voltage (LV) side of power transformers, thus reducing installation costs; these last could be even null, if smart meters are already installed by DSO for energy theft detection purposes. Starting from LV active and reactive power measurements acquired by these instruments in each secondary substation, it was developed a backward–forward load flow (BF-LF) algorithm, which allows determining all the other network state variables. The backward/forward algorithm based on active and reactive powers was used for the real time observability of the grid. The algorithm requires only one additional voltage measurement at medium voltage (MV) bus-bars of the central generating

station; typically, this measurement can already be available in a real distribution network, thus no extra costs are needed for further instrumentation. Thanks to its low computation cost and simplicity of implementation, the BF-LF algorithm is a good solution for this kind of small distribution network.

The algorithm was first proposed in [11] and in this thesis is shown its implementation in LabVIEW and a Monte Carlo analysis for the uncertainty estimation The algorithm was implemented in a LabVIEW environment, because it allows assuring a highly readable and simple use however other environment can be used for the purposes. As regards the metrological characterization of the developed system, a Monte Carlo procedure is also implemented to perform an offline or near real time uncertainty analysis of the calculated power flows, considering the input uncertainties on both the real measurement data and the network parameter knowledge. The presented results show how the proposed architecture allows monitoring the power system in real-time and with good accuracy. Furthermore, the measurement data are acquired and stored in a database; this allows running the offline simulation; in this way, the validated software tool can also be used to perform the simulation of photovoltaic penetration scenarios and to observe its impact on power flows. The algorithm uses as input the measured active and reactive powers of each load and the voltage at the MV bus-bars of the generating substation. Thanks to these measurements, the algorithm is able to univocally determine all the unknown state variables, i.e., node voltages and branch power flows. The PQA at the MV bus bars also allow measuring active and reactive powers at the beginning of the feeder; these data are not used by the BF algorithm; they will be used to validate the algorithm accuracy performance instead. The block diagram for the BF algorithm implementation in LabVIEW is shown in Figure 8, where:

- V is the array of nodes voltages;

- FP and FQ are the arrays of the active and reactive power flows, respectively;

- PL measured and QL measured are the arrays of measured active and reactive powers, respectively;

- DeltaP measured is the array of the calculated power losses the network;

- VMT is the voltage used as reference for the slack bus: its module is equal to the value measured at MV bus-bars, i.e., V measured, and its phase is assumed as 0;

- Tol module and Tol phase are the thresholds used as tolerance in the load flow calculation.

As regard LabVIEW programming two different sequence frames are used for backward and forward sweeps on the whole network: the backward sweep calculates the power flows in each branch, and the

forward sweep calculates the node voltages. These two frames are included in a while lo op, thus they are repeated until a convergence condition is met on both the amplitude and the phase of the voltage at each node (at each iteration, this condition is verified in the third sequence frame).

To analyse the algorithm formulation in more detail, the single-phase network model used is shown in Figure 8. In the model, the voltages are the medium values of the three phases while the active and reactive powers are the total powers of the three phases. Network parameters are shown in Figure 9 and listed in Table 1; they have to be known for each branch and node of the network. As regards this, in practical cases this is a source of uncertainty (as these data are affected by uncertainty); in this viewpoint, next, the impact of such uncertainty on power flow results is analyzed.
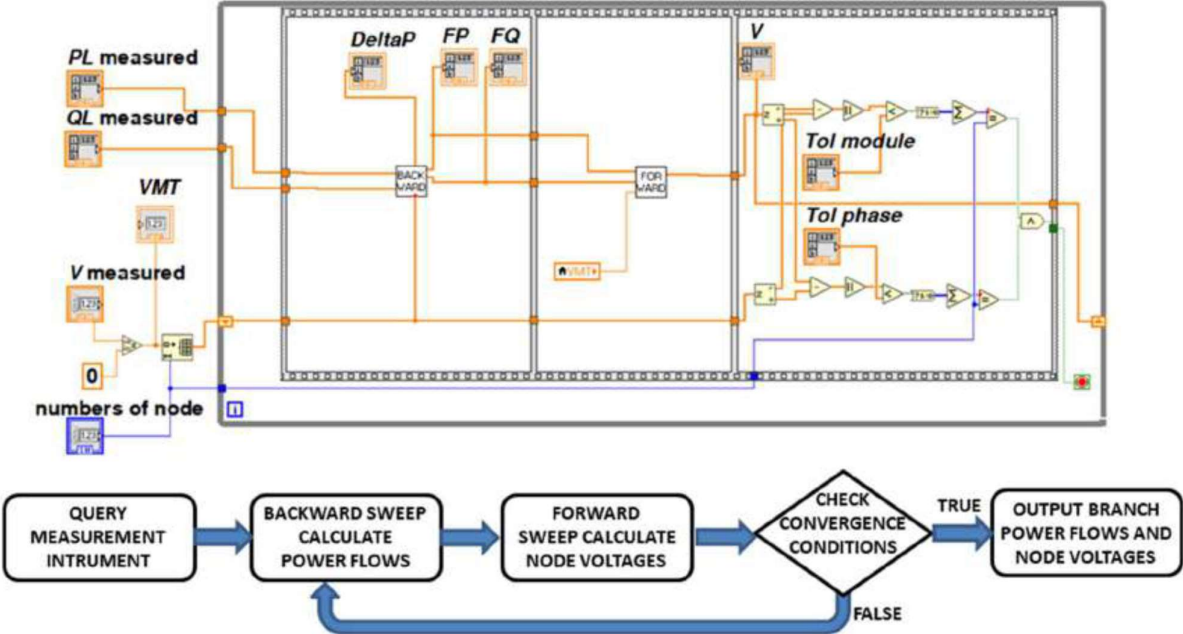

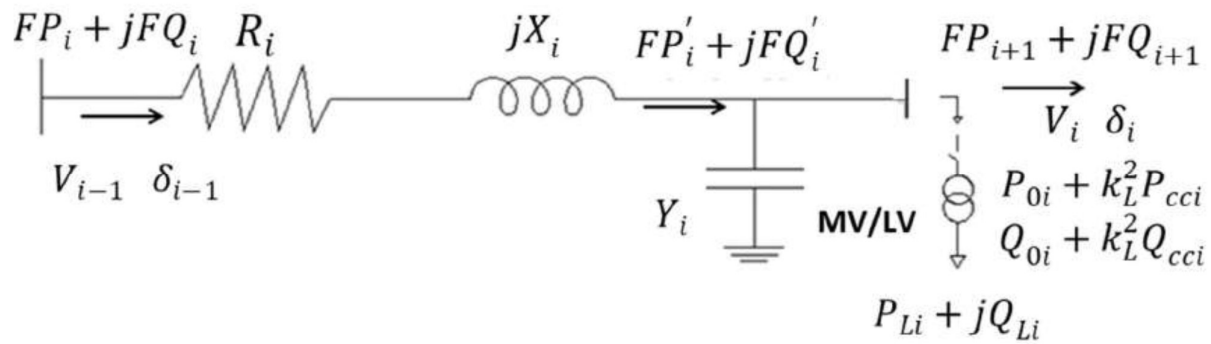*Figure 8 Block diagram for the power flow calculation.*

Figure 9 Scheme of the i-th brunch of the network model

Table 1 Required network parameters.

Branch Line Parameters	R_i	Longitudinal resistance
	X_i	Longitudinal reactance
	Y_i	Shunt admittance
Transformer Parameters	$A_{n,i}$	Rated power
	$P_{0,i}$	No load active power losses
	$Q_{0,i}$	No load reactive power losses
	$P_{cc,i}$	Short circuit active power losses
	$Q_{cc,i}$	Short circuit reactive power losses

Backward sweep

As already mentioned, firstly the backward sweep is performed from the last node to the beginning of the MV feeder. Active and reactive power flows in the longitudinal impedance of each branch are calculated as:

$$FP'_i = FP_{i+1} + \left(P_{Li} + P_{0_i} + k_L^2 \, P_{cc_i}\right) \tag{1}$$

$$FQ'_i = FQ_{i+1} + \left(Q_{Li} + Q_{0_i} + k_L^2 \, Q_{cc_i}\right) - V_i^2 \, Y_i \tag{2}$$

where:

Giuseppe Caravello

V_i is the voltage amplitude at the i-node;

FP_{i+1} e FQ_{i+1} are the power flows downstream from the i-node; these terms are null in the case of a terminal node;

P_{Li} and Q_{Li} are active and reactive powers measured at LV side of power transformers;

to obtain the equivalent MV load, the power transformer losses are added as $P_{0_i} + k_L^2 P_{cc_i}$ and $Q_{0_i} + k_L^2 Q_{cc_i}$ for the active and reactive power, respectively (these terms are not added in the case of MV users, because they are included in P_{Li} and Q_{Li} measured at the MV side of the transformer);

k_L is the load factor, i.e., the ratio between the actually drained apparent power and its rated value:

$$k_L^2 = \frac{P_{Li}^2 + Q_{Li}^2}{A_{n_i}^2} \tag{3}$$

When the virtual tool is used to simulate the distributed generators' connection to the LV network, the generated powers will be summed to P_{Li} and Q_{Li}.

The active and reactive power flows in each branch are finally obtained by summing the line losses as:

$$FP_i = FP_i' + \Delta P = FP_i' + R_i \frac{FP_i'^2 + FQ_i'^2}{V_i^2} \tag{4}$$

$$FQ_i = FQ_i' + \Delta Q = FQ_i' + X_i \frac{FP_i'^2 + FQ_i'^2}{V_i^2} \tag{5}$$

Forward sweep

In the forward sweep, node voltages are calculated starting from the measured voltage at MV bus-bars and the calculated power flows in each branch. The voltage phasor at node i is calculated as:

$$\bar{V}_i = \bar{V}_{i-1} - \sqrt{3}\,\dot{Z}_i\,\bar{I}_i \tag{6}$$

where $\bar{I}_i$ is the phasor of the current flowing in the longitudinal impedance.

It can be obtained from the following expression:

$$\bar{I}_i = \frac{FP_i - jFQ_i}{\sqrt{3} \cdot \bar{V}_{i-1}^*} \tag{7}$$

Combining these last two expressions, the voltage phasor can be finally obtained as:

$$\bar{V}_i = \frac{V_{i-1}^2 - (P_i \cdot R_i + Q_i \cdot X_i) - j(P_i \cdot X_i - Q_i \cdot R_i)}{\bar{V}_{i-1}^*} \tag{8}$$

Convergence calculation

The convergence condition is verified on both the voltage amplitude and phase. In further detail, the difference is calculated between the amplitudes and the phases of two subsequent cycles. If these differences were below a tolerance threshold for all the nodes, the while cycle is stopped, otherwise a further iteration is performed.

Uncertainty analysis

To evaluate the uncertainty on power flows' calculated values, the propagation of uncertainties was studied starting from the measurement uncertainties of the input quantities [64], i.e., the load powers of secondary substations and the voltage of MV bus-bars of a generating station.

The uncertainties on the power measurements acquired at the LV side of power transformers are calculated taking into account the following contributions:

- The PQAs uncertainty of the power measurements, $u_{P\%}$ and $u_{Q\%}$;

- The uncertainty introduced by the current transformers (CTs), due to the ratio and phase angle errors, $\eta_{CT\%}$ and ε_{CT}, respectively.

The uncertainty of power measurements acquired at the MV level in MV user substations is determined taking into account the following contributions:

- The PQAs uncertainty of the power measurements, $u_{P\%}$ and $u_{Q\%}$;

- The uncertainty introduced by the MV CTs;

- The uncertainty introduced by MV voltage transformers (VTs), due to the ratio and phase angle errors, $\eta_{VT\%}$ and ε_{VT}, respectively.

The uncertainty on the voltage measurement at the MV bus-bars of generating stations is determined taking into account the following contributions:

- The PQAs uncertainty of the voltage measurements;

- The uncertainty introduced by the MV VTs.

More in detail, the uncertainties on the active and reactive power measurements for the MV users are calculated, considering a type B evaluation and a rectangular distribution, through the following formulas [50]:

$$u_{P_{MV\%}} = \frac{\sqrt{\eta_{CT\%}^2 + (\tan\theta \ 100 \sin\varepsilon_{CT})^2 + \eta_{VT\%}^2 + (\tan\theta \ 100 \sin\varepsilon_{VT})^2 + u_{P\%}^2}}{\sqrt{3}} \qquad (9)$$

$$u_{Q_{MV\%}} = \frac{\sqrt{\eta_{CT\%}^2 + (\cot\theta \ 100 \sin\varepsilon_{CT})^2 + \eta_{VT\%}^2 + (\cot\theta \ 100 \sin\varepsilon_{VT})^2 + u_{Q\%}^2}}{\sqrt{3}} \qquad (10)$$

where θ is the phase shift between the current and the voltage. For the uncertainties of active and reactive power measurements at the LV level, $u_{P_{LV\%}}$ and $u_{Q_{LV\%}}$, a similar expression is used (where the terms related to the VTs are omitted).

To assess the uncertainty of the load flow output, the law of propagation of uncertainties should be applied to determine the partial derivatives of the measurement model. An alternative solution proposed in the standard [64] performs an iterative analysis with a Monte Carlo method. In more detail, the Monte Carlo procedure suggests repeating the calculation and iteratively varying the input quantities in their uncertainty range, thus obtaining the uncertainty distribution of the output quantities. Following this approach, a second VI was designed to be used offline to validate the load flow algorithm and evaluate its performances in terms of accuracy in the calculated power flows. The VI performs 10^5 times the load flow aforementioned algorithm; at each iteration the input quantities are randomly varied within the related uncertainty intervals through the following expressions:

$$P'_{Li} = P_{Li} \cdot \left(1 + u_{P_{LV\%}} \cdot 100 \cdot R_p\right) \qquad (11)$$

$$Q'_{Li} = Q_{Li} \cdot \left(1 + u_{Q_{LV\%}} \cdot 100 \cdot R_q\right) \qquad (12)$$

$$V'_{MT} = V_{MT} \cdot (1 + u_{V_{MT}} \cdot R_v) \tag{13}$$

where:

- P_i^L e Q_i^L are the estimated values of the power measurements;

- $u_{V_{MT}}$ is the relative uncertainty of the voltage measurements;

- R_p R_q and R_v are the random numbers chosen within a standard normal distribution.

The high number of iterations guarantees that random numbers do not affect the results. Active and reactive powers were considered as uncorrelated quantities. At each run, active and reactive power flows on each branch and node voltages were calculated. At the end of the 10^5 iterations, the frequency distributions of the calculated power flows were evaluated. The average value and the expanded uncertainty were then calculated (confidence level of 95.45%, coverage factor $k = 2$).

Figure 10 Implementation of the Monte Carlo analysis in LabVIEW. shows the implementation of the Monte Carlo analysis in LabVIEW. The sub-VI implementing the load flow algorithm is inside a "for" cycle, which is used to iteratively repeat the calculations. A second "for" cycle is used to extract the frequency distribution for each node and then calculate the mean values and the standard deviations. The expended uncertainties are then obtained as twice ($k = 2$) the standard deviations.

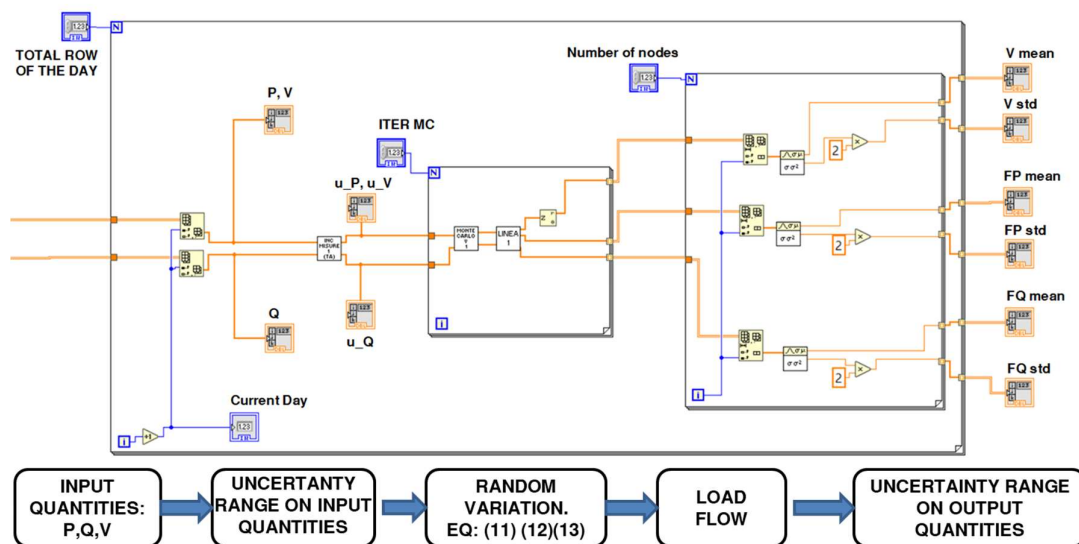obtained as twice ($k = 2$) the standard deviations.

Figure 10 Implementation of the Monte Carlo analysis in LabVIEW.

Implementation of the power flow algorithm

The production, distribution and energy sale on Favignana island are managed by the SEA S.P.A. (Società Elettrica di Favignana). The electricity network of the island of Favignana is currently composed of three medium voltage lines (in the following, named MTL1, MTL2 and MTL3), which depart from a central generating station. The three lines feed both MV/LV secondary substations (which LV lines depart from, to supply LV users), and MV user substations. The central station has seven generation units for a total installed power of 16,120 kVA. The MV lines are mostly equipped with MV cables. Only a few feeder sections are equipped with overhead lines.

The electrical scheme of the MV line named "MT L1" is shown in Figure 11. It is the longest MV line of the island (25,640 m). It powers 28 secondary substations (21 MV/LV secondary substations and seven MV users) mostly placed outside the city center. In Figure 11, each node of the "MTL1" line is indicated with a number, which will be used to show the load flow results. The branches will be indicated with the numbers of the nodes in which they end instead. The black numbers indicate the principal nodal substations. Line parameters and power transformer-rated data were already reported in a first study focused online "MTL1" [65].

The second line of the Favignana MV distribution network was named "MTL2" and it is shown in Figure 12. It is 2281 m long, and this line powers the city center with four MV/LV secondary substations. Its line parameters and related power transformer-rated data are reported in Table 2 and Table 3, respectively.

The third MV line is shown in Figure 13 and it is named "MTL3". It is 3785 m long, and it powers five MV/LV secondary substations and one MV user substation. Its line parameters and related power transformer-rated data are reported in Table 4 and

Table 5, respectively. Finally, in Figure 14 the single line scheme of the grid is shown with the geospatial coordinate.
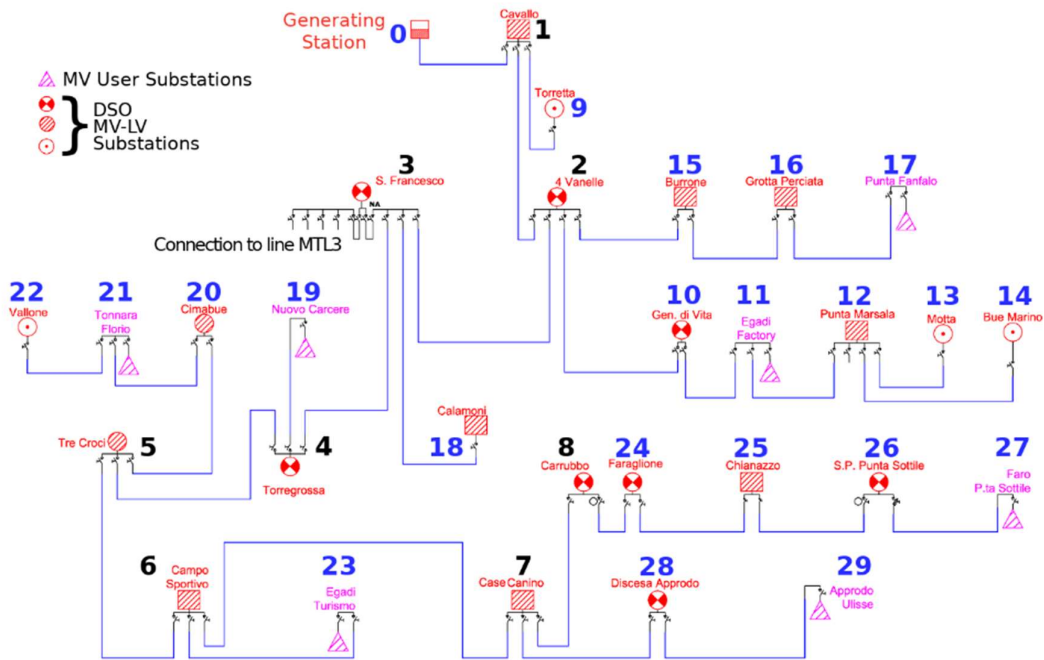
Figure 11 Electrical scheme of the feeder "MT L1" of the Favignana MV distribution network.

Figure 12 Electrical scheme of the feeder "MT L2" of the Favignana MV distribution network.

Table 2 Line parameters of the "MTL2" MV feeder.

Branch	From Node To Node	R (Ω)	X (Ω)	Y (µS)
1	0–1	0.401	0.105	48.35
2	1–2	0.330	0.053	17.84
3	2–3	0.381	0.062	20.61
4	3–4	0.272	0.072	32.83

Table 3 Rated data of the MV/LV transformers powered by MTL2.

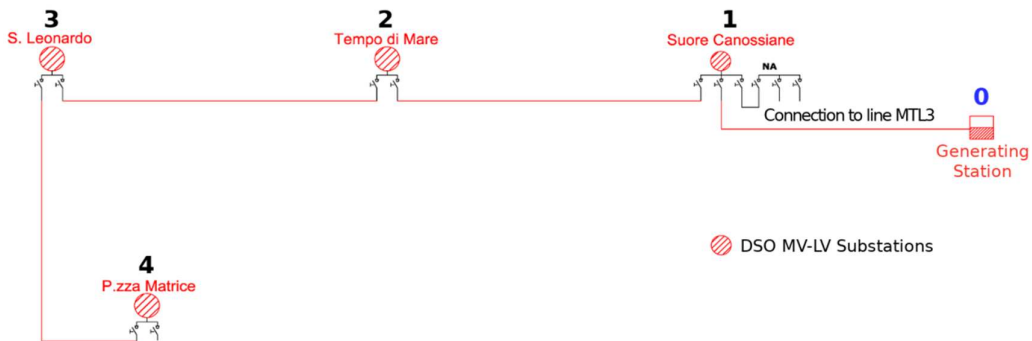| Node	A_n (kVA)	P_0 (W)	Q_0 (VAR)	P_{cc} (W)	Q_{cc} (VAR)
1	160	460	3651	2350	5953
2	800	1900	8592	9000	47,148
3	800	1500	12,717	8500	47,241
4	630	1650	7378	7800	36,986
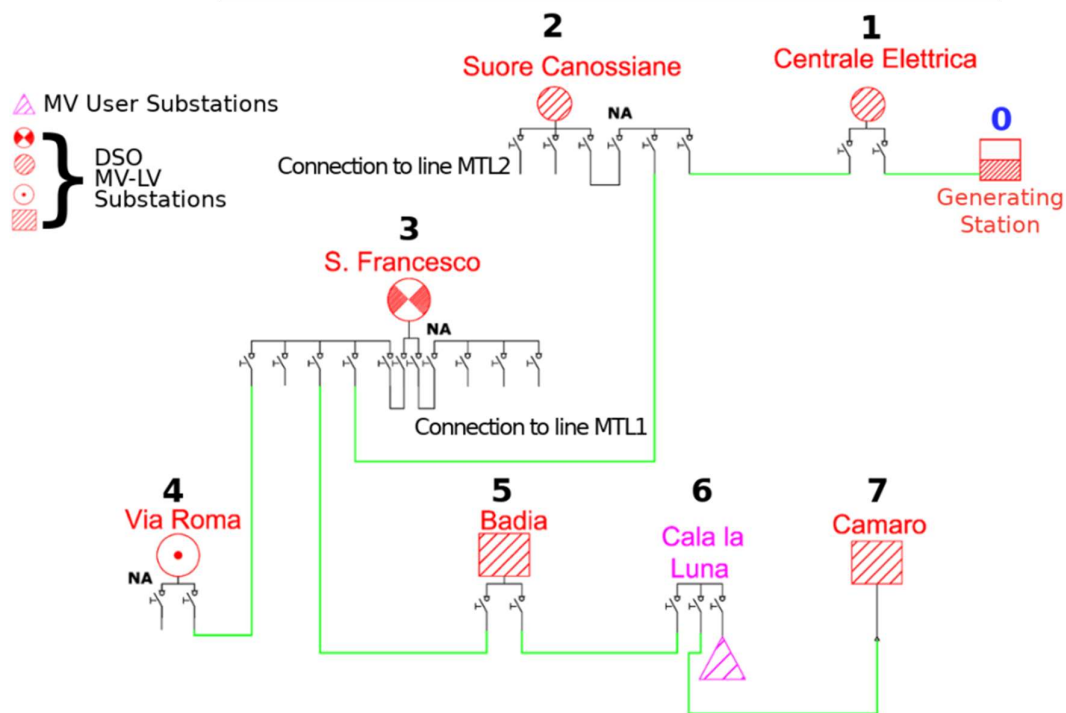
Figure 13 Electrical scheme of the feeder "MT L3" of the Favignana MV distribution network.

Table 4 Line parameters of the "MTL3" MV feeder.

Branch	From Node To Node	R (Ω)	X (Ω)	Y (μS)
1	0–1	0.01	0.003	1.2
2	1–2	0.401	0.105	48.35
3	2–3	0.574	0.151	69.24
4	3–4	0.195	0.032	10.56

5	3–5	0.771	0.125	42
6	5–6	0.135	0.022	7.29
7	6–7	0.353	0.057	19.1

Table 5 Rated data of the MV/LV transformers powered by MTL3.

Node	A_n (kVA)	P_0 (W)	Q_0 (VAR)	P_{cc} (W)	Q_{cc} (VAR)
1, 2, 7	160	460	3651	2350	5953
5	630	1650	7378	7800	36,986
4	800	1900	8592	9000	47,148
3	1250	950	17,474	11,000	74,189

The developed VI can query each instrument via Modbus over TCP/IP. The VI periodically queries each PQA at time intervals of 2 s, to acquire the measured active and reactive powers. The collected measurements are used to run the power flow calculation; then they are stored along with the results. The considered application requires a time accuracy in the millisecond range, thus a network time protocol (NTP) over the Ethernet network is used to synchronize all PQAs. Moreover, a further PQA is installed at the beginning of each MV feeder. As already mentioned, the voltage measurements of these last PQAs are used in the load flow algorithm, while their active and reactive power measurements are used for the algorithm power flow output validation.

Figure 14 Single line electrical scheme of the grid

Real time evaluation

The experimental validation of the BF-LF algorithm results was carried out by comparing calculated active and reactive power flows with active and reactive power values measured by the PQAs installed at the beginning of each MV line. Figure 15 shows the comparison between the measured and the calculated values, for the first branch of the "MTL1" line. The comparison is performed every 2 s for the 24 h of the 31 May 2018. As can be seen, the measured and estimated values are superimposed. To highlight their differences, they are reported in Figure 16. It can be observed that the difference between the measured and estimated values is always very small, in comparison with the measurement uncertainty, thus confirming the correctness of the power flow calculations. Similar graphs are reported for reactive power flows (see Figure 17 and Figure 18). The results obtained for the MTL2 and MTL3 lines are very similar to those by MTL1, thus they are omitted.

The same analysis was carried out for different days. For each day, Figure 19vshows the maximum and average values of the difference between the measured and the calculated values in the percentage of the measured active power flow. Differences of less than 0.1% and 0.2% were observed. These

results demonstrate how the values calculated by the virtual instrument were very close to the measured values. Similar results were obtained for the reactive power flows and for the other lines.
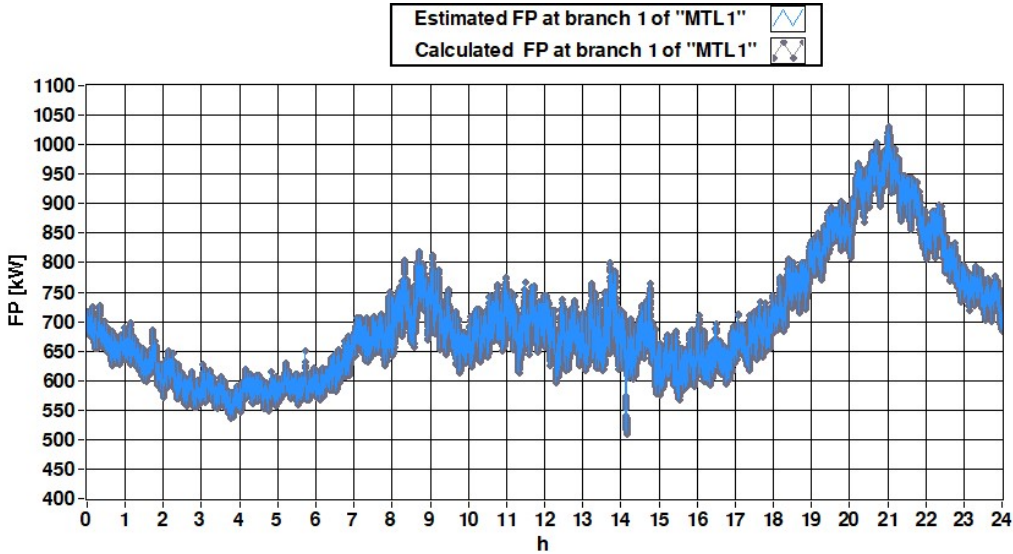

Figure 15 Comparison between the measured and the calculated values of the active power flow of first branch 1 of the "MTL1" line during the day 31 May 2018.
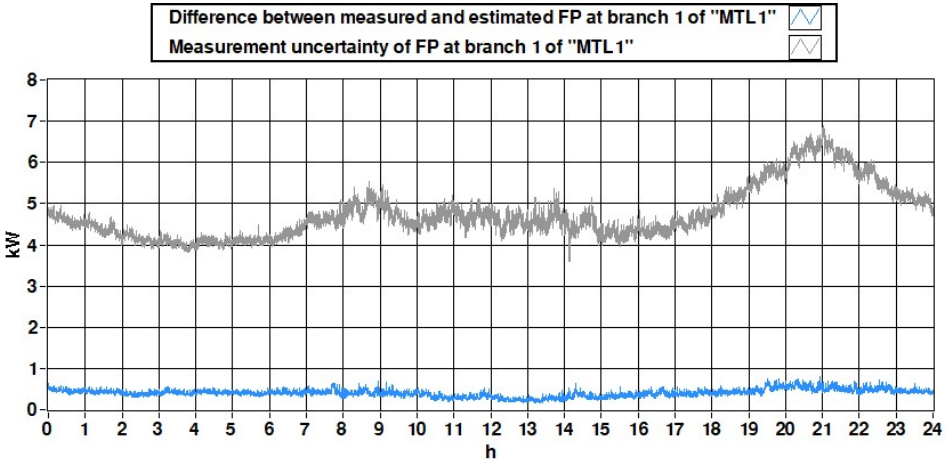

Figure 16 Difference between the measured and the calculated active power flow of branch 1 of the "MTL1" line and the uncertainty in its measurement (31 May 2018).
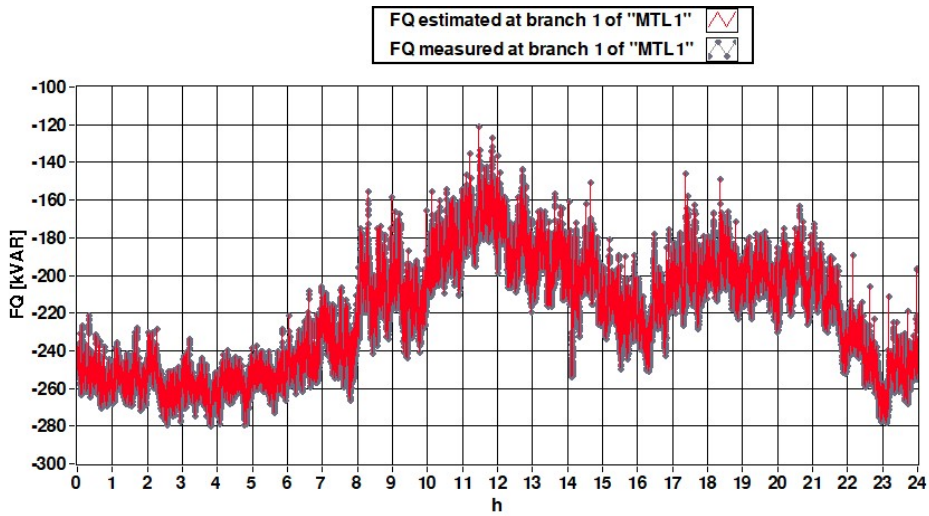
Figure 17 Comparison between the measured and the calculated values of the reactive power flow of branch 1 of the "MTL1" line during the 31 May 2018.
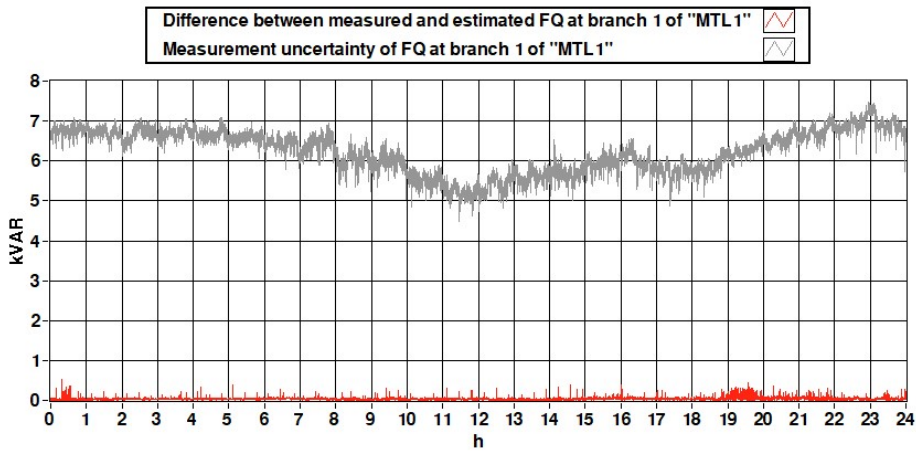

Figure 18 Difference between the measured and the calculated reactive power flow of branch 1 of the "MTL1" line and the uncertainty in its measurement (31 May 2018).
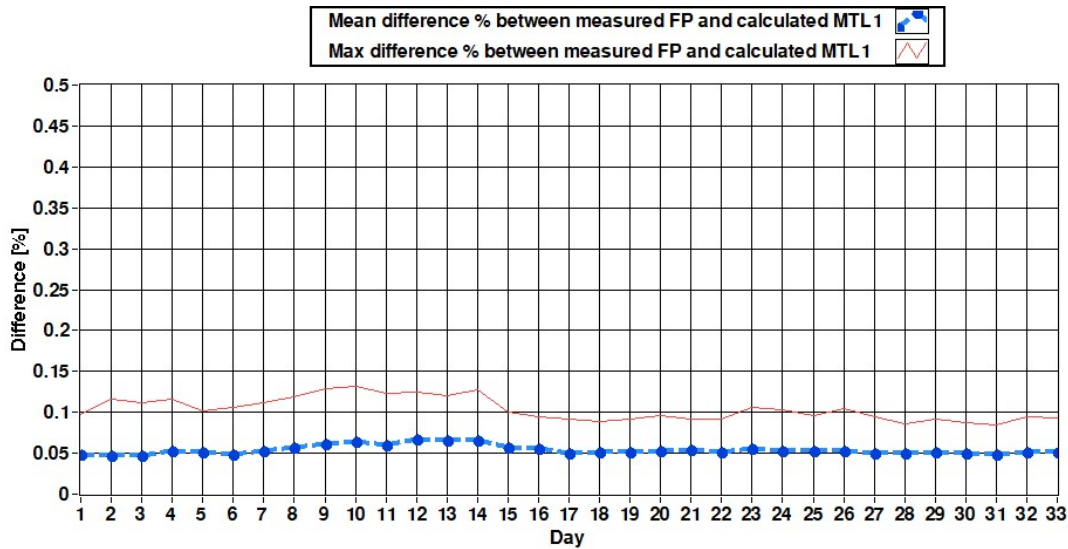
Figure 19 Average and maximum value of the relative difference between the measured and the calculated values of the active power flow of branch 1 of the "MT L1" line for the 33 analyzed days.

Uncertainty power flow evaluation

To evaluate the uncertainty in the output quantities, a Monte Carlo analysis was performed using the VI described before. The Monte Carlo procedure was performed for a whole day, the 31 May 2018; the power flows and related uncertainties were evaluated every 2 s. For each set of measured input quantities, the load flow algorithm was performed 10^5 times. At the end of the 10^5 iterations, an average value and an extended uncertainty are obtained. Then, the process is repeated for the following set of input data, related to the subsequent 2 s.

Figure 20 shows the comparison between the calculated uncertainty with the Monte Carlo procedure and the measurement uncertainty obtained with (9)(10) for the active power flows measured by the PQA installed at the MV level of branch 1 of the "MTL1" line. Figure 21 shows a similar graph for the reactive power flows. It can be seen that calculated uncertainties are comparable with those of measurement power flows.

Maximum, minimum and average uncertainties on the power flows of each branch of "MTL1" line are reported in Figure 22 and Figure 23. The same graphs are shown for the "MTL2" line (Figure 24 and Figure 25and for the "MTL3" line (Figure 26 and Figure 27). In all cases, the results of the measured and calculated power flows were compatible and the calculated uncertainties are comparable with the measurement ones.
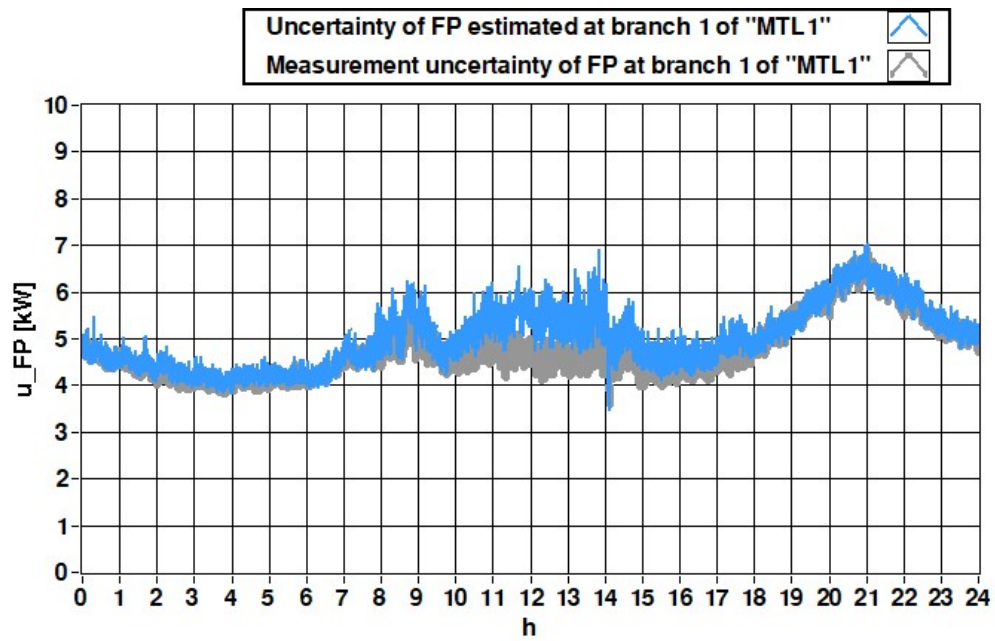
Figure 20. Comparison between the measurement and the calculated uncertainties in the active power flow of branch 1 of the "MTL1" line (31 May 2018).
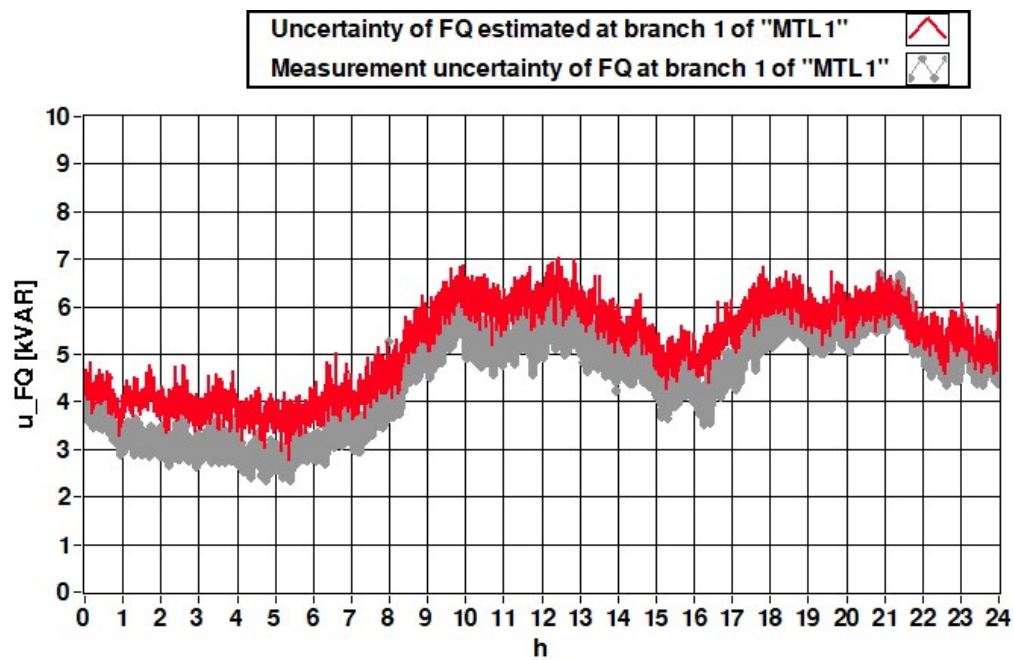
Figure 21 Comparison between the measurement and the calculated uncertainties in the reactive power flow of branch 1 of the "MTL1" line (31 May 2018).

Figure 22 Maximum, average and minimum values of the absolute uncertainties in the calculated active power flows of the "MTL1" line (31 May 2018).
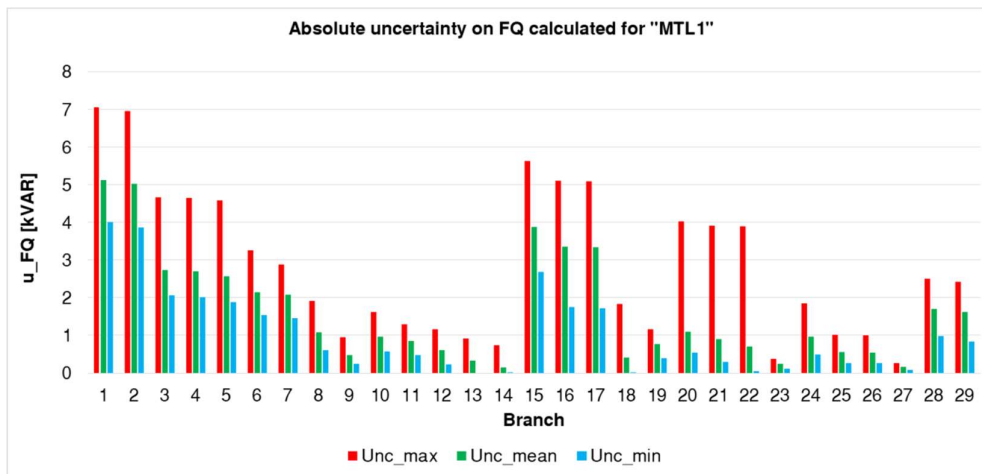
Figure 23. Maximum, average and minimum values of the absolute uncertainties in the reactive power flows calculated of the "MTL1" line (31 May 2018).
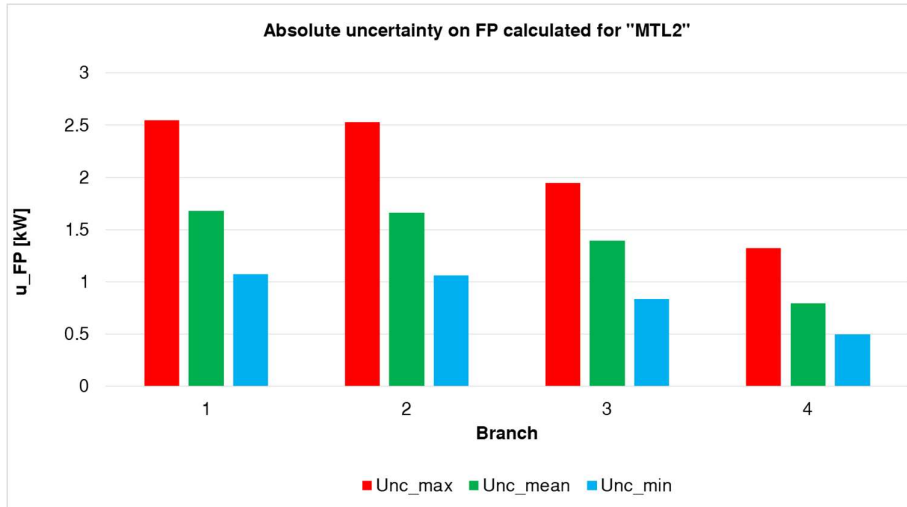
Figure 24 Maximum, average and minimum values of the absolute uncertainties in the calculated active power flows of the "MTL2" line (31 May 2018).
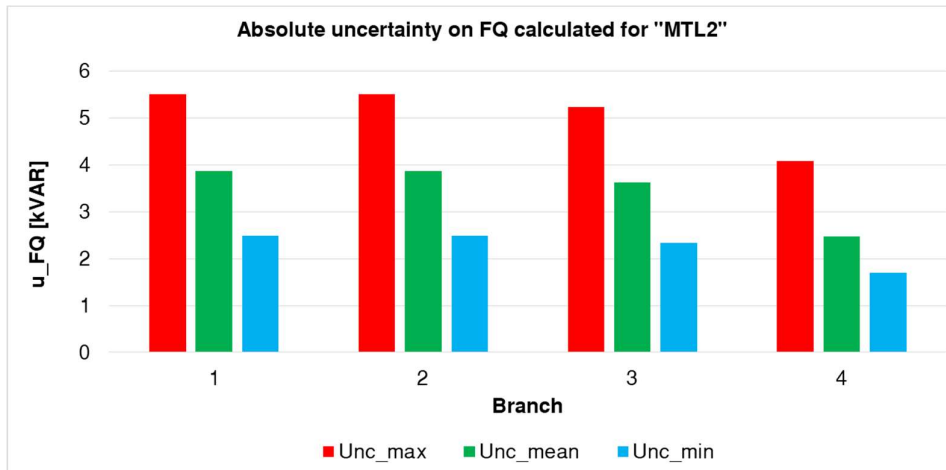
Figure 25 Maximum, average and minimum values of the relative uncertainties in the reactive power flows calculated of the "MTL2" line (31 May 2018).
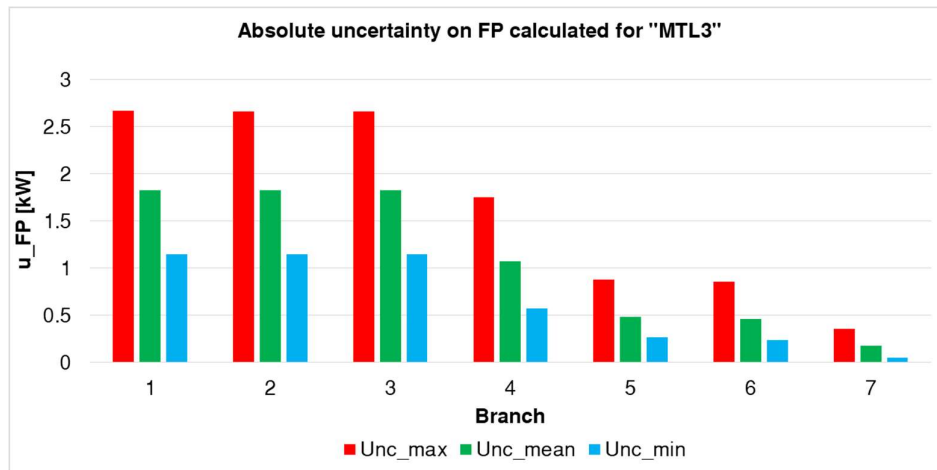
Figure 26 Maximum, average and minimum values of the absolute uncertainties in the calculated active power flows of the "MTL3" line (31 May 2018).
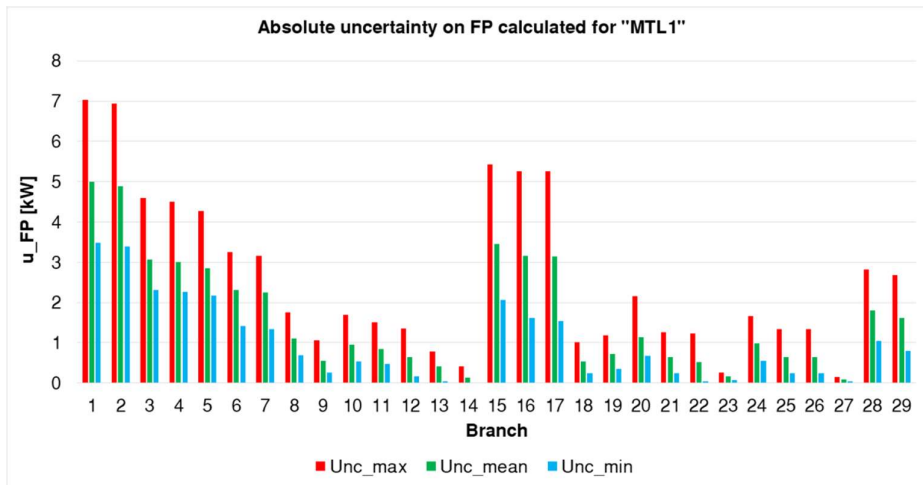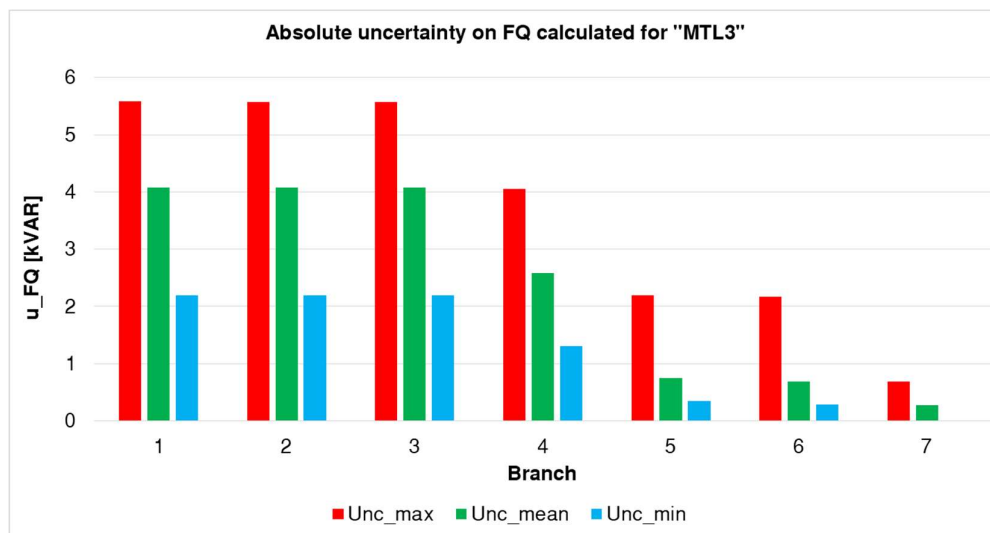

Figure 27 Maximum, average and minimum values of the absolute uncertainties in the reactive power flows calculated of the "MTL3" line (31 May 2018).

Impact of Line Parameters Uncertainties

Since network parameters are also input quantities of the load flow algorithm, their uncertainty influence on the load flow calculation results was also studied. In fact, the network parameter-rated data provided by DSO cannot be exactly equal to the real ones. Thus, an analysis was conducted to assess the influence of the possible deviation of actual line parameter values from the rated ones. In addition, in this case, the evaluation was carried out by means of a Monte Carlo procedure.

In more detail, an uncertainty value was assumed equal for all the network parameters (R, X and Y). Then, for a given condition of all input quantities, the load flow calculation was repeated 10^5 times. At each execution, in addition to the random variation of all the measured quantity inputs, network parameters were also varied inside the assumed uncertainty range. At the end of the 10^5 iterations, an average value and an uncertainty value were obtained for each power flow. The procedure was repeated 16 times, varying the uncertainty value on the network parameters from 0 to 15% with a step equal to 1. The value 15% was chosen as upper limit value. It was determined considering a 10% uncertainty on line length. Moreover, it is lower than the parameter variation correspondent to two subsequent cable subsections (i.e., 25 and 50 mm^2).

Figure 28 shows the trend of the relative uncertainties on the active power flow of branch 1 of the "MTL3" line, due to network parameter uncertainties. Figure 29 shows the same trend for reactive power. The input data are those measured at 13:00:00 on 31 May 2018. It can be seen that the relative uncertainty in the active power flow remains constant. This result can be justified by analyzing the dependence of the active power flow from the network parameters; in fact, it basically depends on the line losses on longitudinal resistance R_i; these losses represent an extremely small percentage of the active power flows. This explains the low dependence of the active power flow from the network parameter uncertainties. A different behavior was observed for the reactive power flow in Figure 29. It is more sensitive to network parameter variability. This is due to the reactive power flow dependence from the line transversal capacitive admittance, i.e., from the term $(-V_i^2/Y_i)$ of Equation (2). It can be seen that network parameter uncertainty variation from 0 to 15% corresponds to a reactive power flow variation from 2% to 9%. Thus, reactive power flow calculations are more sensitive than active power flow ones to grid parameter uncertainty. However, the reactive power flow remains lower than 10% even with a maximum network parameter variation of 15%.
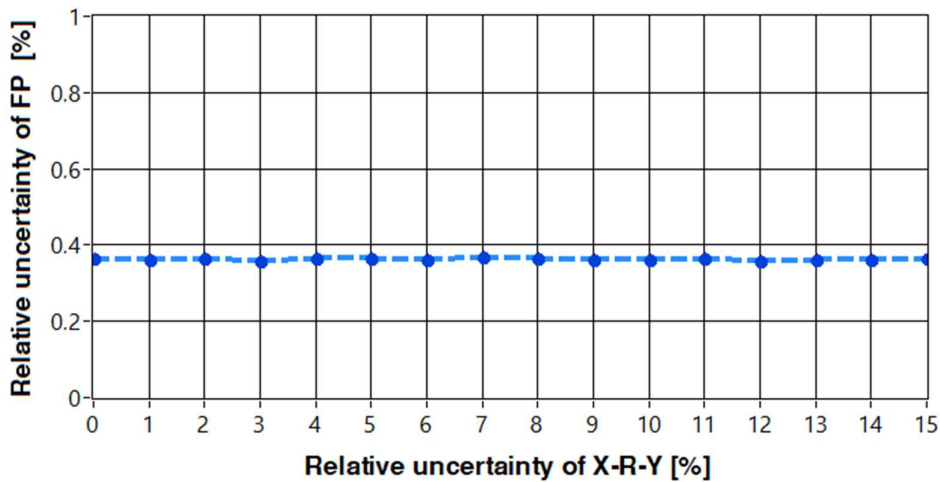
Figure 28 Relative uncertainty in the calculated active power flow of branch 1 of the "MTL3" line in dependence of the line parameter uncertainties
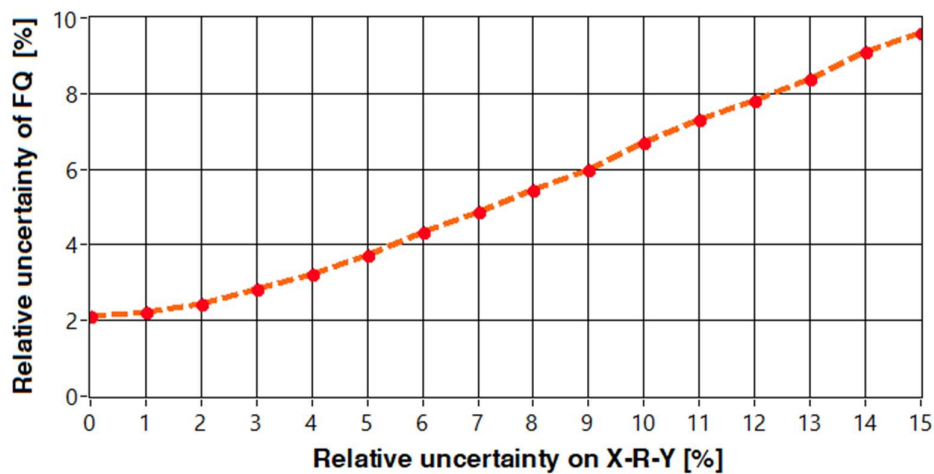
Figure 29 Relative uncertainty in the calculated reactive power flow of branch 1 of the "MTL3" line in dependence of the line parameters uncertainties

Conclusion to power flow implementation

In this chapter a preliminary implementation of a load flow algorithm for a PQA based measurement infrastructure was presented. A backward/forward power based algorithm was implemented in LabVIEW environment and its real-time application was demonstrated. After that, the Monte Carlo analysis was performed to evaluate the uncertainty propagation of the meters. Monte Carlo analysis was also applied in order to evaluate the model impact on active and reactive power flow calculation.

2. Integration of smart prosumer in the distributed measurement system architecture

State of the art on storage energy system integration

The previous architecture was also extended to LV prosumer in order to increase the energy efficiency of the grid and to grow up the profit of the prosumer via demande response paradigm. In particular, distributed storage systems (DSS) of the prosumer can mitigate such phenomena, as they can allow modify DG profiles thanks to proper management of charging and discharging periods [66]. This also foster flexibility in energy exchanges, under demand side management, demand response and dynamic energy price programs at different levels (homes, buildings, virtual power plants, micro-grids and so on). In this framework, a crucial aspect is the interaction between DSO and DSSs [67]–[70]. In fact, in users and prosumers viewpoint, the management logic is governed by economic benefits related to self-consumption of produced/stored energy (energy purchasing savings) and/or to injection of over-production on the grid (energy selling profits). In this sense, users/prosumers are interested in exploiting all their power production capability, regardless of load profiles. In real-time self-consumption logic, during production peaks, once DSS battery has reached its maximum state of charge (SoC), the system aims at injecting energy into the grid; if a large number of DSSs are connected in the same network area, such a logic may cause voltage stability problems, which can require, in the worst case, DSSs power cuts. On the other hand, DSOs are interested in DSSs control, for a better network management. For example, peak shaving strategies implementation can reduce the differences between energy production and consumption profiles throughout the day. To foster the implementation of such logics, users/prosumers should be economically stimulated in the cooperation with DSO. In literature some solutions have been proposed to minimize power fluctuations or to match a given power exchange profile [68], based on short term forecasting of power production and load consumption. However, to obtain an effective result, it is necessary to extend the forecasting at least at daily level (24 hours), in order to allow the best control strategy from both prosumers and DSO viewpoint. In [67] a dynamic programming strategy is proposed, aimed at optimizing both energy cost and battery decay, also taking into account losses deriving from components usage. However, in all such solutions the problem still remains of the interaction between DSSs and DSO [59]–[61]. According to MV/LV distribution grids proposed in Figure 30, already shown, is possible to enable the interaction of different communication solutions and field devices for DGs and DSSs .

In the following, is shown a new scheduling strategy to plan the daily power exchange of the DSS with the grid, which is based on: daily production from renewable sources; electric load; hourly energy

prices; battery model. The advantage of the proposed solution is that it allows minimizing the energy costs for the user, at the same time providing DSO the possibility to request changes in the power exchanges profile between DSS and the grid. The proposed algorithm is very simple; thus it can be easily integrated in the DSS IPS, without adding extra hardware modules. In the following sections the proposed algorithm is described, and some preliminary simulation results are presented, showing the feasibility of the proposed solution on a simple case test system at home level.
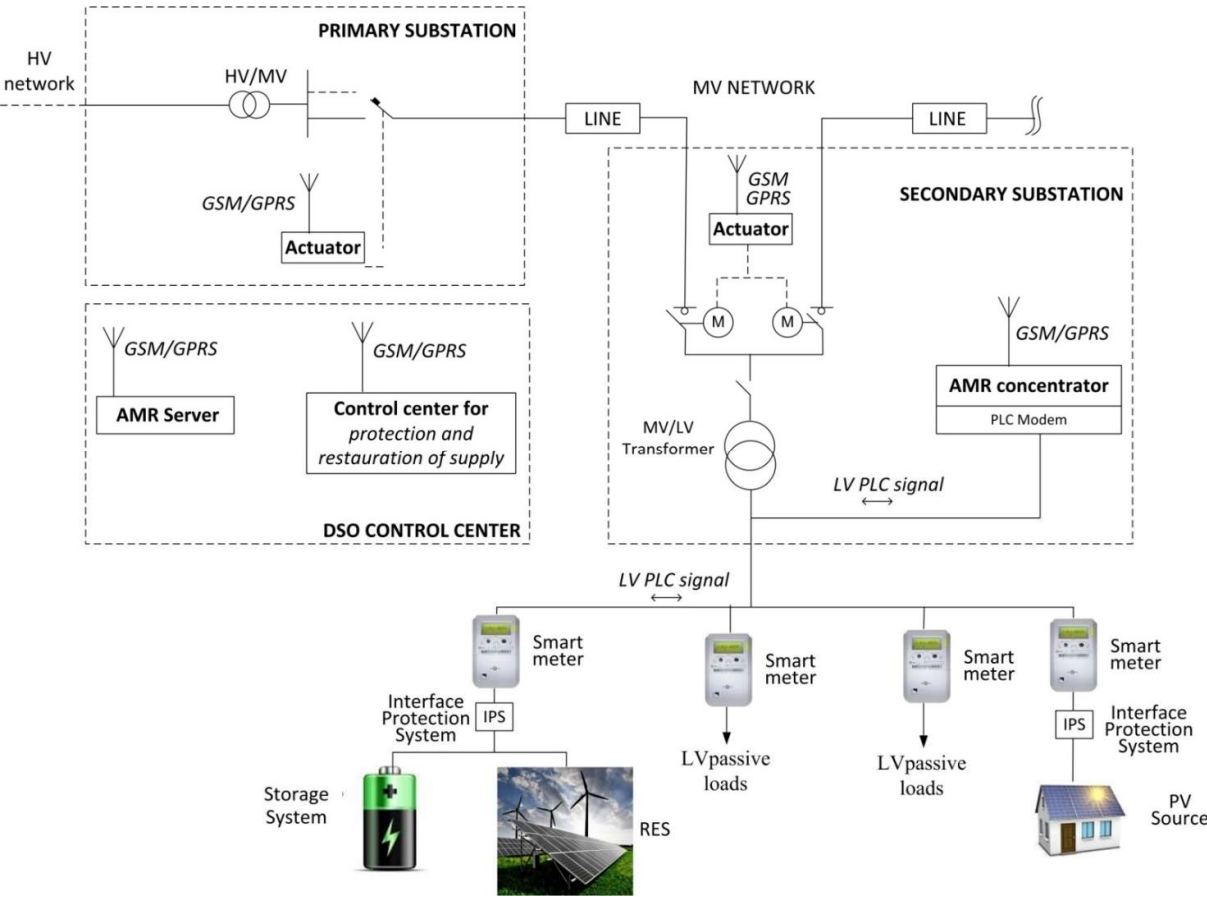

Figure 30 Distributed measurement architecture for DSS interaction

Optimization algorithm for DSS management

The target of the problem is to determine the DSS battery charge and discharge periods, allowing a dynamic response to both load features and the DSO requests.

The proposed solution makes use of the following objective function:

$$OF = \sum_{i=1}^{N} C_{in}(i) * P_{grid-in}(i) * dt + C_{out}(i) * P_{grid-out}(i) * dt \qquad (14)$$

where:

- $P_{grid-out}$ and P_{grid-} are the powers (kW) exchanged with the grid at the delivery point;

- C_{in} and C_{out} are the hourly prices (€/kWh) of energy purchasing and selling ("zone price" Figure 33), respectively;

- dt is the time step for the optimization algorithm; in the case study herein presented, it was chosen equal to one hour, i.e. $N = 24$.

By minimizing the OF function, the battery SoC curve will be obtained, which minimizes the daily cost maximizing the prosumer profit. In the absence of DSO requests, the OF minimization leads to the classical power exchange profile in which energy production and energy absorption are incremented during the hours with higher selling prices and lower purchasing costs, respectively.

In the proposed approach, the interaction with DSO is obtained by changing C_{in} and C_{out}; in more detail, in a given time dt, C_{in} and C_{out} are used as weights for $P_{grid-in}$ and $P_{grid-out}$ and they can be changed by the DSO, in order to request the DSS to act as load or generator (i.e. absorbing or injecting power) according to the operating condition of the grid. Thus, the algorithm evaluates in which hour it is more convenient for the DSS to inject or absorb energy, based on C_{in} and C_{out} coefficients. For example, if in a given hour the selling price is particularly high, it is expected that the DSS will try to sell as much energy as possible. On the other hand DSO can use C_{in} and C_{out} coefficients as incentives for DSS power injection/absorption increase or decrease; for example, if in a given moment dt^* there is an energy overproduction in a node near the DSS, the DSO can encourage the DSS to act as a load (i.e. to absorb energy) by decreasing the value of $C_{in}(t^*)$; similarly, if the DSO wants to encourage the DSS to act as generator, an increase of $C_{out}(t^*)$ can be set. The more is the difference between the modified and the contractual costs, the more the DSS will be encouraged to meet the DSO request.

To obtain the best battery charge/discharge profile, the algorithm requires the knowledge of forecasting data and/or historical measurements of power production and load consumption. As regards load, the scheduling algorithm for peak shaving and self-consumption profiles, needs the estimation of the day-after load diagram, which can be obtained as forecasting or from previous days measurements. For example, for a home user, a typical load profile is shown in Figure 31, where peak consumptions are in early morning and evening hours. Considering the case of photovoltaic (PV) production, such a

profile represents a worst case in the energy efficiency viewpoint, because PV profile typically has its peak production in central hours of the day (depending on weather conditions). As an example, for a clear sky day, the PV profile can be approximated as shown in Figure 32 (parabolic function, with peak value in the middle of the day and zero values before sunrise and after sunset). As regards the energy purchasing and selling prices depend on DSO tariffs and energy market. For example, for a typical home user (rated power 3 kW and energy consumption less than 1700 kWh), the hourly purchasing prices are reported in Figure 33. For the energy selling prices, in the Italian case the hourly zonal price can be considered, which is daily determined according to the "day-ahead" market results; for example, the hourly prices in two days of September 2018 are reported in Figure 34 and Figure 34.
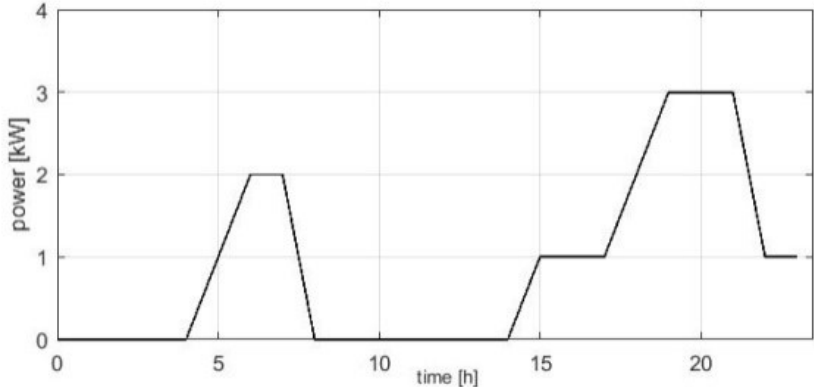
Figure 31 Load profile (average hourly consumptions). Load power vs. hours
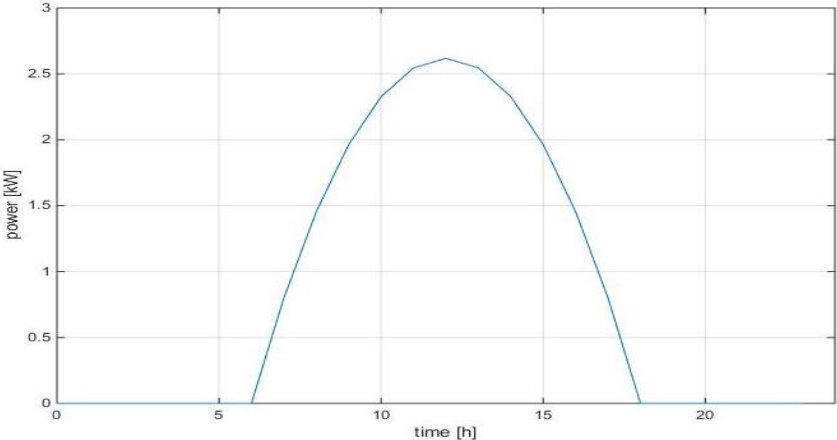
Figure 32 PV generation profile. Generated power vs. hours
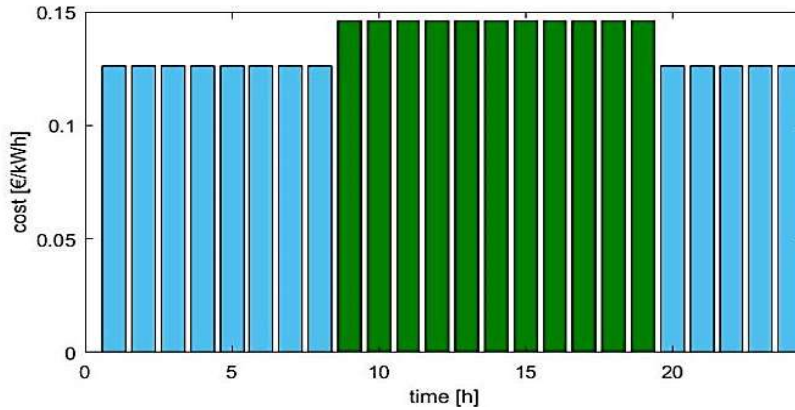
Figure 33 Hourly energy purchasing prices
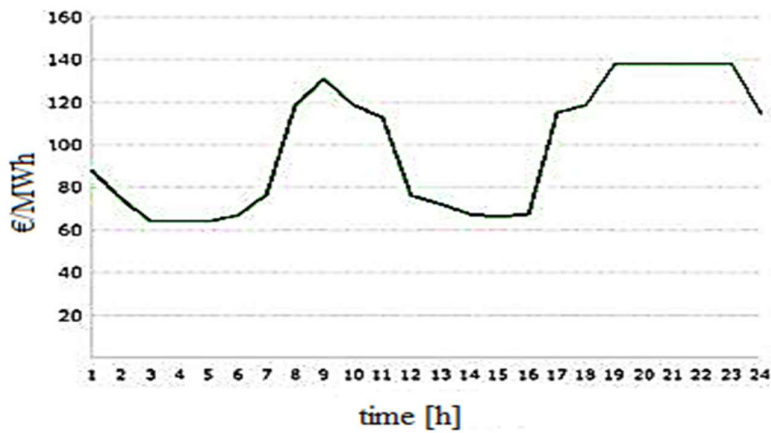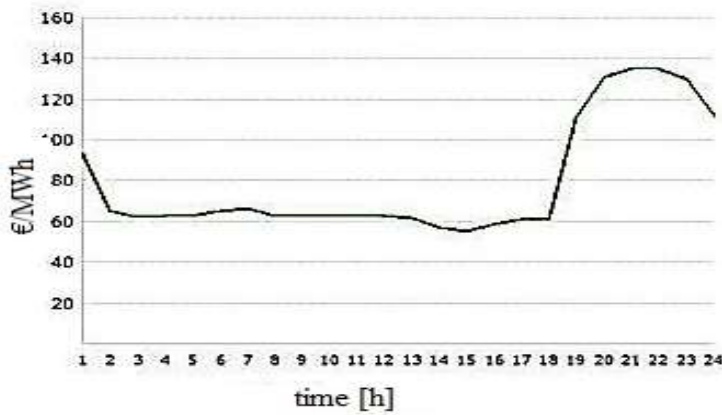
Figure 34 Hourly energy selling zone price in Sicily; (a) Sunday, September 2, 2018; (b) Wednesday September 5th, 2018

Starting from the aforesaid input data, a Particle Swarm Optimization (PSO) algorithm is used to find the OF minimum. In very brief, the PSO is a heuristic method which start from an initial population. In PSO algorithms the population is modeled as a swarm of birds in which the behavior of each agent

inside the swarm can be represented with simple vectors. In the proposed algorithm, the initial population of possible solutions (powers exchanged from battery or SoC) is chosen randomly and it is ordered with respect to solutions daily cost. The second step is combining the previous feasible solutions using the PSO algorithm target to find the optimal solution for OF, according with the equations (15) and (16). In this logic, each agent exploits two pieces of information in decision process. The first is its experience and the related choices results; the second one is other agents experiences. Modification of the agent position is realized by the position and velocity information. Each agent knows its best value (pbest) and its position; moreover, each agent knows the best value so far in the group (gbest) among pbests. These pieces of information are the personal experience of each agent and the knowledge of how the other agents around them have performed, respectively. Each agent tries to modify its position using the following information: current position, current velocity, distance between the current position and pbest, distance between the current position and gbest. Velocity of each agent can be modified by the following equation:

$$v_i^{k+1} = wv_i^k + c_1 rand1 * (pbest - s_i^k) + c_2 rand2 * (gbest - s_i^k)$$

Where:

- v_i^k is the current velocity;

- s_i^k is the current position of the agent E;

- v_i^{k+1} is the modified velocity (ΔE);

- w, c_1, c_2 are weights that can be chosen arbitrarily.

Generally $c_1 \ and \ c_2$ are equal to 2 and w is calculated by the following equation:

$$w = w_{max} - \frac{w_{max} - w_{min}}{iter_{max}} * iter$$

With typical value $w_{max} = 0.9$ and $w_{min} = 0.4$.

The current position is modified by the following equation:

$$s_i^{k+1} = s_i^k + v_i^{k+1}$$

In the our case, a good choice for the vector of position is the daily SoC while the velocity vector is calculated by the following equation:

$$v_i^{k+1} = wv_i^k + c_1 rand1 * (pbestE_i - E_i^k) + c_2 rand2 * (gbestE - E_i^k)$$

For each new feasible solution, the algorithm calculates the power exchanged from battery P_b and then power exchanged with the grid P_{grid}. After that, it calculates the daily cost and upgrade the *pbest* and *gbest*. Obviously, being PSO a heuristic method, the solution will be a sub-optimum and it will be not unique; however, the advantage of using this algorithm is the absence of differential and matrix calculus, thus it can be easily implemented in the DSS IPS directly using the real values without discretization.

Case study. System model and simulation results

The case study power system is compliant with CEI 0-21 requirements (see Figure 35) It represents a typical home user equipped with:

- a DSS (12 kWh, 4kW, 177,6 V) composed by 8 Li-ion battery with 75 Ah connected in series;

- a PV generator with power peak of 2,6 kW;

- different loads with maximum power of 3 kW.

The model of battery is reported in Figure 36. This model allows calculating the injected/absorbed current and determining power losses and daily cycle efficiency. Assuming that power injected on the grid by the DSS has negative sign and power absorbed from the grid has positive sign, it is possible to write the following equations:

$$\Delta E = P_b * \Delta t \qquad (15)$$

$$P_{ext} = P_b + DP \qquad (16)$$

$$P_{grid} = P_{ext} + P_{el} - P_{pv} \qquad (17)$$

$$DP = R * I_b^2 \qquad (18)$$

$$P_b = U * I_b \qquad (19)$$

$$I_b = \frac{U_l - U}{R} \qquad (20)$$

where:

- E is the energy (kWh) stored in the battery and ΔE is its variation in the time step Δt;

- P_{ext} is the power (kW) injected into the grid;

- P_b is the power (kW) exchanged at battery terminals;

- P_{el} is the load power (kW);

- P_{grid} is the power (kW) exchanged with the grid;

- DP are power losses;

- I_b is the current at the battery terminals;

- R is the equivalent resistance of battery and inverter;

- P_{pv} is the power injected from PV generator;

- U is the no-load voltage at battery terminals;

- U_L is the voltage imposed by the inverter.

No-load voltage at battery terminals depends on the battery state of charge (SoC), as shown in Figure 37.

Battery constraints, in terms of power and energy capacity, respectively, are:

$$-P_n < P_b < P_n \qquad (21)$$

$$E_{min} < E_0 + \Delta E < E_{max} \qquad (22)$$
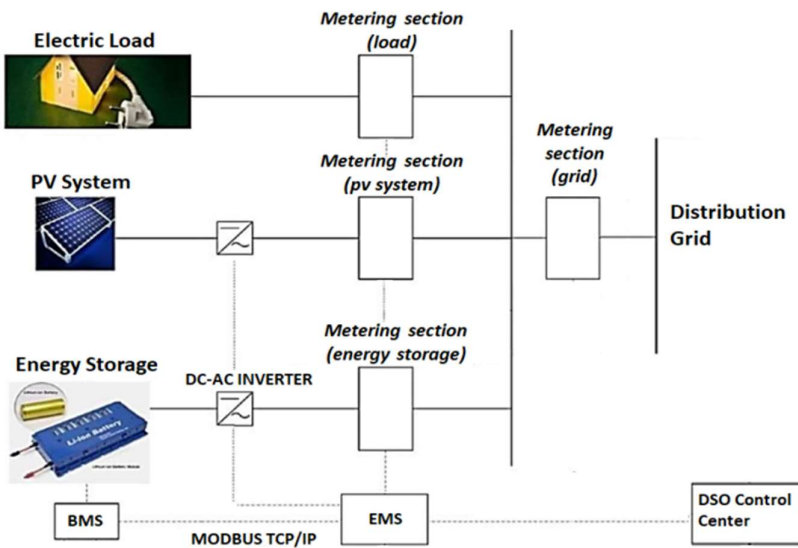
Figure 35 power system case study
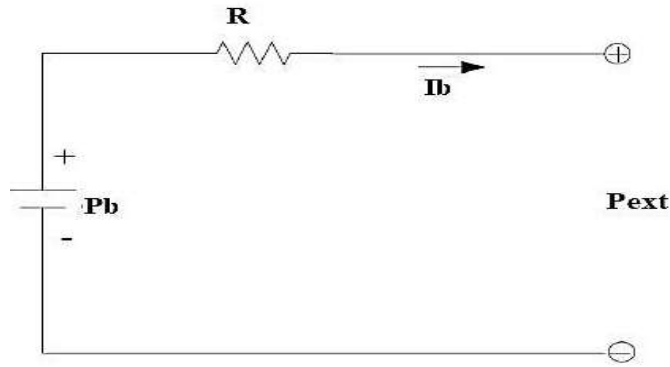
Figure 36 Model of the battery
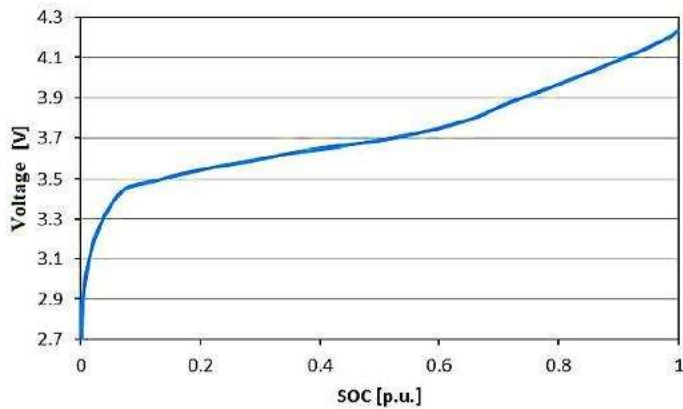
Figure 37 Battery no-load characteristic

Moreover, to ensure the correct scheduling program in subsequent days, the following condition must be met, which represent the constraint on the battery SoC at the end of the day (the smaller is δE the more the final SoC will be equal to the initial state):

$$E(0) = E(24) \pm \delta E \qquad (23)$$

To verify the effectiveness of the proposed optimization solution, different scenarios were simulated, by considering the cases of operation in both the absence and the presence of DSO requests for DSS demand response operation. In the simulations, the following parameters were set: $E_{max} = 12\ kWh$, $E_{min} = 10\%E_{max}$, $\delta E = 10\%E_{max}$, R $= 1\ \Omega$.

Case 1: Initial scenario

This scenario refers to the case in which no requests are made by DSO. The considered day is September 5th, 2018. The initial battery SoC was set a 20%. As shown in Figure 34 (b), this was a day in which selling prices were very high between the 8 and 11 a.m. The SoC and the power flows curves are reported inFigure 38 and Figure 39, respectively. As expected, the algorithm tries to increment the

energy production during the hours with higher selling prices. As shown in Figure 40, the algorithm finds the sub-optimal solution in 300 iterations (in the subsequent iterations, the cost remains constant at the final value).
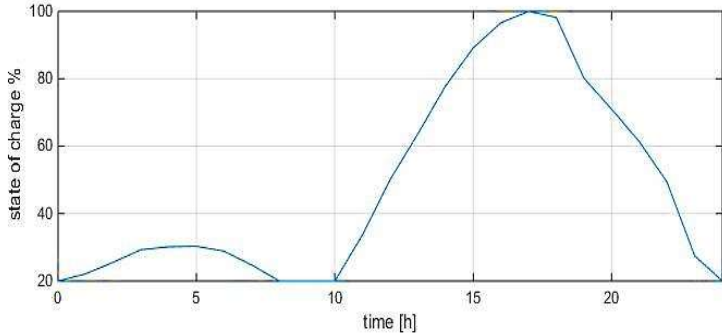
Figure 38 Case 1 scenario. Battery SoC curve
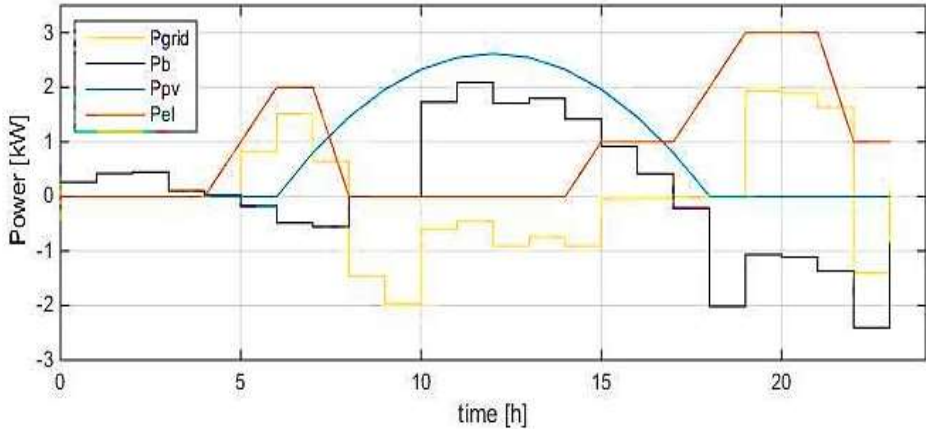
Figure 39 Case 1 scenario. Power flows diagrams.
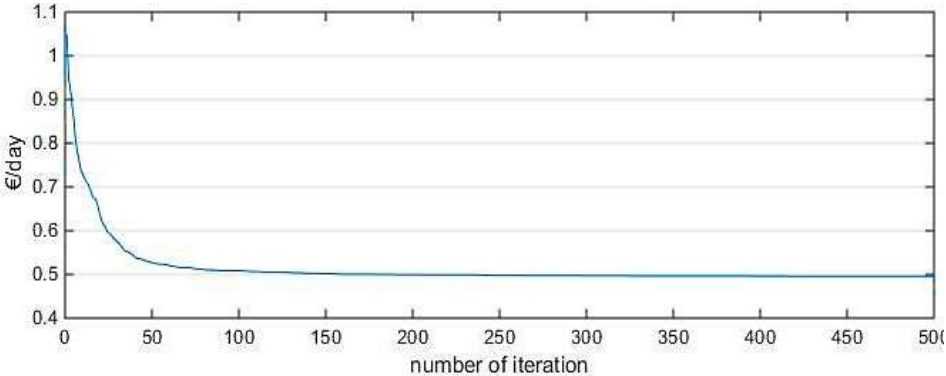
Figure 40 Case 1 scenario. Cost per day optimization diagram

Case 2: Demand Response scenario (load)

The results show the response of the algorithm after DSO requests DSS to work as a load. To simulate this situation, the energy purchasing cost was to zero the at 14-th hour of the day; thus the DSS tries to absorb as much energy as possible, as shown in Figure 41 and Figure 42.
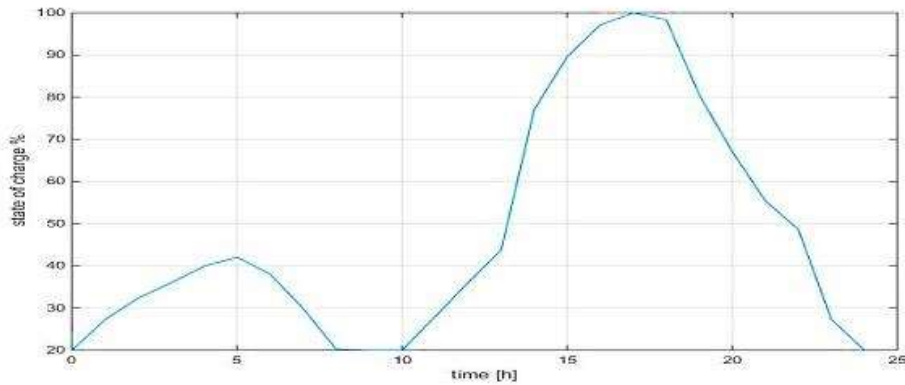
Figure 41 Case 2 scenario. Battery SoC curve
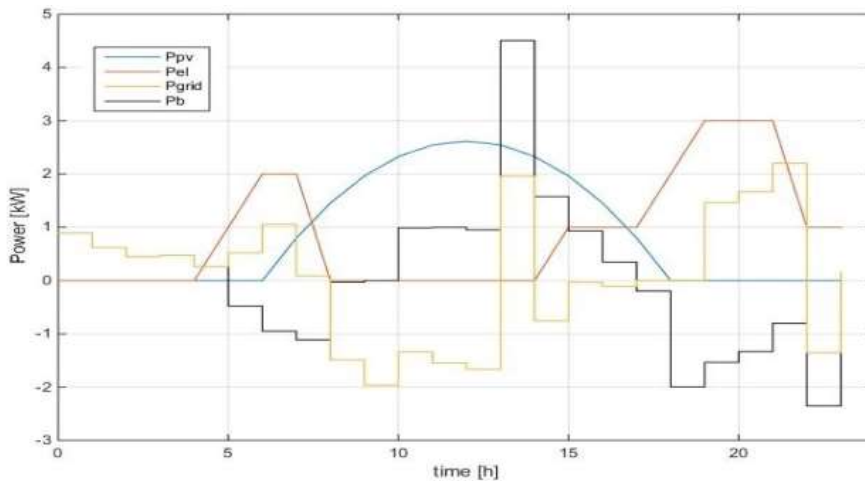
Figure 42 Case 2 scenario. Power flows diagrams

Case 3: Demand Response (generator)

The results show the response of the algorithm after DSO requests DSS to work as a generator. To simulate this condition, an increment of selling price of +0,07 €/kWh was set at 18-th and 19-th hours. In such condition, the system responds to inject as much energy as possible into the grid, as shown in Figure 44 and Figure 44.
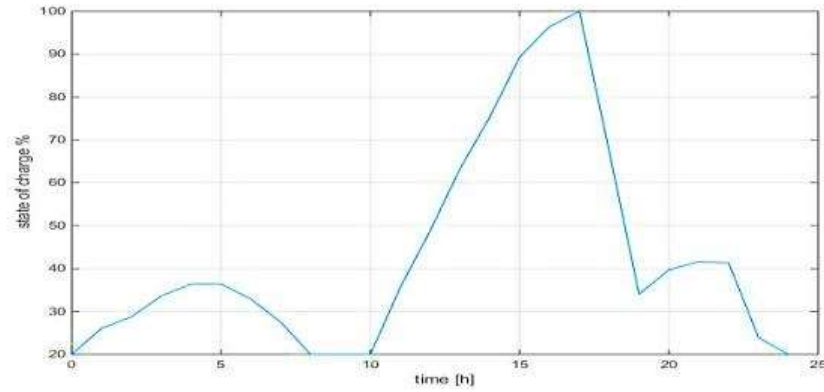
Figure 43 Case 3 scenario. Battery SoC curve
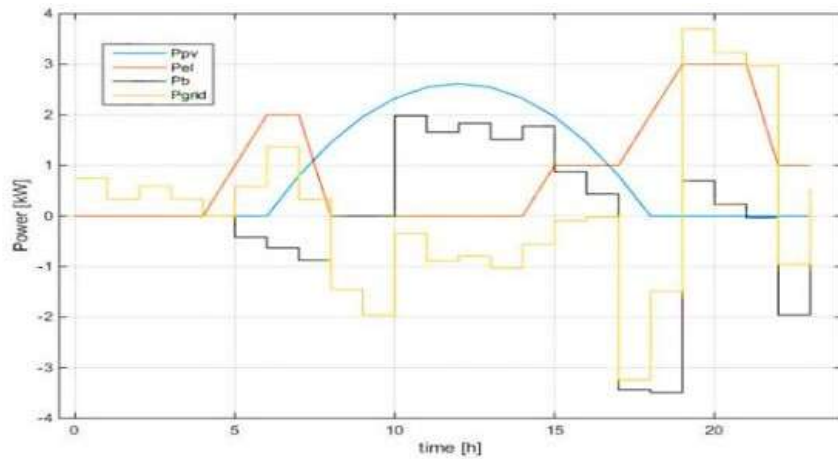
Figure 44 Case 3 scenario. Power flows diagrams

The simulation results show that in the absence of specific DSO requests, the algorithm leads the DSS to the operation with the lowest energy absorption form the grid. On the other hand, when DSO request to work as load or generator the algorithm leads the DSS to follow the DSO request, increasing the total amount of energy exchanged with the grid and also obtaining an economic benefit for the prosumer (see Table 6).

Table 6 Comparison of results of absorbed/produced energy and daily costs for the simulated scenarios

	Case 1	Case 2	Case 3
Energy abs. [kWh]	9.8536	12.1291	14.7086
Energy prod. [kWh]	-8.5665	-10.5062	-12.8112

Daily Cost [€]	0.4980	0.3999	0.3143

Battery model improvement

The previous section the paradigm for the integration of DSSs was shown. The core scheduling algorithm is based on a simplified model of a generic battery. In this section, a model improvement for Lithium cells is shown. In detail, the section proposes a methodology to characterize the single battery. The suggested characterization tests are used to identify the parameters of the battery model and in particular those related to the hysteresis phenomenon and the transition between charging and discharging conditions. To this aim, a linearization method is used to guarantee a good compromise between accuracy and computational cost, in order to facilitate its implementation on common hardware platforms, such as those used for intelligent electronic devices for smart grid applications [4], [59]. Furthermore, since the hysteresis effect causes two different trends in battery charge and discharge conditions, the Li-ion battery model it is modified including two look-up tables and a proper modelling of the transition between charge and discharge condition (and vice versa). Starting from the obtained model, a mixed algorithm is used for SOC estimation, which takes into account both traditional coulomb counting method and the developed model itself. It allows obtaining good estimation accuracies even when low accuracy or drifting measurement transducers are used to acquire the current absorbed or supplied by the battery. In fact, it is known that measurement transducers, if not properly calibrated, can be the main source of uncertainty in both ac and dc power systems applications [6]. The model is verified in a real case study of a grid connected storage system. To this aim, the proposed estimation algorithm was implemented in a PC-based instrument, which acquires voltage and current and estimate the SoC of the battery series. Experimental tests were performed to verify the proposed method accuracy and to compare its performances with those of other estimation methods presented in literature.

Proposed procedure for battery characterization and modelling

The battery behaviour can be modelled starting from the first order circuit Thevenin model shown in Figure 45. This model is widely used in literature [71]–[74], thanks to its low computational cost and its fidelity of response.
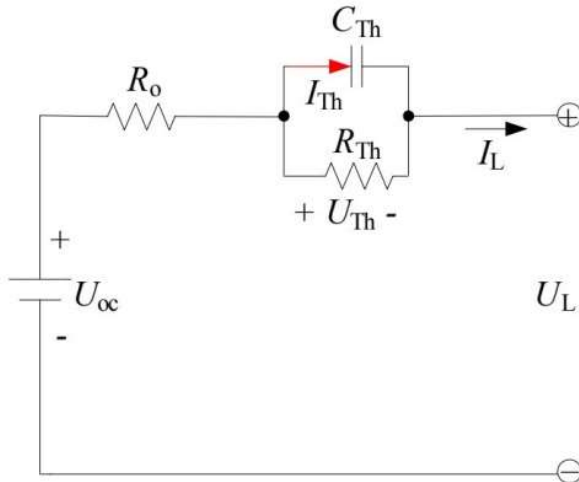
Figure 45 first order Thevenin model

In this model the voltage generator U_{OC} represents the open circuit voltage (OCV) of the battery at different levels of the SoC, the resistance R_0 models the voltage drop that occurs in the transition between no-load and load conditions and the RC group (R_{Th} and C_{Th}) represents the exponential transients phenomena.

Voltages and currents of the model are regulated by the following equations:

$$\begin{cases} \dot{U}_{Th} = -\dfrac{U_{Th}}{R_{Th}C_{Th}} + \dfrac{I_L}{C_{Th}} \\ U_L = U_{oc} - U_{Th} - I_L R_o \end{cases} \qquad (24)$$

where: U_L is the terminal battery voltage, I_L is the current and U_{Th} is the voltage drop in RC group.

Generally, the parameters R_{Th}, C_{Th}, R_O vary with SoC, thus their behavior has to be emulated through functions. This causes an increase of computational cost in SoC estimation. In order to limit such problem, in the proposed approach the mean values of three parameters are used, which are obtained between 10% and 100% of the SoC. The 10% value is chosen because lower SoC values are normally not used, in order to preserve battery life.

To obtain the model parameters, the characterization procedure consists of only 3 tests, in order to have a suitable compromise between execution time, costs and results effectiveness. The three tests are:

1) a capacity test: it is aimed at evaluating the actual capacity of the battery in Ah and Wh;

2) an impulse charge / discharge test: it is necessary for quantifying the circuit parameters;

3) an hysteresis test: it is a test cycle to model the OCV phenomenon of hysteresis.

As regards the battery OCV (U_{OC}), the Li-ion battery has two different trends for charge and discharge conditions, because of the hysteresis effect. In order to take into account such effect, in the proposed method the model it is modified including two look-up tables and a proper modelling of the transition between charge and discharge condition (and vice versa).

The procedure steps are described in the following subsections, including both model parameters evaluation and charging/discharging transition modelling. In next sections it is applied to a case study battery to obtain the model parameters and verify the SoC estimation effectiveness.

Capacity test

The capacity test consists in a constant current charging phase followed by a constant voltage charging phase. This two phases are used to be sure that the battery is fully charged, thus obtaining the total charging capacity, $C_{tot-charge}$, of the battery as the sum of the energy used in these two phases according to the following formulas

$$C_{tot-charge} = C_{CC-charge} + C_{CV-charge} \qquad (25)$$

where $C_{CC-charge}$ is the capacity measured during the constant current charging phase and $C_{CV-charg}$ that measured during the constant voltage charging phase.

Similarly, to obtain the total discharging capacity, a constant current discharge phase is carried out followed by a constant voltage discharge phase. The energy required to discharge the battery, $C_{tot-discharg}$, will be again obtained as the sum of the energy used in these two phases according to the following formulas

$$C_{tot-discharg} = C_{CC-discharge} + C_{CV-discharge} \qquad (26)$$

where $C_{CC-discharg}$ and $C_{CV-discharge}$ are the capacity measured during the constant current and voltage phases, respectively.

The ratio between discharging and charging capacities determines the battery efficiency:

$$\eta_A = \frac{C_{tot-dischar \quad (Ah)}}{C_{tot-charge(Ah)}} \qquad (27)$$

and

$$\eta_E = \frac{C_{tot-discharg \ (Wh)}}{C_{tot-charge(Wh)}} \qquad (28)$$

In equations above, energy capacities are expressed in Ah (for amperometric efficiency) and Wh (for energy efficiency), respectively.

Impulse charge / discharge test

The test is divided in two stages. The first stage starts with a total capacity charge. Then, a sequence of discharging phases is performed. Each discharging phase is performed with a constant current. The phase duration is the time required to discharge the battery to 10% of its total capacity $C_{tot-discharge}$. The amplitude of the test current is chosen as a compromise between the desired accuracy on the model parameter evaluation and the duration of each phase. In fact, in order to have the maximum accuracy in resistance measurement, the current value must be as high as possible but this would limit the duration of the step over time and may not be compatible with the battery time constants (typically hundreds of seconds).

Each discharging phase is followed by a rest phase. The duration of this rest phase is chosen equal to several times the battery time constant, which is generally in the order of hundreds of seconds for electrochemical batteries. This allows assuring that the voltage measured at the end of each rest phase can be assumed as its steady state value, i.e. the OCV. In this way at the end of the test, the OCV characteristic can be drawn for different SoC. This OCV trend is characteristic of the discharging condition. Repeating the impulse test procedure with charging phases, the OCV trend in charging condition is obtained.

The current and voltage samples measured in the test are used to obtain the OCV characteristic at different SoC, which is calculated as follows:

$$SoC(t) = SoC(0) + \frac{\int i(t) * dt}{3600} * \frac{1}{C_n} \qquad (29)$$

where: SoC(t) is the value of SoC at t interval, SoC(0) is the initial SoC, i(t) is the current at t interval and C_n is the total capacity equal to $C_{tot-discharg}$.

The remaining circuit parameters (R_0 R_{Th}, C_{Th}) can be found by processing the pulse test data in the following way. As already mentioned, R_0 models the voltage drop that occurs at the battery terminals when switching between load and no-load operation; it can be determined as the difference between load voltage and open circuit voltage ΔV_0, measured in the instants immediately following the step itself, divided to the current step.

$$R_0 = \frac{(\Delta V_0)}{\Delta I} \qquad (30)$$

As regards R_{Th} and C_{Th}, the RC group models the transient voltage trend and the additional voltage drop that occurs at the ends of the battery after a sufficiently long time. The resistance R_{th} is calculated as a ratio of the additional voltage variation at the battery terminals during the phase with zero current ΔV_1 (rest phase), measured as difference between the voltage after 1 s of current step and voltage at the end of rest phase, and the corresponding current step.

$$R_{th} = \frac{\Delta V_1}{\Delta I} \tag{31}$$

Finally, the capacitance C_{Th} can be calculated by observing the time constant of the system τ:

$$\tau = \frac{(t_1 - t_0)}{\ln\left(\frac{V(t1)}{V(t0)}\right)} \tag{32}$$

where: t_1 e t_0 are, respectively, the initial and final time instants of the rest phases; $V(t1)$ e $V(t0)$ are, respectively, the voltage at instant t_1 and the voltage at instant t_0

Once the time constant of the circuit has been determined, the capacitance C_{th} is obtained as:

$$C_{th} = \frac{\tau}{R_{th}} \tag{33}$$

Starting from the obtained values of the circuit parameters, the model of Figure 45 can be modified, by using the average values related to different states of the SoC; the transition between the two OCVs can be modelled by using a coefficient *lambda* that varies instantaneously depending on whether the current direction is entering or outgoing the battery. This coefficient is then used to linearize the transition between charging and discharging OCV curves. Defining this coefficient, the U_{OC} can be calculated as follow:

$$U_{oc} = lambda * OCV_{charge} + (1 - lambda) * OCV\_discharge \tag{34}$$
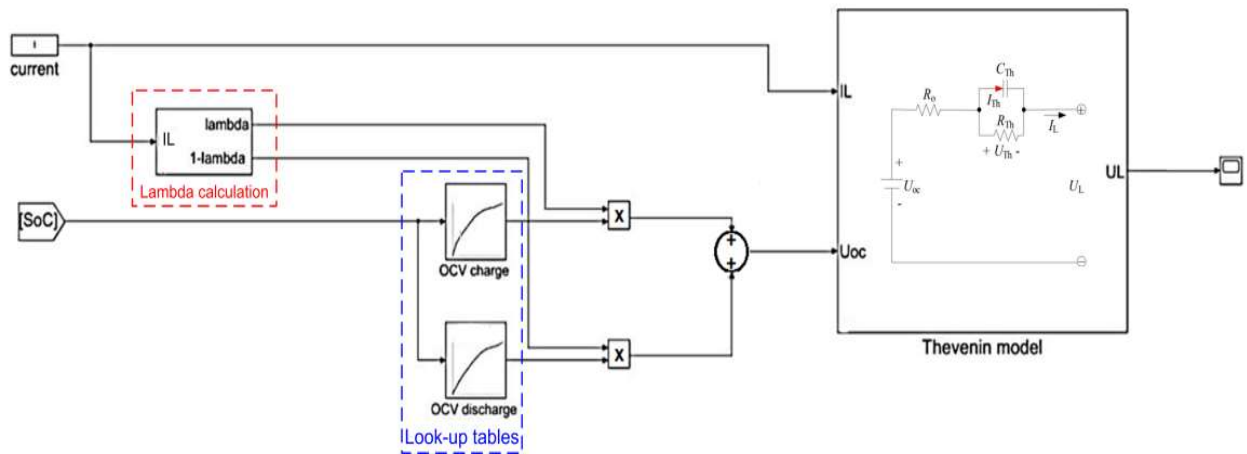
Figure 46 model of battery module (implemented in Matlab/Simulink environment).

Hysteresis test

The proposed test consists of several phases of transition between charge and discharge alternated by rest phases to evaluate the voltage at battery terminals.

In detail, the transition between OCV charge and discharge can be evaluated by performing decreasing deep discharges in order to evaluate the saturation value beyond which there is a certain passage to OCV discharge. Once this value is found, it is assumed that the same value is obtained for the reverse procedure and that the process is linearized during intermediate phases between the two OCV. For example, the test sequence in the case study herein presented consisted of 17 phases.

To further improve the model accuracy, the values of the previous test can be used to identify a logical scheme that allows discriminating among OCV curves (charging, discharging or intermediate phase). The scheme is shown in Figure 47. It shows how lambda parameter depends on both the direction of the current and also an integrator (saturated at the value of 1), according to a coefficient of proportionality K. The greater K or the measured current are, the faster is the transition from one curve to another.
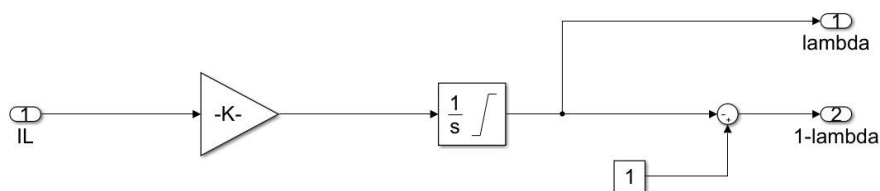
Figure 47 block diagram for lambda calculation (Simulink model).

Case study: test on Li-ion battery pack

To verify proposed procedure and model, a battery composed of 6 Li/Mn cells connected in series was used as case study. It is shown in Figure 48.

Figure 48 test module Li/Mn.

The rated parameters of the battery module are:

- Minimum terminal voltage 16,2 V (2,7 V per cell)

- Maximum terminal voltage 25,2V (4,2 V per cell)

- Rated terminal voltage 22 V

- Rated capacithy 75 Ah or 1,75 kWh

The tests were carried out in an "Angelantoni Discovery 340L" climatic chamber at a temperature of 25 °C. An "Arbin Instruments EVTS-X" system was used to perform charging and discharging cycles on the battery. More in detail, the Arbin cycler is able to impose charging and discharging cycles with constant current, constant voltage or constant power. The battery voltage was acquired each second with an Agilent 34410A multi-meter. The current was acquired with a LEM PR30 or an Agilent N7281A current clamp depending on the maximum current value of the test, i.e. 20 or 150 A respectively. The current clamp was connected to a GDM-8342 multi-meter. The instrumentation rated data are shown in Table 7. The experimental set-up schematic is shown in Figure 49.
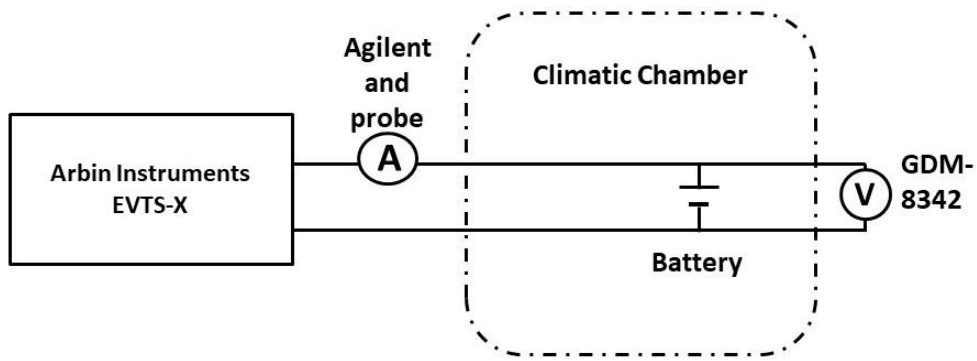
Figure 49 schematic of experimental set-up.

Table 7 Instrumentation used in the experimental set-up.

Climatic Chamber Angelantoni Discovery 340L	**Safety degree EUCAR 6** **Temperature range: -40 °C - +180 °C** **Humidity range: 10% - 98% (+5 °C - +95 °C)** **Dimensions: 850x740x890 mm**
Battery cycler Arbin Instruments EVTS-X	Voltage range 0-150 V Max Current 200 A Max Power 30 kW Voltage accuracy: 0.05V Current accuracy: 0.300A
DMM Agilent 34410A a 6½ count	8500 readings/s at 6½ count sent to PC Voltage accuracy DC 0,003+0,0005 USB communication, driver LabVIEW Multi slope integrator converter
GDM-8342	50000 counts display 40 readings/s for DCV 0.02% DCV basic accuracy true RMS

	USB communication, driver LabVIEW
Agilent N2781A	Bandwith (-3dB): DC to 10MHz
	Current range: 150 A ACRMS or DC
	Output sensitivity: 0.01 V/A
	Amplitude accuracy: 1% of reading (25 °C)
PR30 probe LEM	Current range: 20 A ACRMS or DC
	Output sensitivity: 100 mV/A
	Accuracy: ±1% of reading ±2mA
	Resolution 1mA

Characterization tests

The test procedure described was applied to the case study battery of Figure 48, to obtain the model parameter. The results of each test are reported in the following. Moreover, the charging/discharging transition modeling will be described in detail.

Results of capacity test

Current and voltage measured during the capacity tests are shown in Figure 50.
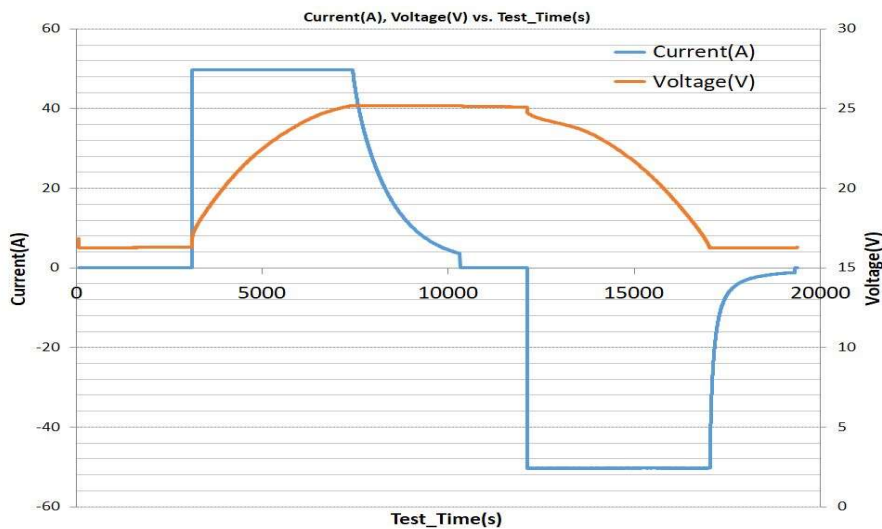
Figure 50 Battery current and voltage measured during the capacity test.

The energy capacities obtained both in Ah and Wh are summarized in Table 8.

Table 8 Capacity test results

Charge		Discharge	
$C_{CC-Charge}$		$C_{CC-discharge}$	
59,95 Ah	1512 Wh	68,11 Ah	1315 Wh
$C_{CV-Charge}$		$C_{CV-discharge}$	
12,95 Ah	314 Wh	3,25 Ah	53 Wh
$C_{tot-charge}$		$C_{tot-discharge}$	
72,9 Wh	1826 Wh	71,36 Ah	1368 Wh

From the results of the test it appears that the module under examination has an amperometric efficiency of: $\eta_A = 0.98$ and an energy efficiency of $\eta_E = 0.75$.

Results of impulse charge / discharge test

The test starts with a total capacity charge, then a sequence of discharging phases is carried out. In the case under study, Each discharging phase was performed at a constant current of 30 A. The phase duration was the time required to discharge the battery of 10% (7,1 Ah) of its total capacity $C_{tot-discharge}$ (i.e. 71,4 Ah see table 2). Each discharging phase was followed by a rest phase of 1h duration. The current and voltage samples measured in the test are shown in Figure 51. Negative values of the current correspond to discharging phases and voltage reduction, while current positive values correspond to charging phases and consequent voltage increase. These data were used to draw the OCV characteristic at different SoC, according to equation (29).
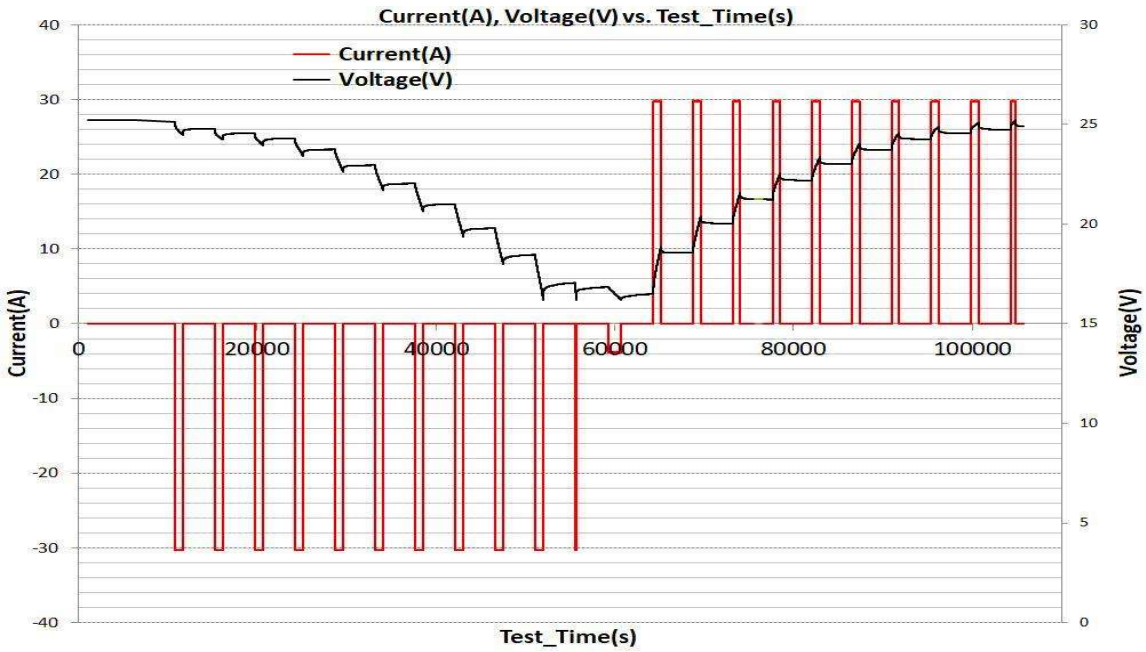
Figure 51 Current and voltage measured in the impulse test.

The OCV trend obtained in charge and discharge conditions are shown in Figure 52. The difference between these two trends gives evidence of the hysteresis behaviour of this type of batteries.
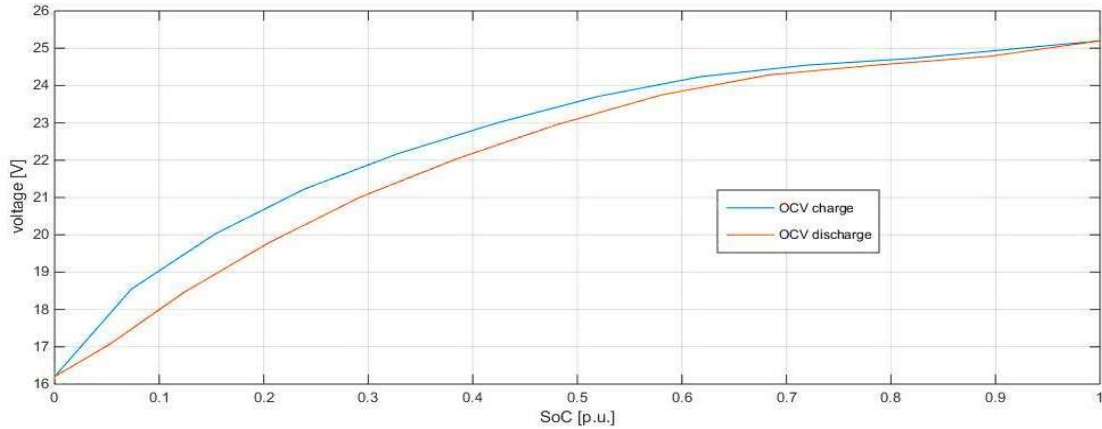
Figure 52 Open circuit voltage measured in the charging and discharging impulse test.

The circuit parameters, R_0, R_{th}, τ and C_{th} were obtained according to equations (30)-(34). The results are shown from Figure 53 to Figure 56. As can be seen, the variability of R_0 and R_{th} is small and it is comparable with the measurement uncertainty. On the other hand, higher variability of τ and C_{th} was found for low values of the SoC. This is due to the higher variability of the voltage measured in the final steps of the discharge phases.
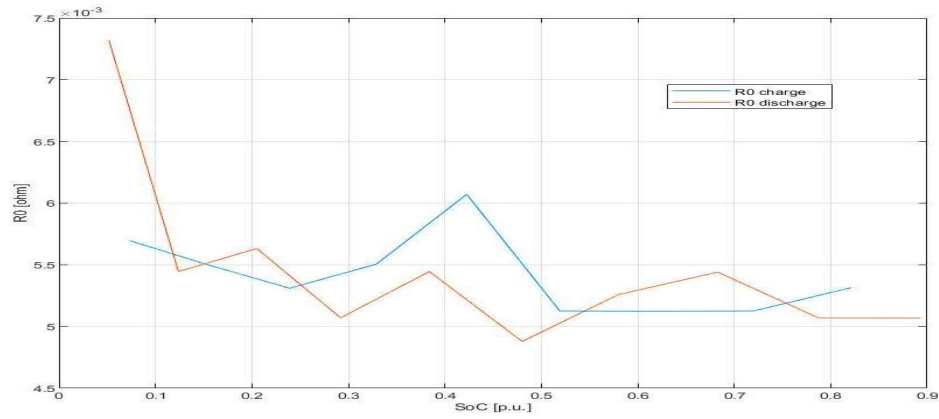
Figure 53 R₀ at different values of SoC.
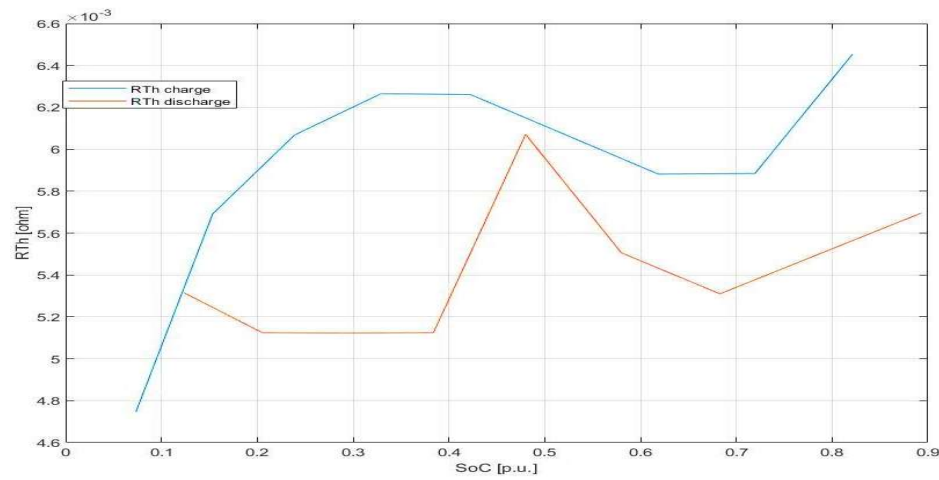
Figure 54 R_{th} at different values of SoC.
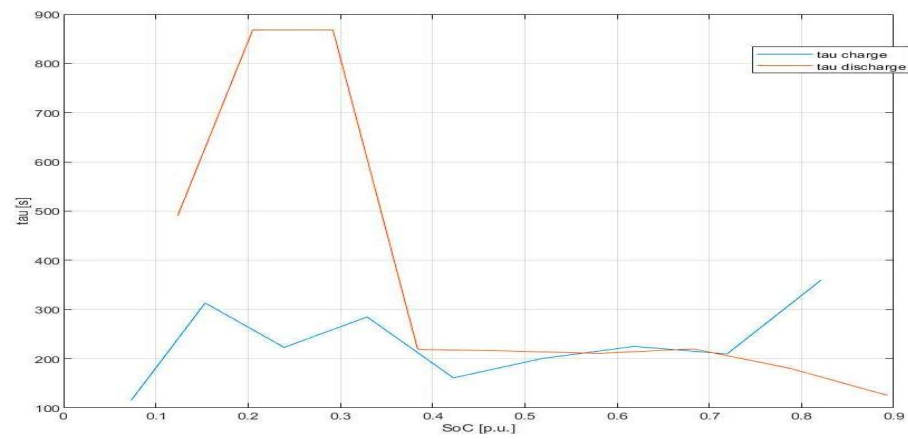
Figure 55 τ at different values of SoC.
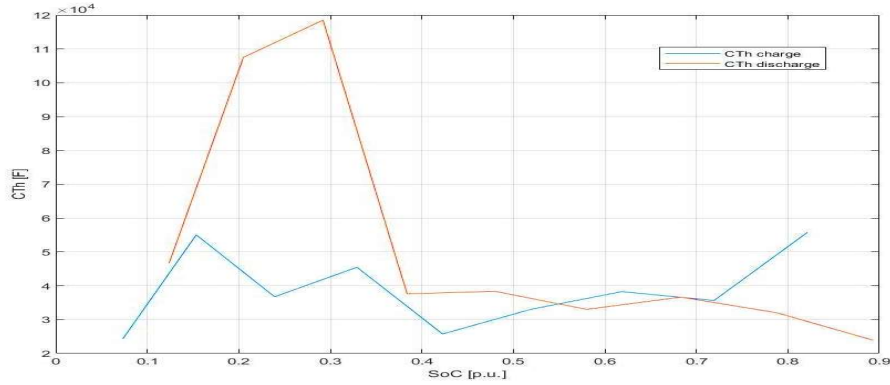
Figure 56 C_{th} at different values of SoC

Table 9 shows the voltage drops used in formulas (30) and (31), during both charging and discharge phases.

Table 9 Charge / discharge test results

Voltage drops ΔV_0 used for R₀ calculation [V] (discharge phase)									
0.153	0.153	0.164	0.159	0.147	0.164	0.153	0.170	0.164	0.221
Voltage drops ΔV_1 used for R$_{Th}$ calculation [V] (discharge phase)									
0.159	0.170	0.181	0.193	0.170	0.176	0.221	0.244	0.318	0.630
Voltage drops ΔV_0 used for R₀ [V] calculation (charge phase)									
0.170	0.164	0.159	0.164	0.181	0.153	0.153	0.153	0.159	0.164
Voltage drops ΔV_1 used for R$_{Th}$ calculation [V] (charge phase)									
0.142	0.170	0.181	0.187	0.187	0.181	0.176	0.176	0.193	

By using the values of the circuit parameters shown in the previous graphs and the Simulink model of Figure 46, the battery output voltage was obtained and it was compared with the voltage values experimentally measured during the test. The results obtained are shown in the following figures. In detail, Figure 57 shows the comparison between the measured battery voltage and the model output voltage (as response to the same current input already shown in Figure 50). In Figure 58, instead, is shown the difference between measured and model output voltages. It can be observed that the largest differences are near the lowest state of charge values (less than 10% of the SoC), which are generally not used to preserve battery life. However, in all cases the differences don't exceed 0.5 V.
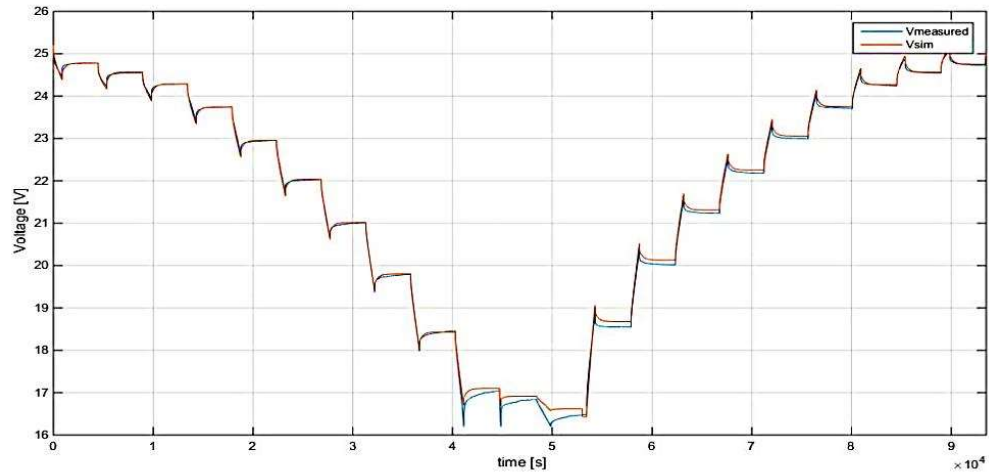
Figure 57 Measured voltage vs. simulated voltage
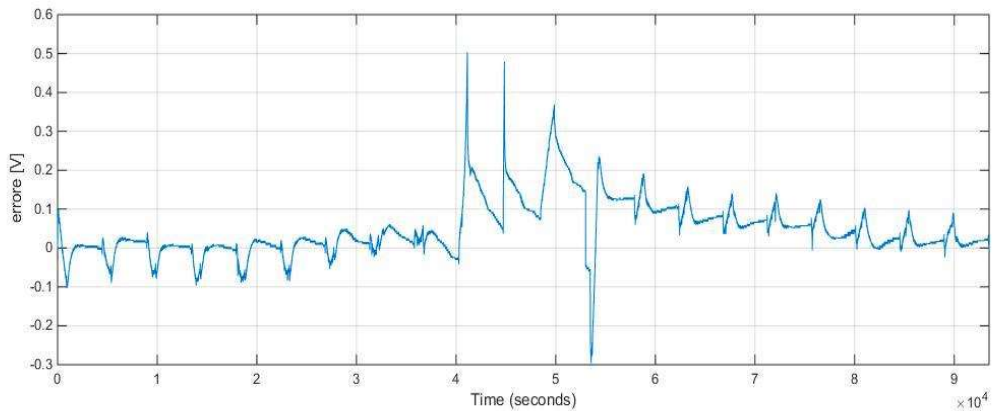
Figure 58 Difference between measured and simulated voltage

Results of hysteresis test

The phases sequence identified for the test is the following (Figure 59):

1. Constant current charging (20 A) from 0% up to 40% of the SoC

2. 30 min rest phase

3. Constant current discharge up to 20% SoC

4. 30 min rest phase

5. Constant current charging up to 40% of the SoC

6. 30 min rest phase

7. Constant current discharge up to 30% of the SoC

8. 30 min rest phase

9. Constant current charging up to 40% of the SoC

10. 30 min rest phase

11. Constant current discharge up to 35% of the SoC

12. 30 min rest phase

13. Constant current charging up to 40% of the SoC

14. 30 min rest phase

15. Discharge at constant current up to 38% of the SoC

16. 30 min rest phase

17. Charge phase up to 80% of the SoC

The 40% of SoC was chosen because it is representative working point where a significant difference is observed between charging and discharging OCV curves as shown in Figure 52. The other charging and discharging percentages were chosen to obtain gradually decreasing variations of SoC and correspondent OCV.
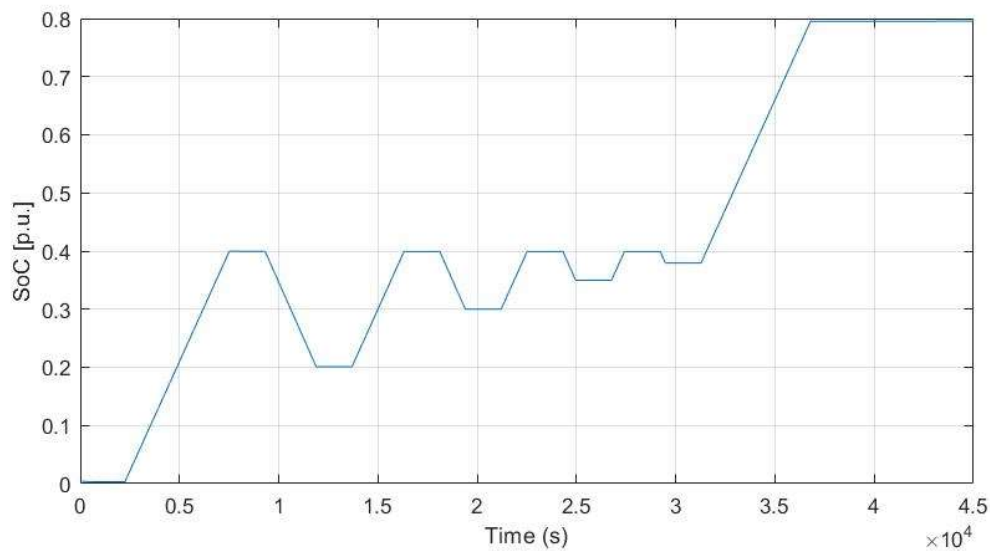
Figure 59 scheduling of the test for hysteresis modelling.

By using the profile of Figure 59 as input of the model, the hysteresis effect was taken into account by considering the instantaneous passage between the two OCV curves of Figure 52 depending on the charging or discharging phases. The results are shown in Figure 60. It can be seen that the difference between the measured and the simulated profiles becomes more marked when the discharges become less deep.
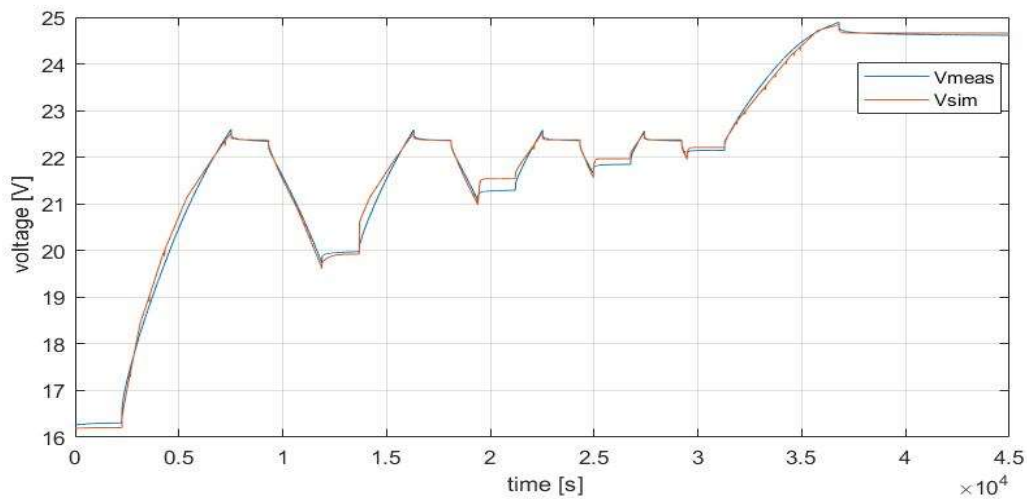
Figure 60 results without hysteresis modeling

On the other hand, considering the enhanced model, where the lambda parameter and its variations are taken into account, the results shown in Figure 61 are obtained. In this case a significantly smaller difference can be observed between modelled and measured voltage.
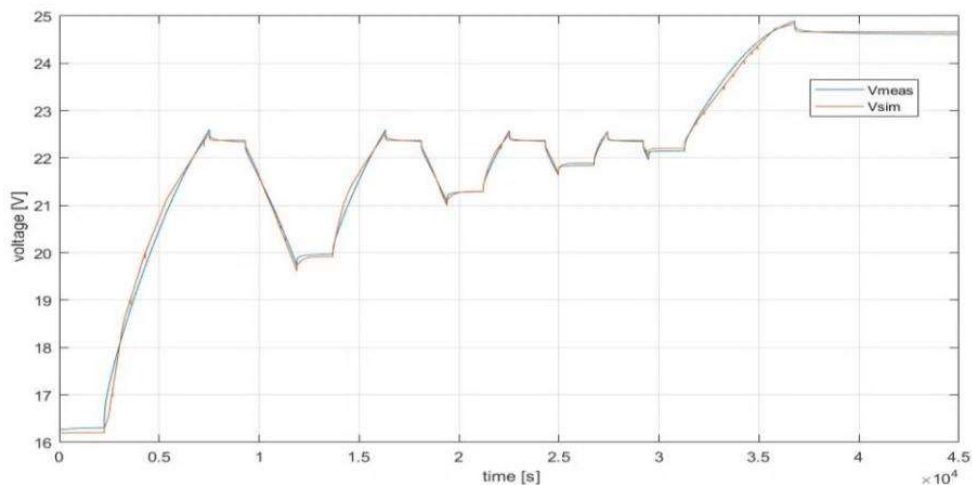
Figure 61 results with hysteresis modelling

Model experimental verification

To verify the model effectiveness in an unconventional test, a work cycle was performed consisting of the following phases of charge and discharge at constant power with rest phases which not exceeding one minute:

1. 1800 W discharge phase

2. 30s rest phase

3. Discharge phase at 1200 W

4. 30s rest phase

5. Charge phase at 900 W

6. Discharge phase at 300 W

The obtained results are reported in Figure 62 and Figure 63. It can be seen how, although the model makes use of average values of the results of the characterization tests previously obtained, the difference between model output voltage and measured voltage does not exceed 250 mV.
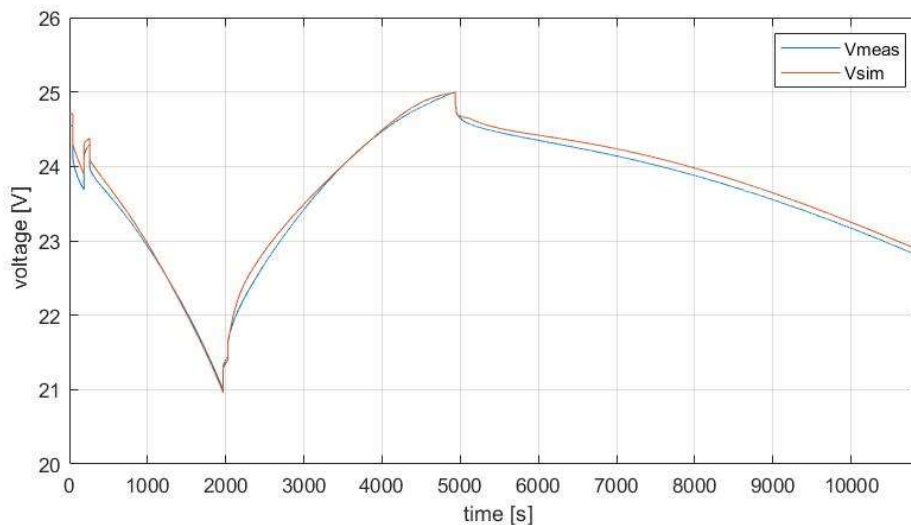
Figure 62 measured voltage and simulated voltage
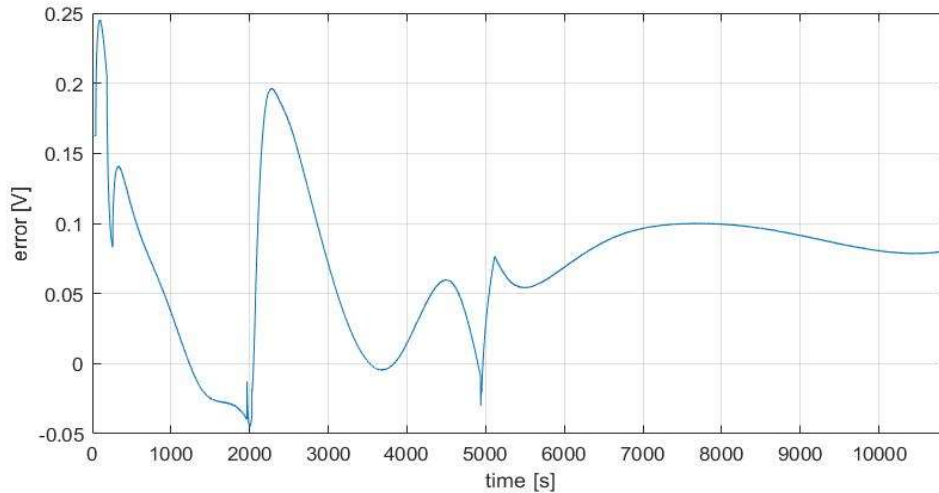
Figure 63 difference between measured voltage and simulated voltage.

Implementation of DSS architecture with model improvement

The developed model can be implemented in the scheduling algorithm shown in chapter "Integration of smart prosumer in the distributed measurement system architecture". The model is highly non-linear and for this reason can be challenge to integrate it in common optimization algorithm however the solver used is not a mixed integer linear programming solver but an heuristics technique and for this reason it became easy to adapt the non linearity of the model to the algorithm rearranging the equations. The feasibility of the proposed solution has been verified in an experimental test system performed on a battery pack of 8 Li/Mn modules. Each module consists in 6 cells with 75 Ah and minimum and maximum voltages of 2.7 V and 4.2 V per cell, respectively. Consequently, the minimum and maximum admissible series voltages are about 130 V and 202 V, respectively. The aforesaid system is able to exchange energy with the network through a DC-AC inverter with nominal power $An = 4\ kVA$ and rated current $In = 70\ A$. A power transformer is connected downstream of the inverter, which raises the voltage from 80 Vrms to the mains voltage (400 Vrms). A BMS coupled to the battery pack performs the balancing between the cells and it also estimates the state of charge. Both BMS and inverter communicate with a local EMS via ModBus TCP on an Ethernet cable. The optimization algorithm is implemented in the EMS, which acts as information hub center. It sends the active power set-points to the inverter every hour and it continuously receives the voltage, current and state of charge readings from the BMS. Furthermore it receives the energy price data from DSO control center via

TCP / IP, according to the architecture of Figure 35. The EMS processes the received data and it calculates the optimal profile of the battery using the algorithm proposed. Firstly it receives the inputs, i.e. the active power required by loads and the active power supplied by the photovoltaic system during the day, as well as the data relating to the energy prices for the next 24 hours. Then, it executes the PSO optimization algorithm and it processes the power profile of the storage system that minimizes the daily energy cost. Once the processing is completed, the EMS performs the real-time management. More in detail, the EMS writes every hour the ModBus registers of the inverter relative to the active power set-points in DC and monitors voltage, current and SoC data every 300 ms to verify that they are within the pre-fixed limits. The following values have been chosen as limit data:

$$SoC_{max} = 95\ \%$$

$$SoC_{min} = 20\ \%$$

$$V_{max} = 202\ V$$

$$V_{min} = 130\ V$$

If the SoC_{max} limit of is exceeded, the EMS blocks all the negative power set-points that lead to a power flow towards the battery, i.e. continuing to charge, but it enables the positive set-points, which lead to a battery discharge. In this way there is no risk of overloading or underloading the storage system.

Experimental results

This section shows the results between experimental and scheduled data using the optimization algorithm. The voltage measured at the series terminals for 24 hours is shown in Figure 64. During the charging phase the measured voltage reaches 202 V, while the corresponding SoC, estimated by BMS, is different from the scheduled SoC, as shown in Figure 65. Since the measured voltage had reached its limit value during the charging phase, then the EMS had forced to cancel all the immediately subsequent charging phases to avoid cells damages. This causes a discrepancy with the scheduled power profile, as shown in Figure 66, until a discharge phase occurred again. Therefore, the real behavior differs from that obtained with the simplified model.

On the other hand, using the second battery model, better agreement is obtained with the experimental results. This can be observed in Figure 67, Figure 68 and Figure 69 which show the comparisons between measured and estimated voltage, SoC and power output, respectively.
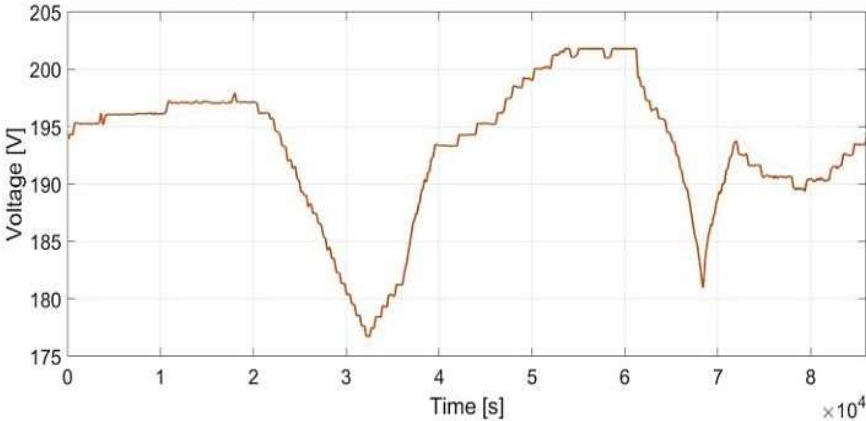
Figure 64 Voltage measured at the series terminals for 24 hours
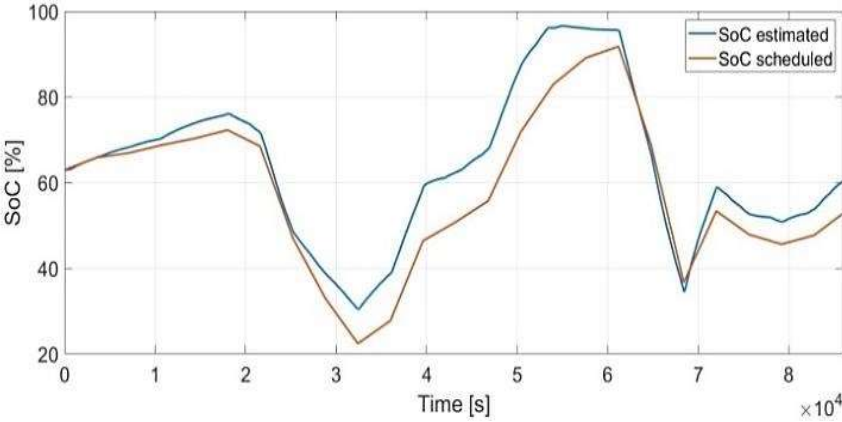
Figure 65 Comparison between SoC estimated and SoC schedulated
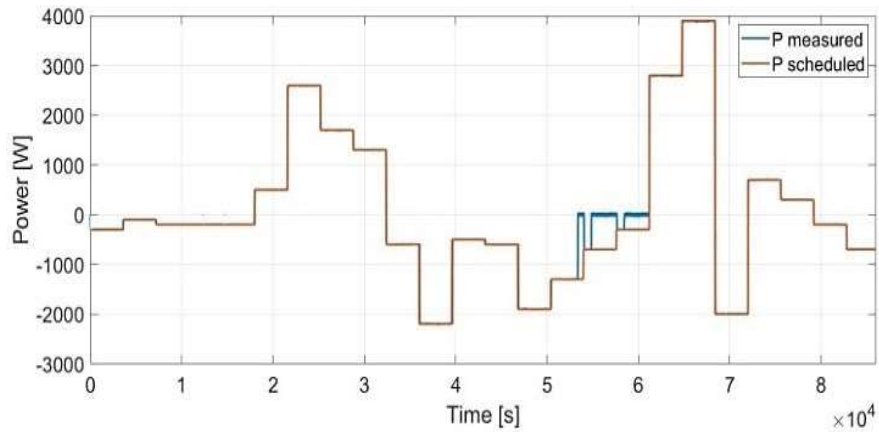
Figure 66 Comparison between measured and scheduled powers in the case of the simplified model
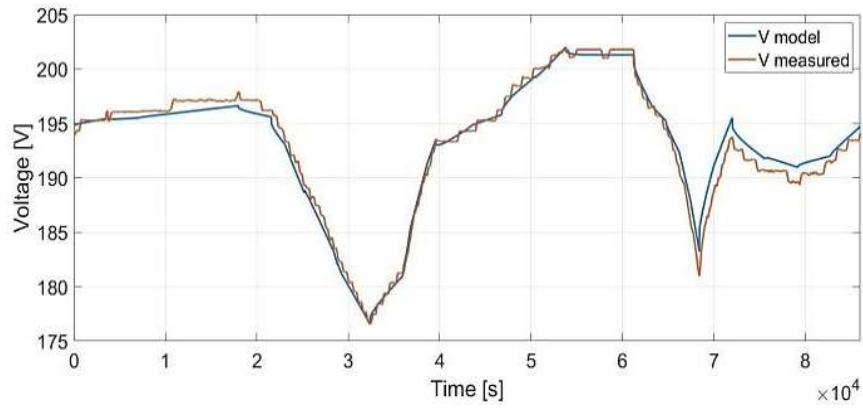
Figure 67 Comparison between modeled and estimated voltages
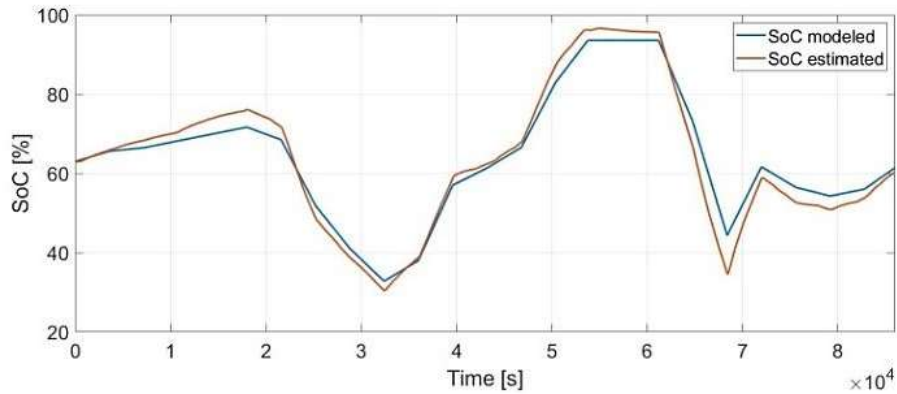
Figure 68 Comparison between modeled and estimated SoC
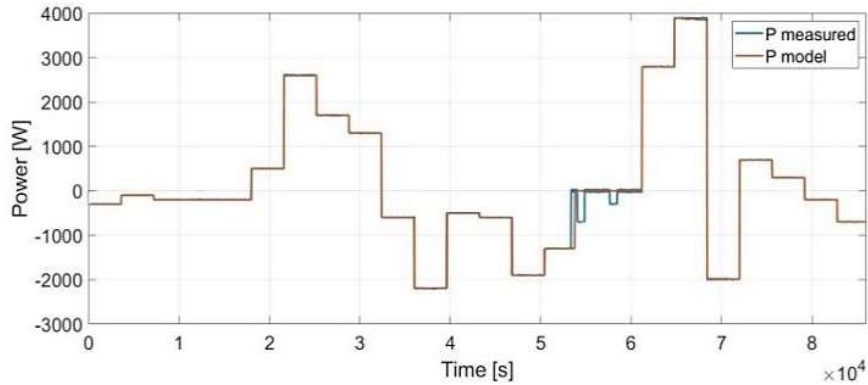
Figure 69 Comparison between measured and modeled powers in the case of the more sophisticated battery model

The experimental tests showed how the second model can guarantee a better agreement with the values measured in a real storage system.

Energy management system based on Fuzzy logic

Different strategies can be found in literature aiming to maximize the economic gain of the prosumer based on forecasting and scheduling algorithms [75]. With regard to the scheduling part, it was proved, in the previous chapter, how an artificial intelligence based optimization algorithm can be implemented, also with the possibility to include request from an aggregator [76]. The main disadvantage of this approach is the high computation cost of the algorithms, so that it could be affordable for large users but low voltage users could be limited on the implementation of this type of solutions.

To better understand the computational burden of the optimization and neural network approach, both of them need the load and production forecasting. This can be made only through on site monitoring campaign and, after this step, a regressor must be built to model the behavior of the input. After the forecasting process, the daily and instantaneous trend of the battery power must be guessed.

Within an optimization approach, the problem solution must be implemented including matrix or vectorial operations [77], [78] while, with a neural network approach a model composed by perceptron must be trained with the optimized data [79].

These new sophisticated logics were born to replace the most common self-consumption algorithm [80] because the self-consumption logic does not exploit the infraday price fluctuations. However, to better exploit the price variation and maximize the profit, the solutions previously explained need the connection between the EMS and the datacenter to share data, such as the weather and prices data. Hence, for the optimal execution of the algorithms, the consumption, production, and price data of the prosumer must be acquired by the local EMS.

Design of the controller

FL is a multipurpose logic that, unlike the Boolean approach, is able to deal with ambiguous, inaccurate, and not exactly defined contexts. The useful exploitation of FL applied on control systems is well known in literature [81] and was introduced by Lofti A.Zadeh [82] in 1965. The FL allows to map a space input into a space output and it is particularly convenient when the system under control is nonlinear and/or the input data are imprecise. These features come from the structure of the controller. Indeed, the controller output depends on how much the inputs belong to a certain class and the whole of these classes are named fuzzy sets. In other words, the fuzzy set is a collection of elements inside a certain range, called universe, and each one is determined from its degree of membership. The degree of membership of a certain input can be determined through the use of membership functions.

The controller design starts from the definition of the inputs and their membership functions. As said, the purpose of the logic is to allow exchange energy with the grid considering the price variations in order to guarantee grater economic gain but keeping low computational cost. Starting from this, the controller was designed to take advantage from the energy purchasing and selling price variations coming from the MGP. To better visualize this concept, Figure 70 shows the fuzzy entities connections (where the main block FUZZY EMS, is usually named Fuzzy Logic Machine, FLM). The power exchanged from the inverter depends on three inputs:

1) The power required / supplied by the system, REQUEST_POWER;

2) The sale price of energy normalized with respect to the average price, C_OUT,

3) The difference between the sale price and the purchase price of normalized energy compared to the average price difference, DELTA.
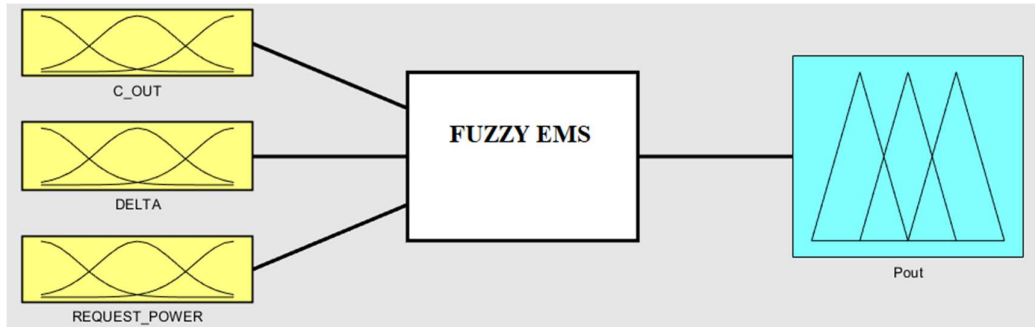
Figure 70 block diagram of the controller

The REQUEST_POWER represents the power generated or absorbed by system load and photovoltaic, assuming positive the absorbed power. Membership functions are visible in Figure 71
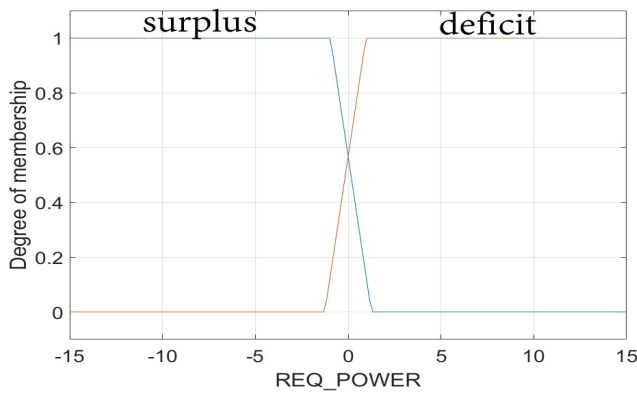
Figure 71 membership functions of REQUEST_POWER

C_OUT is the energy sale price, but in order to compensate for price fluctuations in different days, the MGP price values were divided (normalized) by the average price of the day considered. In this way, the input values will be around the value of one. (Figure 72)
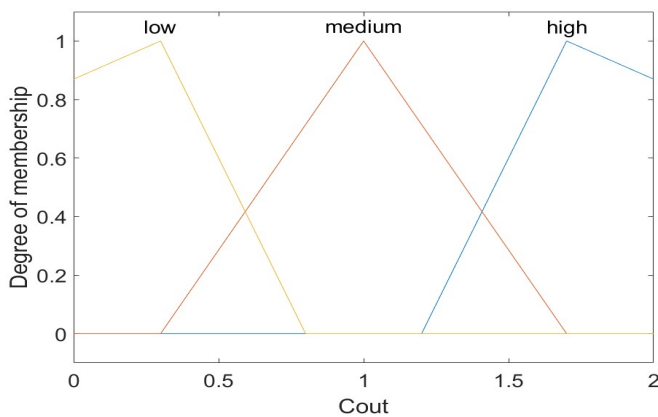
Figure 72 membership functions of second input C_OUT

On the other hand, DELTA represents the difference between the normalized sale and purchase price of energy and the average price difference on that day. Unlike the previous input, the value of the average difference does not necessarily mean that it is around the unity. It is also important to keep track of price trends over a whole day in order to better compare, for example, an instant with a high sale price and high difference between prices with an instant in which there is only a high value of the selling price and a low difference. To keep track of this, the membership functions of the third input between one day and another may differ. In particular, the central membership functions will be a Gaussian with an average equal to the average price difference of the day considered and standard deviation equal to the standard deviation of the difference between the prices, as shown in Figure 73.
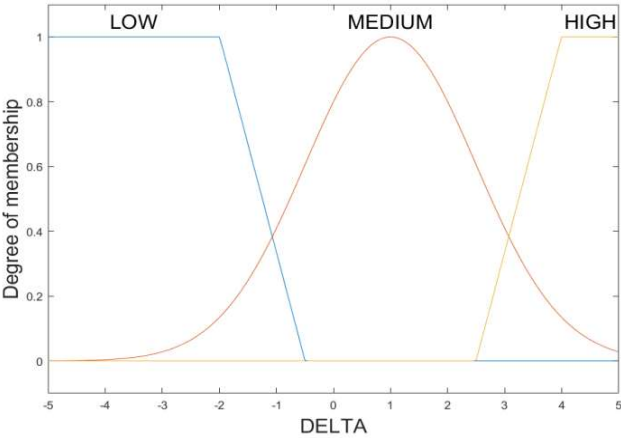
Figure 73 Membership functions of third input DELTA

On the other hand, the membership functions of the output P_{out} are shown in Figure 74. Five membership functions belong to the output, representing different output power scenarios. The output of the fuzzy controller will be then multiplied with the absolute value of the net load (assumed as difference between load and photovoltaic) of the system. In the diagram, the output power is normalized in unit (pu) and the injected power is expressed with positive. As shown in the figure, the output can be even greater than one in order to have the appropriate power value entered in the network. For example, according to the controller output, the ESS injects power into the grid with a value that equals the absolute value of the net load.
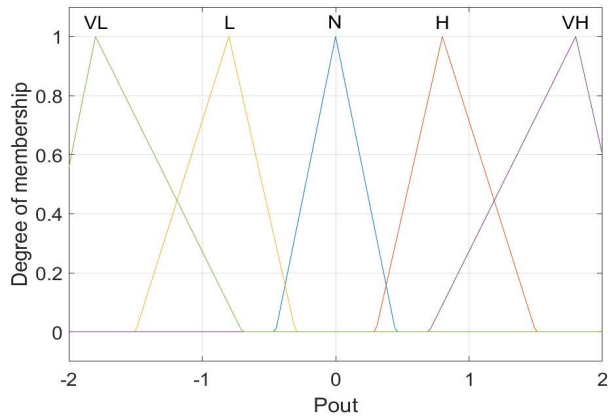
Figure 74 Output membership function Pout

$$P_{AC} = P_{out} * |(netload)|$$

with:

- P_{AC} value of the AC power of ESS expressed in kW;

- P_{out} output of the controller;

- $netload$ difference between load and photovoltaic.

The defuzzification Method used in this controller is the Weighted Averaged Method.

In addition to the fuzzy controller, it is important to underline that the State of Charge (SoC) is not among the inputs and, therefore, it is necessary to set the power set-point to zero as soon as the SoC thresholds exceeds.

Case Study

In this section, a case study is presented in order to test and validate the aforementioned control strategy. The rated parameter of the prosumer system and battery model are the same of the previous chapter.

With respect to the simulation data, only 33 hours of input measures was used in order to reduce the testing time. The data used for the experiment are shown in Figure 75, Figure 76 and Figure 77. At the end of this paragraph, both experimental and simulated results are shown without losing information.
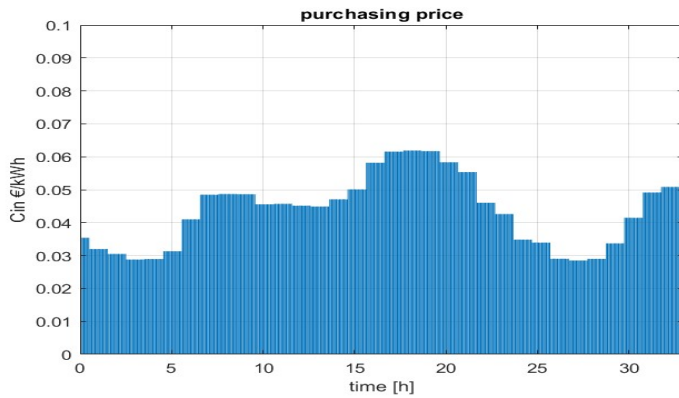
Figure 75 Purchasing price used for the experiment
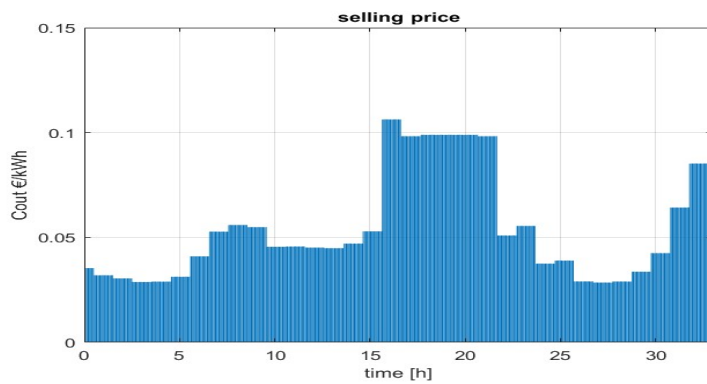
Figure 76 Selling price used for the experiment
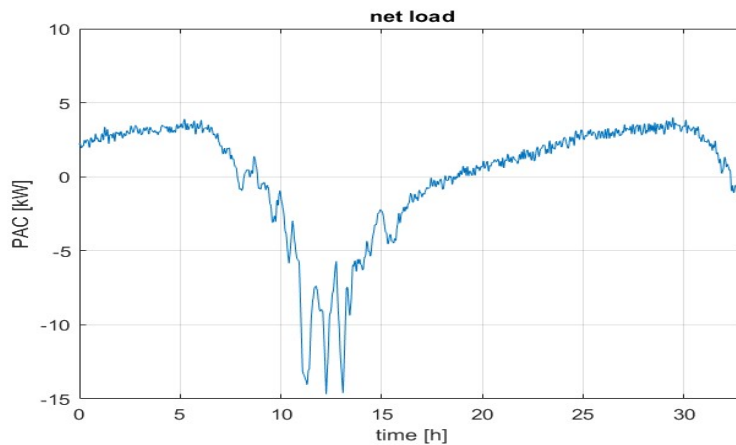
Figure 77 Net load of the system

Figure 78 and Figure 79 show the differences between the measured and simulated power diagrams for the self-consumption and fuzzy logic, respectively. Figure 80 and Figure 81, the comparisons between the state of charge simulated and recorded by the battery BMS (respectively in the case of self-consumption and FL) are shown. The slight SoC discrepancy is attributable to the non-ideal

behavior of the batteries and the difference between the real and ideal capacity of the batteries. However, the real data are well approximated by the model. The spikes in the power diagram are due to self-discharge of the battery which brings back the SoC under the limits of 90%.
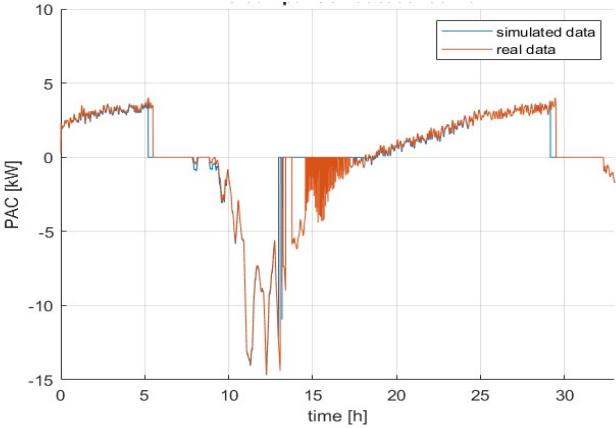
Figure 78 Comparison of the AC power of the inverter (self-consumption)
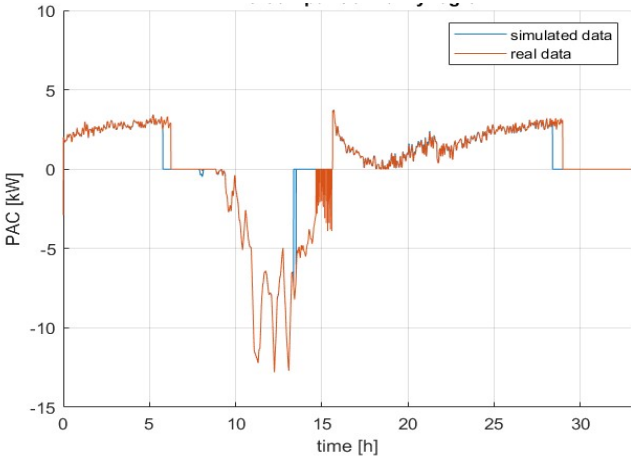
Figure 79 Comparison of the AC power of the inverter (fuzzy logic)
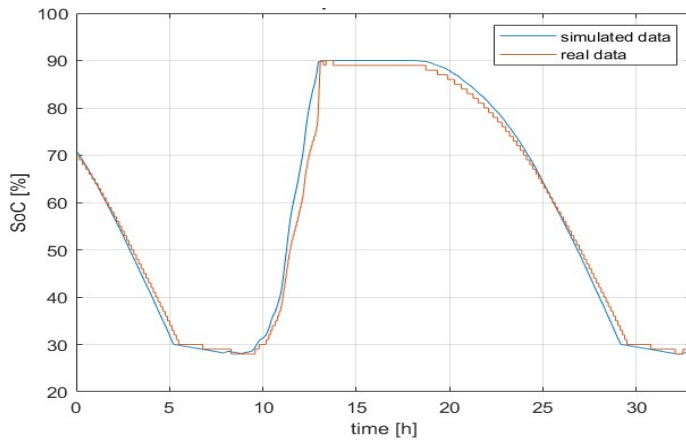
Figure 80 Comparison of SoC simulated and acquired from BMS (self-consumption)
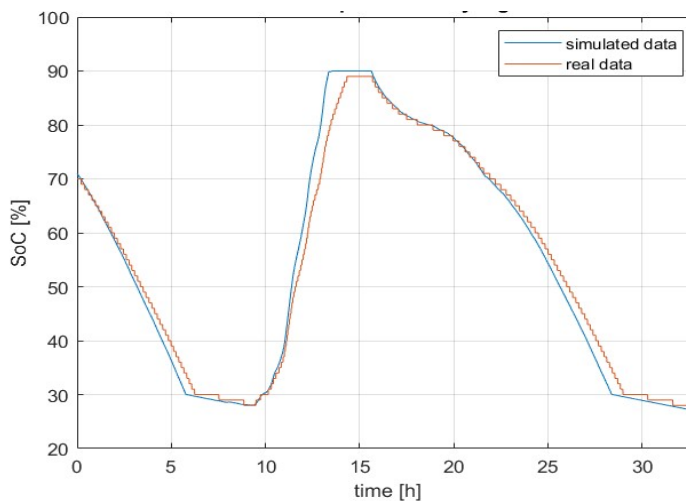
Figure 81 Comparison of SoC simulated and acquired from BMS (fuzzy logic)

The overall energy cost, considering only the energy component without taxes, was calculated and reported in Table 10.

Table 10 Economic comparison

	Simulation	**Measured**
Self-consumption cost	-0.46 €	+0.01 €
Fuzzy logic cost	-0.82 €	-0.56 €

The suitability of the controller has been demonstrated through a comparison with a common self-consumption algorithm. The comparison was made both in energy and economic terms. As shown in the result section, the two control strategies, under some aspect, are equivalent, but the fuzzy controller

allows better exploitation of the energy selling price variations with respect to the self-consumption strategy.

Conclusion to smart prosumer integration in smart grid infrastructure

In this chapter, a distribution measurement and control infrastructure able to integrate also demande response was shown. First, a load flow based monitoring algorithm was implemented in LabVIEW environment and the uncertainty was evaluated using Monte Carlo analysis. After that, it was shown also how to integrate a price based demande response architecture for a smart prosumer, first in simulation and than in a real prototype. The price based demande response architecture was shown in the last part in a simplified form with lower computational cost. In every case the effective of the two control strategies were demonstrated in comparison of the self-consumption algorithm in both cloud control scenario and edge control scenario. In the next chapter the previous architecture will be improved also with the integration of power quality assessment for billing purposes.

3. Power Quality and Harmonic Source Assessment

State of the art on harmonic power quality assessment

The already presented monitor and control architecture can be improved extending the analysis also with the power quality consideration. The spread diffusion of power electronics in the grid forces the system operator to analyse the system with new method. In fact the problem of harmonics are becoming significant and not to underestimate as demonstrated by Qeen Mary II ship disaster, in which a bank of compensator exploded due harmonic overloading [83] in September 2010. In this chapter are presented news metrics for the harmonic sources assessment which can be used for billing purposes or in innovative demande response strategies.

The problem of harmonic propagation is known in literature for a long time but is with the rising of electronic devices that it became a serious problem. There are different standards which establish that limits the amount of harmonic current (IEEE 519) or the harmonic voltage distortion (IEC 61000-3-6) at customer point of delivery however there are not yet tools to establish if the distortion is coming from the customer or the utility. In fact, it is very simple to evaluate the harmonic distortion in every point of the grid but it is a challenge to prove that the one node or another is the harmonic source. In this sense there are several papers concerning the detection of the harmonic source [20], [84]–[86] but there are not standards that give information on how to study the propagation of of the harmonic. IEEE std. 1459-2010 try to give some power definitions and measurements of electrical quantities in nonsinusoidal situation for both three phase and single phase and for both balanced than unbalanced conditions. In [12] the harmonic source detections are categorized in three methods as follows:

- Direction of active power flow

- Reactive power flow

- Voltage-current ratio

As pointed out by other researchers, each method have advantages and drawbacks. Some of the common disadvantages are: the difficulty and the high cost of implementation.

Starting from the definitions of the IEEE std. 1459-2010 the author has issued a new strategy based on single point measurement at the point of common coupling and the power definition of the IEEE std. 1459 which use both active and reactive power. The main scope of the strategy are.

1. Give a single point strategy to assess if the harmonic source is coming from customer or utility;

2. Give an industrial solution easy to implement in low cost platform;

3. Give indicators quickly to understand also for the customer and for future billing strategies.

IEEE standard 1459-2010 overview

The standard introduces some power definition of active and reactive power for balanced, unbalanced, single phase, and three phase systems. The definition are summarized in Table 11 and Table 12. Such indicators are defined as ratios between power quantities, recalling the common concept of power factor, which is normally used for reactive power compensation. This is an approach customers are very familiar with, thus the opportunity to implement a similar strategy also for harmonic pollution assessment and mitigation could be very useful. Furthermore, the measurement of IEEE 1459 power quantities is very simple, since they are based on the separation of the fundamental components from the remaining harmonic content of voltage and current. Many commercial instruments

Table 11 IEEE Std 1459-2010 Apparent power resolution – Single-phase case

Power quantities	Combined	Fundamental	Nonfundamental	Apparent power resolution scheme	Indicators
Apparent [VA]	$S = V I$	$S_1 = V_1 I_1$	$S_n = \sqrt{S^2 - S_1^2}$ $S_H = V_H I_H$		Line utilization
Active [W]	$P = \sum_{h=1}^{n} V_h I_h \cos\theta_h$	$P_1 = V_1 I_1 \cos\theta_1$	$P_h = \sum_{h\neq1} V_h I_h \cos\theta_h = P - P_1$		$PF = P/S$ $PF_1 = P_1 /S_1$
Nonactive [VAR]	$N = \sqrt{S^2 - P^2}$	$Q_1 = V_1 I_1 \sin\theta_1$	$D_I = V_1 I_H$ $D_V = V_H I_1$ $D_H = \sqrt{S_H^2 - P_H^2}$		Harmonic pollution S_N /S_1

V_h and I_h are the rms values of the harmonic components of voltage and current, θ_h is their displacement and h is the harmonic order.

Table 12 IEEE Std 1459-2010 Effective apparent power resolution – Three-phase case

Power quantities	Combined	Fundamental	Nonfundamental	Effective apparent power resolution scheme	Indicators
Apparent [VA]	$S_e = 3\ V_e\ I_e$	$S_{e1}= 3\ V_{e1}\ I_{e1},$ $S_1^+ = 3\ V_1^+\ I_1^+$ $S_{U1} = \sqrt{S_{e1}^2 - S_1^{+2}}$	$S_{eN} = \sqrt{S_e^2 - S_{e1}^2}$ $S_{eH} = 3\ V_{eH}\ I_{eH},$		Line utilization
					$PF=P/S_e$
					$PF_1^+=P_1^+$ $/S_1^+$
Active [W]	$P = \sum_{a,b,c}\sum_{h=1}^{n} V_h I_h \cos\theta_h$	$P_1^+ = 3\ V_1^+\ I_1^+$ $\cos\theta_1^+$	$P_H = \sum_{a,b,c}\sum_{h=2}^{n} V_h I_h \cos\theta_h =$ $= P - P_1$		Harmonic pollution $S_{eN}\,/S_{e1}$
Nonactive [VAR]	$N = \sqrt{S_e^2 - P^2}$	$Q_1^+ = 3\ V_1^+\ I_1^+$ $\sin\theta_1^+$	$D_{eI} = 3\ V_{e1}\ I_{eH}$ $De_V = 3\ V_{eH}\ I_{e1}$ $D_{eH} = \sqrt{S_{eH}^2 - P_H^2}$		Load unbalance $S_{U1}\,/S_1^+$

V_e, V_{e1}, V_{eH}, are the rms values of effective voltages; I_e, I_{e1}, I_{eH}, are the rms values of effective currents (total, fundamental, harmonic)

Starting from the coefficients defined in the standard: PF, PF1 and SN/S1. In [articolo measurement] three new parameters are shown. In the following the single phase and three phase case is discussed and the difference with the IEEE std. 1459 coefficients are discussed.

Single phase

Following the approach of IEEE 1459-2010, the separation of fundamental components of power (active, reactive and apparent) from the rest of the apparent power resolution terms, allows introducing the parameters for line utilization and harmonic pollution assessment. As regards the line utilization, the considered indicators are fundamental and total power factors, PF_1 and PF, respectively. In sinusoidal conditions, $PF_1 = PF$; this is the parameter commonly used for reactive power compensation, typically by means of passive banks of capacitors. In ideal conditions $PF_1 = PF = 1$. On the other hand, in the presence of harmonics $PF_1 \neq PF$ and more sophisticated active filters and compensators are more suitable for compensation purposes, since capacitors may cause harmonic pollution worsening, as their impedance decreases when frequency increases. As regards the harmonic pollution, IEEE 1459-2010 introduces the ratio S_N/S_1, whose behavior is opposite to that of power factors, i.e. in ideal conditions (purely sinusoidal) $S_N/S_1 = 0$.

From the measurement viewpoint, all the aforesaid parameters are very simple to be measured, thus their measurement can be easily integrated in commercial instrumentation and used for line utilization improvement and harmonic pollution reduction. This is already made for power factor correction; a threshold is normally defined by the DSO, typically near to 1, and the comparison between such threshold and the power factor determines a fee payment for reactive power absorption. To avoid such fee, users are promoted to provide for reactive power compensation. On the other hand, similar policies for harmonic emission assessment and billing are not yet implemented. Furthermore, S_N/S_1 approaches zero in ideal conditions and this can introduce some problems on measurement accuracy; in fact, in analogy with power factor correction, a threshold near to zero should be used for reference for harmonic billing and mitigation purposes; to compare the indicator with such threshold, very small values of S_N/S_1 should be expected to be measured, with a consequent measurement uncertainty increase.

To avoid these limitations, the feasibility of some new indicators has been initially investigated, with the aim of replacing IEEE 1459-2010 S_N/S_1 indicator with one or more parameters conceptually similar to the power factors, i.e. approaching 1 in ideal conditions. Such parameters are expressed as a function of IEEE 1459-2010 power quantities, thus they keep the advantage to be easily implemented in practical measuring instruments with limited modifications (even in existing PQAs and SMs). More in detail, the considered power ratio parameters are P_1/S, S_1/S, and Q_1/N.

P_1/S can represent an indicator of the total line utilization amount, taking into account both the fundamental power and the harmonic distortion (which is included in S); in the sinusoidal case, P_1/S = PF_1 = PF, all approaching 1 in optimal line utilization condition. In real situations, $P_1/S < PF_1$ depending on harmonics amount.

S_1/S, can allow quantifying the whole harmonic distortion level, considering both active and reactive powers; in the absence of harmonics, $S_1/S = 1$, thus the indicator behaves as power factors (i.e. it approaches 1 in ideal conditions); in this viewpoint, it can be seen as a indicator complimentary to S_N/S_1; it can provide the same information on harmonic pollution level, but it can be measured more accurately than S_N/S_1 [] and a threshold approach can be implemented, similar to that used for power factor correction.

Q_1/N can represent an indicator for nonactive power components impact and pollution level. In earlier works the authors have studied the behavior of nonactive powers in distorted conditions, showing that it can be related to the load condition (linear or not). In sinusoidal conditions, $Q_1 = N$ and $Q_1/N = 1$; thus also this indicator behaves as power factors, approaching to 1 when the system tends to be purely sinusoidal. On the other hand, when harmonics are present N increases with respect to Q_1 (since it includes all nonactive power components), thus the indicator decreases. Also for this indicator a threshold approach can be implemented, similar to that used for power factor correction and it can be also measured more accurately than S_N/S_1 [].

Three phase

In three-phase systems, the IEEE 1459-2010 introduces the effective apparent power resolution, which allows dealing with both sinusoidal, distorted, balanced and unbalanced situations. In balanced conditions the effective apparent power resolution leads to the same results of summing the phase power quantities.

In this viewpoint, when the power system is balanced the same indicators introduced for the single-phase case can be defined, whose power terms can be evaluated as the sum of the related phase (*a, b, c*) quantities. Thus, for the IEEE 1459-2010 indicators, the power ratios can be evaluated with an "arithmetic approach":

$$PF_1 = \frac{P_1}{S_1} = \frac{P_{1a} + P_{1b} + P_{1c}}{S_{1a} + S_{1b} + S_{1c}} \qquad (35)$$

$$PF = \frac{P}{S} = \frac{P_a + P_b + P_c}{S_a + S_b + S_c} \qquad (36)$$

$$\frac{S_N}{S_1} = \frac{S_{Na} + S_{Nb} + S_{Nc}}{S_{1a} + S_{1b} + S_{1c}} \qquad (37)$$

Similarly, for the newly defined power ratio indicators, the three-phase arithmetic formulation leads to the following expressions:

$$\frac{P_1}{S} = \frac{P_{1a} + P_{1b} + P_{1c}}{S_a + S_b + S_c} \qquad (38)$$

$$\frac{S_1}{S} = \frac{S_{1a} + S_{1b} + S_{1c}}{S_a + S_b + S_c} \qquad (39)$$

$$\frac{Q_1}{N} = \frac{Q_{1a} + Q_{1b} + Q_{1c}}{N_a + N_b + N_c} \qquad (40)$$

It should also be noticed that many commercial instrumentation already implements the measurement of most aforesaid phase quantities, thus this kind of measurement could be implemented without any difficulties or relevant computational burden increase.

On the other hand, in unbalanced conditions the effective apparent power resolution leads to different results than those of the aforesaid arithmetic approach. In this case, the arithmetic power ratio indicators can be still evaluated but they will be different to those obtained by means of the effective apparent power resolution, i.e.:

- $PF_1{}^+ = P_1{}^+ / S_1{}^+$, $PF = P/S_e$ and S_{eN}/S_{e1} (defined in IEEE Std. 1459-2010)

- $P_1{}^+/S_e$, S_{e1}/S_e and $Q_1{}^+/N$ (new additional power ratio indicators for the unbalanced case).

In the IEEE 1459-2010 approach, the fundamental positive sequence power factor PF_1^+ allows evaluating the positive-sequence power flow conditions, which consider the only one power components in ideal sinusoidal and balanced case; PF and S_{eN}/S_{e1} allow evaluating the whole line utilization and the harmonic pollution. As for the single-phase case, the IEEE 1459-2010 parameter S_{eN}/S_{e1} approaches to zero in the absence of distortion respectively. On the other hand, the new additional power ratio indicators approach to 1 in sinusoidal (and balanced) conditions, thus they represent a more suitable alternative from the measurement viewpoint.

As regards the load unbalance degree, in the IEEE 1459-2010 approach it is evaluated by means of the ratio S_{U1}/S_1^+; in the absence of unbalance, $S_{U1}/S_1^+ = 0$, and the effective apparent power decomposition becomes analogous to that of the single-phase case (or even the three-phase arithmetic approach). As for the harmonic pollution indicator, the load unbalance S_{U1}/S_1^+, approaches to zero in the balanced case; thus, a complimentary new power ratio indicator can be introduced, i.e. S_1^+/S_{e1}, which approaches to 1 in the absence of unbalance, instead.

Implementation and experimental validation of the metrics

PC based sampling wattmeter

The first step of the analysis of the previous indicators was the implementation in a controlled environment in order to test their computational cost and their accuracy respect to the indicators of the IEEE 1459-2010.

The single-phase study has been carried out experimentally. A PC-based sampling wattmeter (PC-SW) has been used for measurements and test. Voltage and currents have been generated by means of a calibrator Fluke Electrical Power Standard 6100A (see Figure 82). PC-SW voltage channel is built with a data acquisition board NI USB 9225; current channel include both the data acquisition board NI USB 9239 and a current shunt Fluke A40B. The DAQs have been placed into a chassis NI cDAQ 9172A, thus simultaneous sampling has been performed for the two PC-SW channels; sampling frequency has been set equal to 50 kS/s.
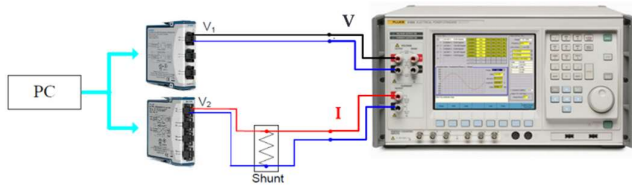
Figure 82 Experimental single-phase test bench

The technical specification of the data acquisition boards taken from the datasheet are shown in Table 13.

Table 13 DAQS NI USB 9225/9239 AND CURRENT SHUNT FLUKE A40B MAIN FEATURES

	FEATURES		
DATA ACQUISITION BOARDS NI USB 9225 NI USB 9239	analog input channels		4
	sampling mode		simultaneous
	sampling frequency		1.613–50 kS/s
	ADC		Delta-Sigma with analog prefiltering (alias-free bandwidth 0.453 fs)
	ADC resolution		24 bits
	input range (nominal/typical)	NI USB 9225	± 300/425 V
		NI USB 9239	± 10/10.52 V
	offset (before correction [a])		0.008 % of range
	offset (after correction)		0.002 % of range
	gain (before correction [a])	NI USB 9225	0.05 % of reading
		NI USB 9239	0.03 % of rdg
	gain (after correction)		0.005 % of rdg
	THD	NI USB 9225	- 95dB
		NI USB 9239	- 99 dB
	noise input	NI USB 9225	2 mV
		NI USB 9239	70 μV
CURRENT SHUNT FLUKE A40B	Nominal current		20 A
	Nominal resistance		0.04 □
	accuracy (95% confidence level)	up to 1 k Hz	±43 μA/A
		up to 10 kHz	±52 μA/A
		up to 1 k Hz	< 0.008°

		typical phase displacements	up to 10 kHz	< 0.075°

ª) Calibrated typ (25 °C, ±5 °C); typical input range

After the acquisition stage, samples have been corrected via software in order to reduce the systematic contributions to the measurement uncertainty due to offset, gain, interchannel delay and filtering [87]. After correction, the acquired samples have been processed to calculate the IEEE Std. 1459-2010 power quantities and the power ratio indicators; measurement uncertainty has been also obtained.

Measurement uncertainty evaluation procedure

Measurement uncertainty has been evaluated by applying the uncertainty propagation law [64] to IEEE 1459-2010 power quantities and power ratio indicators. Generally speaking, it is known that, being f the function between the measured value $\bar{y}$ and the input quantities $(\bar{x}_1, \bar{x}_2, \dots \bar{x}_N)$, the absolute combined standard uncertainty (in terms of squared values) on $\bar{y}$ is:

$$u^2(\bar{y}) = \sum_{i=1}^{N} \left(\frac{\delta f}{\delta x_i}\right)^2 u_{\bar{x}_i}^2 + 2\sum_{i=1}^{N-1}\sum_{j=i+1}^{N} \left(\frac{\delta f}{\delta x_i}\right)\left(\frac{\delta f}{\delta x_j}\right) u(\bar{x}_i, \bar{x}_j)$$

$$= \sum_{i=1}^{N} \left(\frac{\delta f}{\delta x_i}\right)^2 u_{\bar{x}_i} + 2\sum_{i=1}^{N-1}\sum_{j=i+1}^{N} \left(\frac{\delta f}{\delta x_i}\right)\left(\frac{\delta f}{\delta x_j}\right) u_{\bar{x}_i} u_{\bar{x}_j} r(\bar{x}_i, \bar{x}_j)$$

The evaluation of uncertainties on input quantities (i.e. voltage and current amplitudes and phase displacements) was obtained from the FFT analysis of acquired voltages and currents, taking into account the accuracy specifications of PC-SW hardware components (DAQs and current shunt) and the accuracy of instrumentation used for calibration. The full characterization procedure and results can be found in [87].

As regards the correlation analysis, it has been carried out with an experimental procedure, studying the results of series of repeated measurements (Type A evaluation). More in detail, for each test condition, a given number of trials have been carried out and the correlation coefficient r has been evaluated; furthermore, the correlations among the different quantities has been observed by means of scatter diagrams. Generally speaking, the more two quantities are correlated, the more the scatter diagram points appear to band around a straight line. The value of r can be between -1 and +1 and it quantifies the linear relation between the data: when $r = \pm 1$ scatter plot points lie on a straight line

(with a positive or negative slope, depending on the sign, + or -, respectively); when $r = 0$, there is no relation pattern. As reported in [87], the correlation coefficient r of $\bar{x}_i$ and $\bar{x}_j$ can be obtained as:

$$r(\bar{x}_i, \bar{x}_j) = \frac{u(\bar{x}_i, \bar{x}_j)}{u(\bar{x}_i)u(\bar{x}_j)}$$

where $\bar{x}_i$ and $\bar{x}_j$ are the arithmetic means of n independent pairs of simultaneous observations of x_i and x_j under the same measurement conditions, u_{xi} and u_{xj} are their absolute uncertainties and $u(\bar{x}_i, \bar{x}_j)$ is their covariance. It can be obtained as follows:

$$u(\bar{x}_i, \bar{x}_j) = \frac{1}{n(n-1)} \sum_{k-1}^{n} (x_{ik} - \bar{x}_i)(x_{jk} - \bar{x}_j)$$

The complete procedure has been presented in [87], for the uncertainty evaluation of all IEEE 1459-2010 power quantities. For sake of simplicity in uncertainties evaluation, for a given power definition, input quantities have been considered totally uncorrelated if $r < 0.5$, otherwise they have been considered totally correlated.

Measurement uncertainty results for the single phase case study

For the experimental tests, voltage and current signals have been generated by means of a calibrator Fluke Electrical Power Standard 6100A. Several tests have been carried out, with different distorted voltage and current waveforms. For each test condition the uncertainties on the measurement of the considered power ratios have been evaluated. 100 measurements have been carried out in order to evaluate the scatter plot for the power ratio indicators and the correlation coefficients evaluation. Some of the obtained results are reported in the following.

Test 1 (two harmonics)

In this test condition, voltage and current have been generated with two harmonics (third and fifth, THD = 10%); phase displacement between voltage and current has been set to 30°. The obtained results are reported in Figure 83,Table 14 and Table 15. It can be observed that the quantities S_N and S_I are strongly uncorrelated, while all the other pairs show a correlation coefficient higher than 0.5. The highest correlation coefficients have been obtained for the pairs (S_I, S) and (Q_I, N). The highest uncertainty has been obtained for the indicator S_N/S_1; on the other hand, significantly smaller uncertainties have been obtained for S_I/S and Q_I/N.

Table 14 Correlation coefficients between power quantities pairs of power ratio indicators

IEEE Std. 1459 Indicators	$r(P, S)$	$r(P_1, S_1)$	$r(S_N, S_1)$
	0.600	0.588	0.162
New	$r(P_1, S)$	$r(S_1, S)$	$r(Q_1, N)$
indicators	0.590	0.994	0.976

Table 15 Uncertainties on power ratios (ppm)

IEEE Std. 1459 Indicators	$\dot{u}_{PF}$	$\dot{u}_{PF1}$	$\dot{u}_{Sn/S1}$
	235	231	4052
New indicators	$\dot{u}_{P1/S}$	$\dot{u}_{S1/S}$	$\dot{u}_{Q1/N}$
	234	227	651
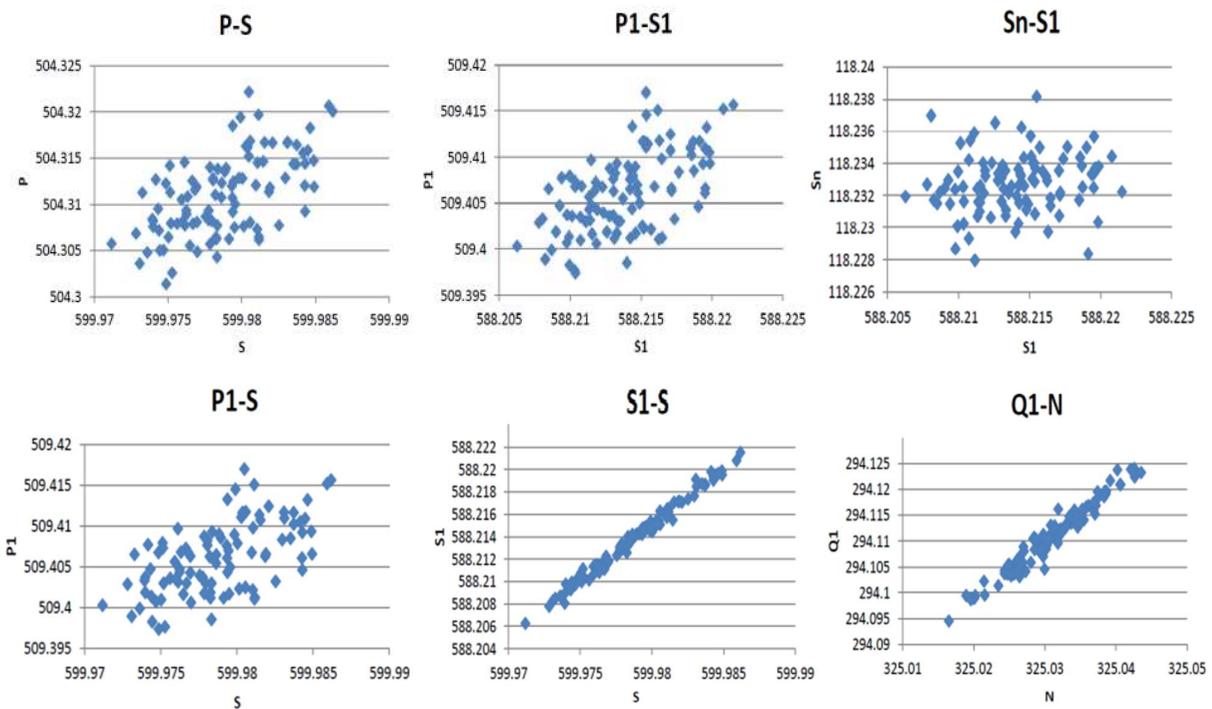
Figure 83 Test 1. Scatter diagrams of power quantities pairs of power ratio indicators

Test 2 (two harmonics and phase displacement)

In this test, harmonic distortion on both voltage and current was the same of previous test; phase displacement between voltage and current has been set to 60°. The obtained results are reported in Figure 84, Table 16 and Table 17 The results obtained are similar to those of the previous case. S_N and S_I are strongly uncorrelated, while the highest correlation coefficients have been obtained for the pairs (S_I, S) and (Q_I, N). The highest uncertainty has been obtained for the indicator S_N/S_1; on the other hand, significantly smaller uncertainties have been obtained for S_I/S and Q_I/N.

Table 16 Test 2. Correlation coefficients between power quantities pairs of power ratio indicators

IEEE Std. 1459 Indicators	**r(P, S)**	**r(P$_I$, S$_I$)**	**r(S$_N$, S$_I$)**
	0.359	0.362	0.072
New	*r(P$_I$, S)*	*r(S$_I$, S)*	*r(Q$_I$, N)*
indicators	0.362	0.992	0.982

Table 17 Test 2. Uncertainties on power ratios (ppm)

IEEE Std. 1459 Indicators	$\dot{u}_{PF}$	$\dot{u}_{PF1}$	$\dot{u}_{Sn/S1}$
	334	330	4066
New	$\dot{u}_{P1/S}$	$\dot{u}_{S1/S}$	$\dot{u}_{Q1/N}$
indicators	331	227	297
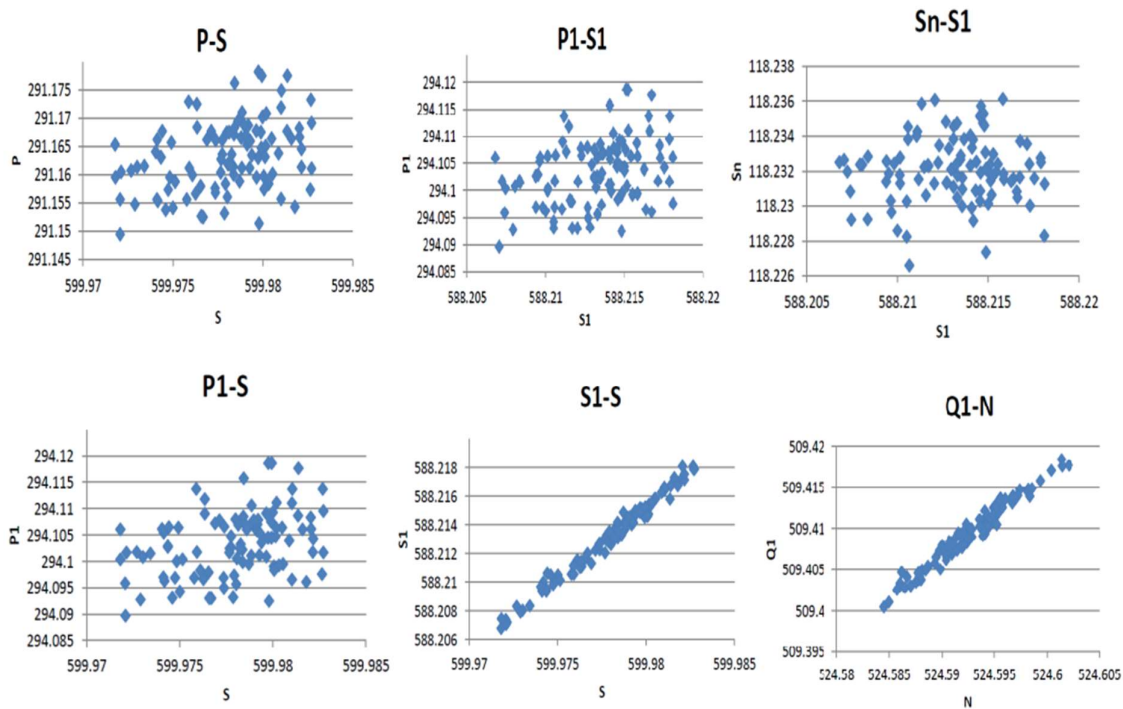
Figure 84 Test 2. Scatter diagrams of power quantities pairs of power ratio indicators

Test 3 (different harmonics)

This test has been carried out with voltage and current waveforms shown in Figure 85 ($THD_V = 2\%$, $THD_I = 50\%$). The phase displacement between the fundamentals of voltage and current has been set equal to 87° (this has been made in order to analyze a case with predominantly reactive power components). The obtained results are reported in Figure 86, Table 18 and Table 19. Even in this case S_N and S_I are strongly uncorrelated, while the highest correlation coefficients have been obtained for the pairs (S_I, S) and (Q_I, N). It can be also observed that in this case the correlation the pairs (P, S), (P_I, S_I) and (P_I, S) is very low. As regards the uncertainties, the highest values have been obtained for power factors and P_I/S; this is due to the fact that the active power components are very small, thus their uncertainty is high. As regards the other indicators, the highest uncertainty has been again obtained for the indicator S_N/S_1; on the other hand, significantly smaller uncertainties have been obtained for S_I/S and Q_I/N.
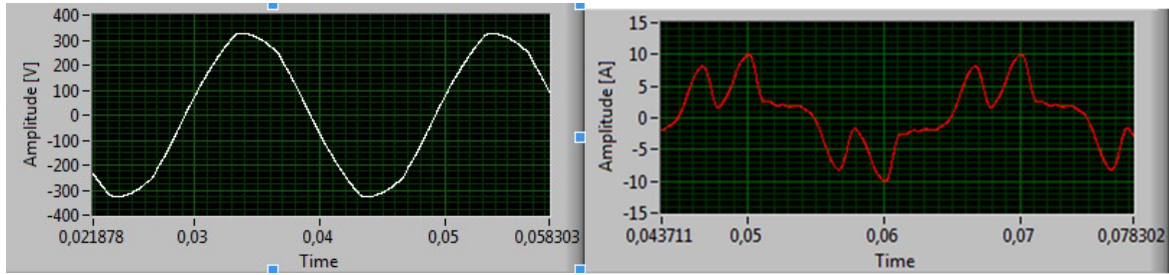
Figure 85 Test 3 voltage and current waveform

Table 18 Test 3. Correlation coefficients between power quantities pairs of power ratio indicators

IEEE Std. 1459 Indicators	$r(P, S)$	$r(P_1, S_1)$	$r(S_N, S_1)$
	0,026	0,017	0,019
New	$r(P_1, S)$	$r(S_1, S)$	$r(Q_1, N)$
indicators	0,039	0,919	0,921

Table 19 Test 3. Uncertainties on power ratios (ppm)

IEEE Std. 1459 Indicators	$\dot{u}_{PF}$	$\dot{u}_{PF1}$	$\dot{u}_{Sn/S1}$
	1498	1546	786
New	$\dot{u}_{P1/S}$	$\dot{u}_{S1/S}$	$\dot{u}_{Q1/N}$
indicators	1547	241	241
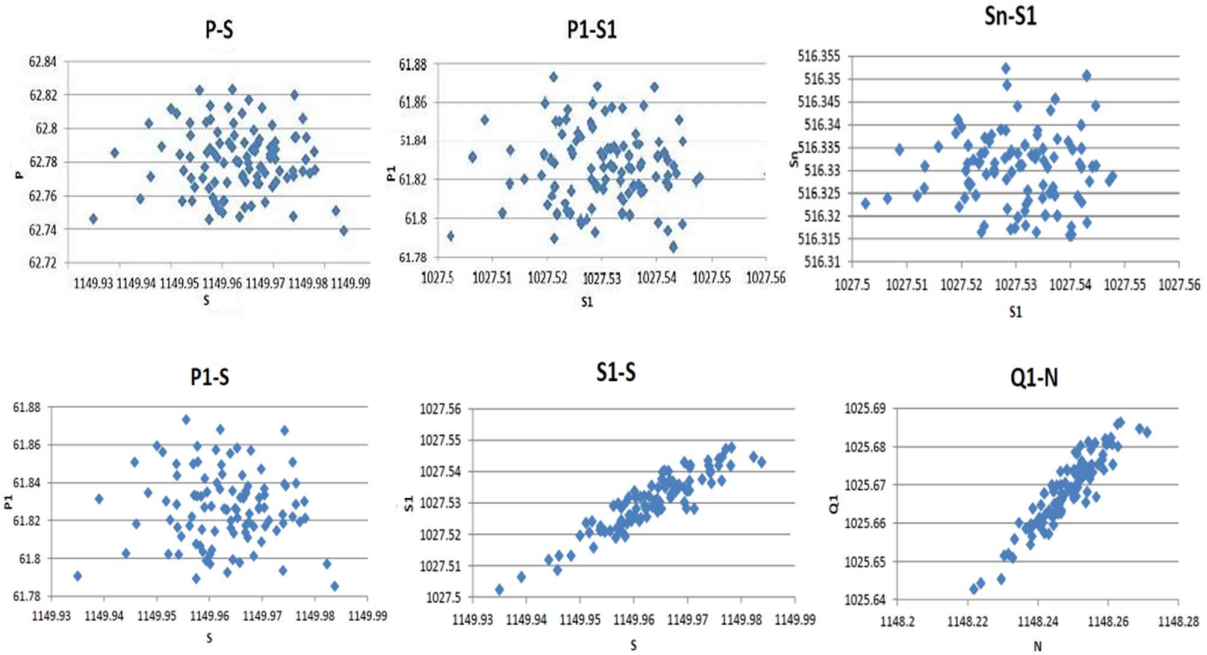
Figure 86 Test 3. Scatter diagrams of power quantities pairs of power ratio indicators

Table 20 IEEE Standard 1459-2010 quantities, correlation between input quantities and relative combined standard uncertainties

Quantity		Correlation	Uncertainty
Apparent power	$S = V \cdot I$	*Uncorrelated*	$\dot{u}_S = \sqrt{(\dot{u}_V)^2 + (\dot{u}_I)^2}$
Fundamental apparent power	$S_1 = V_1 \cdot I_1$	*Uncorrelated*	$\dot{u}_{S_1} = \sqrt{\left(\dot{u}_{V_1}\right)^2 + \left(\dot{u}_{I_1}\right)^2}$
Nonfundamental apparent power	$S_n = \sqrt{S^2 - S_1^2}$	*Correlated*	$\dot{u}_{S_N} = \dfrac{1}{S_N^2}\sqrt{S^4(\dot{u}_S)^2 + S_1^4\left(\dot{u}_{S_1}\right)^2}$
Active power	$P = \sum_{i=1}^{n} V_i \cdot I_i \cdot \cos\varphi_i$	*Uncorrelated*	$\dot{u}_P = \dfrac{1}{P}\sqrt{\sum_{i=1}^{n}\left(\dot{u}_{P_i} \cdot P_i\right)^2}$
Fundamental active power	$P_1 = V_1 \cdot I_1 \cdot \cos\varphi_1$	*Uncorrelated*	$\dot{u}_{P_1}$ $= \sqrt{\left(\dot{u}_{V_1}\right)^2 + \left(\dot{u}_{I_1}\right)^2 + \left(\dot{u}_{cos\phi_1}\right)^2}$

Nonactive power	$N = \sqrt{S^2 - P^2}$	*Uncorrelated*	$\dot{u}_N = \frac{1}{N^2}\sqrt{S^4(\dot{u}_S)^2 + P_1^4(\dot{u}_P)^2}$
Fundamental reactive power	$Q_1 = V_1 \cdot I_1 \cdot \sin\varphi_1$	*Uncorrelated*	$\dot{u}_{Q_1} = \sqrt{\left(\dot{u}_{V_1}\right)^2 + \left(\dot{u}_{I_1}\right)^2 + \left(\dot{u}_{\sin\phi_1}\right)^2}$

In summary in Table 20 is shown how to calculate the uncertainty equation of the proposed power ratio quantities.

Measurement uncertainty in three phase and unbalanced scenario

Uncertainty evaluation test system

Three-phase simulation study was carried out on the IEEE Test System n. 2 [88], whose simplified schemes are reported in Figure 87. This is a MV radial distribution network, with typical residential and industrial loads and equipment (linear RL loads, fluorescent light banks, adjustable speed drives, voltage regulators, shunt capacitors and so on). Complete network and loads data are given in [88]. In this study, loads have been aggregated, obtaining a simplified power system which can be schematized with a power source (at node 50), two PCC (PCC1 and PCC2) and five aggregated loads [89].

- PCC1 is at node 32; the loads connected to PCC1 are:

   ▪ L1 (power transformer at node 33 with single-phase load at node 34; no shunt capacitors);

   ▪ L2 (single-phase load at node 45, phase-phase load at node 46, and half the distributed load between nodes 32 and 71; no shunt capacitors).

- PCC2 is at node 71; the loads connected to PCC2 are:

   ▪ L3 (half the distributed load between nodes 32 and 71, phase-phase load at node 92; single-phase loads at nodes 52 and 911; with shunt capacitors);

   ▪ L4 (three-phase load at node 150);

   ▪ L5 (three-phase load at node 75, with shunt capacitors).
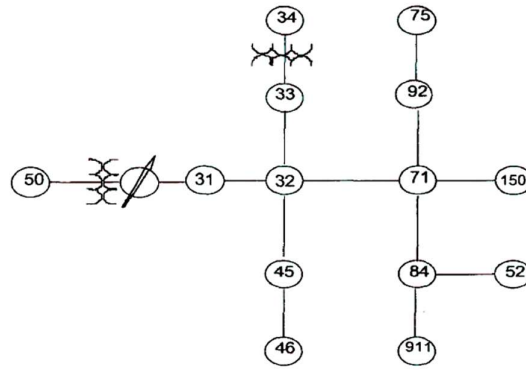
(a)
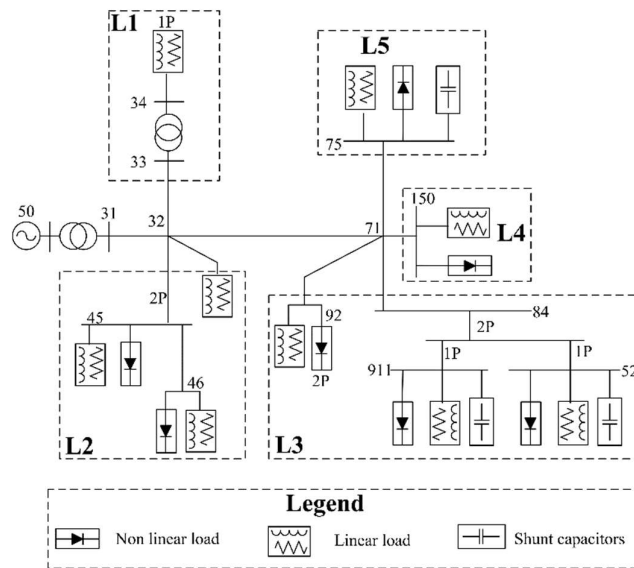
(b)

Figure 87 IEEE Test System. (a) original scheme[]; (b) scheme with aggregated loads [13]

Different working conditions were simulated, both in the original network configuration and by changing one or more loads. In more detail, to reproduce different loads configuration scenarios, some nonlinear and/or unbalanced loads were replaced by equivalent linear and balanced RL loads having the same power size and fundamental power factor of the original ones. For each scenario, IEEE Std. 1459 power quantities were evaluated at each metering section (one for each aggregated load), together with the power ratio indicators, THD factors and unbalance degrees.

For example, the results obtained for the network configuration with all linear loads are shown in Figure 88 and Figure 89. As expected, for all loads PF_1 and PF are equal and S_N/S_1 is zero. For loads

L1 and L2 power factors are low because no shunt capacitors are connected to such loads. As regards the new parameters, P_1/S is equal to PF_1 while S_1/S and Q_1/N are equal to 1. The results obtained in the initial scenario, i.e. in the original network configuration, with all nonlinear/unbalanced loads are shown in Figure 89. Table 21 reports the THD and unbalance degrees for both voltages and currents. It can be observed that for loads L1 and L2 at PCC1, where distortion levels are low, the values of S_1/S and Q_1/N are very near to 1 and P_1/S is almost equal to PF_1. On the other hand, for loads at PCC2 distortion levels are higher; for such loads S_1/S and, even more, Q_1/N are lower than 1 and P_1/S is lower than PF_1. It can also be noted that the lowest values of S_1/S and Q_1/N are obtained for L3 and L5, where shunt capacitors are present. This is due to the fact that capacitors amplify the distortion at the metering section, thus their effect on the considered indicators is similar to that of a nonlinear load. The same considerations can be made by considering the power ratios derived from the effective apparent power resolution (see

Figure 90). In this case the high differences between PF_1^+, PF and P_1^+/S_e are due to the presence of unbalance; the same is for S_{e1}/S_e and Q_1^+/N (in the figure, the unbalance amount is quantified by means of the new indicator S_1^+/S_{e1}). Finally, by comparing the results of Figure 89 and

Figure 90, it can be observed that the power ratios obtained from the arithmetic approach are not affected by the presence of unbalance, thus they could be used for harmonic emission assessment in both balanced and unbalanced situations.

	L1	L2	L3	L4	L5
■ PF	0.868	0.451	0.925	0.908	0.912
▨ PF	0.868	0.451	0.925	0.908	0.912
▨ S_N/S_1	0.000	0.000	0.000	0.000	0.000
▤ P_1/S	0.868	0.451	0.925	0.908	0.912
▨ S_1/S	1.000	1.000	1.000	1.000	1.000
▨ Q_1/N	1.000	1.000	1.000	1.000	1.000
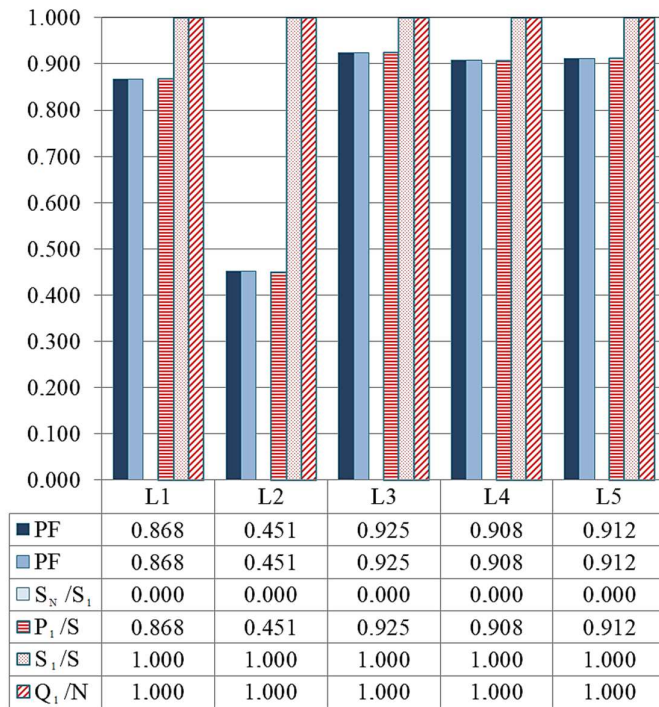
Figure 88 Simulation results of the power ratios in the case of all linear loads. Power ratios from arithmetic approach.

	L1	L2	L3	L4	L5
■ PF_1	0.859	0.437	0.929	0.919	0.907
▨ PF	0.851	0.435	0.903	0.916	0.858
▨ S_N/S_1	0.137	0.083	0.248	0.067	0.341
▤ P_1/S	0.851	0.435	0.902	0.917	0.858
▨ S_1/S	0.991	0.997	0.971	0.998	0.947
▨ Q_1/N	0.968	0.996	0.833	0.981	0.777
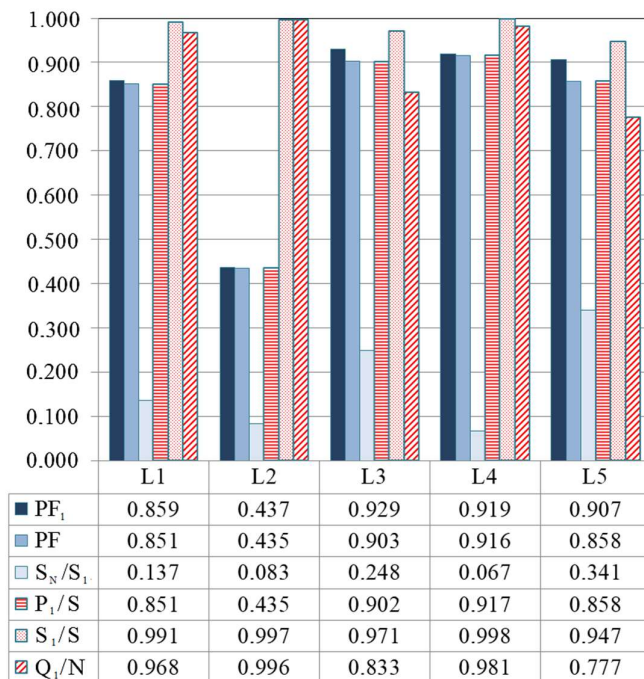
Figure 89 Simulation results of the proposed approach in the case of all nonlinear loads (original configuration). Power ratios from arithmetic approach

	L1	L2	L3	L4	L5
■ PF1+	0.86	0.44	0.93	0.92	0.91
▨ PF	0.65	0.28	0.72	0.91	0.58
▢ SeN/Se1	0.04	0.08	0.16	0.10	0.36
▤ P1+/Se	0.65	0.29	0.72	0.91	0.59
▢ Se1/Se	1.00	1.00	0.99	0.99	0.94
▨ Q1+/N	0.52	0.60	0.42	0.96	0.32
▨ S1+/Se1	0.76	0.65	0.79	1.00	0.68
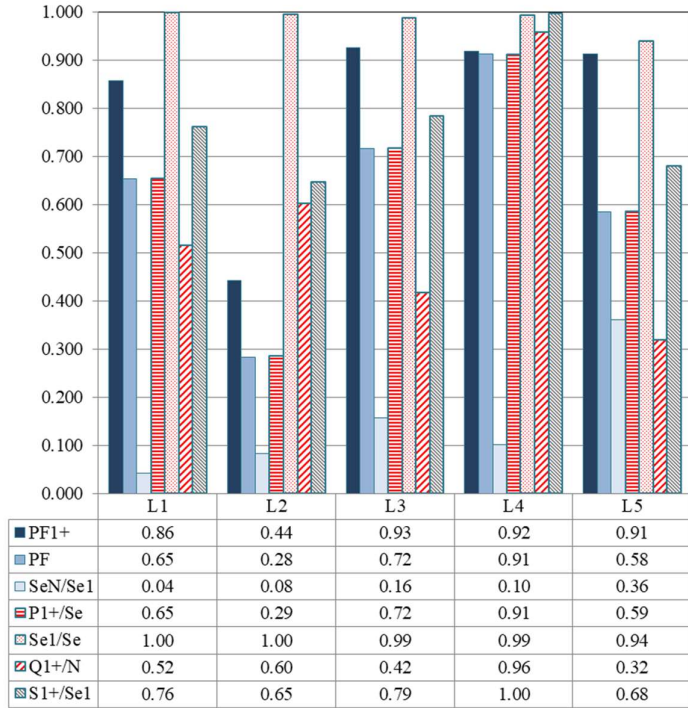
Figure 90 Simulation results of the proposed approach in the case of all nonlinear loads (original configuration). Power ratios from apparent power resolution

Table 21 THD factors and unbalance degrees. Original network configuration

PCC	Loads	THD_V [%] (mean value)	THD_I [%] (mean value)	Vi/Vd [%]	Ii/Id [%]
1	L1	4,4	2,16	0,33	84,6
	L2		6,42	0,33	95,6
2	L3		7,86	0,91	74,3
	L4	7,35	7,34	0,91	3,24
	L5		30,3	0,91	29,7

In order to evaluate the measurement uncertainty impact on power ratios, uncertainty propagation was studied starting from the measurement uncertainties of input variables, i.e. the IEEE 1459 power quantities. The study was carried out by considering the accuracy specifications of measurement instruments and transducers typically used in distribution networks, i.e. voltage and current electronic instrument transformers (VTs, CTs) and power quality analyzers (PQA).

In more detail, PQAs were considered with accuracy class of 0.5 and 2 for active and reactive power measurements, respectively $(e_{PQA_P} = 0.5\%, \ e_{PQA_Q} = 2\%)$, and 0.2 for voltage and current measurements, respectively $(e_{PQA_V} = e_{PQA_I} = 0.2\%)$. As regards VTs and CTs, instruments of class 0.2S and 0.2S, respectively, were considered. According to standard requirements [90], the maximum allowed ratio error and phase displacement for class 0.2S CTs are equal to $\eta_{CT} = \pm 0.2\%$ and $\varepsilon_{CT} = \pm 0.3 \ crad$, respectively, for currents between 20% and 120% of the CT rated current; for currents equal to 5% of the rated current, maximum ratio error and phase displacement allowable are $\eta_{CT} = \pm 0.35\%$ and $\varepsilon_{CT} = \pm 0.45$ crad, respectively; for currents from 5% to 20% of rated value, maximum allowable ratio error and phase displacement are calculated by means of a linear interpolation between the two reference limits. These limits are referred to the rms value of the signal in sinusoidal conditions. For combined quantities, in the case of distorted signals, the standard [90] prescribes incrementing these limits by a 15% factor. On the other hand, for fundamental quantities standard [90] prescribes the following allowable errors: $\eta_{CT1} = \pm 1\%$ and $\varepsilon_{CT1} = \pm 1.8$ crad. The same considerations can be applied to VTs.

Thus starting from the aforesaid error limits, Monte Carlo simulations were performed by assuming uniform distribution for each of the above mentioned errors. In this case, the extremes of the uncertainty range are equal to the aforesaid maximum errors. 10^5 Monte Carlo iterations were performed. At each iteration, i, a random value was chosen inside the uncertainty range for each of the considered uncertainty contribution. For example, fundamental voltage, current and active power are obtained using the following equations:

$$V_{1i} = \left(1 - \frac{\eta_{VT1i}}{100}\right) \cdot \left(1 - \frac{e_{PQA_{V1i}}}{100}\right) V_1 \tag{41}$$

$$I_{1i} = \left(1 - \frac{\eta_{CTi1}}{100}\right) \cdot \left(1 - \frac{e_{PQA_{Ii}}}{100}\right) I_1 \qquad (42)$$

$$P_{1i} = \left(1 - \frac{\eta_{CT1_i}}{100} - sen\varepsilon_{CT1_i} \cdot tg\varphi\right)\left(1 - \frac{\eta_{VT1_i}}{100} + sen\varepsilon_{VT1_i} \cdot tg\varphi\right) \cdot \left(1 - \frac{e_{PQ\_P1i}}{100}\right) \cdot P_1 \qquad (43)$$

where I_1, V_1 and P_1 are the values obtained in the simulation on the IEEE test system for a given working condition and a given node; V_{1i}, I_{1i} and P_{1i} are the quantities obtained considering the uncertainty propagation on the measurement chain at i iteration.

Monte Carlo simulations were performed both for the fundamental and the total quantities in order to obtain the uncertainties in both the power quantities of the IEEE 1459 apparent power resolution and the considered indicators for harmonic emission assessment.

As an example, the frequency distributions obtained with Monte Carlo simulations for load L2 are reported in Figure 91, in the case of all nonlinear loads (original configuration). The uncertainties obtained in this test case for all loads are summarized in Table 21. As can be seen, the uncertainty obtained for the index S_N/S_1 is comparable to the parameter value (cfr. Figure 89), thus it can significantly affect the parameter use for practical applications. On the other hand, the new indicators, S_1/S and Q_1/N, have lower uncertainties, thus confirming their potentiality for a better harmonic emission assessment.

Table 22 relative uncertainties obtained in the case of all nonlinear loads. Original network configuration

Loads	u_P/S	u_P1/S1	u_SN/S1	u_P1/S	u_S1/S	u_Q1/N
L1	0,29%	1,0%	24%	0,89%	0,45%	0,49%
L2	0,55%	2,2%	40%	2,1%	0,49%	0,11%
L3	0,28%	0,95%	12%	0,75%	0,46%	1,0%
L4	0,25%	0,82%	32%	0,63%	0,39%	0,32%
L5	0,26%	0,89%	5,0%	0,69%	0,42%	0,79%
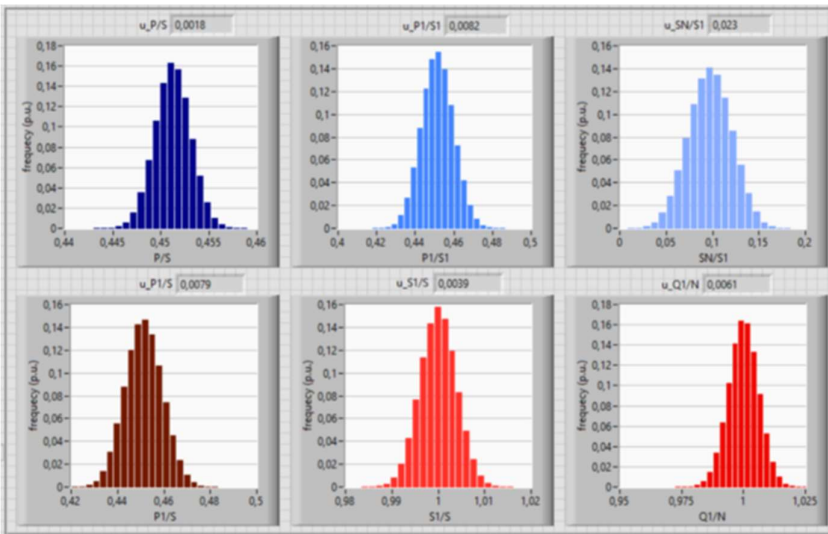
Figure 91 Monte Carlo results in the case of all nonlinear loads (original configuration). Load L2

Comparison of the power ratio approach with the voltage harmonic vector method

In the previous section, starting from apparent power decomposition and related line utilization and harmonic pollution parameters, a critical analysis has been made on measurement issues related to the evaluation of such parameters. To overcome some limitations of the IEEE Std. 1459-2010 indicators, new power ratios have been introduced and analyzed, which are conceptually similar to those defined by IEEE Std. 1459-2010, but they can be more accurately measured with instrumentation and transducers normally employed in distribution power grids. The suitability of the proposed parameters has been discussed for both single-phase and three-phase balanced/unbalanced case, taking into account both their behavior in different scenarios. The obtained results confirm that the proposed parameters have a better behavior than the IEEE Std. 1459-2010 indicators for harmonic pollution; thanks to their simple formulation and the "power factor like" behavior, they are suitable for accurate measurements and they could be easily integrated in common instrumentation for power system measurements and billing purposes.

In this section is instead presented a comparison between the power ratio approach and one of the most known method for the harmonic power quality assessment, the voltage harmonic vector approach or

VHV. The methods were tested in dedicated benchmark test system proposed for the first time in[91] Unlike the previous IEEE test system, this test system was proposed in 2019 by IEEE-PES Task Force on Harmonics Modeling and Simulation with the aim of simplify the architecture and study also the presence of compensator and passive filter to the harmonic detection method.

In the following, first, it is shown the basic principles of the VHV method, after that the benchmark test system is proposed and finally the results of the two methods are shown.

Voltage harmonic vector method

The voltage harmonic vector (VHV) method is described in several papers [21], [23], [91], [92]. The method needs to determine the harmonic voltage sources on customer ($\underline{U}_{C-h}$) and network ($\underline{U}_{U-h}$) side and this is reason why method is based on Thevenin circuit. The equivalent circuit can be seen in Figure 92. The network harmonic voltage source presents the background distortion i.e. the harmonic pollution before the connection of customer. The following equations show the calculations of harmonic voltage sources:

$$\underline{U}_{U-h} = \underline{U}_{PCC-h} + \underline{I}_{PCC-h} \cdot \underline{Z}_{U-h} \qquad (44)$$

$$\underline{U}_{C-h} = \underline{U}_{PCC-h} - \underline{I}_{PCC-h} \cdot \underline{Z}_{C-h} \qquad (45)$$
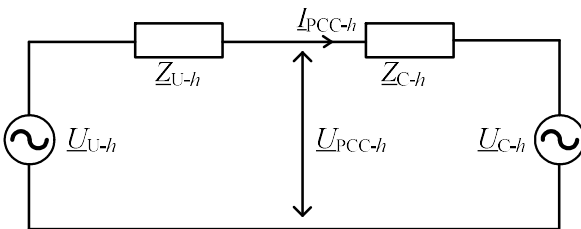
Figure 92 Equivalent Thevenin model at PCC

The harmonic contributions are based on superposition approach, which is shown in Figure 93. The customer contribution ($\underline{U}_{C-ph}$) is based on a voltage drop on network impedance caused by customer harmonic source, while the network contribution ($\underline{U}_{U-ph}$) is based on a voltage drop on the customer impedance caused by network harmonic source:

$$\underline{U}_{U-ph} = \frac{\underline{Z}_{C-h}}{\underline{Z}_{U-h} + \underline{Z}_{C-h}} \underline{U}_{U-h}, \qquad (46)$$

$$\underline{U}_{C-ph} = \frac{\underline{Z}_{U-h}}{\underline{Z}_{U-h} + \underline{Z}_{C-h}} \underline{U}_{C-h} \qquad (47)$$
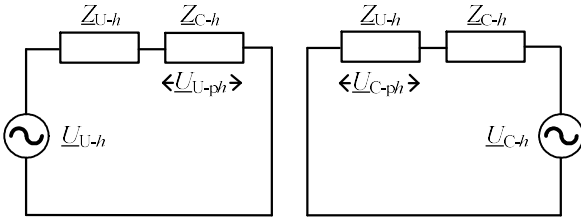
Figure 93 Superposition model (left – network contribution and right – customer contribution)

The final customer harmonic contribution ($U_{C-final-h}$) is a scalar (absolute value of the complex number) value and it has a condition that the contribution is only when customer adds to total distortion. If the customer drops the total distortion, the customer contribution is zero. This condition is shown by the following equation[91]:

$$U_{C-final-h} = \begin{cases} |\underline{U}_{C-ph}|, & |\underline{U}_{PCC-h}| > |\underline{U}_{U-ph}| \\ 0, & |\underline{U}_{PCC-h}| \le |\underline{U}_{U-ph}| \end{cases} \qquad (48)$$

The summation of each contribution gives the total distortion, and this is shown with phasor diagram in Figure 94.
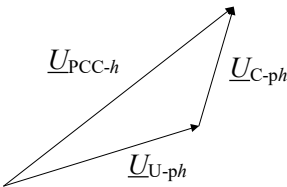
Figure 94 Phasor diagram

The disadvantage of the method is that the harmonic impedance needs to be known. In this paper, the actual harmonic impedance is used to better comparison with the new approach presented in this paper. The actual impedance in real-environment is practically impossible to be measure and for that reason the reference impedance can be used instead of actual impedance. The approach with reference impedance is presented in paper [23]. In real-case, the real impedance could not be used for determining harmonic contribution because the harmonic impedance is changing. Instead of real harmonic impedances, reference harmonic impedances are used. The reference network harmonic impedance can be determined by short-circuit ratio and the harmonic impedance linearly increases with frequency. The reference customer harmonic impedances are determined by active power at 50 Hz because the customer should compensate reactive power. If the customer causes any resonance, this can be seen in increasing its contribution.

Test System Overview

In order to investigates their effectiveness, the two approaches were applied to a case study. It was chosen a test system which represents a generic radial distribution grid with three MV/LV feeders and one MV load (see Figure 95). This benchmark test system was proposed in [91] and more details can be found there. The test system can be configured in different topologies, in order to reproduce different conditions, such as: unbalance condition, resonance conditions and/or background harmonic source. In this paper the basic configuration of the test system was used as case study with all the feeders, loads and reactive power compensators, as described in the next subsection.

The test system is composed by an equivalent 110 kV high voltage coupled with the grid with a HV/MV transformer. After that, there are three MV customers with PCC at MV side of their MV/LV transformer. The customers PCCs are connected through equivalent line model to a 20 kV bus bar. In the MV bus bar, there are an equivalent three phase symmetrical single resistive/inductive load which represents other loads connected to bus bar and a capacitor banks with inrush reactors.
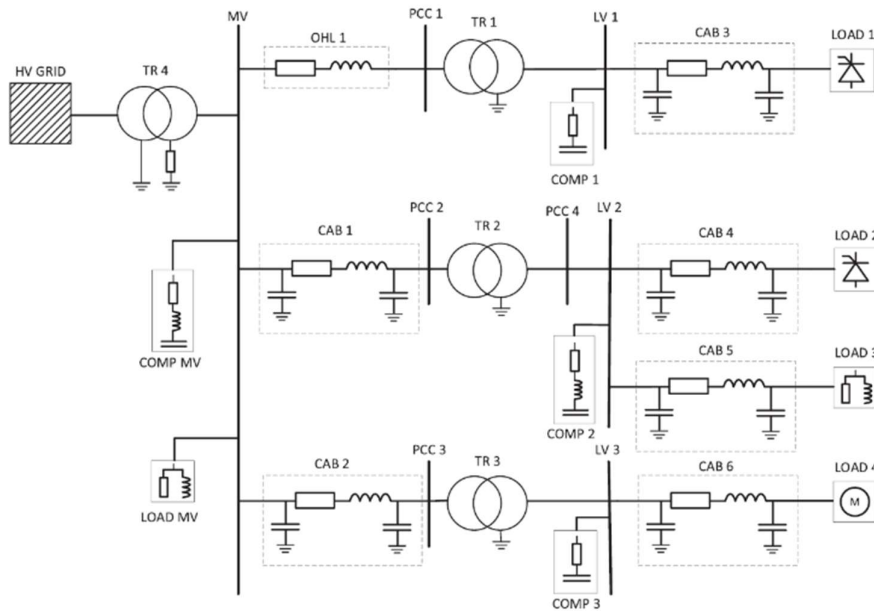
Figure 95 Benchmark test system

As regards the LV side, there are three feeders: first is a purely nonlinear load with a capacitor bank, second is composed by a nonlinear load and a linear load with a passive filter and finally, third is an AC motor with a capacitor bank. Linear loads have been modelled using an inductive simplified equivalent circuit with star configuration. While induction motor is modelled as shown in Figure 96.
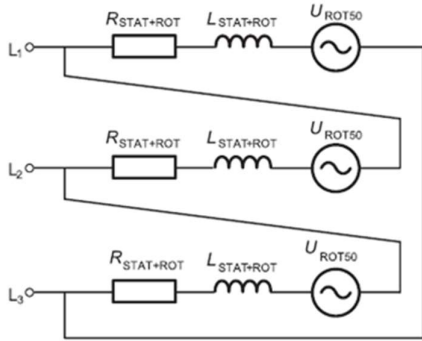
Figure 96 induction motor at customer 3

This test system presents the greatest disturbing contribution coming from Load 1 at PCC1 however also PCC2 contributes to the distortion even if less than PCC1. In Table 23 is possible to compare different harmonic components while in Table 24 are shown the THD of the voltage and current at each node of the grid.

The simulations were conducted with a step of 10^{-5} s and with an observation window of 10 period of the fundamental components. This time step was chosen 10 times greater of the maximum interesting frequency which, for the case under test, is the 50th harmonic. Finally, for the Power Ratio Approach the sapling rate was chosen of 10 kHz in order to be able to compute also the 50th harmonic of the fundamental as required from IEEE std. 1459.

Table 23 Simulation results

Harmonic order	PCC 1			
	URMS [V]	φ [°]	IRMS [A]	φ [°]
1st (50 Hz)	12033.74	-92.71	6.10	-104.31
5th (250 Hz)	39.53	-3.80	1.96	86.78
7th (350 Hz)	36.13	-88.20	1.10	14.39
11th (550 Hz)	38.99	-116.97	0.83	73.45
13th (650 Hz)	16.90	112.44	0.28	-3.86
Harmonic order	PCC 2			
	URMS [V]	φ [°]	IRMS [A]	φ [°]

Harmonic order	URMS [V]	φ [°]	IRMS [A]	φ [°]
1st (50 Hz)	12025.26	-92.72	11.83	-99.61
5th (250 Hz)	39.91	-1.66	0.90	137.58
7th (350 Hz)	35.92	-86.69	0.43	63.12
11th (550 Hz)	39.51	-119.77	0.31	-53.38
13th (650 Hz)	17.72	113.31	0.20	-95.51
Harmonic order	**PCC 3**			
	URMS [V]	φ [°]	IRMS [A]	φ [°]
1st (50 Hz)	12032.88	-92.71	5.73	-106.70
5th (250 Hz)	38.30	-2.09	0.06	-88.95
7th (350 Hz)	35.05	-87.50	0.03	-173.47
11th (550 Hz)	38.77	-118.71	0.01	-59.00
13th (650 Hz)	17.28	111.24	0.01	-166.25

Table 24 THD of curent and voltage at each load

	THDI [%]	THDV [%]
MV	1.7242	0.59907
MV Load	0.57621	0.59907
Pcc 1	39.569	0.61022
Pcc 2	8.3227	0.60937
Load 2	23.505	1.889
Load 3	1.5199	1.889
Pcc 3	1.0339	0.60005

Results of the VHV method

As shown in Table 23 and Table 24The total harmonic distortion at all PCC is comparable because the impedance between PCC is low. The customer 1 (PCC 1) and customer 2 (PCC 2) have only disturbing load. This can be also concluded from the result in Table 25 because the contribution of the customer 3 (PCC 3) is practically zero and the total harmonic distortion (SIM – measured at PCC) should be the same as network contribution. The customer 2 has lower contribution than customer 1 due to using tuned passive filter for the compensation of reactive power.

Table 25 Results of the model based approach

Harm. order	PCC 1		PCC 2		PCC 3	
	customer cont.	SIM	customer cont.	SIM	customer cont.	SIM
	URMS [V]	URMS [V]	URMS [V]	URMS [V]	URMS [V]	URMS [V]
5th	28.44	39.53	15.66	39.91	0.00	38.30
7th	26.64	36.13	12.53	35.92	0.01	35.05
11th	38.48	38.99	11.74	39.51	0.00	38.77
13th	11.34	16.90	10.88	17.72	0.15	17.28

The results of the customer 1 and customer 2 are also shown with phasor diagrams in Figure 97 and Figure 98. On the phasor diagram, the red colour presents customer contribution but this contribution could be also named by emission. The customer contribution of customer 1 (PCC 1) is comparable with the network contribution at PCC 2, which validate that in IEEE Benchmark model, customer 1 and customer 2 only pollute the network.
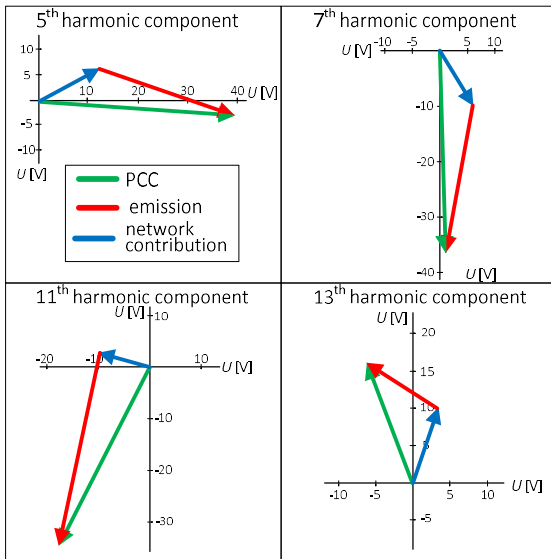
Figure 97 Phasor diagram for customer 1 (PCC 1)
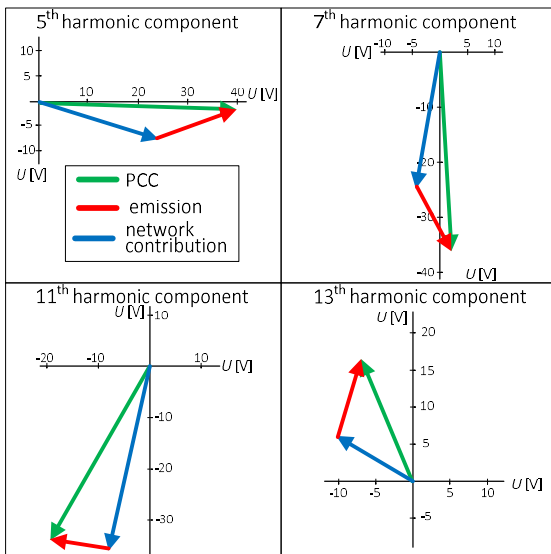
Figure 98 Phasor diagram for customer 2 (PCC 2)

Results of the power ratio method

As shown in Figure 99 and Figure 100, the coefficients highlight the harmonic situation at every PCCs. Looking at the simulation results, is possible to observe that for PCC1, where the distortion levels are higher due to the presence of the most disturbing load, the values of PF and P1/S are lower than PF1 and S1/S and Q1/N are lower than 1. SN/S1 is higher than zero, as expected for a disturbing load. For

PCC2, the indicators behavior is similar to that of PCC1, but the differences between PF, P1/S and PF1 are lower and the value of S1/S is nearer to 1 due to the lower amount of disturbance. SN/S1 is near to zero, and this can affect the reliability of the parameter, when considering the measurement uncertainty [21]; the most sensitive indicator with respect to the harmonic pollution is Q1/N, whose value is still significantly lower than 1, even for PCC2, thus it can be reliable even considering the measurement uncertainty. As regards the linear loads (PCC3 and the MV load), PF, P1/S and PF1 have the same value, S1/S and Q1/N are equal to 1 (and Sn/S1 is equal to zero). Thus, power ratio indicators approach allows identifying the presence of polluting loads (at PCC1 and PCC2), also assessing the amount of disturbance (greater for PCC1 and lesser for PCC2) by means of the power ratios values.

	MV	MV Load	Pcc 1	Pcc 2	Load 2	Load 3	Pcc 3
PF1=P1/S1	0,992	0,961	0,978	0,990	0,919	0,934	0,971
PF=P/S	0,992	0,961	0,909	0,987	0,894	0,920	0,971
SN/S1	0,019	0,000	0,395	0,086	0,236	0,181	0,012
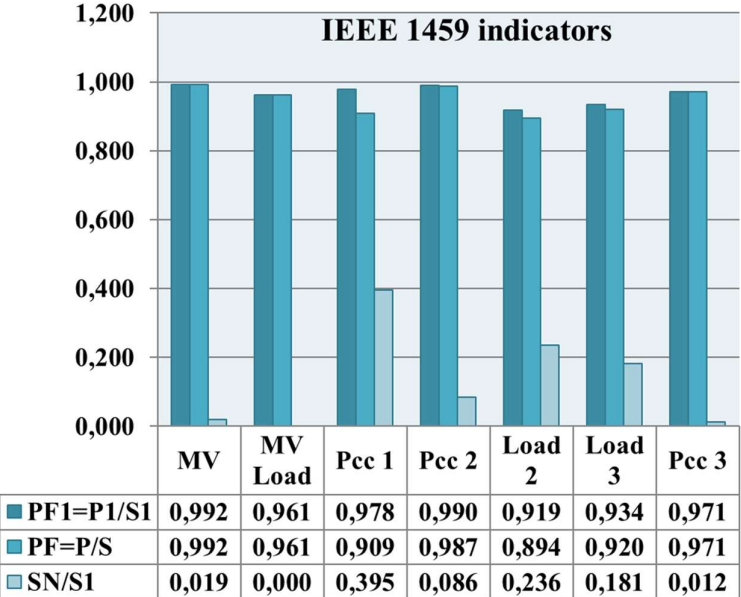
Figure 99 results of IEEE 1459 coefficients

	MV	MV Load	Pcc 1	Pcc 2	Load 2	Load 3	Pcc 3
P1/S	0,992	0,961	0,910	0,987	0,894	0,919	0,971
S1/S	1,000	1,000	0,930	0,996	0,973	0,984	1,000
Q1/N	0,989	1,000	0,463	0,850	0,857	0,895	0,999
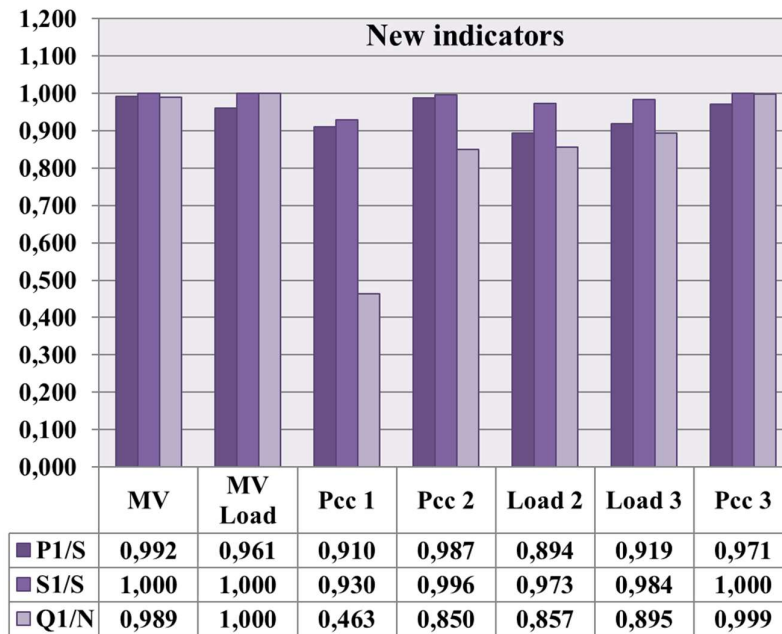
Figure 100 results of new indicators

Comment of the comparison study

In summary, the first approach focuses its attention on the equivalent impedance of customer and utility at the point of PCC. It shows how powerful can be this approach in terms of accuracy of harmonic component generated by each source. However, it presents a not negligible computational cost and suffers from sudden variation of equivalent impedance and related measurement problems. The second approach, instead, is based on the calculation of power ratios for the characterization of the line utilization and harmonic distortion at each PCCs. The main advantage of this method involves, undoubted, on its simplicity due to lower computational cost and its applicability in commercial platforms; in addition, the power factor-like approach looks very promising from a future standardization point of view. However, an unambiguous algorithm for the data interpretation and the decision-making for harmonic source and pollution level assessment must be investigated in future works.

Implementation of PQ metrics in smart meter platform

This chapter presents a feasibility study on how to implement power quality (PQ) metrics in a low-cost smart metering platform. The study is aimed at verifying the possibility of implementing power

PQ monitoring in distribution network without replacing existing smart metering devices or adding new modules for PQ measurements. To this aim, an electronic board, currently used for remote energy metering, was chosen as case study, specifically the STCOMET platform. Starting from the specifications of this device, the possibility of implementing power quality metrics is investigated in order to verify if a compliance with standard requirements for PQ instruments can be obtained. Issues related to device features constraints are discussed; possible solutions and correction algorithms are presented and experimentally verified for different PQ metrics with a particular focus on harmonic analysis. The feasibility study considers both the use of on-board voltage and current transducers for low voltage applications and also the impact of external instrument transformers on measurement results.

To enable diffused PQ measurement, it is important to introduce new technologies that can provide both end-users and distribution system operators with suitable information about the quality of the power supply at reasonable costs. In this framework, some studies and proposals can be found in research papers concerning the use of new energy meters, specifically developed for PQ measurement applications [93]–[99]. However, the use of sophisticated and expensive instrumentation is not economically feasible for a widespread use at user level. On the other hand, low cost devices have been proposed to implement PQ measurement tasks; in this case such additional instrumentation should be installed alongside the currently employed energy meters or new integrated platforms should replace those already used in distribution networks. It should be noticed that, in the viewpoint of widespread diffusion of PQ measurements at the user level, the installation of sophisticated and expensive instrumentation is not economically feasible. On the other hand, low-cost devices have been proposed to implement PQ measurement tasks; in this case, such additional instrumentation should be installed alongside the currently employed energy meters or new integrated platforms should replace those already used in distribution networks

The main reference is the IEC 61000-4-30, which defines the methods for PQ parameters measurement and the related accuracy requirements; for harmonics (and interharmonics) measurements it refers to IEC 61000-4-7. The instruments compliance with such standards is crucial to enable their use for monitoring or even billing purposes. In more detail, IEC 61000-4-30 defines two classes of measurements, i.e. classes A and S (correspondent to classes I and II of IEC 61000-4-7, respectively). Class A instruments are meant to be used for contractual applications or compliance verification with allowed disturbances limits; class S instruments are allowed for statistical applications such as surveys or power quality assessment and they obviously entail processing requirements lower than those of class A. However, as stated in IEC 61000-4-7, to permit the use of simple and low-cost instruments,

consistent with the requirements of the application, the possibility is given to use less sophisticated instrumentation also for emission measurements if the disturbance amount is such that even with increased measurement uncertainty the limits are not exceeded (for harmonics, measured values under 90 % of the allowed limits can be considered).

The metrics were implemented in STCOMET platform of STmicroelectronics which is currently used in different countries for energy meter deployment. The device used for the experimental tests is the EVLKSTCOMET10-1 development kit for smart metering applications. It is based on a Cortex ™ - M4 microcontroller; it includes a metrology section and it is able to communicate through PLC communication protocols. The PLC coupler allows the STCOMET device to transmit and receive communication signals on the AC network line. As regards the measurement transducers, a resistive divider is used as voltage sensor (Figure 101), while a shunt and a current transformer are available for measuring current (the shunt was used in the experimental tests) (Figure 102).
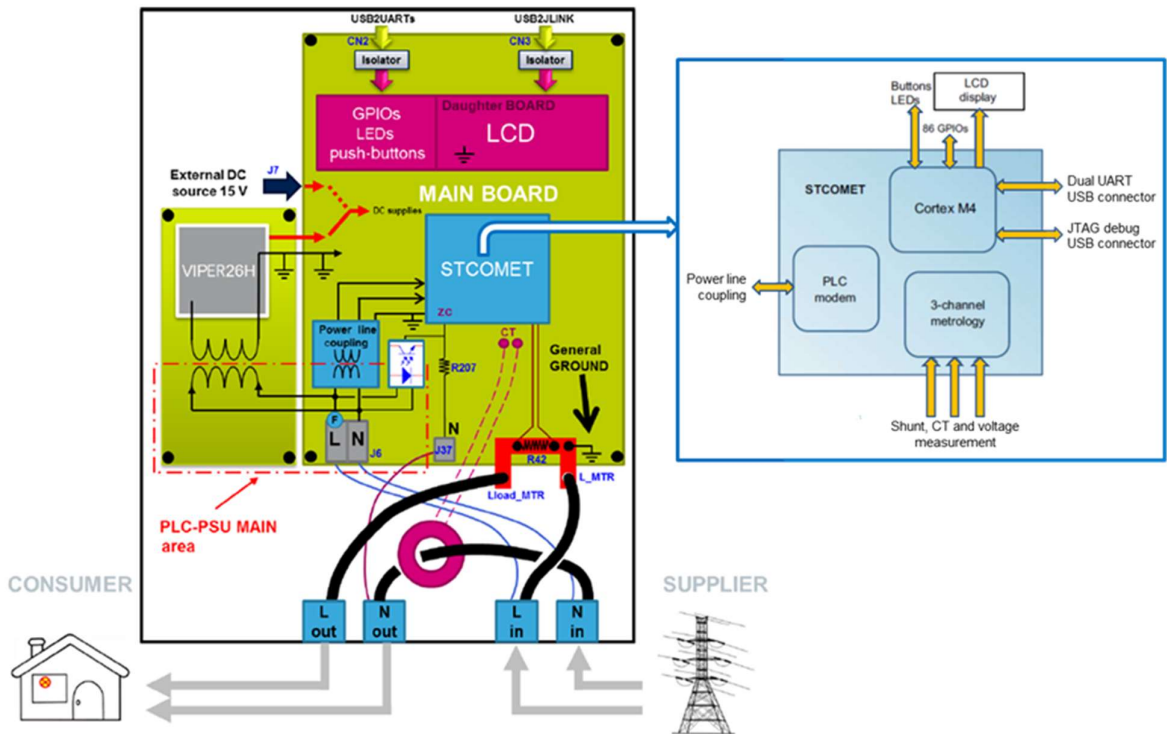
Figure 101 EVLKSTCOMET10-1 functional block diagram
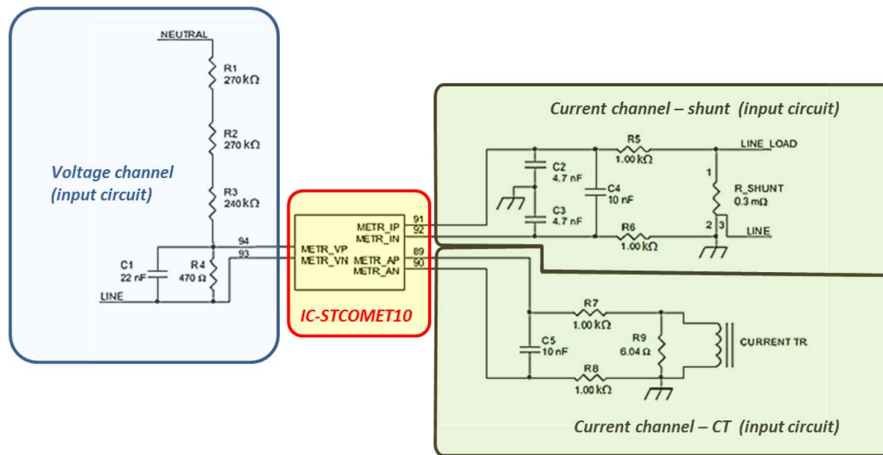
Figure 102 EVLKSTCOMET10-1 metrology reference application schematics

The digital section consists of a DSP and DFE (Digital Front End) wired to the input modulators, and an interconnection bus with the Cortex ™ -M4 core. Available memories are: 640 kB or 1 MB of embedded Flash; 128 kB of embedded SRAM (static RAM); 8 kB of embedded shared RAM. Metrological characteristics of the EVLKSTCOMET10-1 are shown in Table 26.

Table 26 STCOMET metrological characteristics, V=230V, f=50 Hz

Parameter	Value
Nominal input voltage	230 V
Nominal line current	5 A
Nominal input frequency	50/60 Hz
Sampling frequency (Fs)	7.8125 kHz
Bandwidth (- 3 dB)	0 – 3.6 kHz
Voltage/current RMS accuracy	0.5 %

As mentioned in the introduction, IEC 61000-4-30 and IEC 61000-4-7 are the main Standards for PQ and harmonic measurement [100], [101]; IEC 61000-4-30 covers PQ measurement methods and it refers to IEC 61000-4-7 for harmonics measurements. Among the PQ parameters covered by the aforesaid Standards, those measured by STCOMET are: power system frequency, supply voltage

magnitude, dips and swells; metrics for other parameters, such as or harmonics are not implemented in the on-board metrology chip.

As regards harmonic measurements, the IEC 61000-4-7 standard defines the parameters to be measured for the evaluation level of harmonic distortion in a given measurement section, in terms of amplitudes of single voltages/current harmonic components or global parameters such as THD. The standard provides also indications regarding the general structure of measurement instruments, which is preferably based on the use the Discrete Fourier transform (DFT) and implemented by means of Fast Fourier transform (FFT) algorithm for shorter computation time (see Figure 103).
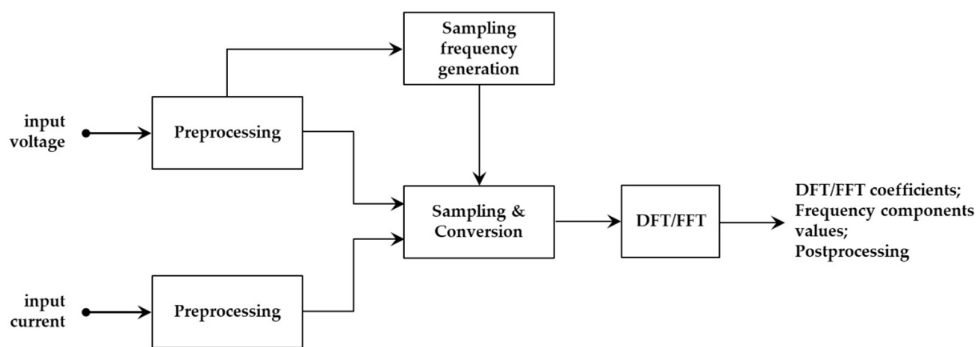
Figure 103 General structure of IEC 61000-4-7 instrument

Phase locked loop or other synchronisation systems are needed to properly generate the sampling frequency, in order to meet the aforesaid synchronisation requirements. Hanning weighting is allowed only in the case of loss of synchronisation, even if in such occurrence the data shall be flagged and not used for the purpose of determining compliance with standard PQ limits.

On STCOMET, input signal period is obtained by means of a zero crossing method. Frequency is obtained from the period measurement. Using this method, it is necessary to filter harmonics and inter-harmonics, in order to minimize the effects of multiple zero crossing. The resolution of zero-crossing is 8 µs.

In more detail, the STCOMET board has a fixed frequency sampling equal to fs = 7812.5 Hz, corresponding to a sampling period Ts = 128 µs. Considering a power system frequency of 50 Hz and the 10 cycles observation window Tw = 200 ms, the number of acquired samples is:

$N = Tw*\text{fs} = 1562.5 \approx 1563$

FFT spectral resolution is:

$\Delta F = fs/N = 5.0016 Hz$

The synchronization error, corresponding to 0.5 samples, is of 64 µs, which can be calculated in percentage terms as follows:

$e\% = (E/Tw)*100 = 0.032\%$

Therefore, the instrument based on STCOMET cannot be classified in class A; thus in the performed feasibility study class S requirements have been considered as target for the implementation and verification of PQ and harmonics measurement metrics.

PQ metrics implementation on STCOMET

As mentioned in the previous section, STCOMET already implements the measurement of: power system frequency; voltage and current RMS; and voltage dips and swells. The comparison between the IEC 61000-4-30 requirements for class S instruments and the STCOMET on-board metrics are reported in Table 27. To meet IEC 61000-4-30 requirements for on-board metrics, some correction algorithms have been implemented, as described in [102]. In brief:

- For frequency measurement, the main difference between IEC 61000-4-30 requirements and STCOMET on-board metric is the measurement time (10 s vs. 8 µs, i.e. STCOMET measurements are updated each 8 µs); thus the measurement over 10 s has been obtained as the mean of the frequency values (updated at each 8 µs) over the time interval of 10 s.

- For voltage/current RMS measurement, the main difference between IEC 61000-4-30 requirements and STCOMET on-board metric is the observation window in subsequent measurements. In fact IEC 61000-4-30 requires that the measurements shall be obtained over the base time interval (e.g. 10 cycles at 50 Hz); subsequent time intervals shall be contiguous, and not overlapping. STCOMET calculates RMS over the aforesaid base time interval; however the RMS measurement is updated every 128 µs, i.e. once a new signal sample is

available from the ADC. Thus, in the correction algorithm, the measurement reading update has been modified, in order to obtain one RMS reading each 10 cycles.

- Main on-board metrics modifications have been made for swells, dips and interruptions. In fact, for swells and dips IEC 61000-4-30 requires to measure a pair of data, i.e the maximum/ residual/ voltage (i.e. the maximum/minimum voltage value recorded during the swell/dip) and the event duration, which is the difference between start and end times of the swell/dip (i.e. the time when the voltage RMS rise above/falls below the swell/dip threshold, and the time when the voltage RMS equals or goes back below/above the threshold); in this case the RMS shall be measured over ½ cycle or 1 cycle (Urms(1/2) or Urms(1), respectively). For interruptions only event duration shall be measured. STCOMET on-board metric was very different from the IEC 61000-4-30 one. Thus, a new algorithm has been implemented, based on the measurement of Urms(1), as summarized in Table 27.

Table 27 STCOMET on-board metrics vs. IEC 61000-4-30 requirements (class S)

Parameter	IEC 61000-4-30			STCOMET metric main features	Correction algorithms
	Measurement range	Time interval (t.i.)	Maximum error		
Frequency Period	42,5 ÷57,5 Hz (for 50 Hz syst.)	10 s (not overlapping)	Number of integer cycles during the 10-s t.i. divided by their cumulative duration Harmonics and interharmonics are attenuated	Measurement from zero-crossing (voltage channel, with a low pass filter). Frequency range between 32.55 and 81.38 Hz. Resolution of 8 μs Period is calculated as mean of last eight measured periods.	Single frequency value is obtained as period reciprocal (on board metric); Frequency measurement is calculated as the mean of single frequency values over 10 s
RMS	20 ÷ 120 % Udin	200 ms (10 cycles for 50 Hz) no gaps	The r.m.s. value includes, by definition, harmonics, interharmonics, etc. Every 10/12-cycle interval	RMS measurement is obtained from voltage/current samples voltage/current are not filtered	No modifications of on-board metric; Measurement reading is updated

			shall be contiguous and not overlapping; Not used for dips, swells, voltage interruptions and transients	Integration time is 10 cycles; RMS value is updated each 128 □s	each 10 cycles, in order to have not overlapping t.i.
Dips Swells Interruptions	---	---	The basic measurement shall be the RMS over ½ cycle or 1 cycle (Urms(1/2) or Urms(1)) Measured data are: maximum/residual voltage (i.e. the max./min. voltage value during the event) and duration (i.e. the difference between start and end times of the event). for interruptions only duration is measured	The fundamental component of voltage (RMS) is compared to a 10-bit threshold An internal time counter is incremented until momentary voltage value is below/above the threshold. Maximum/residual voltage is not calculated Interruptions measurement is not on-board	(Urms(1)) has been implemented; Urms(1) is compared with the event threshold to obtain event start, end and duration. An internal counter is incremented until Urms(1) value is below/above the threshold. Urms(1) measurement is used to store the residual/max. voltage
Harmonics	10÷100 % of harmonic limits, up to 40th order	200 ms (gaps allowed) ± 0.03% max. synchr. error (optional)	DFT / FFT t.i. synchronized to the power system frequency Rectangular window (Hanning in case of loss of synchronisation	Not on-board	New algorithm (see next)

As already mentioned, the EVLKSTCOMET10-1 uses a zero crossing method for measuring the signal period/frequency, therefore this value can be used for the synchronization of the observation window *Tw* of 10/12 cycles of the 50/60 Hz input signal, i.e. 200 ms. If the frequency is not 50 Hz, the window

would be greater or less than 200 ms. In accordance with [100] DFT/FFT algorithms have been evaluated for harmonic analysis. DFT can be performed with any number of samples N, but it has a higher computational cost ($O(N^2)$); on the other the FFT has a much lower computational cost ($O(NlogN)$), however it needs a number of samples equal to a power of 2 to be performed (i.e. N = 1024, 2048, etc). An analysis of the computational time required for the algorithm executions with STCOMET lead to choose FFT (DFT execution time was be not compatible with timing requirements for harmonic analysis even considering gaps).

To use the FFT the closest values for N should be 2048. On the other hand, the STCOMET has a fixed sampling frequency of 7812.5 Hz, then the acquisition of 2048 samples would lead to a not synchronous observation window (i.e. Tw = 2048 * 128 μs ≈ 262 ms ≠ 200 ms). Thus a time-domain interpolation algorithm has been implemented to obtain N = 2048 samples over the time interval of 10 cycles.

Figure 104**Errore. L'origine riferimento non è stata trovata.** shows a Flow Chart representing the operations of the algorithm implemented on STCOMET.

1. Starting from the measurement of the signal period Ts (carried out by STCOMET via zero-crossing, ZRC), an observation window equal to Tw = 10 Ts is set (for example, in the case of a 50 Hz signal, Ts = 20 ms, Tw = 200 ms).

2. The number of samples to be acquired and used for the algorithm is set: N = Tw * fs, where fs = 7812.5 Hz is the STCOMET sampling frequency (M = 1562.5 samples, rounding to the upper integer, i.e. 1563).

3. The time-domain interpolation of the acquired N samples is carried out to obtain 2048 samples for the FFT algorithm (in the implementation a simple linear interpolation algorithm was used, to minimize the computational cost). A virtual sampling frequency is determined, $fs\_virtual$, which, in the same observation window Tw, would lead to the acquisition of the aforesaid 2048 samples:

$$fs\_virtual = 2048/Tw$$

In the case of Tw = 200 ms, $fs\_virtual$ = 10240 Hz.

4. The FFT is calculated on the 2048 samples.

As regards the memory requirements, in the case of f = 50 Hz, Tw = 200 ms and fs = 7812.5 Hz, the number of samples acquired is $M = Tw/fs$ = 1563, so the number of bytes allocated in the STCOMET memory for samples storage is:

$$K = 1563 * 32 = 6.252\ kB$$

Considering that for the FFT calculation it is necessary to store 2048 samples (with both real and imaginary part), memory occupation is equal to 2048 * 32 * 2 = 16 kB. Furthermore, to allow the acquisition of samples of the subsequent observation window while performing the FFT calculation, it is necessary to instantiate a second register of 16 kB size. This was made in order to investigate the possibility of harmonic measurements without gaps between the observation windows. In summary, 32 kB are needed for samples storage and the FFT calculation algorithm; this requirement is compliant with STCOMET features, since the device has a RAM of 128 kB.
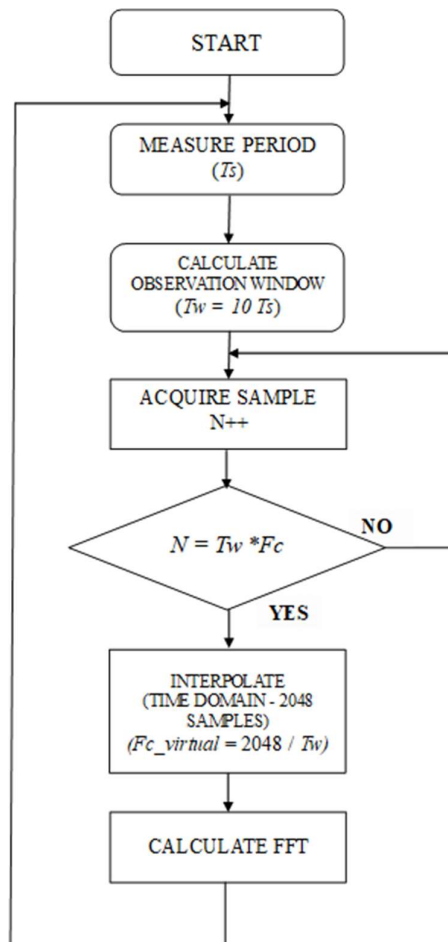
Figure 104 flow chart of the operation perfomed by STCOMET

A measuring test bench has been set up as shown in Figure 105. To evaluate the PQ metric performances, a calibrator was used as a reference for both voltage and current. The calibrator model used for experimental tests is the Fluke 6100A. Full accuracy specifications of the calibrator for PQ parameters are reported in the instrument manual. Main accuracy specifications for the tests herein presented are the following: 50 ppm for frequency (setting resolution of 0,1 Hz); up to $\pm$ (190 ppm of output + 33 mV) for frequencies from 16 to 850 Hz and $\pm$ (524 ppm of output + 33 mV) for frequencies from 850 Hz to 6 kHz for fundamental and harmonic voltage amplitudes, in the range from 70 to 1008 V; up to $\pm$ (267 ppm of output + 720 μA) and for frequencies from 16 to 850 Hz for fundamental and harmonic current amplitudes in the range from 2 to 21 A; up to 0.080° for current to voltage phase shift, for frequencies from 16 to 850 Hz and amplitudes from 0.5% to 40% of range. For the feasibility study presented in this work, the calibrator was assumed as reference for the STCOMET characterization; for each measured quantity, the measurement system error was calculated as the difference between the value set on the calibrator and that measured with STCOMET.

Voltage measurements were directly acquired. To investigate the impact of external measurement transducers, current measurement were carried out with and without an external current transformer (CT); in both cases the STCOMET current channel with internal shunt was used. The external current transformer is an open window CT used by Italian utilities to connect energy meters to low voltage distribution networks. The CT rated data are summarized in Table 28. The window diameter is 3 cm. The EVLKSTCOMET10-1 has been connected to a PC via USB JTAG J-linkOB. STCOMET has been programmed with both the corrected on board metrics and the harmonic analysis algorithm using IAR Embedded Workbench.

Tests were carried out reproducing different PQ phenomena (harmonics, dips, swells interruptions) and for different frequencies of the test signal (in the range of 42.5 ÷ 57.5 Hz). Some results for dips, swells and interruptions can be found in [102]. In the following sections, some results for frequency and voltage/current RMS and harmonics measurements are presented. For current measurements, both amplitudes and phase errors are shown.
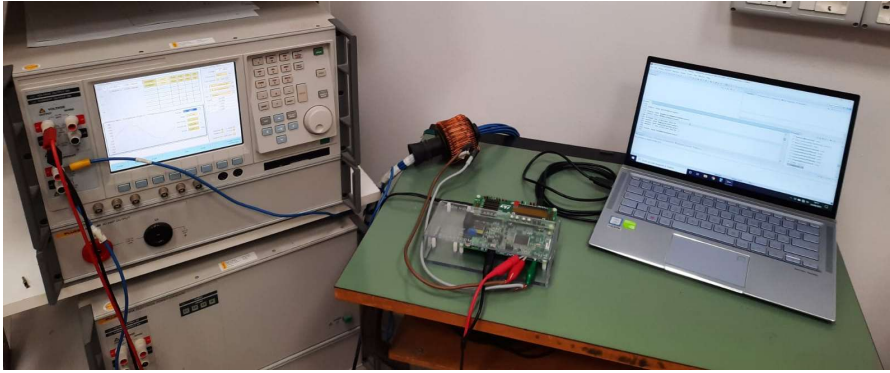
Figure 105 Test bench

Table 28 External current transformer rated data

	CT
Transformer ratio	125/5 A/A
Standard burden.	2.5 VA
Class	0.5
Rated Frequency	50 Hz
Rated voltage	400 V

Voltage measurements

Tests have been made in both sinusoidal and distorted conditions.

Results obtained with FFT algorithm are shown, together with RMS and frequency measurements; as already mentioned, errors between values generated by the calibrator and those measured by STCOMET are calculated and compared with IEC 61000-4-30 and IEC 61000-4-7 accuracy requirements. In more detail, calculated errors are listed in Table 29.

Table 29 error definitions

Parameter	Description
$E = |f_{FFT} - f_{gen}|$	Error, in mHz, on the frequency measurements both for fundamental and harmonics obtained via FFT

$$e\% = 100 * \frac{|V_{FFT} - V_{gen}|}{V_{gen}}$$

Percentage error on amplitude measurements obtained via FFT (fundamental and harmonics of amplitude greater than 3% of the rated voltage, *V_nom*, i.e. 230 V)

$$e\% = 100 * \frac{|V_{FFT} - V_{gen}|}{V_{nom}}$$

Percentage error on amplitude measurements obtained through FFT (harmonics of amplitude less than 3% of the nominal voltage *V_nom*)

where:

- f_{FFT} e V_{FFT} are frequency and amplitude (in RMS) measured by STCOMET (fundamental and harmonics);

- f_{gen} e V_{gen} are frequency and amplitude (in RMS) generated by the calibrator (fundamental and harmonics).

Some results of tests with sinusoidal voltage are reported in Table 30, for different frequency values (50 Hz, 42.5 Hz and 57.5 Hz). Figure 106, Figure 107 and Figure 108 show the spectra obtained at the three frequencies 50 Hz, 42.5 Hz and 57.5 Hz, respectively. The obtained errors are compatible with the limits set by IEC 61000-4-30 for class S instruments (equal to ± 50 mHz and ± 0.5% for frequency and RMS measurements, respectively).

Table 30 Voltage measurements in sinusoidal tests at different frequencies

Calibrator settings		STCOMET measurements and related errors			
		Output FFT			
f_gen (Hz)	V_gen (V)	f1_FFT (Hz)	E (mHz)	V1_FFT (V)	e%
50.0	230	50.0000	0.0	229.26	0.32
42.5	230	42.5025	2.5	229.28	0.31
57.5	230	57.524	24	229.27	0.31
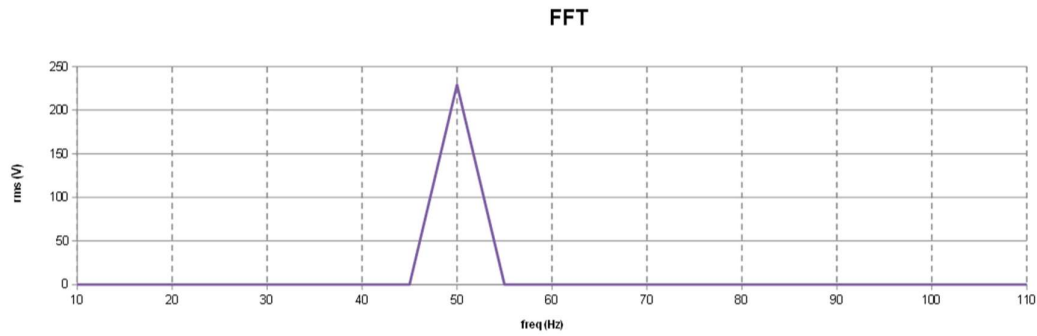
Figure 106 FFT plot values obtained with STCOMET using interpolation (V = 230V, f = 50Hz).
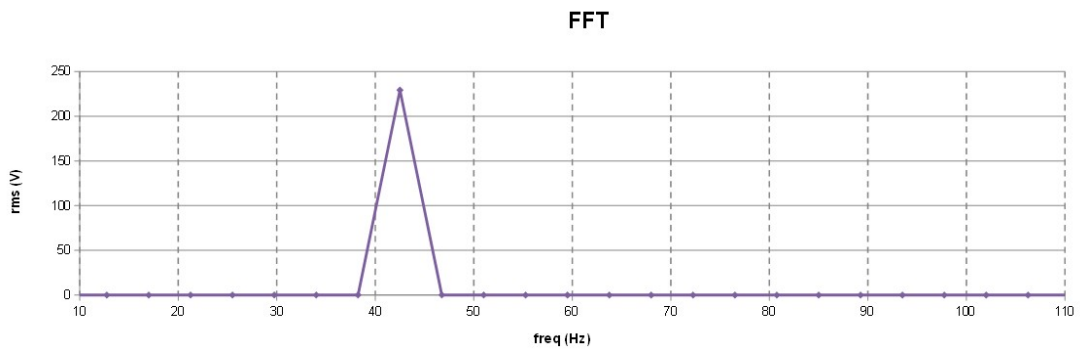
Figure 107 FFT plot values obtained with STCOMET using interpolation (V=230V, f=42.5Hz).
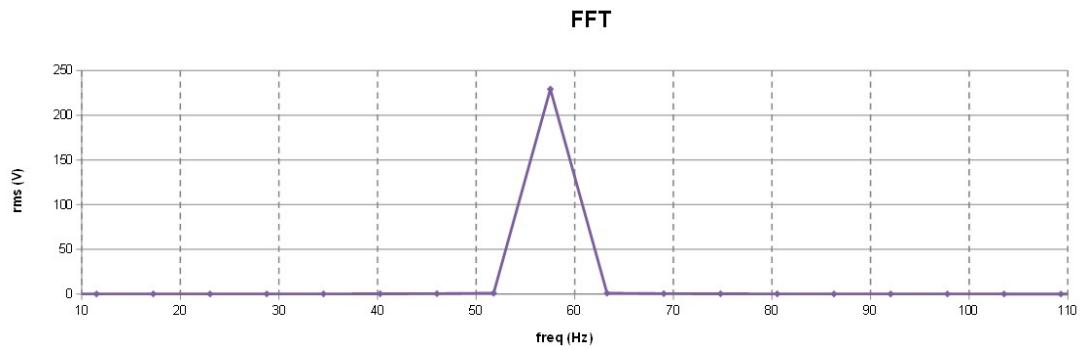
Figure 108 FFT plot values obtained with STCOMET using interpolation (V=230V, f=57.5Hz).

Further tests were performed with distorted voltage signals, with 25 harmonics, choosing the harmonic amplitudes equal to the limit values for electrical networks reported in CEI EN 50160 [15] and shown in Table 31. The voltage of the fundamental harmonic generated by the calibrator is V1=230 V, the RMS voltage is V=231.47 V. The tests were carried out for different frequency values.

Table 31 CEI EN 50160 - Harmonic voltages amplitudes at the power supply terminals (% of the fundamental voltage).

Odd Harmonics				Even Harmonics	
Non multiple of 3		Multiple of 3			
Harmonic order h	Relative Amplitude U_h	Harmonic order h	Relative Amplitude U_h	Harmonic order h	Relative Amplitude u_h
5	6.0%	3	5,0%	2	2.0%
7	5.0%	9	1.5%	4	1.0%
11	3.5%	15	0.5%	6…24	0.5%
13	3.0%	21	0.5%		
17	2.0%				
19	1.5%				
23	1.5%				
25	1.5%				

In Table 32 the results of the first test performed at a fundamental frequency $f_1 = 50$ Hz are reported. As can be seen the measurement results are within the class S requirements (for frequency also class A requirements are met).

Table 32 RMS and frequency measurement results. Distorted voltage signal with 25 harmonics, $f_1 = 50$ Hz

	Supply values	Measured Value	Error	Maximum error IEC 61000-4-30	Class A/S
RMS	231.47 [V]	230.70 [V]	0.33%	±0.5% U_{din}[1]	S
Frequency	50.0 [Hz]	50.0000 [Hz]	0.0 [mHz]	±10 mHz	A

[1] U_{din} is the declared supply voltage

The measured errors for each harmonic are reported in Table 33. Comparing these values with that of the limits reported in Table 31, it is possible to observe that the measuring system is compatible with the class II requirements (in some cases measurement results comply also with class I limits).

Table 33 FFT results. Distorted voltage signal with 25 harmonics; $f_1 = 50$ Hz

Harm	f_gen (Hz)	V_gen (V)	V_gen (%)	f_FFT (Hz)	E (mHz)	V_FFT (V)	Em (%)	En (%)	Class I limits	Class II limits	Class limits
1	50	230	100%	50.0000	0.0	229.25	0.33%	0.32%	TRUE	TRUE	I
2	100	4.6	2.0%	100.000	0.0	4.586	0.30%	0.006%	TRUE	TRUE	I
3	150	11.5	5.0%	150.000	0.0	11.460	0.35%	0.017%	TRUE	TRUE	I
4	200	2.3	1.0%	200.000	0.0	2.289	0.48%	0.005%	TRUE	TRUE	I
5	250	13.8	6.0%	250.000	0.0	13.705	0.69%	0.041%	TRUE	TRUE	I
6	300	1.15	0.5%	300.000	0.0	1.139	0.98%	0.005%	TRUE	TRUE	I
7	350	11.5	5.0%	350.000	0.0	11.38	1.0%	0.051%	TRUE	TRUE	I
8	400	1.15	0.5%	400.000	0.0	1.136	1.3%	0.006%	TRUE	TRUE	I
9	450	3.45	1.5%	450.000	0.0	3.402	1.4%	0.021%	TRUE	TRUE	I

10	500	1.15	0.5%	500.000	0.0	1.130	1.8%	0.009%	TRUE	TRUE	I
11	550	8.05	3.5%	550.000	0.0	7.890	2.0%	0.070%	TRUE	TRUE	I
12	600	1.15	0.5%	600.000	0.0	1.124	2.2%	0.011%	TRUE	TRUE	I
13	650	6.9	3.0%	650.000	0.0	6.720	2.6%	0.079%	TRUE	TRUE	I
14	700	1.15	0.5%	700.000	0.0	1.115	3.1%	0.015%	TRUE	TRUE	I
15	750	1.15	0.5%	750.000	0.0	1.113	3.2%	0.016%	TRUE	TRUE	I
16	800	1.15	0.5%	800.000	0.0	1.106	3.8%	0.019%	TRUE	TRUE	I
17	850	4.6	2.0%	850.000	0.0	4.40	4.3%	0.086%	TRUE	TRUE	I
18	900	1.15	0.5%	900.000	0.0	1.096	4.7%	0.023%	TRUE	TRUE	I
19	950	3.45	1.5%	950.000	0.0	3.27	5.2%	0.079%	FALSE	TRUE	II
20	1000	1.15	0.5%	1000.00	0.0	1.083	5.8%	0.029%	TRUE	TRUE	I
21	1050	1.15	0.5%	1050.00	0.0	1.078	6.2%	0.031%	TRUE	TRUE	I
22	1100	1.15	0.5%	1100.00	0.0	1.070	7.0%	0.035%	TRUE	TRUE	I
23	1150	3.45	1.5%	1150.00	0.0	3.19	7.6%	0.11%	FALSE	TRUE	II
24	1200	1.15	0.5%	1200.00	0.0	1.058	8.0%	0.040%	TRUE	TRUE	I
25	1250	3.45	1.5%	1250.00	0.0	3.15	8.8%	0.13%	FALSE	TRUE	II

- f_gen is the frequency generated by the calibrator

- V_gen is the voltage generated by the calibrator

- f_FFT is the frequency measured using the FFT algotithm

- E is the absolute error between f_FFT and f_gen expressed in mHz

- V_FFT is the measured voltage

- Em is the error on measured value calculated

- En is the error on nominal value

The same test with 25 harmonics was repeated for different signal frequencies. Some results are reported in the following tables for 42.5 Hz (see Table 34 and Table 35) and 57.5 Hz (see Table 36 and Table 37). Even in these cases, measurement results are within the class S maximum allowable errors for RMS and frequency and they are compatible with the class II requirements for harmonic measurements (for frequency also class A requirements are met and in many cases errors on harmonics are within class I limits).

Table 34 RMS and frequency measurement results. Distorted voltage signal with 25 harmonics, f_1= 42.5 Hz

	Supply values	Measured Value	Error with respect to the calibrator	Maximum error IEC 61000-4-30	Class A/S
RMS	231.47 [V]	230.66 [V]	0.35 %	±0.5 % U_{din}	S
Frequency	42.5 [Hz]	42.5025 [Hz]	2.5 mHz	±10 mHz	A

Table 35 FFT results. Distorted voltage signal with 25 harmonics, f_1 = 42.5 Hz

Harm	f_gen (Hz)	V_gen (V)	V_gen (%)	f_FFT (Hz)	E (mHz)	V_FFT (V)	Em (%)	En (%)	Class I limits	Class II limits	Class limits
1	42.5	230	100%	42.5026	2.6	229.33	0.29%	0.289%	TRUE	TRUE	I
2	85	4.6	2.0%	85.0051	5.1	4.588	0.26%	0.005%	TRUE	TRUE	I
3	127.5	11.5	5.0%	127.508	7.7	11.462	0.33%	0.016%	TRUE	TRUE	I
4	170	2.3	1.0%	170.010	10	2.290	0.46%	0.005%	TRUE	TRUE	I
5	212.5	13.8	6.0%	212.513	13	13.726	0.53%	0.032%	TRUE	TRUE	I
6	255	1.15	0.5%	255.015	15	1.1435	0.56%	0.003%	TRUE	TRUE	I

7	297.5	11.5	5.0%	297.518	18	11.408	0.80%	0.040%	TRUE	TRUE	I
8	340	1.15	0.5%	340.020	20	1.1423	0.67%	0.003%	TRUE	TRUE	I
9	382.5	3.45	1.5%	382.523	23	3.415	1.0%	0.015%	TRUE	TRUE	I
10	425	1.15	0.5%	425.026	26	1.138	1.1%	0.005%	TRUE	TRUE	I
11	467.5	8.05	3.5%	467.528	28	7.93	1.5%	0.051%	TRUE	TRUE	I
12	510	1.15	0.5%	510.031	31	1.131	1.7%	0.008%	TRUE	TRUE	I
13	552.5	6.9	3.0%	552.533	33	6.76	2.0%	0.061%	TRUE	TRUE	I
14	595	1.15	0.5%	595.036	36	1.126	2.1%	0.010%	TRUE	TRUE	I
15	637.5	1.15	0.5%	637.538	38	1.122	2.4%	0.012%	TRUE	TRUE	I
16	680	1.15	0.5%	680.041	41	1.118	2.8%	0.014%	TRUE	TRUE	I
17	722.5	4.6	2.0%	722.543	43	4.47	2.9%	0.058%	TRUE	TRUE	I
18	765	1.15	0.5%	765.046	46	1.114	3.1%	0.016%	TRUE	TRUE	I
19	807.5	3.45	1.5%	807.548	48	3.32	3.7%	0.055%	TRUE	TRUE	I
20	850	1.15	0.5%	850.051	51	1.103	4.0%	0.020%	TRUE	TRUE	I
21	892.5	1.15	0.5%	892.554	54	1.101	4.3%	0.021%	TRUE	TRUE	I
22	935	1.15	0.5%	935.056	56	1.094	4.9%	0.024%	TRUE	TRUE	I
23	977.5	3.45	1.5%	977.559	59	3.27	5.2%	0.079%	FALSE	TRUE	II
24	1020	1.15	0.5%	1020.061	61	1.083	5.9%	0.029%	TRUE	TRUE	I
25	1063	3.45	1.5%	1062.564	64	3.23	6.4%	0.095%	FALSE	TRUE	II

Table 36 RMS and frequency measurement results. Distorted voltage signal with 25 harmonics, f_1= 57.5Hz

	Supply values	Measured Value	Error with respect to the calibrator	Maximum error IEC 61000-4-30	Class A/S
RMS	231.47 [V]	230.70 [V]	0.33%	$\pm 0.5\%\ U_{din}$	S
Frequency	57.5 [Hz]	57.4977 [Hz]	2.3mHz	± 10mHz	A

Table 37 FFT results. Distorted voltage signal with 25 harmonics, f_1 = 57.5 Hz

Harm	f_gen (Hz)	V_gen (V)	V_gen (%)	f_FFT (Hz)	E (mHz)	V_FFT (V)	Em (%)	En (%)	Class I limits	Class II limits	Class limits
1	57.5	230	100%	57.4977	2.3	229.31	0.30%	0.300%	TRUE	TRUE	I
2	115	4.6	2.0%	114.9954	4.6	4.585	0.32%	0.006%	TRUE	TRUE	I
3	172.5	11.5	5.0%	172.4931	6.9	11.454	0.40%	0.020%	TRUE	TRUE	I
4	230	2.3	1.0%	229.9908	9.2	2.288	0.52%	0.005%	TRUE	TRUE	I
5	287.5	13.8	6.0%	287.489	12	13.69	0.81%	0.049%	TRUE	TRUE	I
6	345	1.15	0.5%	344.986	14	1.139	0.93%	0.005%	TRUE	TRUE	I
7	402.5	11.5	5.0%	402.484	16	11.36	1.2%	0.062%	TRUE	TRUE	I
8	460	1.15	0.5%	459.982	18	1.132	1.6%	0.008%	TRUE	TRUE	I
9	517.5	3.45	1.5%	517.479	21	3.384	1.9%	0.029%	TRUE	TRUE	I
10	575	1.15	0.5%	574.977	23	1.124	2.2%	0.011%	TRUE	TRUE	I
11	632.5	8.05	3.5%	632.475	25	7.84	2.6%	0.091%	TRUE	TRUE	I

12	690	1.15	0.5%	689.972	28	1.116	3.0%	0.015%	TRUE	TRUE	I
13	747.5	6.9	3.0%	747.470	30	6.66	3.4%	0.10%	TRUE	TRUE	I
14	805	1.15	0.5%	804.968	32	1.10	4.1%	0.021%	TRUE	TRUE	I
15	862.5	1.15	0.5%	862.466	35	1.09	5.2%	0.026%	TRUE	TRUE	I
16	920	1.15	0.5%	919.963	37	1.09	5.1%	0.025%	TRUE	TRUE	I
17	977.5	4.6	2.0%	977.461	39	4.34	5.7%	0.11%	FALSE	TRUE	II
18	1035	1.15	0.5%	1034.959	41	1.07	6.5%	0.032%	TRUE	TRUE	I
19	1093	3.45	1.5%	1092.456	44	3.21	6.9%	0.10%	FALSE	TRUE	II
20	1150	1.15	0.5%	1149.954	46	1.06	7.8%	0.039%	TRUE	TRUE	I
21	1208	1.15	0.5%	1207.452	48	1.05	9.0%	0.045%	TRUE	TRUE	I
22	1265	1.15	0.5%	1264.949	51	1.04	9.3%	0.046%	TRUE	TRUE	I
23	1323	3.45	1.5%	1322.447	53	3.10	10%	0.15%	FALSE	TRUE	II
24	1380	1.15	0.5%	1379.945	55	1.03	10%	0.053%	TRUE	TRUE	I
25	1438	3.45	1.5%	1437.443	58	3.05	11%	0.17%	FALSE	TRUE	II

Further tests were carried out by changing the phase shift between harmonic and fundamental components of the voltage test signal. This allowed investigating the influence of harmonic phase shift, which can negatively affect the measurement accuracy, especially in the presence of measurement transducers. Tests herein presented were performed with a distorted voltage with fundamental frequency f_1 = 50 Hz, fundamental amplitude V_1 = 230V and four harmonics, i.e. the II, III, VI, and XI order harmonic. Each harmonic has amplitude equal to 10% of the fundamental. For each harmonic, phase shift with respect to the fundamental harmonic was changed from -180° to + 180°, with steps of 30°. Table 38 and Table 39 show amplitude and phase errors in harmonic voltage measurements, respectively. The proposed measurement system complies with class I requirements.

Table 38 Voltage module error for II, IV, VI, XI harmonic

Phase/Arm	Amplitude Error		
	Min	Max	Average
II	0.013%	0.13%	0.071%
III	0.001%	0.12%	0.047%
VI	0.084%	0.12%	0.11%
XI	0.12%	0.32%	0.27%

Table 39 Voltage phase error for II, IV, VI, XI harmonic

Phase/Arm	Phase Error [deg]		
	Min	Max	Average
II	0.089	0.15	0.12
III	0.028	0.088	0.043
VI	0.065	0.11	0.086
XI	0.089	0.14	0.12

Current measurements

The tests made for voltage were repeated also for currents. As regards RMS and FFT measurements the results obtained were similar to those obtained for voltage measurements.

As regards the tests with harmonics and different phase phase-shifts between harmonic and fundamental components of current, they were carried out using the STCOMET current input channel, both with and without the external CT; this was made in order to investigate not only the STCOMET behaviour but also the external CT influence on the measurement results. Tests herein presented were carried out at 50 Hz, with fundamental current amplitude I_1 = 5A; II, III, VI, and XI harmonics have

been considered, with amplitude equal to the 10% of fundamental current and variable phase shift from -180° to + 180°, with steps of 30°.

Table 40 and Table 41 show amplitude and phase errors in harmonic current measurements, respectively, for the tests without the external CT. Also in this case, the proposed measurement system complies with class I requirements.

Table 40 Current amplitude error for II, IV, VI, XI harmonic

	Amplitude Error		
Phase/Arm	Min	Max	Average
II	0.087%	0.31%	0.21%
III	0.073%	0.53%	0.28%
VI	0.020%	0.5%	0.32%
XI	0.039%	1.12%	0.27%

Table 41 Current phase error for II, IV, VI, XI harmonic

	Phase Error [deg]		
Phase/Arm	Min	Max	Average
II	0.050	0.31	0.18
III	0.015	0.25	0.096
VI	0.001	0.13	0.062
XI	0.024	0.24	0.11

The aforesaid tests were repeated by inserting the external CT, whose secondary winding was connected to the on-board shunt (see test bench of Figure 105). To obtain the rated current (125 A), a 10 turns primary winding was set up. Each turn had a very large diameter compared to the CT window diameter. Moreover, the 10 loops of the winding were wounded in a compact group, with a small section compared to the CT window area. In this way the current generated by the calibrator was 12.5 A and it had the same magnetic effects as 125 A equivalent current flowing in a single cable.

Table 42 and Table 43 show amplitude and phase errors in current measurements, respectively. Measured errors are higher in comparison to those of Table 40 and Table 41 because they are strongly influenced by the CT behaviour. Moreover, they have a large variability with harmonic phase shift with respect to fundamental. This behaviour agrees with what was found in previous works on the CT metrological performances in distorted conditions [103].

Table 42 Current amplitude error for II, IV, VI, XI harmonic

	Amplitude Error		
Phase/Arm	Min	Max	Average
II	0.57%	1.6%	1.1%
III	0.49%	1.7%	0.96%
VI	0.29%	2.0%	1.0%
XI	0.16%	1.4%	0.73%

Table 43 Current phase error for II, IV, VI, XI harmonic

	Current Phase Error		
Phase/Arm	Min	Max	Average
II	0.017	0.38	0.25

III	0.019	0.44	0.29
VI	0.065	1.8	0.96
XI	0.98	2.4	1.8

Decision strategy based on power ratio approach

This section discuss a possible solution about using a decision making strategy to solve the problem related to a threshold able to establish if the harmonic source is coming from one node or another based on power ratios. Starting from an analysis of the criticalities found in the use of the indicators proposed by the standard for the assessment of harmonic distortion, the authors proposed three new power factor indicators: P_1/S, S_1/S and Q_1/N. With these indicators, the authors showed that it is possible, starting from simple measures, to obtain more comprehensive information both on the level of harmonic pollution of the network and on the origin of this distortion.

The first indicator, P_1/S, has the same structure of the power factor but instead of the active power P, the fundamental active power P_1 is compared with S to evaluate the real utilization of the line; in fact, the useful quantity of power for a load is the non-distorted power i.e., the fundamental.

The ratio S_1/S allows evaluating the whole harmonic emission level, with respect to both active and reactive power components; in purely sinusoidal conditions, $S_1/S = 1$, unlike S_N/S_1 that assumes the value 0 and that cannot be accurately measured.

About last indicator Q_1/N, in previous papers [104], [105] the authors showed that the non-active powers behavior depends on the load nature (linear or nonlinear), therefore, this parameter is suitable identifying the distorting loads. Q_1 is the fundamental nonactive power [VAR], N is the nonactive power [VAR].

It is structured like the PF, that is as a ratio between the useful component of power (in this case reactive) and the total power, approaching to 1 when the system tends to be purely sinusoidal. In non-sinusoidal conditions, Q_1 is lower than N and the ratio between the two quantities is lower than 1.

This indicator has been shown to be the most sensitive to distortion phenomena and one of the most accurate to be measured. Not less important, the nature of the quantities considered Q_1 and N is such as to make this indicator adequate to quantify the distortion even in points of the network that are most affected by the presence of power factor correction capacitors which are precisely related to reactive power

By means of several simulations, the authors have defined a strategy, based on the values assumed by some of the proposed indicators, which allows determining the presence of harmonic pollution sources downstream of the measurement point. In a flow chart of the strategy suggested is reported. Power quantities, obtained from voltage and current measurements at every point of common coupling (PCC), are combined to determinate the values of $S_1/S, Q_1/N, PF_1 = P_1/S_1$ and P_1/S. Proposed strategy provides for compliance with 3 conditions shown in Table 44.

Table 44 Proposed conditions identifying harmonic distortion sources

N.	Condition
1	$S_1/S < 1$
2	$Q_1/N < 0.95$
3	$PF_1 > P_1/S$

The first condition, if verified, reports the presence of harmonic distortion at the PCC; in fact, the indicator concerns the completely harmonic emission level, with respect to both active and reactive power components. However, the fulfillment of this condition alone does not guarantee the detection of a distorting load. So, this indicator is used as a threshold for activating the strategy; it establishes the presence of distortion at the point of measurement, but not the presence of a source of distortion at that point.

Condition 2 is based on the meaning of the reactive power for the harmonic distortion detection; in fact, it depends on the nature of the load. A value of Q_1 different than N implies a nonfundamental reactive power component; the ratio between Q_1 and N less than 0.95 is an indicator of harmonic distortion and of the presence of a non-linear load.

Condition 3 compares two parameters used for evaluating the line utilization but considering the physics nature of the quantities. In absence of distortion, $S_1 = S$ and $PF_1 = P_1/S$; in distorting condition, the value of S_1 is lower than S and the condition 3 is verified.

The last two conditions must be checked simultaneously and indicate the existence of one or more distorting loads at the considered PCC.

Below some significant results obtained from simulations on the benchmark test system described before under different conditions (presence of non-linear loads, absence and presence of unbalance) are reported.

There are two advantages of using this strategy. The first is that the quantities required are easy to be measured and most of the measurement systems already widespread on the network are able to measure these quantities. The second one lies in the fact that all three conditions are unlikely to occur simultaneously except in case of the presence of harmonic distortion source downstream the PCC considered.
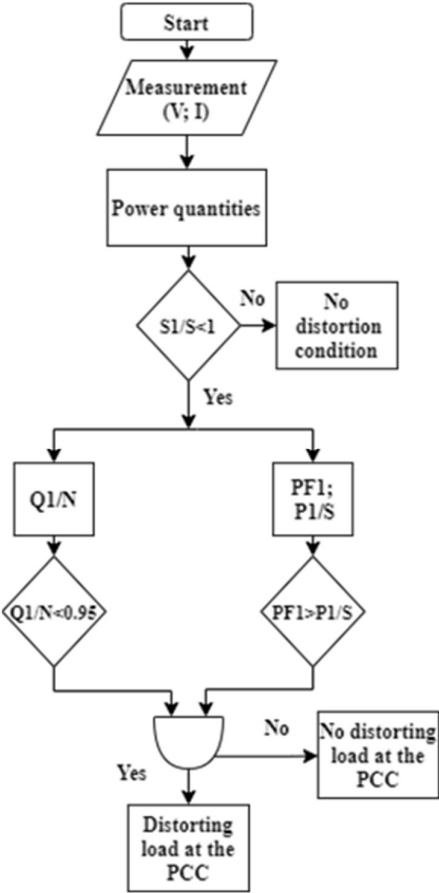
Figure 109 flowchart of the proposed strategy

Case studies

To test the proposed strategy, different simulations were carried out with the Simulink software, starting from the case proposed (base case) and gradually modifying the system architecture, in order to observe the behavior of the indicators in different conditions (with and without unbalance, with only one or more harmonic sources both on LV and MV side, and so on). Five scenarios were analyzed corresponding to the following cases:

- Case A – Base case;

- Case B – LOAD 1 replaced by an equivalent linear load;

- Case C – Base case with no compensators at PCC1 and PCC3

- Case D – LOAD 2 replaced by an equivalent linear load; LOAD 3 is unbalanced

- Case E – LOAD 1 and LOAD 2 replaced by equivalent linear loads; LOAD 3 is unbalance.

For every case, the value of all the proposed indicators were analyzed and compared to the ones introduced by the IEEE Std. 1459. In the following are reported the results obtained.

Base case

Case A represents the base case, in which there are two low-voltage non-linear loads (LOAD 1 and LOAD 2).

Values assumed by indicators

	MV	MV Load	Pcc 1	Pcc 2	Load 2	Load 3	Pcc 3
■ PF1=P1/S1	0,992	0,961	0,978	0,990	0,919	0,934	0,971
▫ P1/S	0,992	0,961	0,910	0,987	0,894	0,919	0,971
▫ S1/S	1,000	1,000	0,930	0,996	0,973	0,984	1,000
■ Q1/N	0,989	1,000	0,463	0,850	0,857	0,895	0,999
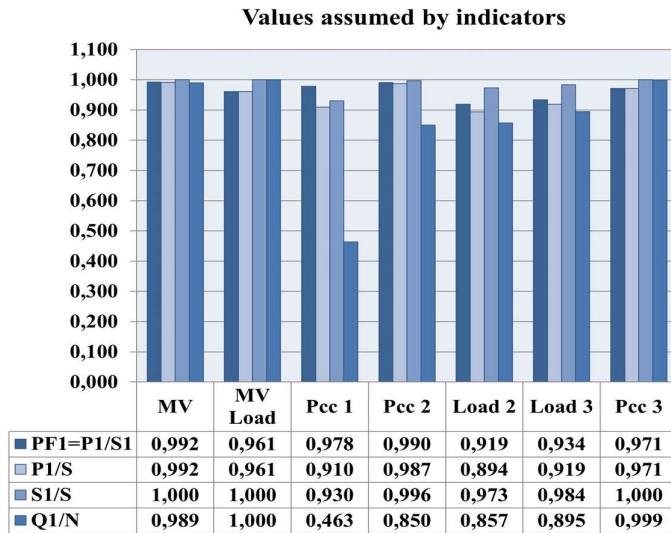
Figure 110 Values assumed by indicators in Case A simulation

Table 45 Result check – case A

Measurement point	Condition	outcome
PCC1	$S_1/S < 1$	*yes*
	$Q_1/N < 0.95$	*yes*
	$PF_1 > P_1/S$	*yes*
PCC2	$S_1/S < 1$	*yes*
	$Q_1/N < 0.95$	*yes*
	$PF_1 > P_1/S$	*yes*
PCC3	$S_1/S < 1$	*no*
	$Q_1/N < 0.95$	*no*
	$PF_1 > P_1/S$	*no*

As visible in Figure 110, lower values of Q_1/N are in correspondence of PCC1 and PCC2, while the ratio is almost equal to 1 at PCC3. S_1/S is lower than 1 both at PCC1 and PCC2. According to Table

45, considering the values of PF_1 and P_1/S too, the strategy confirms the presence of distorting loads both at PCC1 and PCC2, as expected.

LOAD 1 replaced by an equivalent linear load

In Case B the non-linear load LOAD 1(three-phase thyristor rectifier; P = 214.5 kW, N = 98.48 kVAR) has been replaced by an equivalent linear load (symmetrical load comprised of a parallel resistor and inductor in the wye connection; R = 0.66 Ω, L = 3.2 mH). The values of the parameters have been chosen in order to keep the absorbed power values constant at the point of common coupling PCC1. The only non-linear load is LOAD 2.

Values assumed by indicators

	MV	MV Load	Pcc 1	Pcc 2	Load 2	Load 3	Pcc 3
■ PF1=P1/S1	0,991	0,961	0,909	0,990	0,919	0,919	0,971
□ P1/S	0,991	0,961	0,909	0,987	0,894	0,919	0,971
■ S1/S	1,000	1,000	1,000	0,996	0,973	1,000	1,000
■ Q1/N	0,999	1,000	0,999	0,841	0,858	1,000	1,000

Figure 111 Values assumed by indicators in Case B simulation
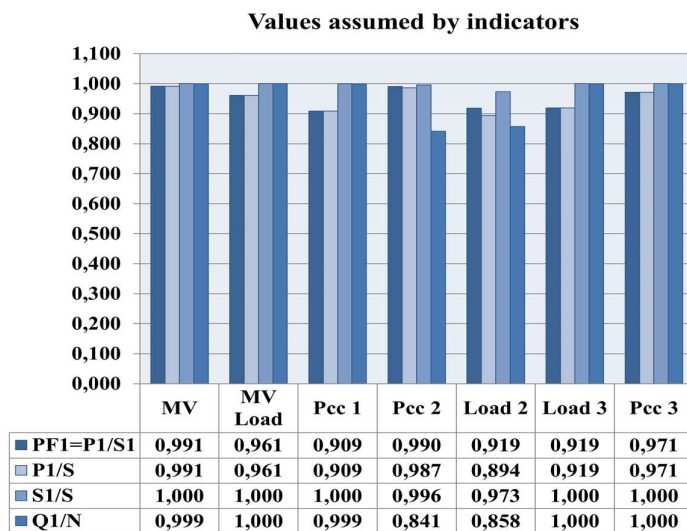
Table 46 Result check – case B

Measurement point	Condition	outcome
PCC1	$S_1/S < 1$	no
	$Q_1/N < 0.95$	no

	$PF_1 > P_1/S$	*no*
PCC2	$S_1/S < 1$	*yes*
	$Q_1/N < 0.95$	*yes*
	$PF_1 > P_1/S$	*yes*
PCC3	$S_1/S < 1$	*no*
	$Q_1/N < 0.95$	*no*
	$PF_1 > P_1/S$	*no*

Removing the non-linear load at PCC1, the only harmonic source remains the three-phase rectifier (LOAD 2) connected at PCC2. The results show that the ratio S_1/S is equal to 1 at PCC1 and a value of Q_1/N at the same measurement point is almost equal to 1. The PF_1 decreased from 0.978 to 0.909 but is equal to PF.

For PCC2 the values of the indicators are approximately the same of case A. The same is for the indicators at PCC3.

According to Table 46, the strategy confirms the presence of a distorting load at PCC2.

Base case with no compensators at PCC1 and PCC3

In Case C the capacitors at PCC1 and PCC3 are removed in order to study the effects of the capacitors banks on harmonic pollution. Compensators in the considered PCCs are used only to correct the power factor and have non-linear nature, so their behavior amplifies distortion.
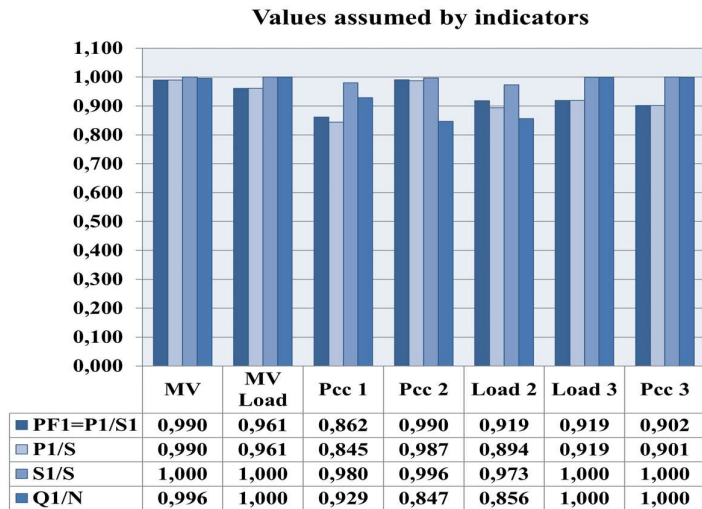
Values assumed by indicators

	MV	MV Load	Pcc 1	Pcc 2	Load 2	Load 3	Pcc 3
PF1=P1/S1	0,990	0,961	0,862	0,990	0,919	0,919	0,902
P1/S	0,990	0,961	0,845	0,987	0,894	0,919	0,901
S1/S	1,000	1,000	0,980	0,996	0,973	1,000	1,000
Q1/N	0,996	1,000	0,929	0,847	0,856	1,000	1,000

Figure 112 Values assumed by indicators in Case C simulation

Table 47 Result check – case C

Measurement point	Condition	*outcome*
PCC1	$S_1/S < 1$	*yes*
	$Q_1/N < 0.95$	*yes*
	$PF_1 > P_1/S$	*yes*
PCC2	$S_1/S < 1$	*yes*
	$Q_1/N < 0.95$	*yes*
	$PF_1 > P_1/S$	*yes*
PCC3	$S_1/S < 1$	*no*
	$Q_1/N < 0.95$	*no*
	$PF_1 > P_1/S$	*yes*

As visible in Figure 111, the values of PF and PF_1 at PCC1 and PCC3 in Case C are lower than the same indicators in Case A; the same is for P_1/S. This is obliviously a consequence of the absence of

capacitors banks. The indicator Q_1/N at PCC1, on the contrary, has more than doubled its value. At PCC3 the same indicator value in this case is 1. The indicator S_1/S, that quantify the total power distortion, has increased his value too, at PCC1, passing from 0.93 in Case A to 0.98 in case C. The total distortion is lower than in Case A, showing the negative influence of capacitors on harmonic pollution.

Even in absence of capacitors banks, the strategy confirms the presences of distorting loads both at PCC1 and PCC2.

LOAD 2 replaced by an equivalent linear load; LOAD 3 is unbalanced

In Case D the non-linear load LOAD 2 (three-phase thyristor rectifier; P = 258.8 kW, N = 130 kVAR) has been replaced by an equivalent linear load (symmetrical load comprised of a parallel resistor and inductor in the wye connection; R = 0.99 Ω, L = 8.8 mH). The values of the parameters have been chosen in order to keep the absorbed power values constant at the point of common coupling PCC2. The only non-linear load is LOAD 1. Furthermore, the RL three-phase load LOAD 3 has been replaced by an equivalent unbalanced load (in which the values of the resistances and inductances on phase 1 on phase 3 have been varied respectively by +10% and -10% with respect to the nominal values, which remain unchanged on phase 2. The measurement of the overall unbalance (in current) on the load is equal to 3%.
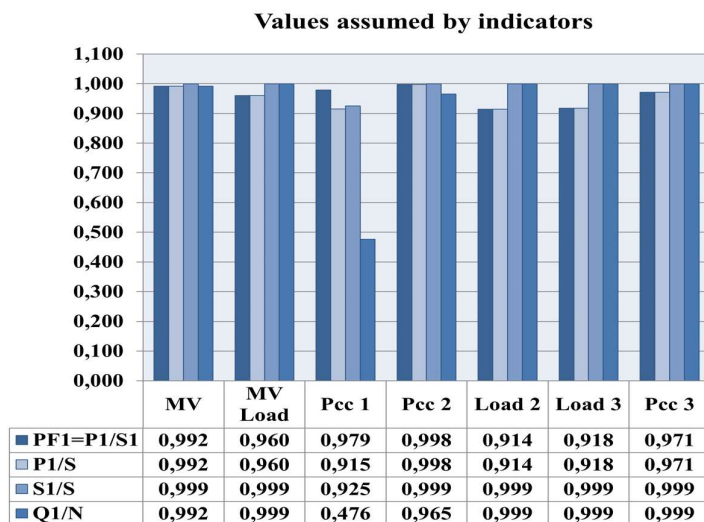
Values assumed by indicators

	MV	MV Load	Pcc 1	Pcc 2	Load 2	Load 3	Pcc 3
■ PF1=P1/S1	0,992	0,960	0,979	0,998	0,914	0,918	0,971
▫ P1/S	0,992	0,960	0,915	0,998	0,914	0,918	0,971
■ S1/S	0,999	0,999	0,925	0,999	0,999	0,999	0,999
■ Q1/N	0,992	0,999	0,476	0,965	0,999	0,999	0,999

Figure 113 Values assumed by indicators in Case D simulation

Table 48 Result check – case D

Measurement point	Condition	*outcome*
PCC1	$S_1/S < 1$	*yes*
	$Q_1/N < 0.95$	*yes*
	$PF_1 > P_1/S$	*yes*
PCC2	$S_1/S < 1$	*yes*
	$Q_1/N < 0.95$	*no*
	$PF_1 > P_1/S$	*no*
PCC3	$S_1/S < 1$	*yes*
	$Q_1/N < 0.95$	*no*
	$PF_1 > P_1/S$	*no*

LOAD 2 has been replaced with a symmetrical load comprised of a parallel resistor and inductor; the only harmonic source in the test system is the three-phase rectifier connected at PCC1.

At PCC2 the value of S_1/S is less than one; this implies harmonic pollution on the line at the PCC considered, but the values of Q_1/N, PF_1 and PF do not verify the condition 2 and 3 of the strategy. LOAD 2 is a linear load and can't be a source of harmonic distortion, so the strategy works correctly.

For PCC3 the same consideration can be made.

The strategy, according with Table 48, confirms the presence of a distorting load at PCC1.

LOAD 1 and LOAD 2 replaced by equivalent linear loads; LOAD 3 is unbalance

In Case E the non-linear loads LOAD 1 and LOAD 2 have been replaced by equivalent linear loads (symmetrical load comprised of a parallel resistor and inductor in the wye connection) as reported

before for case B and D. Furthermore, the RL three-phase load LOAD 3 has been replaced by an equivalent unbalanced load as reported in case D.
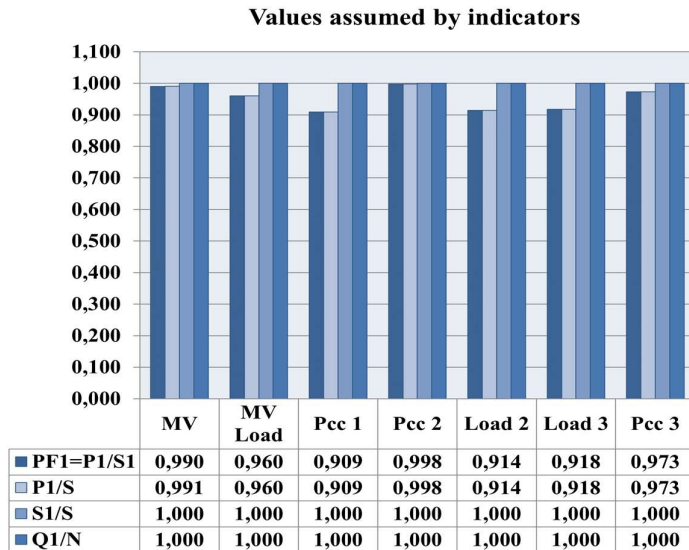

Values assumed by indicators

	MV	MV Load	Pcc 1	Pcc 2	Load 2	Load 3	Pcc 3
PF1=P1/S1	0,990	0,960	0,909	0,998	0,914	0,918	0,973
P1/S	0,991	0,960	0,909	0,998	0,914	0,918	0,973
S1/S	1,000	1,000	1,000	1,000	1,000	1,000	1,000
Q1/N	1,000	1,000	1,000	1,000	1,000	1,000	1,000

Figure 114 Values assumed by indicators in Case E simulation

Table 49 Result check – case E

Measurement point	Condition	*outcome*
PCC1	$S_1/S < 1$	*no*
	$Q_1/N < 0.95$	*no*
	$PF_1 > P_1/S$	*no*
PCC2	$S_1/S < 1$	*no*
	$Q_1/N < 0.95$	*no*
	$PF_1 > P_1/S$	*no*
PCC3	$S_1/S < 1$	*no*
	$Q_1/N < 0.95$	*no*

	$PF_1 > P_1/S$	*no*

In the test system there are no non-linear loads, i.e., distorting loads. PF_1 and P_1/S have the same values for every PCC; in the same way, the Q_1/N ratio is equal to 1. The ratio S_N/S_1 is 0.025 and for PCC1 and is 0 for both PCC2 and PCC3; the strategy shows the absence of harmonic sources.

Conclusion to harmonic power quality assessment

This chapter shown new indicators based on active and reactive power decomposition according to IEEE 1459-2010. It was shown how these indicators can be applied for harmonic power quality assessment and for future billing strategy. It was also shown how the metrics of this strategy can be easily implemented in low-cost smart meter platform. In the final part, author proposed a new strategy for the localization of harmonic distortion sources, based on the evaluation of simplified indicators.

Several simulations conducted on a Benchmarck Test System to test the proposed strategy are reported. The simulations were carried out on different scenarios: presence of non-linear loads, presence of capacitors banks and unbalance condition, to test the strategy in different situation.

The results show that with the proposed strategy is possible to detect the presence of harmonic source at the PCC even if there is more than one source in the network or in presence of unbalanced loads. Furthermore, using three and not only one conditions, the strategy is able to exclude the presence of harmonic sources at the measurement point considered even if the voltage is distorted because of sources not directly connected at the PCC.

4. DC Fault Characterization and Diagnostic

Through the knowledge of digital signal processing acquired with the studies on AC power quality, it was possible to approach one of the problems that affect the direct current system. As said in the introduction, DC systems doesn't suffer of power quality deterioration but circuit faults can appear anyway. In this framework a very important issue is the detection of arc faults occurrence [106], [107]. Specifically, arc faults are unintentional arcing conditions which may lead to fire ignition, unless they are promptly detected and extinguished by de-energizing the electrical circuit. The arc fault phenomenon can occur in both AC and DC electrical circuits. In PV systems, arc faults events can happen, due to various reasons, such as worn electrical insulation, components aging, stress, overheat or damaged wires and connectors. Arc faults can be basically classified in series arcs and parallel arcs [108]. Series arcs are due to a loss of continuity of a conductor, connection, module or other PV system components, while parallel arcs occur between two conductors or between a conductor and ground. Typically, series arcs detection is more challenging than parallel arcs detection. In fact, parallel arcs behaves as a sort of short-circuit and they are characterized by levels of current higher than the normal one; on the other hand, in the case of a series arc, the current amount is limited by the load of the PV system components themselves, thus normal and arcing current amplitudes can be very similar. Furthermore, the arc fault phenomenon is intrinsically random and intermittent; during a fault event, normal and arcing current portions can follow each other in the current waveform; the arcing signal can be also filtered, masked or attenuated because of several factors, such as inverter distortion and noise or PV system topology, health and operating conditions, which can modify the arcing signal waveform and characteristics. Due to these reasons, the arcing condition may go undetected or a normal operating condition can be mistaken for an arcing one.

At regulatory level, in order to protect against fire risk due to arcing occurrence, arc-fault circuit interrupters (AFCIs) have been introduced also for PV systems, as previously done for AC applications in dwelling units [108]. Since 2011, the U.S. National Electrical Code (NEC) requires that all PV systems with DC circuits operating at 80 V or greater on a building must be protected by AFCIs [109]. The Standard UL 1699B was then introduced in 2012 and further updated on 2018. It covers requirements for DC PV arc fault circuit protection devices with rated voltage of 1500 V or less. These requirements cover devices including PV AFCIs, arc fault detectors (AFDs), interrupting devices and inverter, converters and charge controllers with integrated arc fault circuit protection. The Standard provides both construction and performance requirements, including arc fault detection tests, "unwanted tripping" tests and related risk analysis, in order to cope with situations in which the AFCI

may not trip even if an arc fault is present (trip failure), or it may trip, even when an arc is not present (unwanted trip). On the other hand, the Standard does not provide any specific requirement on the arc fault detection methodology.

As regards the arcing current characteristics, there are some important features in both AC and DC arcs. In AC systems, a typical arcing current is characterized by some distinctive features, such as "shoulders" (i.e. nearly flat zero-current segments in each half cycle, as current extinguishes before and reignites after the normal zero-crossing), high rates of rise and peaks, high-frequency broadband noise (from tens of kilohertz to about 1 GHz), non-stationarity. Such characteristics can be more or less distinguishable, depending on load conditions; for example, in the presence of masking loads, normal current can be very similar to that of an arcing condition and thus arc detection can be more difficult [24]. In comparison with AC phenomenon, a DC arc does not have zero crossing segments, thus it can be more persistent. Broadband noise remains a prominent characteristic of a DC arc (up to about 1 MHz). Typically, due to the inductive behavior of cables, the noise level decreases as frequency increases. As already mentioned, DC arc characteristics can be affected by noisy conditions and disturbances due to the normal operation of the electric system [110]–[115]. Generally speaking, arc noise and variation depend on a lot of factors, such as electric circuit materials and topologies, voltage and current level, load and supply characteristics. Cables length can act as an antenna, introducing noise in the frequency band of hundreds of kilohertz. Crosstalk effects and power electronic components can introduce harmonics and high frequency noise. Current steps and variations due to load shifting, inverter power adjustment or environmental phenomena (fast moving clouds, wind vibrations, etc.) can determine current waveforms similar to arc faults.

Several papers and patents can be found in literature concerning arc fault detection in AC systems[24], and the research on DC arc faults is ongoing too, concerning both DC arc fault modeling and detection methods [116]–[119]. More or less realistic arc fault models have been introduced to develop and verify in simulation the arc fault detection methodologies. They can be classified in physics-based models (i.e. based on physical principles), V-I empirical models (i.e. obtained from experimental measurements) and heuristic models (which include additional parameters in the model to better correlate simulation and experimental data). Some of them can be usefully applied for applications on PV arc faults. However, even if such models can be useful for preliminary arc fault detection studies, they have some limitations due to implementation difficulties, validity ranges (in terms of arc type, current level or arc length), as well as for characterization of data acquisition and signal processing techniques, where real measurement issues should be taken into account (such as sampling requirements or computational burden, as well as accuracy features). Thus experimental studies are

needed, in order to reproduce real arcing conditions, as well as to test real measurement and protection equipment. Due to difficulties of modeling the arc condition some new data based or machine learning based techniques were developed. Also the arc fault detection methodology is still a challenging issue and a unique and complete solution, able to correctly operate in all working condition is not yet available. In fact, different problems can arise when measuring typical arcing parameters, such as those in the broadband frequency range; for example, such measurements can require the employment of sophisticated signal processing systems, with high processing speed and/or sampling frequencies, or they can be affected by current transducers and data acquisition systems, which may have a poor frequency response and a low signal-to-noise ratio.

In this thesis is presented an approach based on low signal sampling. With the proposed solution, it is possible to reach a good tradeoff between sampling parameters and computational burden, without the need of sophisticated measurement instrumentation. This can also allow the implementation of metrics for arc fault detection in measurement platforms commonly used for smart metering purpose, as well as their integration in commercial equipment installed in PV systems for various monitoring and management purposes (fault detection, efficiency and power quality measurements, field data acquisition, islanding detection and so on) [120]–[122]. In this perspettive, in [123] is presented a preliminary study, which showed a qualitative comparison among waveforms and low frequency spectra of DC arcing and non-arcing currents; the comparison results confirmed that low frequency current spectra can be suitably exploited to distinguish the arc fault occurrence from normal operation.

Starting from the preliminary results of [124], this chapter presents an extended experimental characterization of the series arcs in DC systems, based on the measurement of the set of indicators proposed in [123]. The aim of the study is to investigate their suitability for DC arcs detection purpose, taking into account also the impact of measurement equipment, i.e. transducers and data acquisition systems, on their effectiveness.

Both preliminary laboratory experiments and on-field tests are reported, where arcing and non-arcing current signals are compared and the behavior of the proposed set of indicators is analyzed. On field tests have been carried out on a real PV system, in accordance with some tests requirements of UL 1699B Standard. In all tests, current signals have been acquired with different measurement equipment; in detail, the experimental measurements have been carried out with the following different experimental setup configurations: a high resolution data acquisition board, with both a current shunt and a Hall effect current transducer; a low resolution data acquisition board with both the current shunt and the Hall effect current transducer; a commercial platform for smart metering applications, with

embedded transducer and data acquisition. The comparison among the results obtained with different metering equipment allowed verifying the feasibility of using common smart metering platforms even for arc detection purposes.

State of the art on DC arc fault detection method

The research on DC arc faults detection has been recently fostered by the growing interest and protection needs in DC power systems applications such as microgrids, electric vehicles, PV systems. Some arc faults detection methods have been specifically developed for PV systems; other solutions have been proposed for different applications, such as DC microgrids or electric vehicles, but they can be adapted also for PV arcs recognition[118], [119], [125]. Most methods are based on current (and, less frequently, voltage) signal analysis, in both frequency and time domain.

In the frequency domain, one of the most studied signal characteristics is the broadband noise (typically from tens of kilohertz up to 100 kHz). Some studies make a specific analysis of frequency components within the aforesaid bands; for example in [123] frequency components from 5 to 40 kHz are investigated, by means of a "circuit modeling" test setup, configured as those of UL1699B (i.e. test circuit setup for PV system emulation). Fast Fourier Transform (FFT) is generally used to evaluate amplitude and/or power of signal spectrum in specified frequency bands; measured values are compared with given thresholds to discriminate between normal and arcing conditions. In this viewpoint, when predetermined thresholds are used, some limitations can arise with respect to methods robustness in real operating conditions, where arc characteristics can vary depending on noisy conditions, inverter operation and so on. To improve detection accuracy, the use of adaptive thresholds has been proposed, which are statistically determined from the analysis of the signal in subsequent observation windows; in these cases a problem to cope with is related signal changes during the normal operation of the system (for example start-up or power changes). As regards the measurement equipment and signal processing requirements, broadband spectral analysis poses some issues concerning sampling parameters choice, observation window, frequency resolution and reasonable computational burden and complexity. In fact, for the implementation of the aforesaid methods, required sampling frequencies and number of acquired samples are relatively high, if compared with the typical sampling and memory features of commercial platforms typically used for power systems measurements applications.

Methods based on time domain and statistical analysis can allow lower sampling frequencies and computational costs. In such methods, RMS, magnitude or peak values of the current/voltage signal are measured for the arc detection purpose. To individuate distinctive high and random variations of arcing conditions, signal rate of change or difference of maximum and minimum value are monitored and compared with given thresholds. Statistical analysis, proper estimators and outlier analysis are proposed to evaluate the variance of the signal and to determine anomalies with respect to V-I characteristics which can be related to an arc fault occurrence. As for frequency domain analysis, main limitations of such approaches are related to threshold values used for distinguishing arcing from normal operating conditions and to noise and disturbances introduced by PV system equipment which can affect the arc detection capability.

Some "multi criteria" methods have been also proposed to improve the arc detection accuracy; in such methods both time and frequency domain characteristics are simultaneously monitored (for example time domain fluctuations and specific frequency components spikes). Some solutions make use of Short Time Fourier Transform (STFT) analysis, where the trend is analyzed of the considered frequency components over time. In other cases, methods based on Discrete Wavelet Transform (DWT) or Wavalet Packet Decomposition (WPD) have been proposed to improve signal analysis resolution into the frequency bands of interest. Further methods are based on Artificial intelligence (AI) techniques, such as artificial neural network (ANN), support vector machine (SVM) or other machine learning techniques; In [126] an innovative algorithm for detecting L-L faults in PV arrays based on support vector machine (SVM) was proposed. However this approach was not tested in a series arc fault condition and also has the drawback of needing a large amount of data. The authors in [127] try to mitigate this drawback with the use of graph-based semi-supervised learning models. Generally speaking, for most aforesaid methods, main problems still remain concerning high computational burden, complexity and reliability.

Only few methods for fault detection in PV systems make use of signal analysis in low frequency range (up to few kilohertz or lower). This is mainly due to the fact that environmental noise due to PV power electronics may overlap with low frequency components of the arc signals, and this can potentially affect the detection methods based on such signatures. However, as observed in [123], the possibility of exploiting low frequency analysis can allow reducing sampling requirements and computational burden, thus enabling the use of commercial acquisition and signal processing systems which typically have low sampling frequency and limited memory and computational capabilities. In this framework, the choice of sampling frequency and number of acquired samples is crucial to obtain a good tradeoff between spectral resolution and the observation window. In fact, typical processing algorithms for

frequency-domain analysis (such as FFT) are known to require the signal stationarity in the observation window. On the other hand, arc signal, in both AC and DC systems, is typically non stationary, thus the observation window should be as small as possible, in order to maintain valid the condition of stationary signal. This can cause a poor spectral resolution. Thus, the algorithm used for the frequency analysis should be able to ensure a good spectral resolution even with very short observation windows. Furthermore, when dealing with the measurement chain, attention should be paid to the measurement transducers, whose behavior can be critical when high frequency components must be acquired and processed. The possibility to use low frequency analysis can allow to better face all the aforesaid problems.

UL 1699B. Arc fault detection tests and unwanted tripping tests

As already mentioned, the Standard UL 1699B provide construction and performance requirements of DC arc fault circuit protection devices, which are intended for use in PV electrical energy systems. The arc fault detector (AFD) provide protection from the risk of fire ignition due to arcing occurrence, by detecting the fault and enabling the power interruption.

Requirements regarding the constructions of the different parts of the protection devices cover various aspects, such as corrosion resistance, internal wiring, type of insulation, type of power supply, operating mechanisms, programmable electronic components, safety requirements for operation under power. As regards the devices performance, several tests are required, in order to verify the correct devices functioning. Tests are specified under varying environmental conditions (temperature, humidity, corrosion, electromagnetic and power quality disturbances) and in presence of leakage currents, overvoltages, insulation tests, mechanical tests. Arc fault detection tests and unwanted tripping tests are also considered to test the capability of correctly detecting the arcing conditions and distinguish them from normal operating conditions, even when noise or other disturbances may occur.

As regards arc fault detection tests, the UL 1699B defines the various application cases in which the device under test (DUT) must be tested, including the circuit requirements for the applicable use cases. For example, Figure 115depicts the scheme for tests in the use case of one string PV and one Maximum Power Point Tracker (MPPT), where the different positions of the arc generator used for tests are highlighted. Other configuration tests involve the presence of two strings combined and one MPPT. In this case the arc generator can be positioned near the inverter or between two strings. If a combiner is involved in PV plant, the arc generator can be positioned near inverter or between two strings.

Instead, if DC-DC converters are involved, the arc generator shall be inserted near the converter or in the end of the string. If more input module are connected to a DC-DC converter, arc generator shall be inserted between two strings connected to the converter. In case of microinverter, the arc generator shall be connected between panel and inverter.

The Standard UL1699B provides also guidelines for the construction of the arc generator. In summary, the arc generator electrodes, one moveable and one stationary, shall be cylindrical, with 6,35mm diameter, and made of solid copper or tungsten alloy; the electrode mating surfaces shall be parallel, flat, and vertical.

The test procedure for series connection arcing test is also defined in UL1699B, with specific requirements for the arc generator positioning and movements, sequence and number of tests to be performed, arcing tests conditions, voltage and current recording, DUT detection time. In summary, for each test the arc generator must be placed in one of the considered positions; at the beginning of the test the arc generator electrodes are in contact with each other and then they are separated to create the arcing condition. The DUT must detect the arc within the specified intervention time.
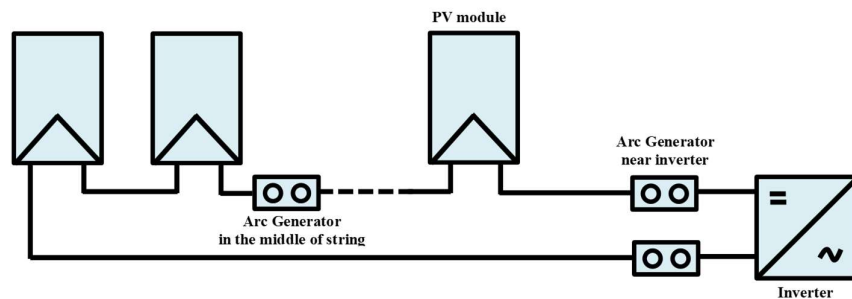
Figure 115 Scheme of UL1699B use case for arc detection tests. Use case of One string, one MPPT

A section of UL1699B is dedicated to the unwanted tripping tests, i.e. tests where particular operating conditions are reproduced where the DUT shall not trip. Different loading conditions are described, which cover the following situations: different inverters, converters and charge controllers (in both single-phase and three-phase cases); DC switch operation; irradiance step changes. For every loading condition, test circuits include one string and two strings configurations and the use of a DC/DC converter with one or two input modules.

The DUT should be tested for each use case as applicable. To emulate the on-field operating conditions of a real PV plant, the UL1699B provide electrical circuits schemes values for building suitable test setups. They include full details for DC source, decoupling network and half/full string model (module and line impedance), with specified values for all circuit components, according to the different use cases. For example, in the use case of Figure 115, two DC sources, decoupling networks and half string circuits are considered, in order to allow reproducing both tests with arc generator near to inverter or in middle of the string.

With respect to the aforesaid requirements, in the experimental study presented in this paper, both laboratory and on-field tests were carried out. Laboratory tests were carried out on a simplified test setup with a DC source and a simple resistive load, in order to make a preliminary characterization of the measurement setup and to investigate the behavior of the considered indicators (previously defined for the AC case) for DC arc faults detection. The aim was to take into account the impact of measurement equipment features on the indicators effectiveness, without considering the influence of PV systems components and the inverter, which can introduce further noise and distortion on current waveform. On the other hand, the on-field tests were carried out on a real PV plant, according to the UL1699B use case of Figure 115.

Proposed arc fault detection method

The experimental characterization has been carried out with the aim of investigating the feasibility of low frequency spectral analysis of current for DC arc faults occurrence detection. Furthermore, during the tests, the current signal were acquired by using different transducers and data acquisition devices, in order to analyze to what extent such equipment can affect the measurement of the considered indicators and their effectiveness for the arc fault detection purpose.

In detail, in [24] the authors proposed an arc-fault detection strategy for AC systems, based on the measurement of a set of indicators mainly derived from low frequency spectral analysis of current; to allow obtaining a good resolution even with short observation windows, the chirp zeta transform (CZT) algorithm was chosen to measure the considered indicators. In this paper the indicators proposed in [24] have been evaluated in the case of DC arcs, in order to investigate their effectiveness in the DC case. In detail, the following four indicators defined in [24] have been considered:

1. *diff_czt*, i.e. the mean value of the differences between the N samples (S_n) of two low-frequency amplitude spectra of the current, measured in two successive observation windows ($T(k)$ and $T(k-1)$); it is given by

$$diff\_czt = \frac{1}{N} \sum_{n=0}^{N-1} \left| S_{nT(k)} - S_{nT(k-1)} \right| \qquad (49)$$

2. *diff_IIarm*, i.e. the relative value of the difference between the maximum values of spectra samples S_n in the frequency interval [$f2\_min$; $f2\_max$], around the second harmonic (of the fundamental power system frequency), measured in two subsequent observation windows, $T(k)$ and $T(k-1)$; it is given by:

$$diff\_IIarm = \frac{\left| max\left[S_{T(k)} \big|_{(f2\_min)}^{(f2\_max)} \right] - max\left[S_{T(k-1)} \big|_{(f2\_min)}^{(f2\_max)} \right] \right|}{max\left[S_{T(k-1)} \big|_{(f2\_min)}^{(f2\_max)} \right]} \cdot 100 \qquad (50)$$

3. *NF*, i.e. the noise floor, evaluated as the mean value of the N' samples of residual current spectrum $S'_{T(k)}$, which is obtained by removing the samples of both odd and even harmonics main lobes from the current spectrum $S_{T(k)}$; it is given by:

$$NF = \frac{1}{N'} \sum_{n \in N'} S'_{nT(k)} \qquad (51)$$

4. *diff_i*, i.e. the mean value of the difference between the N samples of current (i_n) acquired in two subsequent observation windows, $T(k)$ and $T(k-1)$; it is given by

$$diff\_i = \frac{1}{N} \sum_{n=0}^{N-1} \left| i_{nT(k)} - i_{nT(k-1)} \right| \qquad (52)$$

In previous formulas:

- $S_{T(k)}$ is amplitude spectrum of the current $i_{T(k)}$ acquired in the observation window $T(k)$;

- N is the number of samples of $S_{T(k)}$;

- $S_{nT(k)}$ and $S_{nT(k-1)}$ are the n-th sample of the spectra $S_{T(k)}$ and $S_{T(k-1)}$, measured in the observation windows $T(k)$ and $T(k-1)$, respectively;

- f_{2_max} and f_{2_min}, is the frequency interval corresponding to the main lobe of the second harmonic of the current spectrum S;

- $max\left[S_{T(k)}\vert_{(f_{2\_min})}^{(f_{2\_max})}\right]$ is the maximum value of $S_{T(k)}$ in the specified frequency interval $[f_{2\_min}; f_{2\_max}]$;

- $max\left[S_{T(k-1)}\vert_{(f_{2\_min})}^{(f_{2\_max})}\right]$ is the maximum value of $S_{T(k-1)}$ in the specified frequency interval $[f_{2\_min}; f_{2\_max}]$;

- $S'_{T(k)}$ is residual amplitude spectrum of the current $i_{T(k)}$ acquired in the observation window $T(k)$, which is obtained by removing the samples of main lobes of both odd and even harmonics from the current spectrum $S_{T(k)}$;

- N' is the number of samples of $S'_{T(k)}$;

- $i_{nT(k)}$ and $i_{nT(k-1)}$ are the n-th sample of the currents $i_{T(k)}$ and $i_{T(k-1)}$, measured in the observation windows $T(k)$ and $T(k-1)$, respectively.

As detailed in [123], *diff_czt* and *diff_i* indicators are representative of the signal non-stationarity; in fact, if the signal is stationary, they assume a very small value (ideally zero); on the other hand, if signal is non-stationary, the value two indicators increase. *NF* is one of the most significant parameters for arc recognition; in fact, it typically increases in arc presence. Finally, *diff_IIarm* is an indicator of the trend of second harmonic (of the power system fundamental frequency); as shown in the following, in the study herein presented this indicator has been considered because during the experimental on-field tests it was observed that the acquired current signal was affected by harmonics even in non-arcing conditions; in detail a ripple at 100 Hz, i.e. twice the fundamental power line frequency of 50 Hz (because of the inverter switching) [124].

In Figure 116 the algorithm flowchart is shown. Current is acquired and for each observation window T(k) the indicators (49)-(52) are evaluated. The length of the observation window is set in order to have a good resolution for CZT spectral analysis, even with short time windows; in the results presented in this paper, the observation window was set equal to 80 ms (as made in [123]). For each observation window, *diff_i* is evaluated starting from current samples, i.e. in the time domain, according to (52). The other indicators are evaluated in the frequency domain, from the current spectrum obtained with the CZT algorithm.

In detail, the measurement of the frequency domain indicators, i.e. *diff_czt*, *diff_IIarm* and *NF*, is made starting from a low frequency spectral analysis, in a frequency band up to few kHz. Most existing methods are focused on frequency components in higher frequency bands (tens or even hundreds of kilohertz), instead. However, the possibility of using low frequency spectral analysis allows using low sampling frequencies, such as those commonly used in commercial smart metering equipment (for example in the experimental tests herein presented, values up to 10 kHz were used), with the advantages of reaching a suitable trade-off between sampling frequency, observation window length, memory requirements, computational burden and cost effectiveness.
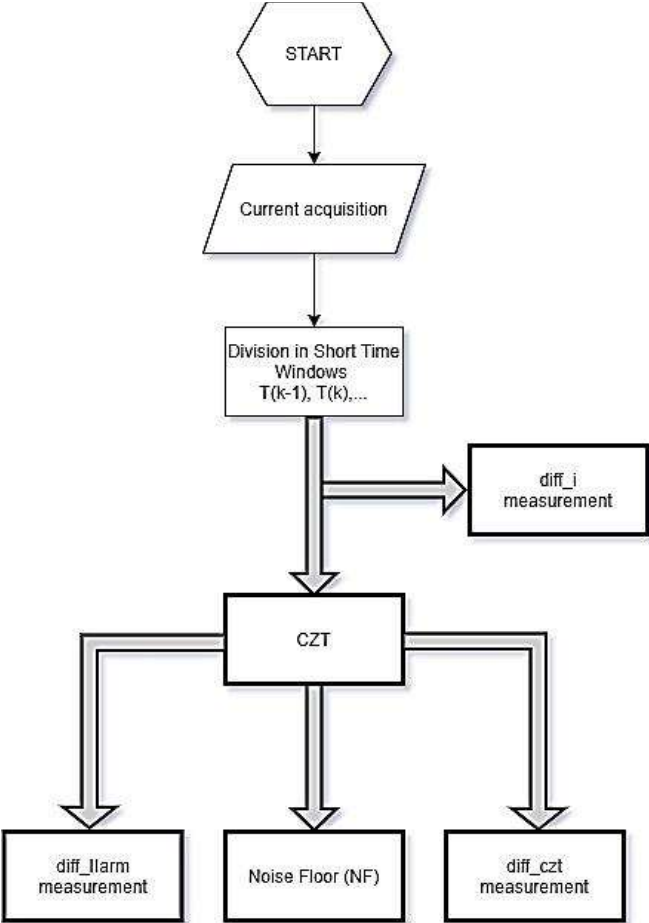
Figure 116 Arc Fault analysis flowchart

Experimental tests have been carried out both in laboratory and on-field, by reproducing both non-arcing and arcing conditions, in order to compare the current waveforms and low frequency spectra and the indicators behavior in both the absence and presence of the faulty condition. The following subsections describe the test bench and metering equipment, the preliminary laboratory characterization and the on-field tests.

The test benches for laboratory and on-field tests are schematized in Figure 117 and Figure 118, respectively. In summary, the test bench equipment for laboratory measurements (Figure 117) were the following: (1) DC Power supply; (2) Hall effect current clamp-on transducer (HECT); (3) Current Shunt; (4) Arc generator; (5) Resistive Load; (6) STCOMET board; (7) NI-DAQ NI6009; (8) NI-DAQ NI9239. Current signals were acquired and processed by PC. As shown in Figure 118, for on-field tests the arc generator and the metering section were between the PV field (1) and the inverter (5), in according to the scheme of Figure 115 (arc generator near inverter [124]). The arc generator was built according to UL1699B. During both laboratory and on-field tests, the arc generator was inserted or short-circuited, in order to reproduce both normal (non-arcing) and arcing conditions.

Two types of current transducers and two data acquisition boards were used to sense and acquire the signal. Their main features are listed below.

- Current Shunt: Fluke A40B, maximum current 5 A, nominal resistance 0.16 Ω, accuracy ± 21 µA/A DC, ± 71 µA/A up to 100 kHz (95% confidence level).

- Hall effect current clamp-on transducer (HECT): LEM PR 30, maximum current 20 A, instrument constant 100 mV/A, frequency range from DC to 100 kHz, accuracy ± (1% rdg + 2 mA), resolution 1 mA.

- NI-DAQ NI9239: four analog voltage differential input channels, simultaneous sampling, input range ± 10 V, maximum sampling frequency 50kS/s (10 kS/s was used in the tests herein presented), 24-bit ADC delta-sigma with analog anti-aliasing prefiltering, alias-free bandwidth 0.453 of sampling frequency, offset 0.008% of range, gain 0.03% of reading, THD – 99 dB, noise 70 µV.

- NI-DAQ NI6009: multifunction I/O device, four analog voltage differential input channels (eight in single-ended mode), multiplexed, input range from ± 1 V to ± 20 V, maximum sampling frequency 48 kS/s (10 kS/s was used in the tests herein presented), 14 bit ADC,

absolute accuracy at full scale up to 14.7 mV, noise 0,5 mVrms for ± 1 V input range and 5 mVrms for ± 20 V input range).

The measurement of considered indicators was implemented in LabVIEW environment.

The measurements were carried out also with a further device, i.e. an EVLKSTCOMET10-1 by STMicroelectronics (named STCOMET in the following). It is a development kit for smart metering applications, based on STCOMET chip, which integrates both a modem for power line communication (PLC) and a metrology section. Main features of the metrology section are: nominal voltage 230 V, nominal current 5 A, sampling frequency 7.8125 kHz, - 3 dB bandwidth 0 – 3.6 kHz, 24-bit ADC delta-sigma. As regards voltage and current transducers, the STCOMET board includes a resistive divider used as voltage sensor, while both a shunt and a current transformer are available for measuring current; the shunt was used in the experimental tests.

Thus, for each test, measurements were carried out with the following metering equipment configurations:

- NI-DAQ NI9239 with current shunt;

- NI-DAQ NI9239 with HECT;

- NI-DAQ NI6009 with current shunt;

- NI-DAQ NI6009 with HECT;

- STCOMET with embedded current shunt.

In this way it has been possible to investigate not only the indicators feasibility for arc fault detection, but also the impact of both transducers and data acquisition equipment on their measurement and effectiveness.

Laboratory results

In laboratory tests a DC power supply (Elind mod 500KL) and a 20Ω/100W resistor were used for power generation and load, respectively. This allowed measuring the indicators and characterizing the data acquisition systems in a sort of ideal condition, without any disturbance or noise typical of real operating conditions (such as PV inverter noise or current variations). The arc generator was connected in series with the load, in order to reproduce series arcs conditions. During the tests, the arc generator was inserted or short circuited, in order to have both arcing and non-arcing conditions.

As an example, Figure 119 shows the plots of the acquired current and the indicators of eq. (49)-(52) during a laboratory test with NI-DAQ NI9239 and current shunt. In the current plot of Figure 119 (a), the normal (without arc) and arcing portions are highlighted. The plots of Figure 119 (b)-(f) show that all indicators values are essentially constant during the normal operation, while they assume higher values and variability in the presence of arc. In Table 53, segments of normal and arcing current and related indicators are compared. Table 54 shows mean values and standard deviations of the measured indicators, for both normal and arcing segments of the current. It can be observed that the indicators variations from normal to arcing condition are significant thus they can be potentially used for arc detection purpose. Furthermore, in almost all cases, the amount of the indicators variations are higher than the related standard deviations. The best behavior is observed for NF; in fact a variation of about 30 dB is observed from normal to arcing condition, while the standard deviation of the measured values is not higher than 2 dB.

Similar plots measured values and standard deviations were obtained with the NI-USB 6009 and STCOMET. This suggests the possibility to use also them for arc detecting purposes, even if the lower ADC resolution of NI-USB 6009 and the STCOMET conditioning circuit can significantly affect the indicator absolute values. For example, for noise floor, in normal conditions (DC power supply and no arc), differences of about 25-30 dB were observed between NI9239 *NF* measurements and those of the other devices. These phenomena have been observed also during on-field tests and they will be further explained in next subsection.
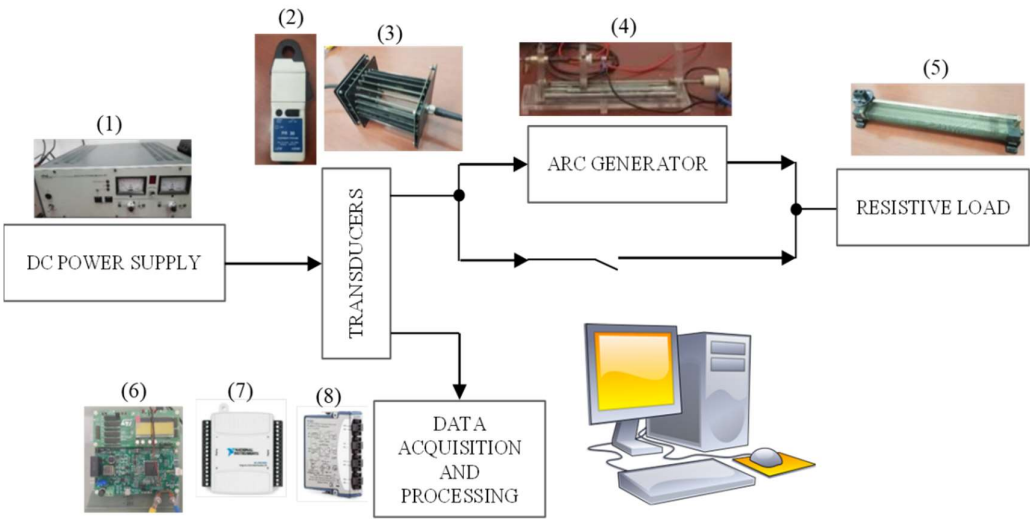
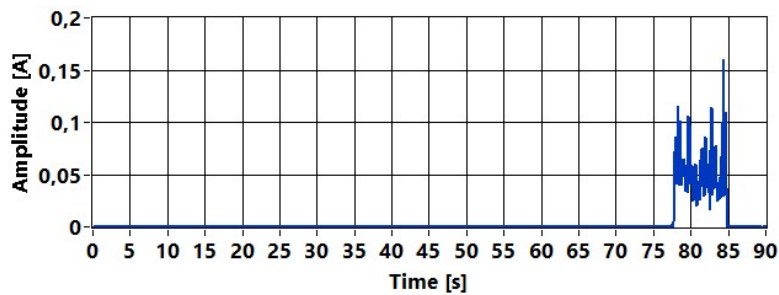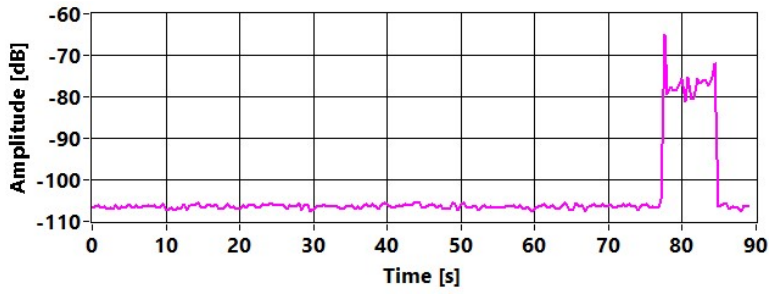*Figure 117 Scheme of the laboratory test bench*
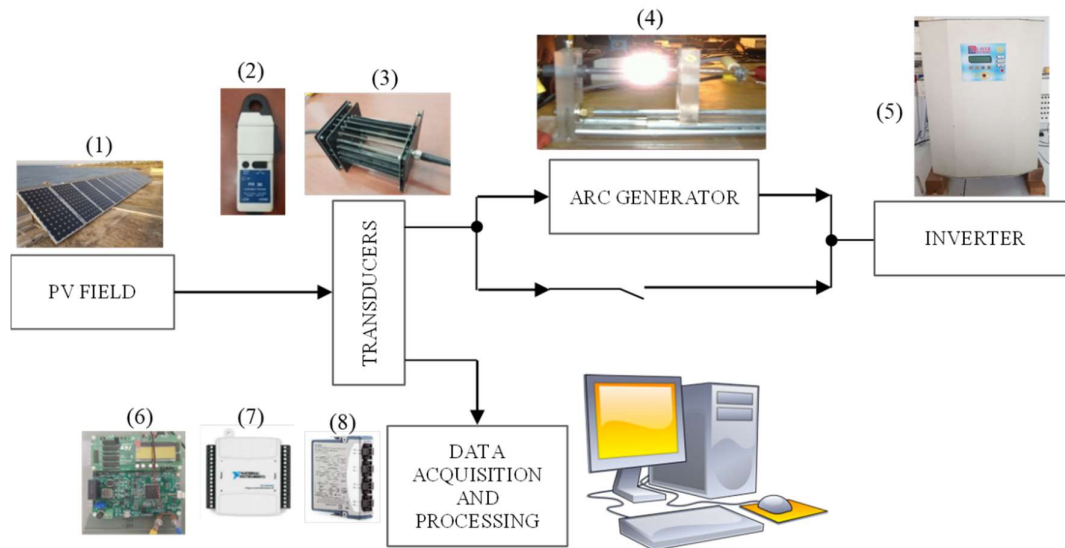
Figure 118 Scheme of the on-field test bench
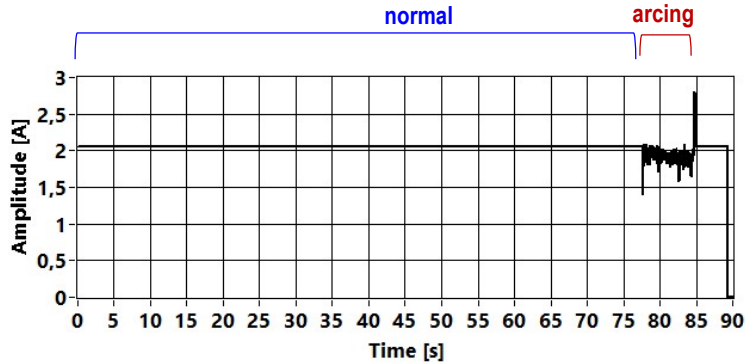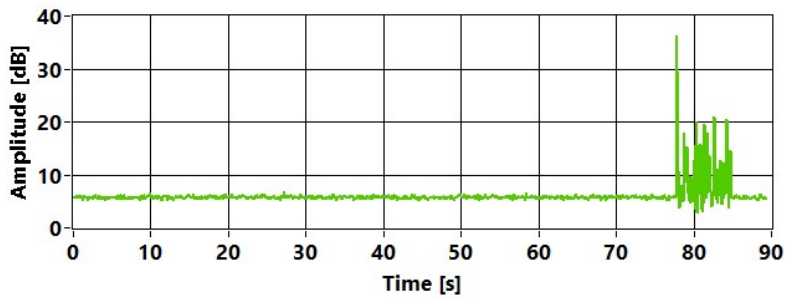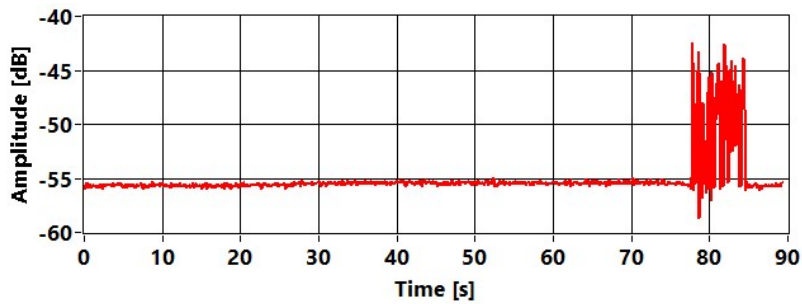

(a) Acquired signal (Time [s]; Amplitude [A])
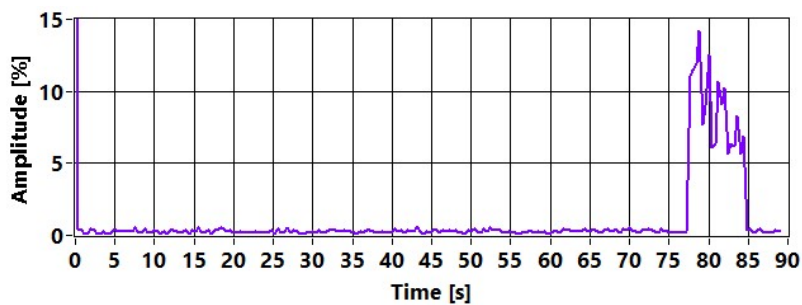

(b) diff_i (Time [s]; Amplitude [A])

(c)　NF (Time [s]; Amplitude [dB])

(d)　*diff_CZT* (Time [s]; Amplitude [dB])

(e)　2nd harmonic (100 Hz) (Time [s]; Amplitude [dB])

(f)　*diff_IIarm* (Time [s]; Amplitude [%])

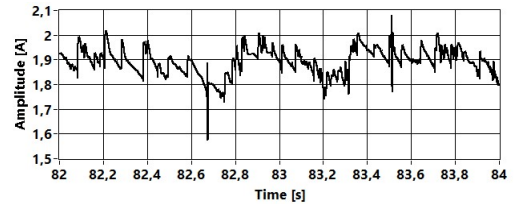*Figure 119 Laboratory test with NI9239 and current shunt. Acquired current and measured indicators*
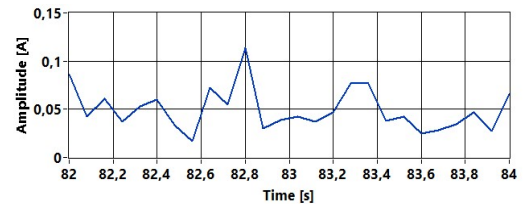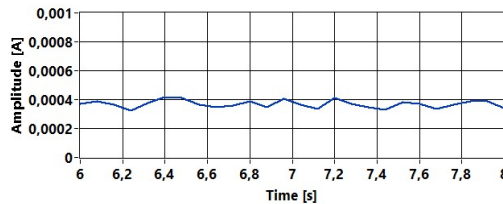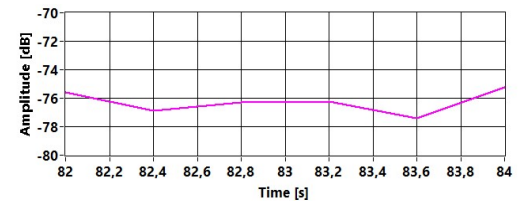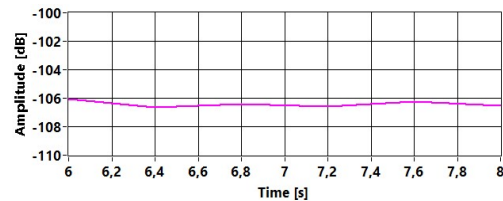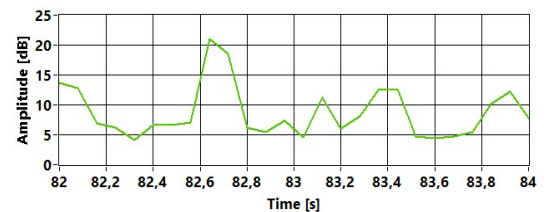
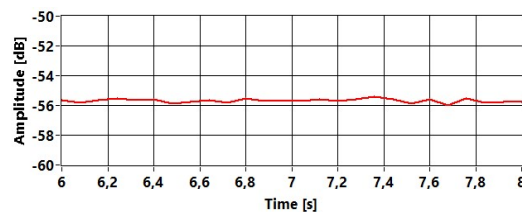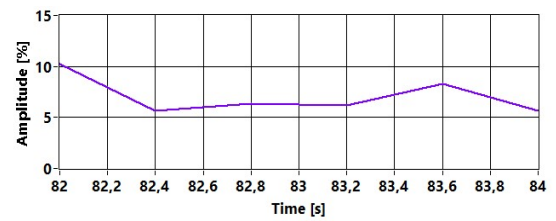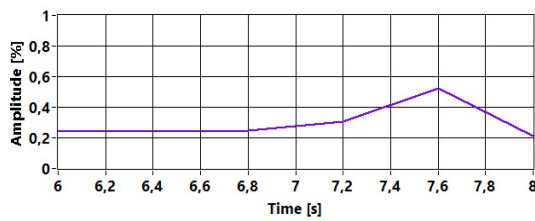| Acquired current and indicators	Normal segment	Arcing segment
Acquired signal (Time [s]; Amplitude [A])		
diff_i (Time [s]; Amplitude [A])		
NF (Time [s]; Amplitude [dB])		
diff_CZT (Time [s]; Amplitude [dB])		
2ⁿᵈ harmonic (100 Hz) (Time [s];		
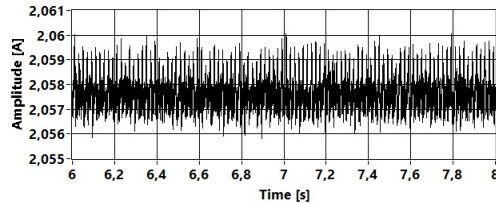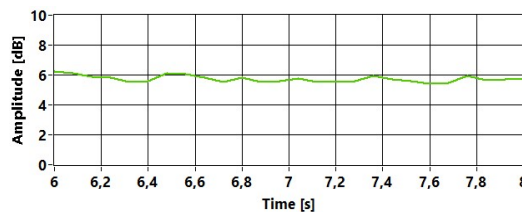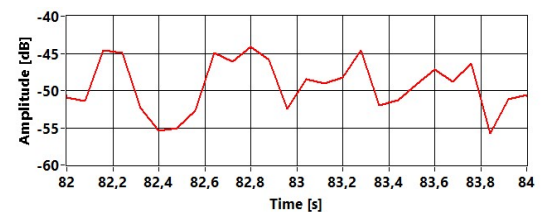
Amplitude [dB])

diff_IIarm (Time [s]; Amplitude [%])

Table 51 Laboratory test with with NI9239 and current shunt. Measured indicators. Comparison between normal and arcing conditions. Mean values and standard deviations of measured indicators

Indicator	Normal/arcing condition	Mean value	Standard deviation
diff_i	Normal	0.004 A	0.001 A
	Arcing	0.05 A	0.02 A
NF	Normal	- 106.4 dB	0.5 dB
	Arcing	- 77 dB	2 dB
diff_czt	Normal	5.8 dB	0.2 dB
	Arcing	9 dB	4 dB
II harmonic	Normal	- 55.5 dB	0.2 dB
	Arcing	- 50 dB	4 dB
diff_IIarm	Normal	0.3 %	0.1 %
	Arcing	9 %	2 %

On-field results

On field tests were carried out in a 2 kW PV plant installed at the industrial site of Layer Electronics Srl (Erice, Italy). The on-field test bench built at Layer Electronics is shown in Figure 118. The arc

generator and the metering section were placed near the inverter, according to the use case of Figure 115. The current was simultaneously acquired with all metering equipment configurations previously described, i.e. NI-DAQ NI9239 and NI-DAQ NI6009 with both current shunt HECT and STCOMET with embedded current shunt. Acquired signals were stored and processed by means of two laptops (one for managing data from NI-DAQ boards, the other one for managing data from STCOMET board).
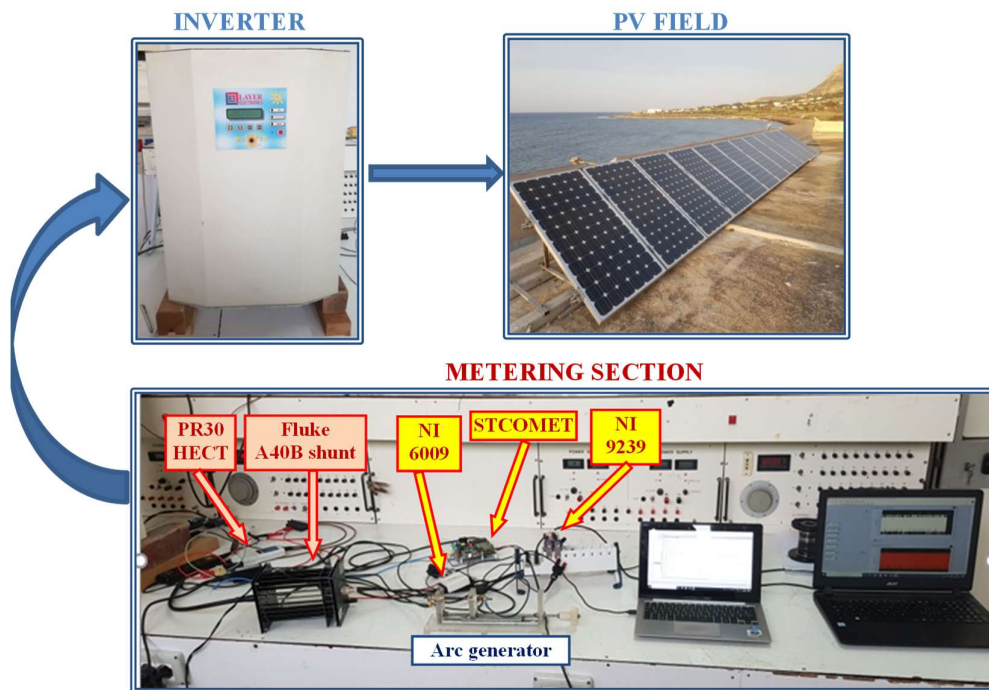
Figure 120 On-field test bench

Table 52 shows some results obtained with the NI 9239 board and the two current transducers (Current shunt and HECT). By comparing the plots of acquired current and measured indicators, it can be observed that results are quite similar, thus the transducers does not impact significantly the indicators measurement.

Table 53 shows a comparison between two segments of normal and arcing current and related indicators. It can be seen that the current plot is very noisy and it has a high variability, even in normal condition, due to inverter noise and variations on PV panels solar irradiance. However even in these on field tests, the indicators assume lower and almost constant values during the normal operation, while they have higher values and variability in the presence of arc. The indicators variations from

normal to arcing condition are always significant, thus confirming their effectiveness for arc detection purpose. The worst behavior is observed for the indicator *diff_IIarm*, due to the inverter ripple. As for the laboratory tests, similar plots and variation rates were obtained with the other measurement devices (NI 6009 and STCOMET).

Table 54 shows the comparison between mean values and standard deviations of the indicators measured with the different metering equipment configuration listed in section IV.B (NI-DAQ NI9239 with current shunt; NI-DAQ NI9239 with HECT; NI-DAQ NI6009 with current shunt; NI-DAQ NI6009 with HECT; STCOMET with embedded current shunt). The results are related to the normal and arcing current segments of Table 53. It can be seen that the indicators measured with the different metering equipment have slightly different values; this happens even in normal conditions (and it is more visible for noise floor), due to the differences among the metrological features of employed instrumentation and (particularly the data acquisition boards and the STCOMET). However, in all cases the indicators variation between normal and arcing conditions are higher than the variation due to the metering equipment features or time variability of operating conditions. Standard deviations are small if compared with the differences between the indicators values in normal and arcing conditions. Thus the indicators obtained with low frequency analysis of the current signal can allow to achieve reliable information on arc occurrence, even with common equipment for smart metering applications or low-cost data acquisition boards, such as STCOMET or NI-USB 6009.

Furthermore, the on-field results are consistent with those obtained in laboratory, where noise and distortion due to real PV systems components and the inverter were not present. This confirms the feasibility of the proposed indicators for arc faults detection in PV systems, even in the presence of noise, distortion and non-stationary currents due to PV plant normal operation. For example, in the on-field tests, the current waveform in normal conditions was not stationary and distorted, showing a second harmonic (100 Hz) ripple, due to the operation of the inverter; however, this did not affect the feasibility of the proposed indicators.

Table 52 On-field test with NI9239 and current shunt and PR30. Acquired current and measured indicators

Acquired current and indicators	NI9239 with current shunt	NI9239 with PR30

Acquired signal (Time [s]; Amplitude [A])		
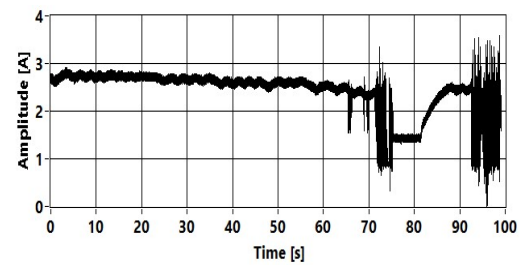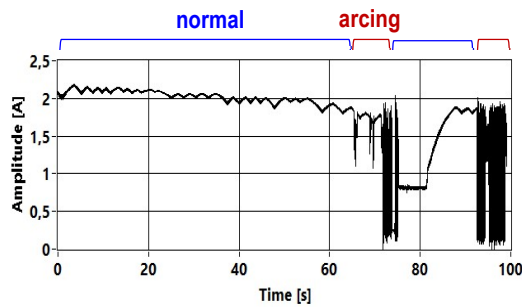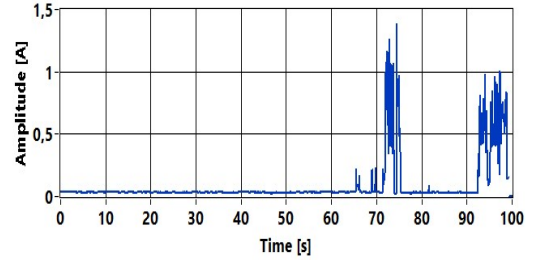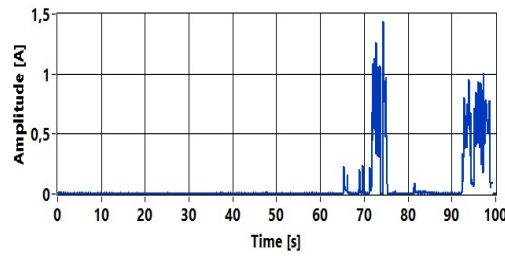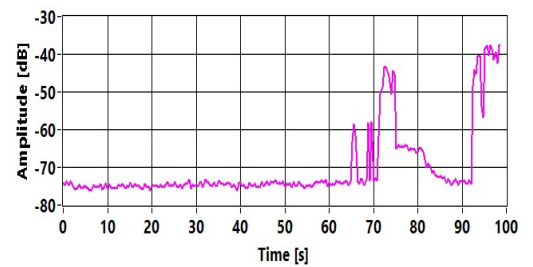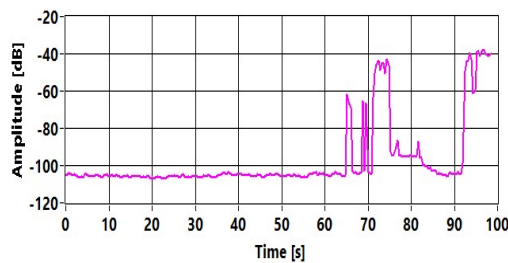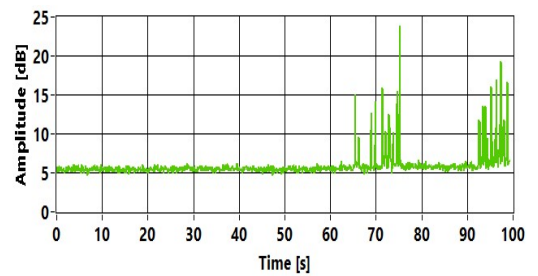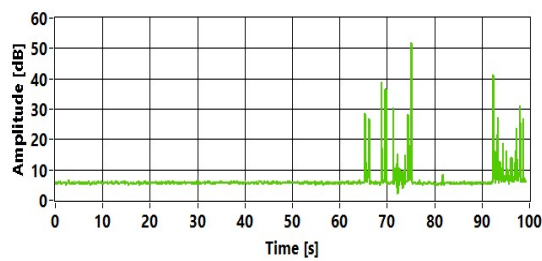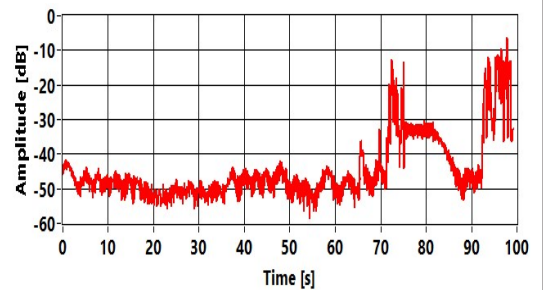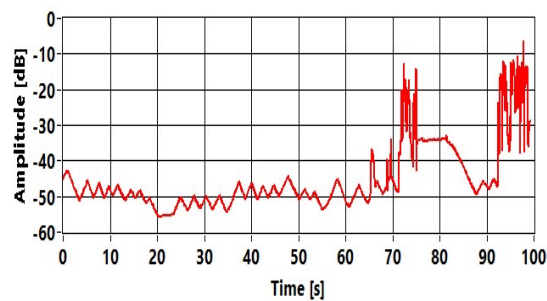
diff_IIarm (Time [s]; Amplitude [%])		
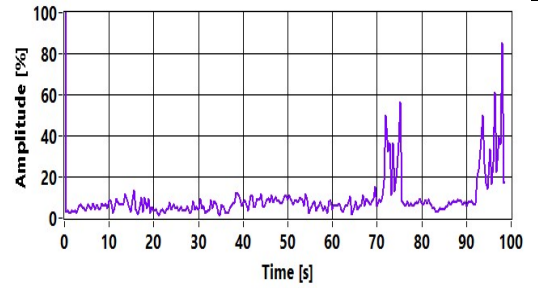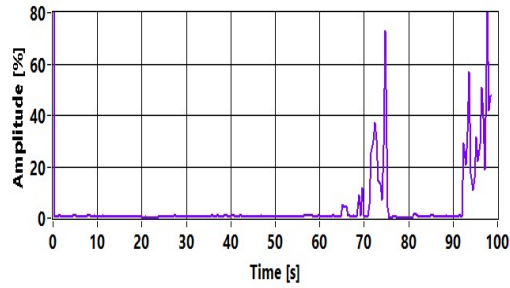
Table 53 On-field test with ni9239 and current shunt. Acquired current and measured indicators. Comparison between normal and arcing segments

Acquired current and indicators	Normal segment	Arcing segment
Acquired signal (Time [s]; Amplitude [A])		
diff_i (Time [s]; Amplitude [A])		
NF (Time [s]; Amplitude [dB])		

diff_czt (Time [s]; Amplitude [dB])			
2nd harmonic (100 Hz) (Time [s]; Amplitude [dB])			
diff_IIarm (Time [s]; Amplitude [%])			
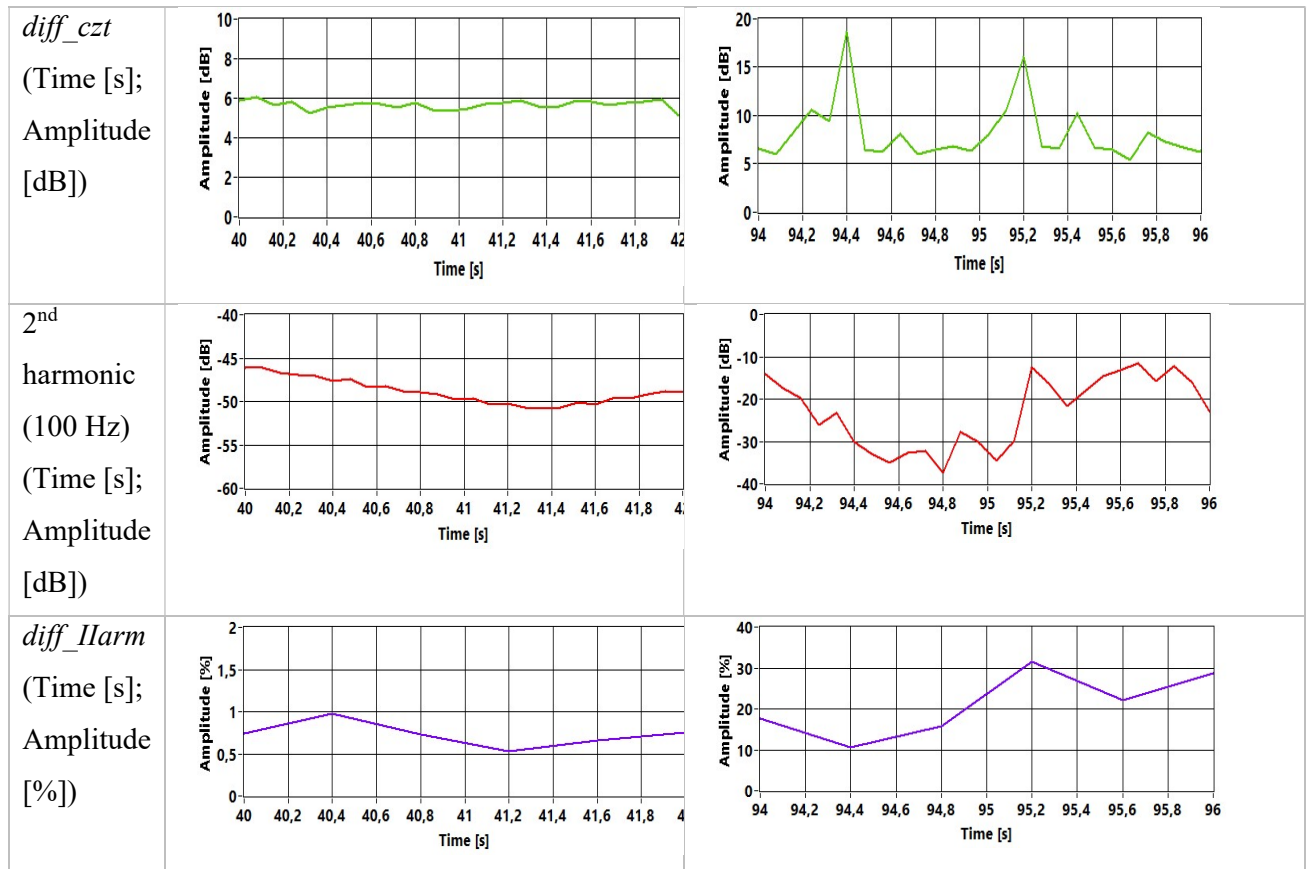
Table 54 On-field test with various metering equipment. Measured indicators. Comparison between normal and arcing conditions. Mean values (and standard deviations) for current segments of Table 53

Indicator	Normal/arcing condition	NI 9239 with current shunt	NI 9239 with HECT	NI 6009 with current shunt	NI 6009 with HECT	STCOMET with internal current shunt
diff_i	Normal	0.005 A (0.003 A)	0.006 A	0.022 A (0,004 A)	0.024 A	0.025 A

	Arcing	0.40 A	0.41 A	0.45 A	0.45 A	0.45 A
		(0.25 A)		(0.25 A)		
NF	Normal	- 105 dB	- 104 dB	-78 dB	-75 dB	-72 dB
		(1 dB)		(1 dB)		
	Arcing	- 47 dB	- 48 dB	- 44 dB	- 45 dB	-50 dB
		(10 dB)		(8 dB)		
diff_czt	Normal	5.7 dB	5.9 dB	5.5 dB	5.5 dB	5.3 dB
		(0,2 dB)		(0.2 dB)		
	Arcing	8 dB	11 dB	10 dB	10 dB	10 dB
		(2 dB)		(2 dB)		
II harmonic	Normal	- 48 dB	- 47 dB	- 49 dB	- 47 dB	- 47 dB
		(2 dB)		(3 dB)		
	Arcing	- 23 dB	- 24 dB	- 25 dB	- 22 dB	- 26 dB
		(8 dB)		(7 dB)		
diff_IIarm	Normal	0.7 %	0.5 %	5 %	5 %	7 %
		(0,1 %)		(2 %)		
	Arcing	20 %	19 %	21 %	22 %	23 %
		(8%)		(8%)		

Conclusion to arc fault strategy

This chapter has presented an experimental study on DC series arc faults in PV systems using a set of parameters derived from low frequency spectral analysis of current signal. The indicators used for this study were previously proposed by the authors for AC arc fault detection. The experimental characterization herein presented has been aimed at verifying both the indicators suitability for the DC case and the impact of different transducers and data acquisition systems on their measurement and effectiveness.

Both laboratory and on-field tests on a real PV system have been carried out; the experimental setup has been built in accordance with tests requirements of UL 1699B Standard for protection devices

against PV DC arc faults. Arcing and non-arcing current signals are acquired and compared verifying the behavior of each proposed indicators.

Preliminary laboratory tests allowed comparing the different metering equipment (data acquisition boards and a commercial platform for smart metering applications) in stationary conditions and in non-arcing conditions; the results put in evidence the different performances of the equipment under test, in terms of noise and distortion due to ADCs and/or on-board signal conditioning. The same test in the presence of arcs gave first positive feedback about the use of the proposed indicators also for the DC case.

On field tests allowed investigating the behavior of the considered indicators in a more realistic case, where, even in the absence of arcing, the current signal is not stationary, due to inverter noise or operating conditions variations. According to UL 1699B such conditions can create problems in discriminating normal operation from arc faults occurrence. Tests have been carried out in both arcing and non-arcing conditions by using different transducers and data acquisition systems. The obtained results showed that: the employed transducers (current shunts and HECT) do not affect significantly the indicators measurement; the data acquisition equipment can have a higher impact on the measured values but the proposed indicators in any cases allow detecting arc faults occurrence, even with in the noisy and non-stationary conditions of the real case.

In conclusion, presented results show that the considered indicators are suitable for detecting the arc presence even with commercial devices normally used for smart metering applications. In this viewpoint, the possibility of using low frequency analysis can allow reaching a good tradeoff between sampling parameters and computational burden. This can make feasible the use of low cost commercial platforms for power system measurements, with low sampling frequencies and limited computational and memory capabilities. This could also allow the implementation and integration of arc fault detection algorithms in measurement devices commonly installed at both AC and DC side of systems for various monitoring and management purposes, where low frequency spectral analysis can be suitable (fault detection, efficiency and power quality measurements, field data acquisition, islanding detection and so on).

Conclusions

In this thesis, new tools for MV/LV smart-grid monitoring and management system were presented. These tools have been thought with the limitations and constraints, shown in the introduction, of the distribution system. The main focus of the presented algorithms was the overcoming of the RES problems for a safety development.

In the first chapter, was shown the implementation of a load flow monitoring algorithm based on active and reactive power measurements coming from power quality analyzers. The main contribution to the research was the Monte Carlo technique used for uncertainty and sensitivity analysis. The uncertainty analysis proved how the method can be accurate enough for grid observability.

In the second chapter, a new architecture aimed to integrate the next generation of smart prosumer was shown. The prosumer was intended as generic consumer with DER and energy storage system (ESS) and the communication between system operator and the prosumer was supposed. In this context, a new algorithm was tested in simulation for the optimization of the prosumer energy cost. The solution presented is able to satisfy the needs of the consumer, interested in maximizing its profit, and the needs of the system operator that in the proposed architecture is able to control the storage system and avoid reverse power flow. After the preliminary studies, characterization tests were performed in order to model the battery behavior. With the new battery model, the algorithm was improved and implemented in a real system in order to demonstrate its feasibility. Finally, the optimization algorithm was substitute with a more efficient algorithm based on fuzzy logic and the economic advantage of the system was proved again first in simulation and then in a real system.

Third chapter presents new indicators for power quality assessment aimed to identify the harmonic distortion sources also for billing purposes. First, the state of the art on harmonic distortion assessment was presented both from standard point of view than from emerging technology point of view. After that, the strengths of the proposed indicators were shown in terms of efficacy and accuracy. In addition, their implementability was tested first in a FPGA platform and then in a common microcontroller for energy metering. In the final part, a decision-making strategy was proposed with a power factor like concept in order to univocally demonstrate the harmonic sources.

In the last chapter a diagnostic algorithm for the fault monitoring of a series arc fault in a generic DC system was shown. The new algorithm was aimed to identify the series arc fault of a photovoltaic system but it can be used also in generic DC system. The main contribution is the using of low frequency analysis to identify series arc fault in a generic DC system. This can make feasible the use

of low cost commercial platforms, with low sampling frequencies and limited computational and memory capabilities.

List of Acronyms

AC	Alternate current
AFCI	Arc Fault Detection Interface
AFD	Arc Fault Detector
AMR	Automatic Meter Reading
ANN	Artificial Neural Network
BMS	Battery Management System
CT	Current Transformer
CZT	Chirp Zeta Transformation
DC	Direct current
DER	Distributed Energy Resources
DFT	Discrete Fourier Transform
DG	Distributed Generation
DR	Demande Response
DSO	Distribution System Operator
DSS	Distributed Energy Storage
DWT	Discrete Wavelet Transformation
EMS	Energy Management System
ESS	Energy Storage System
FFT	Fast Fourier Transformation
HV	High Voltage
HVAC	High Voltage Alternate Current
ICT	Information and Communication Technology
IED	Intelligent Electronics Device
IPS	Interface Protection System

LF	Load Flow
LV	Low Voltage
MPPT	Maximum Power Point Tracking
MV	Medium Voltage
NTP	Network Time Protocol
OCV	Open Circuit Voltage
OF	Objective Function
PCC	Point of Common Coupling
PLC	Power Line Communication
PMU	Phasor Measurement Unit
PQA	Power Quality Analyzer
PSO	Particle Sword Optimization
PV	Photovoltaic
RMS	Root Mean Square
SE	State Estimation
SM	Smart Meter
SOC	State Of Charge
STFT	Short Time Fourier Transform
SVM	Support Vector Machine
THD	Total Harmonic Distortion
TSO	Transmission System Operator
VI	Virtual Instrument
VHV	Voltage Harmonic Vector method
VT	Voltage Transformer

WPD   Wavelet Package Decomposition

ZRC   Zero Crossing

References

[1]   J. Ekanayake, K. Liyanage, J. Wu, A. Yokoyama, and N. Jenkins, *Smart Grid: Technology and Applications*. 2012. doi: 10.1002/9781119968696.

[2]   A. Elrayyah, Y. Sozer, and M. E. Elbuluk, "A novel load-flow analysis for stable and optimized microgrid operation," *IEEE Transactions on Power Delivery*, vol. 29, no. 4, 2014, doi: 10.1109/TPWRD.2014.2307279.

[3]   H. Nikkhajoei and R. Iravani, "Steady-state model and power flow analysis of electronically-coupled distributed resource units," 2007. doi: 10.1109/PES.2007.385665.

[4]   G. Artale *et al.*, "Smart interface devices for distributed generation in smart grids: The case of islanding," *IEEE Sensors Journal*, vol. 17, no. 23, 2017, doi: 10.1109/JSEN.2017.2726185.

[5]   P. Tosato, D. Macii, M. Luiso, D. Brunelli, D. Gallo, and C. Landi, "A Tuned Lightweight Estimation Algorithm for Low-Cost Phasor Measurement Units," *IEEE Transactions on Instrumentation and Measurement*, vol. 67, no. 5, 2018, doi: 10.1109/TIM.2017.2775458.

[6]   G. Crotti, D. Gallo, D. Giordano, C. Landi, and M. Luiso, "A Characterized Method for the Real-Time Compensation of Power System Measurement Transducers," *IEEE Transactions on Instrumentation and Measurement*, vol. 64, no. 6, 2015, doi: 10.1109/TIM.2015.2398971.

[7]   P. A. Pegoraro, A. Meloni, L. Atzori, P. Castello, and S. Sulis, "PMU-Based Distribution System State Estimation with Adaptive Accuracy Exploiting Local Decision Metrics and IoT Paradigm," *IEEE Transactions on Instrumentation and Measurement*, vol. 66, no. 4, 2017, doi: 10.1109/TIM.2017.2657938.

[8]   A. Angioni, T. Schlösser, F. Ponci, and A. Monti, "Impact of pseudo-measurements from new power profiles on state estimation in low-voltage grids," *IEEE Transactions on Instrumentation and Measurement*, vol. 65, no. 1, 2016, doi: 10.1109/TIM.2015.2454673.

[9]   M. Ghasemi Damavandi, V. Krishnamurthy, and J. R. Martí, "Robust Meter Placement for State Estimation in Active Distribution Systems," *IEEE Transactions on Smart Grid*, vol. 6, no. 4, 2015, doi: 10.1109/TSG.2015.2394361.

[10]   S. Prasad and D. M. Vinod Kumar, "Optimal Allocation of Measurement Devices for Distribution State Estimation Using Multiobjective Hybrid PSO-Krill Herd Algorithm," *IEEE Transactions on Instrumentation and Measurement*, vol. 66, no. 8, 2017, doi: 10.1109/TIM.2017.2674718.

[11]   A. Cataliotti, V. Cosentino, D. di Cara, P. Russotto, E. Telaretti, and G. Tine, "An Innovative Measurement Approach for Load Flow Analysis in MV Smart Grids," *IEEE Transactions on Smart Grid*, vol. 7, no. 2, 2016, doi: 10.1109/TSG.2015.2430891.

[12]   R. Sinvula, K. M. Abo-Al-Ez, and M. T. Kahn, "Harmonic Source Detection Methods: A Systematic Literature Review," *IEEE Access*, vol. 7. 2019. doi: 10.1109/ACCESS.2019.2921149.

[13] G. Cai, L. Wang, D. Yang, Z. Sun, and B. Wang, "Harmonic detection for power grids using adaptive variational mode decomposition," *Energies*, vol. 12, no. 2, 2019, doi: 10.3390/en12020232.

[14] C. Xiao, Z. Qiu, S. Ding, C. Xu, Z. Wang, and V. Leng, "Effectiveness analysis of determining the main harmonic source by harmonic active power direction method," 2017. doi: 10.1109/ICPRE.2016.7871117.

[15] CENELEC, "EN 50160," *European Standard*, 2005.

[16] International Electrotechnical Commission, *Electromagnetic compatibility (EMC) Part 3-6: Limits — Assessment of emission limits for the connection of distorting installations to MV, HV and EHV power systems*, no. July 2012. 2008.

[17] IEEE, "IEEE Trial-Use Standard Definitions for the Measurement of Electric Power Quantities Under Sinusoidal, Non-sinusoidal, Balanced, Or Unbalanced Conditions," *IEEE Std 1459-2000*, 2000.

[18] S. Vlahinić, D. Brnobić, and N. Stojković, "Indices for harmonic distortion monitoring of power distribution systems," in *IEEE Transactions on Instrumentation and Measurement*, 2009, vol. 58, no. 5. doi: 10.1109/TIM.2008.2009132.

[19] G. v. de Andrade, S. R. Naidu, M. G. G. Neri, and E. G. da Costa, "Estimation of the utility's and consumer's contribution to harmonic distortion," *IEEE Transactions on Instrumentation and Measurement*, vol. 58, no. 11, 2009, doi: 10.1109/TIM.2009.2020819.

[20] C. Muscas, L. Peretto, S. Sulis, and R. Tinarelli, "Investigation on multipoint measurement techniques for PQ monitoring," *IEEE Transactions on Instrumentation and Measurement*, vol. 55, no. 5, 2006, doi: 10.1109/TIM.2006.880954.

[21] A. Spelko *et al.*, "CIGRE/CIRED JWG C4.42: Overview of common methods for assessment of harmonic contribution from customer installation," 2017. doi: 10.1109/PTC.2017.7981195.

[22] Ö. Gül and T. Gündoğdu, "Harmonic Contributions of Utility and Customer Based on Load Model Using Field Measurements," *Journal of Power and Energy Engineering*, vol. 03, no. 05, 2015, doi: 10.4236/jpee.2015.35002.

[23] T. Pfajfar, B. Blažič, and I. Papič, "Harmonic contributions evaluation with the harmonic current vector method," *IEEE Transactions on Power Delivery*, vol. 23, no. 1, 2008, doi: 10.1109/TPWRD.2007.911165.

[24] G. Artale, A. Cataliotti, V. Cosentino, D. di Cara, S. Nuccio, and G. Tine, "Arc Fault Detection Method Based on CZT Low-Frequency Harmonic Current Analysis," *IEEE Transactions on Instrumentation and Measurement*, vol. 66, no. 5, 2017, doi: 10.1109/TIM.2016.2627248.

[25] K. J. Lippert and T. A. Domitrovich, "AFCIs-from a standards perspective," *IEEE Transactions on Industry Applications*, vol. 50, no. 2, 2014, doi: 10.1109/TIA.2013.2272670.

[26] D. A. Dini, P. W. Brazis, and K. H. Yen, "Development of arc-fault circuit-interrupter requirements for photovoltaic systems," 2011. doi: 10.1109/PVSC.2011.6186301.

[27] W. Zheng and W. Wu, "Detecting low-voltage arc fault based on lifting multiwavelet," in *PACIIA 2009 - 2009 2nd Asia-Pacific Conference on Computational Intelligence and Industrial Applications*, 2009, vol. 2. doi: 10.1109/PACIIA.2009.5406646.

[28] C. E. Restrepo, "Arc fault detection and discrimination methods," 2007. doi: 10.1109/HOLM.2007.4318203.

[29] J. C. Engel, "Combination AFCIs: What they will and will not do," 2012. doi: 10.1109/ESW.2012.6165548.

[30] G. D. Gregory, K. Wong, and R. F. Dvorak, "More about arc-fault circuit interrupters," *IEEE Transactions on Industry Applications*, vol. 40, no. 4, 2004, doi: 10.1109/TIA.2004.831287.

[31] A. E. Ibhaze, M. U. Akpabio, and T. O. Akinbulire, "A review on smart metering infrastructure," *International Journal of Energy Technology and Policy*, vol. 16, no. 3. 2020. doi: 10.1504/IJETP.2020.107019.

[32] L. Hernández-Callejo, "A comprehensive review of operation and control, maintenance and lifespan management, grid planning and design, and metering in smart grids," *Energies*, vol. 12, no. 9. 2019. doi: 10.3390/en12091630.

[33] G. Dileep, "A survey on smart grid technologies and applications," *Renewable Energy*, vol. 146, 2020, doi: 10.1016/j.renene.2019.08.092.

[34] Y. Kabalci, "A survey on smart metering and smart grid communication," *Renewable and Sustainable Energy Reviews*, vol. 57. 2016. doi: 10.1016/j.rser.2015.12.114.

[35] N. Andreadou, M. O. Guardiola, and G. Fulli, "Telecommunication technologies for smart grid projects with focus on smart metering applications," *Energies*, vol. 9, no. 5. 2016. doi: 10.3390/en9050375.

[36] S. Prasad and D. M. V. Kumar, "Trade-offs in PMU and IED deployment for active distribution state estimation using multi-objective evolutionary algorithm," *IEEE Transactions on Instrumentation and Measurement*, vol. 67, no. 6, 2018, doi: 10.1109/TIM.2018.2792890.

[37] A. D. Femine, D. Gallo, C. Landi, and M. Luiso, "The design of a low cost phasor measurement unit," *Energies*, vol. 12, no. 14, 2019, doi: 10.3390/en12142648.

[38] M. Bertocco, G. Frigo, C. Narduzzi, C. Muscas, and P. A. Pegoraro, "Compressive Sensing of a Taylor-Fourier Multifrequency Model for Synchrophasor Estimation," *IEEE Transactions on Instrumentation and Measurement*, vol. 64, no. 12, 2015, doi: 10.1109/TIM.2015.2450295.

[39] A. von Meier, E. Stewart, A. McEachern, M. Andersen, and L. Mehrmanesh, "Precision Micro-Synchrophasors for Distribution Systems: A Summary of Applications," *IEEE Transactions on Smart Grid*, vol. 8, no. 6, 2017, doi: 10.1109/TSG.2017.2720543.

[40] E. Dusabimana and S. G. Yoon, "A survey on the micro-phasor measurement unit in distribution networks," *Electronics (Switzerland)*, vol. 9, no. 2. 2020. doi: 10.3390/electronics9020305.

[41] Y. Liu, L. Wu, and J. Li, "D-PMU based applications for emerging active distribution systems: A review," *Electric Power Systems Research*, vol. 179. 2020. doi: 10.1016/j.epsr.2019.106063.

[42] M. Hojabri, U. Dersch, A. Papaemmanouil, and P. Bosshart, "A comprehensive survey on phasor measurement unit applications in distribution systems," *Energies*, vol. 12, no. 23. 2019. doi: 10.3390/en12234552.

[43] T. M. Soares, U. H. Bezerra, and M. E. de Lima Tostes, "Full-observable three-phase state estimation algorithm applied to electric distribution grids," *Energies*, vol. 12, no. 7, 2019, doi: 10.3390/en12071327.

[44] M. Ginocchi, A. Ahmadifar, F. Ponci, and A. Monti, "Application of a smart grid interoperability testing methodology in a real-time hardware-in-the-loop testing environment," *Energies*, vol. 13, no. 7, 2020, doi: 10.3390/en13071648.

[45] E. de Din, M. Pau, F. Ponci, and A. Monti, "A coordinated voltage control for overvoltage mitigation in LV distribution grids," *Energies*, vol. 13, no. 8, 2020, doi: 10.3390/en13082007.

[46] G. Artale *et al.*, "Incremental heuristic approach for meter placement in radial distribution systems," *Energies*, vol. 12, no. 20, 2019, doi: 10.3390/en12203917.

[47] C. Lin, W. Wu, and Y. Guo, "Decentralized Robust State Estimation of Active Distribution Grids Incorporating Microgrids Based on PMU Measurements," *IEEE Transactions on Smart Grid*, vol. 11, no. 1, 2020, doi: 10.1109/TSG.2019.2937162.

[48] X. Kong *et al.*, "A hybrid state estimator based on SCADA and PMU measurements for medium voltage distribution system," *Applied Sciences (Switzerland)*, vol. 8, no. 9, 2018, doi: 10.3390/app8091527.

[49] L. Kamyabi, S. Esmaeili, and M. H. Rezaeian Koochi, "Power quality monitor placement in power systems considering channel limits and estimation error at unobservable buses using a bi-level approach," *International Journal of Electrical Power and Energy Systems*, vol. 102, 2018, doi: 10.1016/j.ijepes.2018.05.002.

[50] D. B. Avancini, J. J. P. C. Rodrigues, S. G. B. Martins, R. A. L. Rabêlo, J. Al-Muhtadi, and P. Solic, "Energy meters evolution in smart grids: A review," *Journal of Cleaner Production*, vol. 217, 2019, doi: 10.1016/j.jclepro.2019.01.229.

[51] L. Wen, K. Zhou, S. Yang, and L. Li, "Compression of smart meter big data: A survey," *Renewable and Sustainable Energy Reviews*, vol. 91. 2018. doi: 10.1016/j.rser.2018.03.088.

[52] D. Alahakoon and X. Yu, "Smart Electricity Meter Data Intelligence for Future Energy Systems: A Survey," *IEEE Transactions on Industrial Informatics*, vol. 12, no. 1, 2016, doi: 10.1109/TII.2015.2414355.

[53] K. Sharma and L. M. Saini, "Power-line communications for smart grid: Progress, challenges, opportunities and status," *Renewable and Sustainable Energy Reviews*, vol. 67. 2017. doi: 10.1016/j.rser.2016.09.019.

[54] A. Sendin, I. Peña, and P. Angueira, "Strategies for power line communications smart metering network deployment," *Energies*, vol. 7, no. 4. 2014. doi: 10.3390/en7042377.

[55] S. Rinaldi *et al.*, "On the mobile communication requirements for the demand-side management of electric vehicles," *Energies*, vol. 11, no. 5, 2018, doi: 10.3390/en11051220.

[56] G. Artale *et al.*, "A resilient distributed measurement system for smart grid application," in *Communications in Computer and Information Science*, 2020, vol. 1284 CCIS. doi: 10.1007/978-3-030-59000-0_11.

[57] A. Cataliotti *et al.*, "An Improved Load Flow Method for MV Networks Based on LV Load Measurements and Estimations," *IEEE Transactions on Instrumentation and Measurement*, vol. 68, no. 2, 2019, doi: 10.1109/TIM.2018.2847818.

[58] G. Artale *et al.*, "Real-Time Power Flow Monitoring and Control System for Microgrids Integration in Islanded Scenarios," *IEEE Transactions on Industry Applications*, vol. 55, no. 6, 2019, doi: 10.1109/TIA.2019.2932967.

[59] A. Cataliotti, V. Cosentino, D. di Cara, S. Guaiana, N. Panzavecchia, and G. Tinè, "A New Solution for Low-Voltage Distributed Generation Interface Protection System," *IEEE Transactions on Instrumentation and Measurement*, vol. 64, no. 8, 2015, doi: 10.1109/TIM.2015.2421691.

[60] G. Artale *et al.*, "A new PLC-based smart metering architecture for medium/low voltage grids: Feasibility and experimental characterization," *Measurement: Journal of the International Measurement Confederation*, vol. 129, 2018, doi: 10.1016/j.measurement.2018.07.070.

[61] G. Artale *et al.*, "A New Low Cost Coupling System for Power Line Communication on Medium Voltage Smart Grids," *IEEE Transactions on Smart Grid*, vol. 9, no. 4, 2018, doi: 10.1109/TSG.2016.2630804.

[62] Italian Electrical Committee (CEI), "CEI 0-21:2014-09. Reference technical rules for the connection of active and passive users to the LV electrical Utilities," *Technical standard CEI*. 2014.

[63] I. Hussain, S. Mohsin, A. Basit, Z. A. Khan, U. Qasim, and N. Javaid, "A review on demand response: Pricing, optimization, and appliance scheduling," in *Procedia Computer Science*, 2015, vol. 52, no. 1. doi: 10.1016/j.procs.2015.05.141.

[64] Joint Committee for Guides in Metrology, "Evaluation of measurement data — Supplement 1 to the 'Guide to the expression of uncertainty in measurement' — Propagation of distributions using a Monte Carlo method," *Evaluation*, vol. JCGM 101:2, 2008.

[65] A. Cataliotti, V. Cosentino, S. Nuccio, D. di Cara, N. Panzavecchia, and G. Tine, "A simplified approach for load flow analysis in MV smart grids based on LV power measurements," 2017. doi: 10.1109/I2MTC.2017.7969686.

[66] P. Y. Kong, "A Distributed Management Scheme for Energy Storage in a Smart Grid with Communication Impairments," *IEEE Transactions on Industrial Informatics*, vol. 14, no. 4, 2018, doi: 10.1109/TII.2017.2761819.

[67] I. Ranaweera and O. M. Midtgård, "Optimization of operational cost for a grid-supporting PV system with battery storage," *Renewable Energy*, vol. 88, 2016, doi: 10.1016/j.renene.2015.11.044.

[68] M. Z. Daud and A. Mohamed, "Heuristic optimisation of state-of-charge feedback controller for hourly dispatch of hybrid PV/BES system," 2014. doi: 10.1109/ISGT-Asia.2014.6873774.

[69] Mc. C. Guerrero Delgado, J. Sánchez Ramos, S. Álvarez Domínguez, J. A. Tenorio Ríos, and L. F. Cabeza, "Building thermal storage technology: Compensating renewable energy fluctuations," *Journal of Energy Storage*, vol. 27, 2020, doi: 10.1016/j.est.2019.101147.

[70] A. Nottrott, J. Kleissl, and B. Washom, "Energy dispatch schedule optimization and cost benefit analysis for grid-connected, photovoltaic-battery storage systems," *Renewable Energy*, vol. 55, 2013, doi: 10.1016/j.renene.2012.12.036.

[71] X. Hu, S. Li, and H. Peng, "A comparative study of equivalent circuit models for Li-ion batteries," *Journal of Power Sources*, vol. 198, 2012, doi: 10.1016/j.jpowsour.2011.10.013.

[72] M. A. Hannan, M. S. H. Lipu, A. Hussain, and A. Mohamed, "A review of lithium-ion battery state of charge estimation and management system in electric vehicle applications: Challenges and recommendations," *Renewable and Sustainable Energy Reviews*, vol. 78. 2017. doi: 10.1016/j.rser.2017.05.001.

[73] J. Jiang and C. Zhang, *Fundamentals and application of lithium-ion batteries in electric drive vehicles*. 2015. doi: 10.1002/9781118414798.

[74] H. He, R. Xiong, and J. Fan, "Evaluation of lithium-ion battery equivalent circuit models for state of charge estimation by an experimental approach," *Energies*, vol. 4, no. 4, 2011, doi: 10.3390/en4040582.

[75] P. Siano, "Demand response and smart grids - A survey," *Renewable and Sustainable Energy Reviews*, vol. 30. 2014. doi: 10.1016/j.rser.2013.10.022.

[76] G. Artale *et al.*, "A monitoring and management system for energy storage integration in smart grids," in *I2MTC 2019 - 2019 IEEE International Instrumentation and Measurement Technology Conference, Proceedings*, 2019, vol. 2019-May. doi: 10.1109/I2MTC.2019.8826964.

[77] G. Hao and W. Hongtao, "Day-ahead generation scheduling for variable energy resources considering demand response," in *Asia-Pacific Power and Energy Engineering Conference, APPEEC*, 2016, vol. 2016-December. doi: 10.1109/APPEEC.2016.7779852.

[78] L. A. Arias, E. Rivas, F. Santamaria, and V. Hernandez, "A review and analysis of trends related to demand response," *Energies*, vol. 11, no. 7. 2018. doi: 10.3390/en11071617.

[79] K. G. di Santo, S. G. di Santo, R. M. Monaro, and M. A. Saidel, "Active demand side management for households in smart grids using optimization and artificial intelligence," *Measurement: Journal of the International Measurement Confederation*, vol. 115, 2018, doi: 10.1016/j.measurement.2017.10.010.

[80] R. Luthander, J. Widén, D. Nilsson, and J. Palm, "Photovoltaic self-consumption in buildings: A review," *Applied Energy*, vol. 142. 2015. doi: 10.1016/j.apenergy.2014.12.028.

[81] J. A. M. Sm, X. W. Ma, and K. Tomsovic, "Overview and literature survey of fuzzy set theory in power systems," *IEEE Transactions on Power Systems*, vol. 10, no. 3, 1995, doi: 10.1109/59.466473.

[82] L. A. Zadeh, "Fuzzy sets," *Information and Control*, vol. 8, no. 3, 1965, doi: 10.1016/S0019-9958(65)90241-X.

[83]   J. Mindykowski and T. Tarasiuk, "Problems of power quality in the wake of ship technology development," *Ocean Engineering*, vol. 107, 2015, doi: 10.1016/j.oceaneng.2015.07.036.

[84]   A. E. Emanuel, "On the assessment of harmonic pollution," *IEEE Transactions on Power Delivery*, vol. 10, no. 3, 1995, doi: 10.1109/61.400958.

[85]   E. J. Davis, A. E. Emanuel, and D. J. Pileggi, "Evaluation of single-point measurements method for harmonic pollution cost allocation," *IEEE Transactions on Power Delivery*, vol. 15, no. 1, 2000, doi: 10.1109/61.847222.

[86]   A. Ferrero, A. Menchetti, and R. Sasdelli, "Measurement of the Electric Power Quality and Related Problems," *European Transactions on Electrical Power*, vol. 6, no. 6, 1996, doi: 10.1002/etep.4450060607.

[87]   A. Cataliotti, V. Cosentino, D. di Cara, A. Lipari, and S. Nuccio, "A DAQ-based sampling wattmeter for IEEE Std. 1459-2010 powers measurements. Uncertainty evaluation in nonsinusoidal conditions," *Measurement: Journal of the International Measurement Confederation*, vol. 61, 2015, doi: 10.1016/j.measurement.2014.10.033.

[88]   R. Abu-hashim *et al.*, "Test systems for harmonics modeling and simulation," *IEEE Transactions on Power Delivery*, vol. 14, no. 2, 1999, doi: 10.1109/61.754106.

[89]   A. Cataliotti, V. Cosentino, and S. Nuccio, "Comparison of nonactive powers for the detection of dominant harmonic sources in power systems," *IEEE Transactions on Instrumentation and Measurement*, vol. 57, no. 8, 2008, doi: 10.1109/TIM.2008.925338.

[90]   International Electrotechnical Commission., "IEC 61000-4-15, Electromagnetic compatibility (EMC). Part 4: Testing and measurement techniques-General guide on harmonics and interharmonics measurements and instrumentation, for power supply systems and equipment connected thereto," *Iec 61000-4-7*, vol. Second edi, no. Agosto, 2002.

[91]   I. Papic *et al.*, "A Benchmark Test System to Evaluate Methods of Harmonic Contribution Determination," *IEEE Transactions on Power Delivery*, vol. 34, no. 1, 2019, doi: 10.1109/TPWRD.2018.2817542.

[92]   W. Xu and Y. Liu, "A method for determining customer and utility harmonic contributions at the point of common coupling," *IEEE Transactions on Power Delivery*, vol. 15, no. 2, 2000, doi: 10.1109/61.853023.

[93]   E. M. G. Rodrigues, R. Godina, M. Shafie-Khah, and J. P. S. Catalão, "Experimental results on a wireless wattmeter device for the integration in home energy management systems," *Energies*, vol. 10, no. 3, 2017, doi: 10.3390/en10030398.

[94]   T. Atalik *et al.*, "Multipurpose platform for power system monitoring and analysis with sample grid applications," *IEEE Transactions on Instrumentation and Measurement*, vol. 63, no. 3, 2014, doi: 10.1109/TIM.2013.2281556.

[95]   G. Pellegrinelli, M. Baù, F. Cerini, S. Dalola, M. Ferrari, and V. Ferrari, "Portable energy-logger circuit for the experimental evaluation of energy harvesting solutions from motion for wearable autonomous sensors," in *Procedia Engineering*, 2014, vol. 87. doi: 10.1016/j.proeng.2014.11.405.

[96] P. Castello, C. Muscas, P. A. Pegoraro, and S. Sulis, "Low-cost energy meter with power quality functionalities," 2020.

[97] F. Leccese, M. Cagnetti, S. di Pasquale, S. Giarnetti, and M. Caciotta, "A new power quality instrument based on raspberry-pi," *Electronics (Switzerland)*, vol. 5, no. 4, 2016, doi: 10.3390/electronics5040064.

[98] E. Viciana, A. Alcayde, F. G. Montoya, R. Baños, F. M. Arrabal-Campos, and F. Manzano-Agugliaro, "An open hardware design for internet of things power quality and energy saving solutions," *Sensors (Switzerland)*, vol. 19, no. 3, 2019, doi: 10.3390/s19030627.

[99] E. Viciana *et al.*, "OpenZmeter: An efficient low-cost energy smart meter and power quality analyzer," *Sustainability (Switzerland)*, vol. 10, no. 11, 2018, doi: 10.3390/su10114038.

[100] IEC TC 77, "Electromagnetic compatibility (EMC) Part 4-7: Testing and measurement techniques - General guide on harmonics and interharmonics measurements and instrumentation, for power supply systems and equipment connected thereto," 2009.

[101] International Electrotechnical Commission, "Electromagnetic compatibility (EMC) Part 4-30: Testing and measurement techniques Power quality measurement methods," *IEC Standard*, vol. 61000-4–30, 2003.

[102] G. Artale *et al.*, "PQ Metrics Implementation on Low Cost Smart Metering Platforms. A Case Study Analysis," 2018. doi: 10.1109/AMPS.2018.8494866.

[103] A. Cataliotti *et al.*, "Compensation of Nonlinearity of Voltage and Current Instrument Transformers," *IEEE Transactions on Instrumentation and Measurement*, vol. 68, no. 5, 2019, doi: 10.1109/TIM.2018.2880060.

[104] G. Artale *et al.*, "Measurement of Simplified Single- And Three-Phase Parameters for Harmonic Emission Assessment Based on IEEE 1459-2010," *IEEE Transactions on Instrumentation and Measurement*, vol. 70, 2021, doi: 10.1109/TIM.2020.3037949.

[105] G. Artale *et al.*, "Measurement uncertainty of harmonic emission indicators based on IEEE Std. 1459-2010," 2020. doi: 10.1109/I2MTC43012.2020.9128679.

[106] Z. Wu, Y. Hu, J. X. Wen, F. Zhou, and X. Ye, "A Review for Solar Panel Fire Accident Prevention in Large-Scale PV Applications," *IEEE Access*, vol. 8. 2020. doi: 10.1109/ACCESS.2020.3010212.

[107] K. Klement, "DC Arc Flash Studies for Solar Photovoltaic Systems: Challenges and Recommendations," *IEEE Transactions on Industry Applications*, vol. 51, no. 5, 2015, doi: 10.1109/TIA.2015.2431639.

[108] J. Yuventi, "DC electric arc-flash hazard-risk evaluations for photovoltaic systems," *IEEE Transactions on Power Delivery*, vol. 29, no. 1, 2014, doi: 10.1109/TPWRD.2013.2289921.

[109] J. A. Petersen, "National fire protection association standards in fire litigation," in *Engineering Standards for Forensic Application*, 2018. doi: 10.1016/B978-0-12-813240-1.00011-X.

[110] D. Giordano, D. Signorino, C. Landi, A. Delle Femine, M. Luiso, and G. Crotti, "Power quality in DC railway system: A facility to characterize the on-board detection systems," 2020.

[111] A. D. Femine, D. Gallo, D. Giordano, C. Landi, M. Luiso, and D. Signorino, "Power Quality Assessment in Railway Traction Supply Systems," *IEEE Transactions on Instrumentation and Measurement*, vol. 69, no. 5, 2020, doi: 10.1109/TIM.2020.2967162.

[112] G. Crotti *et al.*, "Pantograph-To-OHL Arc: Conducted Effects in DC Railway Supply System," *IEEE Transactions on Instrumentation and Measurement*, vol. 68, no. 10, 2019, doi: 10.1109/TIM.2019.2902805.

[113] Z. Zhang, Q. Chen, R. Xie, and K. Sun, "The Fault Analysis of PV Cable Fault in DC Microgrids," *IEEE Transactions on Energy Conversion*, vol. 34, no. 1, 2019, doi: 10.1109/TEC.2018.2876669.

[114] K. Abdulmawjood, S. S. Refaat, and W. G. Morsi, "Detection and prediction of faults in photovoltaic arrays: A review," 2018. doi: 10.1109/CPE.2018.8372609.

[115] Q. Xiong *et al.*, "Series arc fault detection and localization in DC distribution system," *IEEE Transactions on Instrumentation and Measurement*, vol. 69, no. 1, 2020, doi: 10.1109/TIM.2019.2890892.

[116] S. Liu, L. Dong, X. Liao, X. Cao, X. Wang, and B. Wang, "Application of the Variational Mode Decomposition-Based Time and Time-Frequency Domain Analysis on Series DC Arc Fault Detection of Photovoltaic Arrays," *IEEE Access*, vol. 7, 2019, doi: 10.1109/ACCESS.2019.2938979.

[117] W. Miao, X. Liu, K. H. Lam, and P. W. T. Pong, "Arc-Faults Detection in PV Systems by Measuring Pink Noise with Magnetic Sensors," *IEEE Transactions on Magnetics*, vol. 55, no. 7, 2019, doi: 10.1109/TMAG.2019.2903899.

[118] W. Fenz, S. Thumfart, R. Yatchak, H. Roitner, and B. Hofer, "Detection of Arc Faults in PV Systems Using Compressed Sensing," *IEEE Journal of Photovoltaics*, vol. 10, no. 2, 2020, doi: 10.1109/JPHOTOV.2020.2965397.

[119] M. Ahmadi, H. Samet, and T. Ghanbari, "Series Arc Fault Detection in Photovoltaic Systems Based on Signal-to-Noise Ratio Characteristics Using Cross-Correlation Function," *IEEE Transactions on Industrial Informatics*, vol. 16, no. 5, 2020, doi: 10.1109/TII.2019.2909753.

[120] A. Reatti, M. K. Kazimierczuk, M. Catelani, and L. Ciani, "Monitoring and field data acquisition system for hybrid static concentrator plant," *Measurement: Journal of the International Measurement Confederation*, vol. 98, 2017, doi: 10.1016/j.measurement.2015.06.022.

[121] R. I. S. Pereira, I. M. Dupont, P. C. M. Carvalho, and S. C. S. Jucá, "IoT embedded linux system based on Raspberry Pi applied to real-time cloud monitoring of a decentralized photovoltaic plant," *Measurement: Journal of the International Measurement Confederation*, vol. 114, 2018, doi: 10.1016/j.measurement.2017.09.033.

[122] N. Erraissi, M. Raoufi, N. Aarich, M. Akhsassi, and A. Bennouna, "Implementation of a low-cost data acquisition system for 'PROPRE.MA' project," *Measurement: Journal of the*

International Measurement Confederation, vol. 117, 2018, doi: 10.1016/j.measurement.2017.11.058.

[123] G. Artale *et al.*, "Characterization of DC series arc faults in PV systems based on current low frequency spectral analysis," *Measurement: Journal of the International Measurement Confederation*, vol. 182, 2021, doi: 10.1016/j.measurement.2021.109770.

[124] G. Artale *et al.*, "DC series arc faults in PV systems. Detection methods and experimental characterization," 2020.

[125] S. Lu, B. T. Phung, and D. Zhang, "A comprehensive review on DC arc faults and their diagnosis methods in photovoltaic systems," *Renewable and Sustainable Energy Reviews*, vol. 89. 2018. doi: 10.1016/j.rser.2018.03.010.

[126] Z. Yi and A. H. Etemadi, "A novel detection algorithm for Line-to-Line faults in Photovoltaic (PV) arrays based on support vector machine (SVM)," in *IEEE Power and Energy Society General Meeting*, 2016, vol. 2016-November. doi: 10.1109/PESGM.2016.7742026.

[127] Y. Zhao, R. Ball, J. Mosesian, J. F. de Palma, and B. Lehman, "Graph-based semi-supervised learning for fault detection and classification in solar photovoltaic arrays," *IEEE Transactions on Power Electronics*, vol. 30, no. 5, 2015, doi: 10.1109/TPEL.2014.2364203.